

Raman Spectroscopy applied to the mineralogical analysis of flooded chalk

by

Laura Borrromeo

Thesis submitted in fulfilment of
the requirements for the degree of
PHILOSOPHIAE DOCTOR
(PhD)



Faculty of Science and Technology
Department of Energy Resources, University of Stavanger, Norway
2018

University of Stavanger
NO-4036 Stavanger
NORWAY
www.uis.no

©2018 Laura Borrromeo

ISBN:

ISSN:

PhD: Thesis UiS No.

Acknowledgements

First of all, I would like to express my immense gratitude to my supervisor **Prof. Udo Zimmermann** for providing me with the possibility to conduct and complete this PhD project. He gave me the freedom that I needed to grow up like, always helping me when I needed him. It is not common to find a person that takes in consideration other people's necessities and ideas as he does. In these four years he entrusted my independence, giving me the chance to build up my PhD project with my imprinting, but never the less guiding and inspiring me.

Vorrei ringraziare il mio co-supervisor **Prof. Sergio Andò** per avermi insegnato grandissima parte di quello che so, per avermi sopportato per oltre una decade nonostante il mio brutto carattere. La tua spinta costante mi rende ogni giorno migliore... Sembra di no, ma ascolto sempre.

Inoltre vorrei ringraziare il **Prof. Eduardo Garzanti** per avermi ospitato durante il mio dottorato nel suo gruppo ed avermi trattato come se fossi ancora una di voi, nonostante fossi scappata via. Grazie di cuore anche per tutti i consigli ed aiuti... da te si impara sempre. Grazie anche per tutti i pranzi con quelle chiacchierate provocatorie che, in fondo, ci divertono tanto.

Infinite grazie anche al **Prof. Danilo Bersani** per aver tentato, spero con successo, di trasmettermi qualche goccia delle sue vaste conoscenze e al **Dr. Riccardo Tagliapietra** per avermi aiutato spesso e volentieri.

Furthermore I would like to really thank **Chiara, Mona, and Nina** for their constant help and support, and for the happy times we spent together.

I would like to thank **Prof. Merete Vadla Madland, Dr. Reidar I. Korsnes,** and **Prof. Anders Nerموen,** who accomplished the flooding experiments performed on the three chalk samples investigated in this study and to all the co-authors of my publications and contributions.

Un grande grazie anche a **Giovanni Coletti** e alla **Prof. Daniela Basso** per avermi fatto dare una sbirciata nel loro bellissimo mondo marino.

I would like to thank all the people that helped me during these years at UiS, especially **Emera** that opened me her marvellous family and made me always feeling welcome in Norway. I will never forget what you did for me. Another thank also to **Lena** and **Caroline** that have been always very friendly to me.

Grazie anche a Marco, Giovanni, Alberto, Mara, Giuditta, Chiara, per il tempo e le chiacchiere insieme.

Moreover I would like to thank the NIOR Centre of Norway for the grant to carry out this study, to the Research Council of Norway and to the industry partners: ConocoPhillips Skandinavia AS, Aker BP ASA, Eni Norge AS, Maersk Oil Norway AS, Statoil Petroleum AS, ENGIE EandP NORGE AS, Lundin Norway AS, Halliburton AS, Schlumberger Norge AS, Wintershall Norge AS, DEA Norge AS of The National IOR Centre of Norway for support.

In ultimo vorrei ringraziare la mia famiglia, amici, ballerini e allievi che hanno sopportato e supportato la mia doppia vita.

Summary

Understanding the interactions between chalk and injected fluids is a major goal in Enhanced Oil Recovery (EOR), because the consequent mineralogical and mechanical alterations modify the mechanical strength, the porosity, and the permeability of injected rocks. In turn, these changes affect the oil flow pathways and the reservoir potential. For this reason, a thorough investigation of the crystallization of secondary minerals after the injection of MgCl_2 , a common brine used in EOR, is of paramount importance.

Firstly, this PhD project has demonstrated that Raman spectroscopy is sufficiently sensitive to chemical and structural changes in magnesian calcites to allow us to estimate the ratio between Ca^{2+} and Mg^{2+} in the solid solution calcite-magnesite. It is important to keep in mind that the magnesium content in fossil faunas and floras provides information about the habits and the habitat of organisms. Therefore, this powerful tool opens up new perspectives in provenance, marine-biology, and palaeontological studies.

Secondly, Raman spectroscopy and Tip-Enhanced Raman Spectroscopy (TERS), together with complementary research methods (SEM-EDS, WDS, TEM), were used to investigate the mineralogical changes that follow dissolution and compaction in MgCl_2 injected chalk. These two methodologies provided a full range of new information on three flooded-chalk cores.

This project confirmed that Raman spectroscopy is a robust, user-friendly, and relatively cheap point-analysis technique that, with almost no sample preparation and in a non-destructive way, allows us to quickly obtain semi-quantitative mineralogical and chemical data down to the micrometric scale.

Until today, Raman spectroscopy has been only occasionally applied in the oil industry. It is high time for it to become a routine analytical method, on-shore and off-shore, for the exploration of conventional and unconventional reservoirs, including siltstones, sandstones, and chalk.

Finally, this PhD project has documented the first application of TERS on rocks, including chalk. These results qualify TERS as an interesting investigation tool in this field, even if it is quite expensive and if the complex sample preparation required and the long acquisition times prevent its general use as a characterization tool. The best way to exploit the potentiality of TERS in hydrocarbon research is to investigate those key samples where nano-scale information is essential.

Table of Contents

Acknowledgements.....	iii
Summary.....	v
1 Introduction.....	1
2 Objective.....	7
3 Raman spectroscopy.....	9
3.1 The discovery of the Raman scattering.....	9
3.2 The Theory behind the method.....	18
3.2.1 Quantum-mechanical model.....	21
3.3 The Raman spectrum.....	24
3.4 The Raman spectrometer.....	28
3.4.1 Lasers.....	29
3.4.2 The confocal microscope.....	33
3.4.3 The Raman spectrometer.....	36
3.5 Tip-Enhanced Raman Spectroscopy.....	40
3.6 Raman spectra of carbonate minerals.....	44
3.7 Spectra of non-carbonate minerals.....	47
3.8 Advantages and disadvantages of Raman spectroscopy.....	49
3.9 Nowadays Raman spectroscopy technical improvements and applications	51
4 Samples for this research project.....	63
4.1 Carbonate minerals.....	63
4.2 Biological magnesium calcites.....	66
4.3 Flooded chalk.....	70
4.3.1 Liège chalk.....	72
4.3.2 Previous studies and characterisation of the sample material.....	75
4.3.3 Flooding experiments.....	79
5 Methodology.....	82
5.1 Raman Spectroscopy.....	82
5.2 Tip-Enhanced Raman Spectroscopy, TERS.....	84
5.3 How to perform an analysis with a confocal Raman spectrometer.....	88
5.4 Additional procedure to perform an analysis with a TERS spectrometer.....	91

5.5	Processing of Raman spectra.....	95
5.6	EDS - SEM and EMPA - WDS microprobes	97
6	Publications.....	101
6.1	Raman Spectroscopy as a tool for magnesium estimation in Mg-calcite; Borromeo et al. 2017a	102
6.2	Quick, easy and economic mineralogical studies of flooded chalk for EOR experiments using Raman spectroscopy; Borromeo et al. 2018a	114
6.3	Application of Tio-Enhanced Raman Spectroscopy for the nanoscale characterization of flooded chalk; Borromeo et al. 2018b.....	134
7	Other contributions.....	164
7.1	Conferences	164
7.2	Fieldwork and Laboratory work as student assistant.....	167
8	Discussion	169
9	Conclusions.....	176
10	References.....	179
	Appendices	198

Table of Figures

Figure 1 - When a monochromatic light (laser; in green on the left) beam a molecule of calcite, 1/1.000.000 photon is scattered with a different wavelength that is characteristic of the sample and its chemical bonds (inelastic scattering, Raman signal, in red). The major part of the photons is scattered with no change in wavelength, constituting the Rayleigh scattering (in green, on the right).....	2
Figure 2a and 2b - C. V. Raman with his first spectrometer to the left and the stamp at him dedicated to the right.	9
Figure 3 - Sir Kariamanickam Srivasa Krishnan.	10
Figure 4 – a) The Figure shows the experiment carried out by C. V. Raman to demonstrate the existence of the inelastic scattering: a telescope was aimed at the sun, and the light so collected was made passing first through a monochromatic filter and then to several liquids. The Indian scientist could proved that the wavelength was changed from the initial one as, by observing the light with a crossed filter that blocked the monochromatic portion of the light, a portion of light could still pass the filter, demonstrating that a change in wavelength was happened. Figure and caption from: Dissemination of IT for the Promotion of Materials Science (DoITPoMS), Teaching and learning packages (TLPs), University of Cambridge http://www.doitpoms.ac.uk/tlplib/raman	12
Figure 5 - a): C. V: Raman and his disciples/colleague K.S. Krishnan reported their discovery in March 1928 on the famous journal Nature. ^(Raman and Krishnan, 1928a)	14
Figure 6 - Quartz, calcite and selenite Raman spectra and their peaks position, reported in Krishnan, 1929.....	15
Figure 7 - The Soviet physicists Leonid Mandelstam (a) and Grigory Landsberg (b) that discovered the Raman scattering at the University of Moscow, one week before C.V. Raman, naming it “ <i>combinatorial scattering of light</i> ”.....	16
Figure 8 - Most photons will scatter from the sample with no change in wavelength: so-called Rayleigh scattering. A small number	

(1/1.000.000) of photons will however change frequency and this phenomenon is called Raman scattering (formed by Stokes and Anti-Stokes scatterings). Modified after Butler et al. 2016..... 18

Figure 9 - In-plane and out-plane vibrational modes types. 20

Figure 10 - Energy level diagram (Jablonski diagram) showing the interactions of the different light scatterings with molecules at different energy states. Modified after Neuville et al. 2014..... 21

Figure 11 - Comparison of the Stokes ($\nu - \nu_{\text{vibr}}$) and anti-Stokes ($\nu_0 + \nu_{\text{vibr}}$) parts of the Raman spectrum. Spectrum of crocoite (Callenberg, Germany) excited with the Ar⁺ 514.5 nm line (which corresponds to 19435 cm⁻¹). Raman bands in the Stokes and anti-Stokes parts of the spectrum have the same Raman shift values (= relative wavenumbers, with 0 cm⁻¹ Raman shift set at the Rayleigh line). Note that Stokes bands are always higher in intensity than their anti-Stokes counterparts, with the intensity ratio increasing with increasing Raman shift. Note also that some workers use an opposite convention, with Stokes called negative and anti-Stokes called positive on the grounds that the Stokes Raman bands are actually lower in absolute cm⁻¹ than the Rayleigh line. To elucidate the interrelation of absolute and relative wavenumbers, frequencies and wavelengths, the X axis is given with three additional scales at the top. Figure and caption from Nasdala et al. 2004..... 25

Figure 12 - Magnesite Raman spectrum with its four stronger vibrational modes. T, *translational mode*; L, *librational mode*; ν_1 , *symmetric stretching mode*; ν_4 , *in-plane bending mode*. This spectrum was collected with the Renishaw InVia spectrometer. 26

Figure 13 - Studying its Raman spectrum, lots of information can be obtained about a mineral, such as chemistry and symmetry (from the peaks position), structural disorder (from peaks width), concentration (from peaks intensity), orientation of the crystal (from the relative intensity of a peak in comparison to the other bands present in the spectrum) and sometimes also about the temperature and stress condition of crystallization (from

the shift in position respect the ones observed in standard crystals). Modified after Durickovic, 2016.	27
Figure 14 - General scheme of the processes involved in collecting a Raman spectrum. Modified after Murphy et al. 2011.	28
Figure 15 - Different laser lines in use in various scientific fields, with their colour, and wavelength. From Gourzoulidis et al. 2017.	29
Figure 16 - Raman spectra of the same sample of aragonite, recorded with a different spectral resolution with 632.8 and 473.1 nm excitation wavelengths. Figure and caption from Bersani et al. 2016.	30
Figure 17 - Three Raman spectra of the same pigment acquired with a 532 nm, a 633 nm and a 785 nm laser lines. Spectra are courtesy of Horiba scientific: Lecture on Raman Scattering and Fluorescence Emission.	32
Figure 18 - Simplified schematic diagram of a confocal microscope. The confocal aperture allows all of the in-focus light (in blue) from the sample region of interest to pass through to the detector and avoid that the out-of-focus signal reaches the CCD. As such very little of this light gets through to the detector. Mofied after: Lecture on Photonics and Nanophotonics Trinity College Dublin.	33
Figure 19 - As a simple example for confocality effects, we present two Raman spectra taken from a carbon dioxide inclusion (~ 12 µm diameter) inside a topaz grain in a polished rock slice of a greisen from Cinovec, Czech Republic. In the regular, i.e., the non-confocal mode (upper spectrum), a complex Raman spectrum is obtained, which consists of vibrational bands of the included CO ₂ gas, the host mineral and also the araldite epoxy used to attach the polished section to a glass slide (about 20 µm behind the CO ₂ inclusion). With a narrow confocal diaphragm placed in the optical beam path (lower spectrum), internal CO ₂ vibrations are clearly obtained whereas topaz bands are largely suppressed and araldite bands are completely suppressed. Figure and caption from Nasdala et al. 2004.	34

Figure 20 - Sri Lanka Sapphire with an inclusion in P1; b) diaspore and CO ₂ inclusions present in P1, whose combined Raman spectrum is shown in panel c). Figure and caption from Palanza et al. 2008.....	35
Figure 21 - General scheme of a Raman Spectrometer. Sketch courtesy of Danilo Bersani.....	36
Figure 22 - On the diffraction grating, the inelastic scattering is decomposed into its wavelengths and detected by the CCD, Charge-Coupled-Device. At the same focal distance, a denser grating permits to collect a higher resolution spectrum, but can report, on the other hand, the detection of a limited Raman shifts interval. Modified after A. and B. Adl-Zarrabi, 2016.	38
Figure 23 - Photo of a typical CCD detector. From Swaminathan, 2012.	39
Figure 24 - TERS setup used in the present work, showing a tuning fork (TF) based AFM (Atomic Force Microscopy), scanning a surface composed of two phases, A and B, and a red laser is used at 60° and is focused on the apex of the tip. A near field spectrum would detect only the B component, where the tip is positioned. In case far field is detected, the spectrum would be the sum of the two components spectra (A+B). Figure and caption from Borromeo et al. 2018b.	40
Figure 25 - Example of the capabilities of the TERS instrument: on the left a topographic 1 μm x 1μm image of an azobenzenethiol self-assembled monolayer on gold, in the middle a TERS spectrum acquired in the area showing the peaks characteristic of the molecule and on the right the TERS mapping displaying the 1135 cm ⁻¹ peak intensity in the scanned region as a colour scale. It is worth noticing that the molecular monolayer does not give any signal in standard Raman, due to the low amount of material. It is therefore remarkable how the field enhancement due to the tip allows detecting clearly molecular features. Additional details on these systems can be found in Picardi, et al. (2014) and Toccafondi et al. (2016). Figure and caption from Borromeo et al. 2017b.	42
Figure 26 - Raman spectra of calcium and magnesium carbonates: dolomite (UNIMIB standard sample, Selvino, Italy); magnesite (M.A.C.	

certificated standard); calcite (UNIMIB standard sample, Chihuahua, Mexico, ~ 0 mol% MgCO₃), aragonite (UNIMIB – University of Milano Bicocca – standard sample, Val Formazza, Italy). Spectra with ‘R’ were analysed by the Renishaw inVia confocal Raman microscope and spectra with ‘H’ by Horiba Xplora. Stars represent the neon lamp emission line at 476.8 cm⁻¹ used for calibration with the Horiba XploRA spectrometer. Peak positions are reported without decimals. Figure and caption from Borromeo et al. 2018a. 44

Figure 27 - A brookite spectrum (identified in LT1_p1G) and one of a rutile (identified in LT2_D).The main peak of magnesite (labelled in red) is present in both of them at 1093 and 1094 cm ⁻¹ , since the two minerals are surrounded by this carbonate, species, which have a strong signal. Both spectra were collected whit the Horiba Xplora spectrometer. Stars represent the neon lamp emission line at 476.8 cm ⁻¹ used for calibration. Peak positions are reported without decimals. Figure and caption from Borromeo et al. 2018a.	48
Figure 28 - 2D mapping: single X-Y (a) and X-Z (b) optical sections on a sample. From Princeton Instruments, confocal Raman notes, http://forum.sci.ccny.cuny.edu/cores/microscopy-imaging/raman/Confocal-raman-note.pdf	52
Figure 29 - Structure of a 3D Data Cube: X and Y dimensions store spatial information, while Z-dimension stores spectral information from each spatial spot. From Princeton Instruments, confocal Raman notes, http://forum.sci.ccny.cuny.edu/cores/microscopy-imaging/raman/Confocal-raman-note.pdf	53
Figure 30 - Some of the most common mobile and portable Raman spectrometers. Photo courtesy of Danilo Bersani, for more information see Jehlička et al. 2014.	54
Figure 31 - Raman spectroscopy does not need sample preparation and can be performed directly on minerals, thin sections or cut gems.....	55
Figure 32 - Raman spectra of silicon and SiO ₂ crystalline polymorphs and amorphous states (New Raman spectra made with T64000	

	Raman spectrometer, with 488 nm excitation line). Figure and caption from Neuville et al. 2014.....	56
Figure 33 – a)	Monochrome image of diamond JUC29 taken under incident light, with the ringwoodite-walstromite inclusion pair highlighted by a red square. The irregular shape and hexagonal pits in the diamond are signs of significant resorption. b) Enlarged view of the area of the host diamond (rotated 90° relative to a) containing the ringwoodite - walstromite inclusion pair. The shadow behind the rectangular area outlining the inclusion pair is probably a stress fracture in the diamond. c) Raman spectra of ringwoodite and walstromite inclusions in Juína diamond JUC29. Raman spectra (unsmoothed, background-subtracted, in relative intensity units, stacked for clarity, shown in grey) for two-phase inclusion within JUC29 diamond, Juína. Spectra are complex, displaying SiO ₄ ²⁻ stretching modes for ringwoodite ([Mg,Fe]SiO ₄) that are broadened, probably by disordering induced by incipient retrogression, as well as the characteristic modes for Ca-walstromite (CaSiO ₃). Modified after Pearson et al. 2014.....	57
Figure 34 -	Pictures and micro-Raman spectra collected with both 785- and 473-nm lines on red gems identified as ruby simulants, as examples. Natural simulants: (a) R1, garnet; (b) R14, tourmaline. Artificial simulant: (c) R10, glass. Composite gem: (d) R15, doublet (data collected with 473-nm line are shown). Figure and caption from Barone et al. 2016.	58
Figure 35 - a)	Part of a mobile Raman system sitting on top of a very large precious Florentine black marble table in stone marquetry protected by 1.6 cm thick plate glass (reflections visible). Note the incrustated gemstones forming various ornamental designs, especially birds and flowers. Note the tripod suspending the remote head with its long focal length lens (black tube). Verification of the mineral species of a yellowish-white petal of an inlaid flower, using a red 632.8 nm laser beam (spot is seen as bright circle). The collection lens is suspended 7.5 cm above the crystal. b) The Raman spectrum obtained from one	

of the yellowish-white petals of the flower (corrected for background luminescence; solid graph) is shown in comparison with the spectrum of dolomite from Freiberg, Germany (dotted). The obtained spectrum reveals the four principal bands of dolomite. Photographs were taken by D.C. Smith; pictures and caption modified after Nasdala et al. 2004.	60
Figure 36 - Raman image of a tablet used for the treatment of Parkinson's disease. It contains two API's (levodopa – yellow, and benserazid - red) and four excipients (anhydrous citric acid – green, maize starch – cyan, magnesium stearate – magenta, and microcrystalline cellulose – blue). Photo courtesy of Renishaw plc.	61
Figure 37 – Calcite (a) and aragonite (b) crystals.	63
Figure 38 - Magnesite (a) and Dolomite (b) minerals.	65
Figure 39 - a) SEM-micrograph of unflooded chalk from the end-piece of the LTT-core (from Zimmermann et al. 2015a). Main components are coccoliths and fragments with a calcitic composition. b) SEM-micrograph of the severely altered part of the flooded core (LTT) towards the inlet of the core (from Zimmermann et al. 2015a). Coccoliths and other fossils are no longer visible, only crystals mainly below 1 µm in size, with high magnesium content. c) SEM-micrograph of unflooded chalk of the ULTT with main components as observed in a). d) SEM-micrograph from slice 5 of the ULTT after flooding with MgCl ₂ . Texture and composition is as observed in b). Figure and caption from Borromeo et al. 2018a.	72
Figure 40 – a) An example of a chalk rock sample , centimetric scale bar . b) A SEM micrograph of Liège chalk before flooding . Scale bar: 2 micron. From Wang et al. 2016.	73
Figure 41 - The most famous chalk cliff, the White cliff, near Dover.	73
Figure 42 - Chalk cliff at the Hallembaye CPL cave, near Liège in Belgium. 1.Top layer: displaced cover strata; 2. Upper bench: Lanaye (with regular flint layers) and top Lixhe members; 3. Middle bench: Lixhe member (unlayered small flint appearance) and Vijlen member (grey chalk); 4. Lowermost bench: Zeven	

Wegen Member (with/light grey chalk). After W.M. Felder (1975).....	74
Figure 43 - X-ray diffraction mineralogy of the flooded slices of the core (LT 1–6) and unflooded chalk (LT 7 and LT 8) from Liège. Cal = calcite; Mag = magnesite; Qz = quartz; Ant = anthophyllite; Gy = gypsum; Till = tilleyite; Chrys = chrysotile. Gray rectangle marks the range where most significant changes are observed from slice LT1 to LT4. Figure and caption from Zimmermann et al. 2015a.	77
Figure 44 - SEM images of tested core material from slice 2 of the Ultra Long Term Test. Complete reworking of the microstructure and new growth of rhombohedral crystals. Scale bar: 8 μm in a), 2 μm in b). Figures and captions from Nerموen et al. 2015.....	78
Figure 45 – a) One of the triaxial cells in the laboratory at the University of Stavanger where the rocks were exposed to mechanical compression tests under reservoir conditions. b) Picture of the ULTT core. Arrow indicates flow direction. Photo courtesy of Nina Egeland.....	79
Figure 46 - Schematic drawings of how the three cores were cut after the flooding experiments, from the left to the right: Long Term Test, Medium Long Term Test, and Ultra Long Term Test.....	80
Figure 47 - The Horiba XploRA confocal Raman spectrometer (a) and the Renishaw inVia Reflex (b), both present at the Department of Earth and Environmental Sciences, University of Milano-Bicocca, Milano, Italy.	82
Figure 48 - The TERS system coupling the SPM SmartSPM™-1000 system (AIST) and the confocal Raman spectroscopy Labram HR800 (Horiba) present at the École Polytechnique, Université Paris Saclay. Details of the tuning fork with the gold tip, and of the sample are shown on the right side.	84
Figure 49 - Examples of AFM images acquired in non-contact mode using a tuning fork oscillator on chalk samples. Panels a) and b) show 3 μm x 3 μm topographic images of an unflooded and a flooded (MLTT) sample, respectively. Panels c) and d) show a 1 μm x 1 μm images of a flooded sample acquired detecting	

the height signal (c) and the oscillation magnitude one (d). Figure and caption from Borromeo et al. 2018b.	85
Figure 50 - TERS mapping acquired on Medium Long Term Test (MLTT) chalk sample; a) 1 μm x 1 μm topography acquired with tuning-fork based AFM; b) Magnitude signal acquired in the same 1 μm x 1 μm area; c) typical TERS spectrum obtained on a single point, showing peaks at 1086 cm^{-1} (calcite), 1094 cm^{-1} (magnesite) and 1112 cm^{-1} (bicarbonatic ion); d) TERS mapping showing the distribution of the 1086 cm^{-1} calcite ν_1 peak (<i>symmetric stretching mode</i>) in the investigated area; e) TERS mapping showing the distribution of the 1094 cm^{-1} magnesite ν_1 peak in the investigated area; f) superimposition of the TERS mappings of calcite and magnesite, following the colour code used in the previous panels; g) superimposition of the TERS mappings of calcite and magnesite and of the topography image in a). Figure and caption from Borromeo et al. 2018b.	87
Figure 51 - The best way to study chalk samples by TERS is to drill out little disks from cores thin section and carefully polish them.	88
Figure 52 - A spectrum of the silicon wafer used for the calibration.	89
Figure 53 - Two Raman spectra collected on Mg-calcite. Top: spectrum collected on a Barnacles (Rosignano, Italy) bearing 0.38 % MgCO_3 (EDS analysis). Bottom: spectrum collected on a Coralline algae (Magodhoo, Maldives) bearing 6.98 % MgCO_3 (chemical result from EDS analyses). Both spectra were collected with the Horiba XploRA spectrometer. Peaks positions are reported without decimals.	90
Figure 54 Two Raman spectra collected on the first slice of the Long Term Test. The occurrence of the original calcite (LT1_p1C_6) and the presence of recrystallized magnesite (LT1_p1B_6) are shown. Both spectra were collected with the Horiba XploRA spectrometer. Peaks positions are reported without decimals.	
Figure 55 - TERS analysis performed on the MLTT sample. Panels a-b): 500x500 nm height (a) and oscillation magnitude (b) images. Panel c): magnesite spectra acquired with the tip engaged (red) and retracted (black), demonstrating that the signal measured	

is actually near field (TERS). Panel d): TERS spectra acquired in 3 different locations in the selected area. Each spectrum (all zoomed in the region 1000-1200 cm⁻¹) shows the presence of two minerals: calcite (CaCO₃) at 1086 cm⁻¹ and magnesite (MgCO₃) at 1095 cm⁻¹. Also, the presence of the (HCO₃)₂⁻ is detected. The locations are identified in panel a) and follow the symbol/colour legend in panel d). Figure and caption from Borromeo et al 2018b..... 92

Figure 56- TERS mapping acquired on the Ultra Long Term Test (ULTT) sample: a) 4 μm x 4 μm topography showing a circular structure that may resemble a coccolith; b) a typical TERS spectrum obtained, showing a magnesite vibrational mode at 330 cm⁻¹ (L, *librational mode*) and an asymmetric peak at 1095 cm⁻¹, which is the sum of the high ν₁ (*symmetric stretching mode*) of magnesite and a peak of the bicarbonatic ion (HCO₃)₂⁻ present at 1112 cm⁻¹ (Bischoff et al. 1985) that produces a shoulder on the right; c) TERS mapping acquired in the area selected in a) with a step-size of 250 nm and using a red color scale based on the intensity of the 1095 cm⁻¹ peak, according to the color legend; d) if we superimpose the topography to the intensity of magnesite and (HCO₃)₂⁻ peaks, we see that magnesite recrystallization is pervasive in the investigated region. On the top-right of d), the bicarbonatic ion Raman signal is present. Figure and caption from Borromeo et al. 2018b..... 94

Figure 57 - *Screenshot* of the software *Labspec 5*, Horiba. The spectrum LT1_p2_D3 is shown before (black) and after (blue) the *Baseline subtraction correction*. The Baseline button is named “BL”, the one to determinate the peaks positions is named “PK”. The peaks positions, automatically identified by the deconvolution method, are shown in the Figure (cm⁻¹)..... 96

Figure 58 - *Screenshot* of the *Crystal Sleuth* software, which was used to perform an automatised research of a calcite spectrum. 97

Figure 59 - The EDS spectrometer coupled to SEM (Scanning Electron Microscope) present at the Milano-Bicocca University (a) and its sample holder (b)..... 97

Figure 61 - Comparison between pros and cons of Raman and Tip-Enhanced Raman spectroscopies	173
---	-----

List of Tables

Table 1 - Main peaks (T, <i>translational mode</i> ; L, <i>librational mode</i> ; ν_4 , <i>in plane bending mode</i> ; ν_1 , <i>symmetric stretching mode</i>) of calcium and magnesium carbonates, from the present study and the literature: 1. Bischoff <i>et al.</i> 1985; 2. Herman <i>et al.</i> 1987.; 3. Kuebler <i>et al.</i> 2006.; 4. Borromeo <i>et al.</i> 2017a. To stay in line with literature data, peak positions are reported without decimals. Spectra with “ R ” were analysed by Renishaw inVia confocal Raman microscope, spectra with “ H ” were analysed by Horiba Xplora. Table and caption fter Borromeo <i>et al.</i> 2017a.....	47
Table 2 – List of the Magnium calcite analysed in this PhD project, with their magnesium content, age, location and water temperature. From Borromeo <i>et al.</i> 2017a.	70

Appendices

Appendix 1 – Peaks position of the Mg-calcite spectra.....	198
Appendix 2 – Peaks position of the flooded chalk spectra	203

1 Introduction

EOR (Enhanced Oil Recovery) methods on the Norwegian Continental Shelf,^(Hermansen et al. 2000; Nagel et al. 2001, amongst many others) where they have been especially applied to carbonate reservoirs. At high temperatures, seawater tends to weaken chalk and consequently the oil recovery factor of such fields is affected.^(Risnes et al. 2005; Heggheim et al. 2005; Korsnes et al. 2006, 2008a; Madland et al. 2008, 2011; Zangiabadi et al. 2009; Andreassen et al. 2010) It is important to comprehend how fluids interact with reservoir rocks because mineralogical and textural alterations in the pores affect how water will absorb and expel oil from the rock.^(Risnes et al. 2005; Zhang et al. 2007; Strand et al. 2007; Austad et al. 2008; Hiorth et al. 2010; Fathi et al. 2010; Ali et al. 2011; Madland et al. 2011; Megawati et al. 2013) The injected seawater might cause several mechanisms such as dissolution, precipitation, adsorption, desorption and ion exchange, to interplay at the same. Compaction is a major consequence of the injection and caused sea-bed subsidence in famous chalk reservoirs like Ekofisk.^(Johnson et al. 1988; Taufel et al. 1991; Jensen et al. 2000) Therefore, the monitoring of the mineralogical changes is of utmost importance during those experiments, since they influence porosity and permeability as well as specific density and the specific surface areas in a rock.^(Zimmermann et al. 2015a; Wang et al. 2016; Andersen et al. 2017) Hence, a straight and important relationship exists between mineralogical changes in composition and EOR experiments that demands successful and ideally indestructible, quick/rapid methodologies to identify or pre-screen mineralogical composition of rocks. A variety of methods are in use such as field Emission Gun Scanning Electron Microscopy– Energy-Dispersive X-Ray Spectroscopy (FEG-SEM-EDS),^(Risnes et al. 2003, 2005; Korsnes et al. 2006; Hjulær and Fabricius et al. 2007; Hiorth et al. 2010; Madland et al. 2011; Zimmermann et al. 2015a; Minde et al. 2017) X-ray diffraction (XRD),^(Zimmermann et al. 2015) whole-rock geochemistry techniques.^(Zimmermann et al. 2015a; Minde et al. 2016; Wang et al. 2016) Raman spectroscopic analyses allow the reliable recognition of substances down to 1µm in size, which is exactly what is necessary to

Introduction

analyse in experiments related to EOR applications. Here, micron-sized crystals grow within the matrix or on calcite crystals surfaces newly after flooding of chalk with different fluids.

Raman spectroscopy is an efficient and user-friendly technique representing the ideal tool to perform mineralogical and chemical analysis of minerals. (Raman, 1928a; 1928b; Krishanmurti, 1956; Griffith, 1969; Kuebler et al. 2001; Downs, 2006; Schmitt and Popp, 2006; Bersani et al. 2009; Andò and Garzanti, 2013)

Moreover is totally versatile, allowing the reliable recognition of almost any kind of substances (with exception of metals and some ionic materials) at any physical state (solids, liquids, gases), in every kind of setting, from space (Viking landers in 1972 and future expeditions on Mars) (Ellery 2004; Perez et al. 2006) to deep ocean exploration. (Zhang et al. 2012)

Additionally it is non-destructive, rapid, and economic. On top of that Raman spectroscopy does not require any sample preparation, as it can be performed, in a non-destructive way, directly on rock samples, grain mounts or thin sections. The intensity of the Raman bands in a Raman spectrum (also called peaks) is proportional to the concentration of the corresponding molecules and thus can be used for quantitative analysis. Furthermore water vibrational modes are usually small and easily subtracted in water solution (at the contrary of what happens with infrared technique).

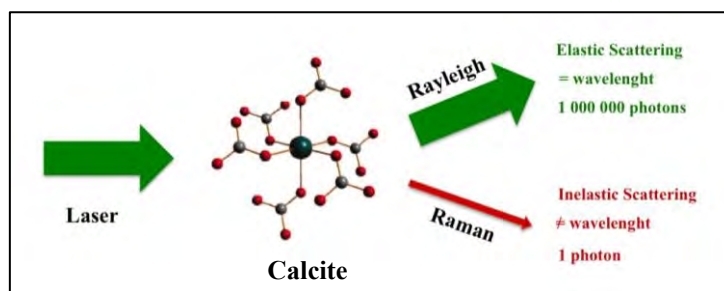


Figure 1 – When a monochromatic light (laser; in green on the left) beam a molecule of calcite, 1/1.000.000 photon is scattered with a different wavelength that is characteristic of the sample and its chemical bonds (inelastic scattering, Raman signal, in red). The major part of the

Introduction

photons is scattered with no change in wavelength, constituting the Rayleigh scattering (in green, on the right).

This method is based on the inelastic scattering which is produced when a source of light beams the sample:^(Raman 1928; Raman and Krishnan 1928a; 1928b;1929) Consequently, the molecule vibrates and most of the scattered light present the same frequency of the incident one. A very small amount of photons (1/1.000.000) is scattered with a change in frequency and wavelength that is the direct reflection of the chemical bonds present in the sample (see Fig.1). Each chemical bond vibrates in a different way, which is, in turn, unique. Raman peaks are the graphic expression of these vibrational modes.

The results of the analyses are represented by spectra made by sharp bands - called peaks - which positions (cm^{-1}) are unique for each substance and diagnostic of its composition. Identification of single phases is achieved by comparing a chemical and calibrated database with the unknown Raman spectrum. To build up an appropriate and comprehensive database, certificated standards (provided by M.A.C., Micro-Analysis Consultants) were used for carbonates, sulphides and feldspars with well-known chemical properties.^(Borromeo et al. 2017a) Particular attention was given to carbonates, principally on calcium/magnesium species.

In order to develop the utilization of Raman spectroscopies in the oil exploration research field, I applied Raman spectroscopy and Tip-Enhanced Raman Spectroscopy to flooded chalk cores, investigating how oil research could better benefit from these two state-of-the-art technologies.^(Borromeo et al 2017b, 2018a, 2018b)

The final goal of this study was to employ the method on MgCl_2 flooded chalk, investigating the change of mineralogy that occurs after flooding and the change in porosity and permeability that it may provoke.

Introduction

Chalk is a sedimentary rock that is known for its very porous and fine nature, with grain sizes between 5 to 0.5 μm . The major challenge besides the often small grain-size is the softness of the material (as this thesis will show as a major challenge), and for this reason it is testing to study chalk with traditional and new techniques as it is really difficult to obtain polished surfaces.

During the first phase of my PhD project I have been focussed on investigating whether Raman spectra of carbonates are sensitive to structural and chemical changes occurring when Mg^{2+} substitutes Ca^{2+} in the calcite lattice.^(Borromeo et al. 2017a) Several carbonate samples with variable magnesium content (0 - 20 mole % MgCO_3) of biological and inorganic origin, have been first analysed with a Raman spectrometer and then studied by Scanning Electron Microscopy-Energy Dispersive Spectrometer (SEM-EDS) and Electron Probe Micro-Analyser-Wavelength Dispersive Spectrometer (EMPA-WDS) to determine their chemistry (Borromeo et al. 2017a). Biological samples were collected from areas situated at different latitude, water temperature and saturation, factors affecting the skeletons magnesium content.^(Chave 1954a; 1954b; Mackenzie 1983; Mutti et al. 2003)

Carbonate-group minerals show a very strong Raman scattering, and are easily identifiable by Raman spectroscopy: their band positions (see chapter “3.3 *The Raman spectrum*” and Borromeo et al 2017a) are directly linked to the magnesium content and allow to easily distinguish calcite from magnesite, dolomite, and even from aragonite or Mg-calcite.^(Krishanmurti, 1956; Rutt and Nicola, 1974; Bischoff et al. 1985; Herman et al. 1987; Unvros et al. 1991; Kuebler et al. 2001; Edwards et al. 2005; Dandeu et al. 2006; De La Pierre et al. 2014; Sun et al. 2014; Purgstaller et al. 2016; Borromeo et al. 2017)

During the second phase of my PhD, knowing that Raman spectroscopy was a valid method to discriminate between carbonates, this methodology was tested on two MgCl_2 flooded chalk samples (Liège, Belgium) that have been flooded with MgCl_2 for c. 1.5 (Long Term

Introduction

Test, LTT) and 3 years (Ultra Long Term Test, ULTT) under reservoir conditions (130°C, 1 PV/day, 10.4 MPa effective stress),^(Borromeo et al, 2018a) comparable to important hydrocarbon reservoirs in the North Sea. Raman spectroscopy could identify confidently, rapidly and economically the presence of recrystallized magnesite along the core of the Long Term Test (1.5-years-test, LTT) up to 4 cm from the injection surface. In the Ultra Long Term Test core (3-years-test, ULTT) the growth of MgCO₃ affected nearly the entire core (7 cm). Furthermore, this method permitted to exclude the presence of dolomite, aragonite and high-Mg calcite. For more information see Borromeo et al. 2018a.

However, the small grain size of newly grown minerals far below 1 micron (50-600 nm) asked for a different imaging and smaller laser spots, since the only issue with the application of Raman spectroscopy on chalk was that the very little grain-size of the coccoliths and the secondary grown crystals prevented from achieving a satisfactory imaging of the spotted area. For this reason, during the third step of my PhD research, higher resolution chemical analyses were carried out using TERS (Tip-Enhanced Raman Spectroscopy), which combines Raman Spectroscopy with Atomic Force Microscopy (AFM), a particular type of scanning force microscopy.^(Borromeo et al. 2017b, 2018b) To the contrary of Raman spectroscopy, this methodology provides an outstanding spatial resolution (~ 20 nm), indicating this method as a new frontier technique. On the other hand this methodology turned out to be time-consuming, requiring sample preparation and considerable expertise to perform the analyses. Other highly sophisticated and expensive methods like Scanning Transmission Electron Microscopy-Energy Dispersive Spectrometer (STEM-EDS), can reach a comparable resolution and amount of information, but provide only chemical information, and the mineralogical interpretation is sometimes difficult and not totally reliable. During this third PhD phase, TERS was used to investigate injected chalk and produce mineralogical and topography maps, down to an incredible spatial resolution.

Introduction

Throughout the PhD, as well clastic rocks have been analysed to demonstrate the useful application of Raman spectroscopy to clastic rocks (see “7. *Other contributions*” chapter and, for example Matthews et al. 2015) one more time again. However, this application is well known^(Raman, 1928; Krishnamurti, 1956; Griffith, 1969; Kuebler et al. 2001; Downs, 2006; Bersani et al. 2009; Andò and Garzanti, 2013, Delmonte et al. 2017) and lies out of the main focus of this study here. Nevertheless it is of importance to mention that these studies as well have been carried out during this thesis project as well to indicate very clearly that coarser-grained rocks than chalk are perfect candidate for the same here discussed issues in relation to EOR.

2 Objective

Brine injection is one of the most used and challenging procedure in Enhanced Oil Recovery: comprehending the associated mineralogical and mechanical alteration of chalk is nowadays one major goal, because it will change the oil flow pathways and the reservoir potential. (Risnes et al. 2005; Zhang et al. 2007; Strand et al. 2007; Austad et al. 2008; Hiorth et al. 2010; Fathi et al. 2010; Ali et al. 2011; Madland et al. 2011; Megawati et al. 2013)

Chalk-fluid interactions are complex; porosity, permeability and mechanical strength of chalk are linked to calcite dissolution. (Madland et al. 2011; Wang et al. 2016)

Moreover, mineralogical changes (dissolution + precipitation) can be a controlling factor, as pointed out in previous laboratory experiments. (Zhang et al. 2007; Austad et al. 2008; Hiorth et al. 2010; Zimmermann et al. 2015a)

These changes affect geomechanical parameters (Risnes et al. 2005; Heggheim et al. 2005; Hiorth et al. 2013; Korsnes et al. 2006, 2008; Madland et al. 2006, 2011; Zangiabadi et al. 2009) ; in

leading to chalk weakening or compaction (Madland et al. 2011) and to a change of the surface charge which, affecting wettability, (Strand et al. 2003, 2007; Zhang et al. 2006) will also have a direct consequence for the recovery of hydrocarbons (a negatively charged mineral surface promotes a more water-wet surface, when the oil is negatively charged; whereas a positively charged mineral surface promotes a more oil-wet surface). (Hiorth et al. 2010)

The major focus of this study is to show how micro- and nano-Raman spectroscopies can be applied to these EOR related experiments, in order to investigate after brine injection mineralogical changes with a reliable, fast, and economical approach. This PhD project does demonstrate that Raman spectroscopy can be considered as a noteworthy work perspective in petroleum exploration of unconventional reservoirs, such chalk or siltstone thanks to its quickness and capability to recognize minerals. I present the first application of micro- and nano-Raman spectroscopies on chalk cores, which were flooded with $MgCl_2$ under reservoir conditions. As mention

Objective

above, Raman spectroscopy is non destructive and easy to use; it permits to perform, in a rapid and cheap way, mineralogical analyses, identifying even polymorphs. Nano-Raman (TERS, Tip-Enhanced Raman Spectroscopy), instead, is a new frontier imaging technique that allows impressively high-resolution chemical analyses down to an outstanding spatial resolution (~ 20 nm).

The imaging of newly grown minerals can be difficult as some of the components of the cores are at sub-micrometre scale and very low concentration ($< 5\%$). Exploring methods with high resolution on both imaging and compositional analyses is therefore paramount to understand the mineralogical alterations made by EOR processes, important input for modelling, simulation and up-scaling.

3 Raman spectroscopy

The spectral information in confocal microscopy can be obtained through different techniques such as Absorption, Reflection, Transmission, Emission, Photoluminescence, Fluorescence, and Raman spectroscopy. The word “spectroscopy” defines the study of the interaction between matter and radiated energy; it is a particular type of smectrometry. It can be interpreted as the science of studying the interaction of matter and radiation, that is registered in spectra. The most common radiations studied (that can be incident, absorbed or emitted) are visible light, monochromatic light, X-Rays, infrared and ultraviolet rays and their source can be external or internal to the system. Their spectra are always intensity versus frequency plot.

When Raman spectroscopy is coupled with an optical microscope, it can be called **micro-Raman spectroscopy**, to highlight the micrometric resolution of the analysis.

3.1 The discovery of the Raman scattering

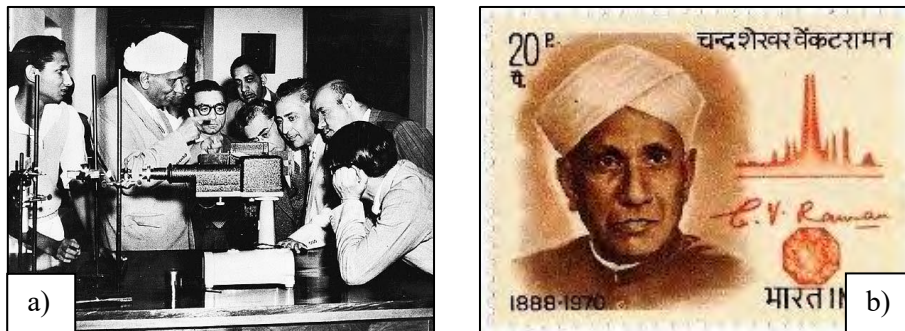


Figure 2a and 2b - C. V. Raman with his first spectrometer to the left and the stamp at him dedicated to the right.

The Raman effect was studied and formalized for the first time in 1928 by the Indian scientist **Sir Chandrasekhara Venkata Raman** (Trichinopolis 1888 - Bangalore 1970, Figs. 2a and 2b), a physics

professor at the University of Kolkata who, thanks to this discovery, won the Nobel Prize for Physics only two years later. Moreover, in his honour the Indian Science Day is celebrated on **February 28th**, to celebrate the day when the line spectrum of the new radiation was first seen (28 February 1928).

The discovery was achieved thanks to his collaboration with a devoted student that was working with him since 1920, **Sir Kariamanickam Srivasa Krishnan** (1898 Madurai, Tamil Nadu – Delhi 1961, Fig. 3): they were not just “student and master” as it could be meant nowadays, especially in the Western world, they were “*guru and sishyahe*”, they had what was called “Gurukulavasam” (teacher and students living together in a isolated place to perform their research).



Figure 3: Sir Kariamanickam Srivasa Krishnan.

Sir C.V. Raman was a brilliant optic, crystallography and acoustic researcher; he wrote his first scientific paper when he was only 18 (Raman, 1906) and after his second paper^(Raman, 1911) published in *Philosophical Magazine*, Raman received a letter from Lord Rayleigh, the eminent physicist and Nobel Prize-winner. The British researcher, unaware that Raman was just a teenage student, impressed by the level of the study, sent his letter to “*Professor Raman*”. Afterwards, Sir C.V. Raman achieved his master degree in physics at 19 years, awarded with highest distinction.

Although Raman's will was to begin a scientific career, he had to work in the Civil service, as their family was deeply in debt. For 10 years Raman carried out two jobs: the first as a civil servant in the Indian Finance Department (IFD) in Kolkata, and the second as optics/spectroscopy physicist at IACS (Indian Association of Cultivation of Sciences) a small scale research institute. He was invited to visit the institute laboratories with no pay, early in the morning and late in the night (after and before his 8 hours shift at the IFD). Raman's part-time research work and his free lectures to divulgate science were so impressive to establish his reputation as talented physicist. In 1917 the University of Kolkata offered him the Palit Chair of Physics. Although it meant a substantial cut in pay, Raman, at the age of 28, accepted.

A significant episode about Raman tells that one day, in the summer of 1921, Raman was on the deck of a boat in the Mediterranean Sea, going to the Congress of Universities of the British Empire at Oxford. Looking at the blue colour of the Sea, he began to doubt Rayleigh's explanation of its colour. The British was the first to explain that the sky is blue because of a phenomenon he called **Rayleigh scattering**.^(Rayleigh 1918) and explained that the sea's colour it is simply a reflection of the sky's colour.^(Krishnan, 1981; Nasdala et al. 2004) Rather than coming straight to our eyes from the sun, sunlight is scattered in all directions by the atmosphere. The blue wavelength is scattered most, meaning that it comes to our eyes from everywhere in the sky, therefore the sky looks blue. Yellow and red light are scattered least, so we usually see a yellow or red sun. Photons lose no energy when they interact with gases, and the light, therefore, stays the same colour. Raman found that the sea does scatter light. When he sailed back to India in September 1921 Raman had with him some simple physics equipment: a miniature spectroscope, a prism, and a diffraction grating. Studying the sky and the sea, he discovered that the sea does scatter

light: therefore when Rayleigh said the sea's colour is simply a reflection of the sky's one, he was not wholly correct.^(Raman, 1922)

When he went back to his university, Raman and his students began an exhaustive program of investigation into light scattering especially in gases and liquids. They showed that the colour of the sea was the result of the intrinsic diffusion of light by the water molecules. These observations were then collected in "*The Molecular Diffraction of Light*",^(Raman, 1922) in which he exposed the physical concepts concerning molecular diffusion and diffraction, quantum light theory and the description of the experiments carried out in his career.

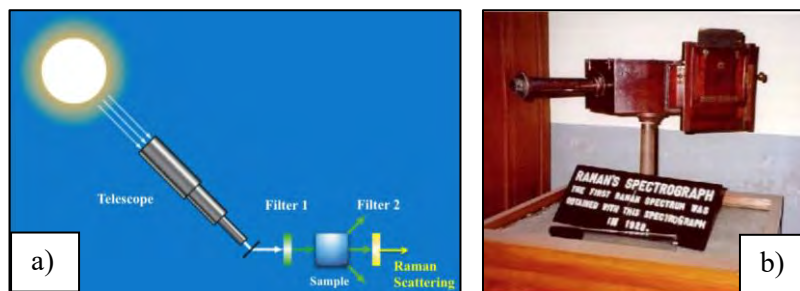


Figure 4 – a) The Figure shows the experiment carried out by C. V. Raman to demonstrate the existence of the inelastic scattering: a telescope was aimed at the sun, and the light so collected was made passing first through a monochromatic filter and then to several liquids. The Indian scientist could prove that the wavelength was changed from the initial one as, by observing the light with a crossed filter that blocked the monochromatic portion of the light, a portion of light could still pass the filter, demonstrating that a change in wavelength was happened. Figure and caption from: Dissemination of IT for the Promotion of Materials Science (DoITPoMS), Teaching and learning packages (TLPs), University of Cambridge <http://www.doitpoms.ac.uk/tlplib/raman>

b) The spectrograph used by Raman and his team to collect the first spectrum in 1928, exhibited in IACS.

Raman used **monochromatic light** – sunlight that had been filtered to show only one colour – and found that several liquids – sixty of them – did indeed change the colour of the light (Fig. 4a). He, with his students, then observed this first in April 1923, but only as a very weak effect. Only after four years of investigations, they could find a particularly strong colour change in light scattered by glycerine.

Raman's team observed the effect in gases, crystals and glass with a spectrograph (Fig.4b). The effect might have been mistaken for fluorescence, another phenomenon in which light has its colour changed, but in Raman's work the light scattered by liquids was polarized, which ruled out fluorescence.

With his student and co-discover of the Raman effect, Sir Kariamanickam Srivasa Krishnan, he performed numerous experiments at the Indian Association for the Cultivation of Science, Kolkata (then Calcutta) predominantly on liquids, but also on organic vapours, crystals' and amorphous solids, using a low-pressure mercury and toluene lamp, that required hours of accumulation to collect a single spectrum. Their conclusions were exhibited in the talk held on March 16, 1928^(Raman 1928) at the South Indian Science Association in Bangalore. In the same year, in a publication for the illustrious *Nature* magazine (Fig. 5),^(Raman and Krishnan 1928a) Already, Raman was able to understand the theoretical principle at the base of the inelastic diffusion of light: in fact he realized that between the incident photon and the excited medium an exchange of energy took place. Afterwards other two important studies were published, where further information and examples were given (Fig. 5).^(Raman and Krishnan 1928b, 1929)

What came to be known as the Raman effect had never been seen before. And, by the way, the inelastic scattering at its heart was a further, very strong confirmation, of the quantum theory. (Further comments in chapter "3.2.1 *Quantum-mechanical model*".

A New Type of Secondary Radiation.

If we assume that the X-ray scattering of the 'unmodified' type observed by Prof. Compton corresponds to the normal or average state of the atoms and molecules, while the 'modified' scattering of altered wave-length corresponds to their fluctuations from that state, it would follow that we should expect also in the case of ordinary light two types of scattering, one determined by the normal optical properties of the atoms or molecules, and another representing the effect of their fluctuations from their normal state. It accordingly becomes necessary to test whether this is actually the case. The experiments we have made have confirmed this anticipation, and

shown that in every case in which light is scattered by the molecules in dust-free liquids or gases, the diffuse radiation of the ordinary kind, having the same wave-length as the incident beam, is accompanied by a modified scattered radiation of degraded frequency.

The new type of light scattering discovered by us naturally requires very powerful illumination for its observation. In our experiments, a beam of sunlight was converged successively by a telescope objective of 18 cm. aperture and 230 cm. focal length, and by a second lens of 5 cm. focal length. At the focus of the second lens was placed the scattering material, which is either a liquid (carefully purified by repeated distillation *in vacuo*) or its dust-free vapour. To detect the presence of a modified scattered radiation, the method of complementary light-filters was used. A blue-violet filter, when coupled with a yellow-green filter and placed in the incident light, completely extinguished the track of the light through the liquid or vapour. The reappearance of the track when the yellow filter is transferred to a place between it and the observer's eye is proof of the existence of a modified scattered radiation. Spectroscopic confirmation is also available.

Some sixty different common liquids have been examined in this way, and every one of them showed the effect in greater or less degree. That the effect is a true scattering and not a fluorescence is indicated in the first place by its feebleness in comparison with the ordinary scattering, and secondly by its polarisation, which is in many cases quite strong and comparable with the polarisation of the ordinary scattering. The investigation is naturally much more difficult in the case of gases and vapours, owing to the excessive feebleness of the effect. Nevertheless, when the vapour is of sufficient density, for example with ether or amylene, the modified scattering is readily demonstrable.

C. V. RAMAN.
K. S. KRISHNAN.

210 Bowbazar Street,
Calcutta, India,
Feb. 16.

a)

The Optical Analogue of the Compton Effect.

The presence in the light scattered by fluids, of wave-lengths different from those present in the incident light, is shown very clearly by the accompanying photographs (Fig. 1). In the illustration (1)

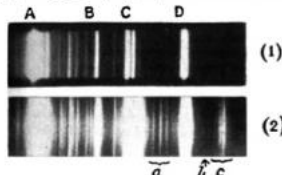


Fig. 1.—(1) Spectrum of incident light; (2) spectrum of scattered light.

represents the spectrum of the light from a quartz mercury vapour lamp, from which all wave-lengths greater than that of the indigo line have been filtered out. This line (4358 Å.) is marked D in the spectrogram, and C is the group of lines 4047, 4078, and 4109 Å. Spectrogram (2) shows the spectrum of the scattered light, the fluid used being toluene in this case. It will be seen that besides the lines present in the incident spectrum, there are several other lines present in the scattered spectrum. These are marked a, b, c in the figure, and in addition there is seen visually another group of lines which is of still greater wave-length and lies in a region outside that photographed. When a suitable filter was put in the incident light to cut off the 4358 line, this latter group also disappeared, showing that it derived its origin from the 4358 line in the incident radiation. Similarly, the group marked c in spectrogram (2) disappeared when the group of lines 4047, 4078 and 4109 was filtered out from the incident radiation by quinine solution, while the group due to 4358 Å. continued to be seen. Thus the analogy with the Compton effect becomes clear, except that we are dealing with shifts of wave-length far larger than those met with in the X-ray region.

As a tentative explanation of the new spectral lines thus produced by light-scattering, it may be assumed that an incident quantum of radiation may be scattered by the molecules of a fluid either as a whole or in part, in the former case giving the original wave-length, and in the latter case an increased wave-length. This explanation is supported by the fact that the diminution in frequency is of the same order of magnitude as the frequency of the molecular infra-red absorption line. Further, it is found that the shift of wave-length is not quite the same for different molecules, and this supports the explanation suggested.

Careful measurements of wave-length now being made should settle this point definitely at an early date.

C. V. RAMAN.
K. S. KRISHNAN.

210 Bowbazar Street,
Calcutta, Mar. 22.

No. 3053, VOL. 121]

b)

Figure 5 - a) C. V: Raman and his disciples/colleague K.S. Krishnan reported their discovery in March 1928 on the famous journal Nature. (Raman and Krishnan, 1928a) b) A following more detailed paper, published in May 1928 on the same journal. (Raman and Krishnan, 1928b)

In the years that followed their discovery, almost 50 papers per year were published (the one shown in Fig. 6 is an example) focusing on the

theory and its possible application on minerals, glasses, liquid, gases, and organic matter.^(Neuville et al. 2014) and their work^(Raman and Krishnan 1928a) has been quoted as reference almost 55.000 times from 1980 to 1997.

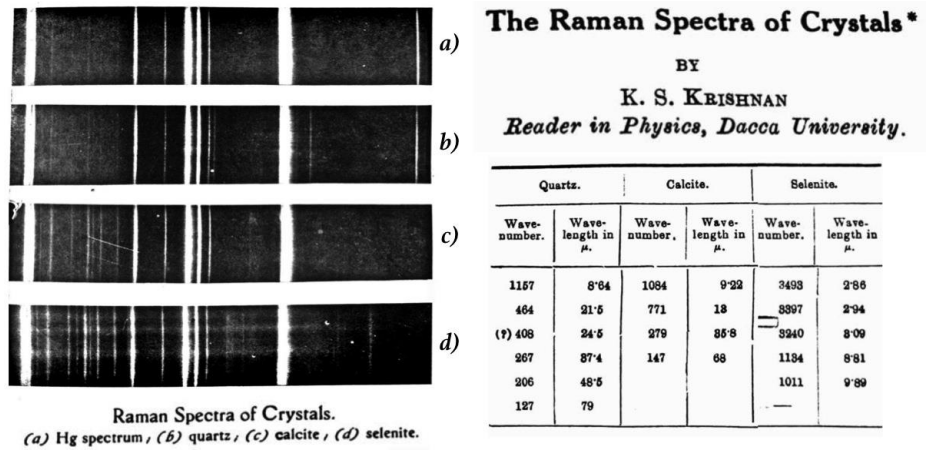


Figure 6 - Quartz, calcite and selenite Raman spectra and their peaks position, reported in Krishnan, 1929.

Raman, however, had several precursors that prepared the way for him: in fact other researchers had described several phenomena, afterwards recognized as examples of Raman effect. In 1878 **Eugen von Lommel**^(Lommel 1878) had shown how fluorescence characteristics were dependent on the nature of the sample and the frequency of the incident radiation. Moreover, the Austrian theoretical physicist **Adolf Gustav Stephan Smekal**,^(Smekal, 1923) in 1923 was the first to mathematically predict the inelastic scattering of photons. For this reason, the official name of this effect is *Smekal-Raman effect*.

Other researchers that helped with their brilliant work to achieve the discovery of the Raman effect were the Nobel Prize-winners **Erwin Schroedinger**, **Paul Dirac**, **Werner Karl Heisenberg**, pioneers of quantum mechanics who predicted the Raman scattering by applying quantum mechanics to molecules.

During the 1920's, parallel to Raman and Krishnan, other physics groups worked on the same project around the world: while Raman and Krishnan focused their investigations on liquids and vapours in India, in the Ex-URSS the Soviet physicists **Grigory Landsberg** and **Leonid Mandelstam** (Figs. 7a and b) studied the inelastic scattering of light in minerals.^(Landsberg and Mandelstan, 1928) In 1928, the same year in which Raman published on Nature, they discovered the same phenomenon in crystals and called it “*combinatorial scattering of light*”. Their discovery had occurred at the Moscow State University on 21 February 1928, one week earlier than the discovery in Calcutta. They presented their discovery for the first time at a colloquium on 27 April 1928 and published experimental results with theoretical explanation in Russian and in German and then published a comprehensive paper in Zeitschrift für Physik. Despite this incredible discovery was achieved first by these Russian physicists, the phenomenon became, perhaps unjustly, internationally known as Raman effect. In Russian scientific literature it is still often called “*combinatorial scattering of light*” but in English it is named after Raman.

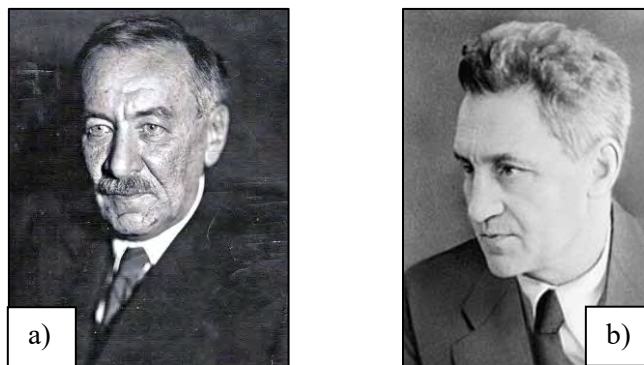


Figure 7 –The Soviet physicists Leonid Mandelstam (a) and Grigory Landsberg (b) that discovered the Raman scattering at the University of Moscow, one week before C.V. Raman, naming it “*combinatorial scattering of light*”.

As mentioned, at the end of the 1920s several laboratories in different parts of the world focused their attention on the diffusion of light, with the result that ten years later Raman spectroscopy was the most used method of non-destructive chemical analysis. Several papers were written in these fruitful years, in order to make the spectra of the different substances known when published.

However, vibrational spectroscopy was more actively applied to analytical chemistry only after the Second World War, when the needed instrumentations became commercially available, since at first Raman spectroscopy did not guarantee accurate analyses, as the signal was so weak that hours were needed to collect a spectrum. Raman's discovery gained more importance in the 1960s, in conjunction with the invention of monochromatic laser light. This new light source, being a spot beam, is much easier to focus on the sample and is of several orders greater in magnitude than any other incoherent source, which is fundamentally important, as the inelastic scattering is really weak.

Anyway, it is only in the 1980's and 1990's that the method became increasingly accessible for everyday analyses. This is the consequence of decades of technical development, such as the invention of charge-coupled device (CCD) and filters to isolate the Raman scattering. Another important push was also given by the coupling with microscope optics enabling to really increase analyses resolution.

3.2 The Theory behind the method

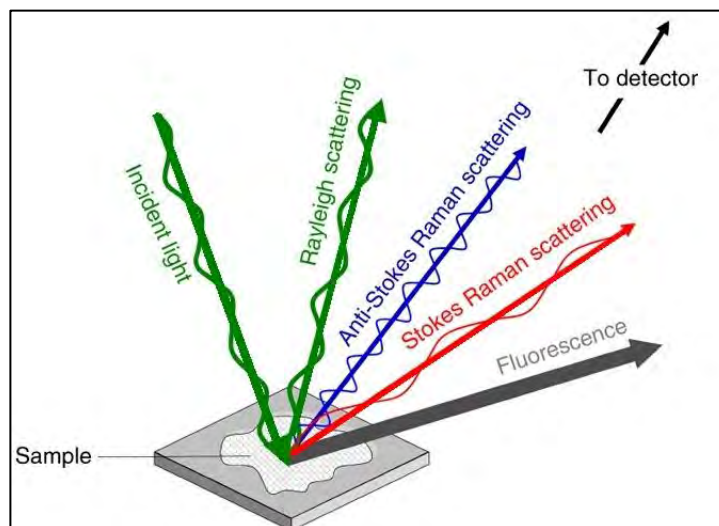


Figure 8 - Most photons will scatter from the sample with no change in wavelength: so-called Rayleigh scattering. A small number (1/1.000.000) of photons will however change frequency and this phenomenon is called Raman scattering (formed by Stokes and Anti-Stokes scatterings). Modified after Butler et al. 2016.

Most of the scattered light consists of the "**Rayleigh scattering**" (elastic scattering), which is an intrinsic feature of light and does not depend on the chemical or optical properties of the sample. Since it is the result of an elastic collision between photons and the molecules of the material, the scattered light has the same frequency and wavelength as the incident beam of light, but with lower intensity (less than three orders of magnitude) and it is in most cases immediately released by the production of diffuse light. Only a little fraction of the scattered photons (approximately 1 /1.000.000) are scattered by an excitation, and are usually characterized by a lower frequency than the one of the incident photons: this is the **Raman signal**, an **inelastic scattering** (Fig. 8). This portion of scattered light does not show the same wavelength/frequency as the incident light. The Raman spectrum shows a set of peaks that expresses the shifts from the incident light; it is

unique and diagnostic for each substance like a fingerprint, as it is the direct consequence of the chemical covalent bonds characteristics (such as atomic weight, length and strength of the bonds) present in the sample: Raman shift provides information about vibrational and rotational energies of the molecular bonds. This small difference in frequency between the incident light (characterized by known intensity and frequency) and the re-emitted one is induced by the inelasticity of the collision, which occurs with a transfer of energy between the photon and the sample (for more information “3.2.1 *Quantum-mechanical model*” chapter. The intensity of the Raman signal is very weak, because it is equal to 10^{-7} to 10^{-6} of the intensity of the incident light.

The energy of a molecule is the sum of several components:

$$E_{\text{(molecule)}} = E_{\text{(nucleus)}} + E_{\text{(electronic)}} + E_{\text{(translational)}} + E_{\text{(rotational)}} + E_{\text{(vibrational)}}$$

Rotational energy is associated with the rotation of the molecule itself, around one or more axes, while vibrational energy is associated with the reciprocal movement of atoms in the molecule.

In a polyatomic molecule there are several main types of vibrations (Fig. 9):

- *Stretching vibrations*
- *Bending vibrations (deformation, scissoring, rocking)*
- *Wagging and twisting, vibrations out of the plane.*

Each material has only a few vibrational modes allowed, whose frequency depends on the elements present, the type of bonds and the structure.

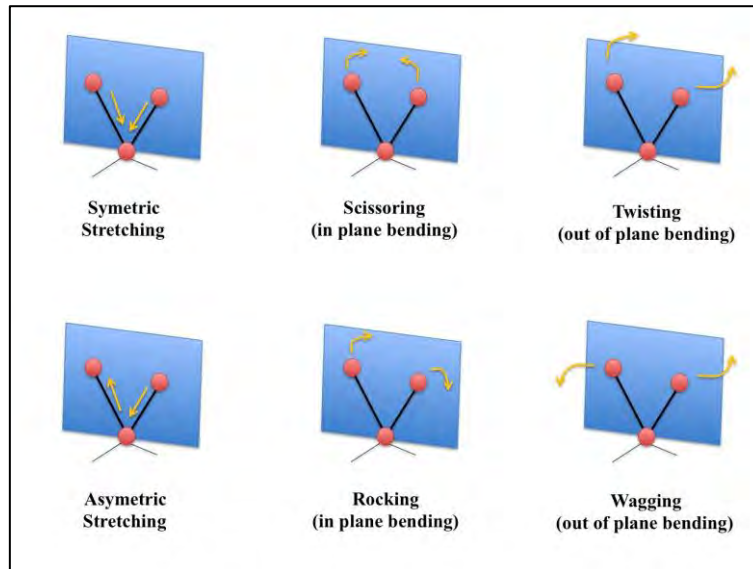


Figure 9 - In-plane and out-plane vibrational modes types.

3.2.1 Quantum-mechanical model

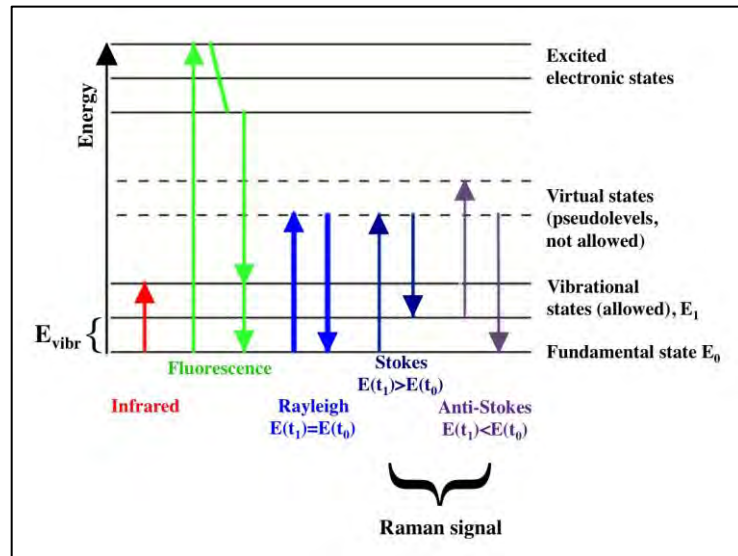


Figure 10 - Energy level diagram (Jablonski diagram) showing the interactions of the different light scatterings with molecules at different energy states. Modified after Neuville et al. 2014.

A way to describe the Raman Effect is based on the quantisation of the energy by taking into account the vibrational states of molecules and crystals (see Fig. 10).^(Nasdala et al. 2004; Neuville et al. 2014) A thorough quantum mechanical description of the Raman effect is difficult and beyond the scope of this PhD project. The reader is referred to one of the classic texts for a full comprehension (e.g. Wilson et al. 1955; Long 2002).

Vibrational levels of molecules cannot have any arbitrary amount of energy, since their vibrational state is determined by vibrational quanta discrete portions (in solids, are usually called phonons). After an irradiation, a molecule can be transferred to an excited state through the absorption of a **light photon** and the excitation of a **vibrational phonon**. A necessary condition for the absorption, however, is that the energy of the incoming photon is equivalent to the energy difference between two allowed vibrational states of the molecule or crystal. The

absorption of a photon generates a phonon (vibrational quantum) with the same energy. This is the case for **Infrared** (IR) light, on which IR absorption spectroscopy technique is based. **Fluorescence**, instead, uses a high-energy radiation (often UV) that, after hitting a molecule, makes the electrons pass to a very high energy excited state. The molecule vibrates, and then relaxes releasing energy, usually as heat. After its energy has been decreased, the molecule returns to the elementary state. The photon is released after the impact with the molecule, with less energy (and thus longer wavelength) than before: commonly this increase in wavelength causes the emitted light to enter the visible portion of light.

As mentioned above, for the quantum mechanical model, only photons with certain discrete energies can be absorbed; visible light cannot be absorbed through phonon excitation because its photon energy is too high, and therefore visible photons can be absorbed through electronic excitation. When a real electronic state is not present at the required energy, electrons can be forced to a virtual state (with low probability of transition) from which the system recovers immediately. The molecule will go back to the same electronic and vibrational state as before the interaction and, correspondingly, the photon energy of the scattered light will correspond to the initial value (**Rayleigh** elastic scattering). In one case in a million, the molecule reaches a higher or lower vibrational state than before the interaction, producing an inelastic scattering with a transfer of energy: the Raman signal. As result, the energy of such scattered light is decreased (**anti-Stokes Raman** scattering) or increased (**Stokes Raman** scattering) with respect to the exciting photon. This energy difference (**Raman shift**) corresponds to the energy difference between vibrational levels of the molecules before and after their interaction with the beam of light.

There are two different types of Raman inelastic scattering (Fig. 10 and 11):

- ***Stokes Raman scattering***: when a photon hit a molecule at the fundamental state E_0 , it gives part of its energy, thus making the molecule passes from the fundamental state E_0 to an excited pseudolevel, which does not correspond to an allowed state. Therefore, the photon is immediately re-emitted with lower energy and frequency than the incident ($\nu_0 - \nu_{\text{vibr}}$). The molecules fall to an excited vibrational level E_1 .
This type of Raman diffusion forms the *Stokes lines*, it is the most common, since in a sample the molecules in the fundamental state E_0 are much more than the excited ones.
- ***Anti-Stokes Raman scattering***: when the incident photon hits an excited E_1 molecule, the photon yields part of its energy to the molecule. The particle thus passes to high excited pseudolevel, from which it falls to the fundamental vibrational state E_0 releasing a lot of energy: it is consequently transferred from the molecule to the photon and the result is a diffused radiation with frequency and energy greater than the incident ($\nu_0 + \nu_{\text{vibr}}$).
The intensity of this signal is much lower than Stokes one, as the amount of the molecules at the excited state E_1 is really little compared to those in the state E_0 (it is possible to compare the intensity of the two scatterings in Fig. 11).

Another way to explain the Raman effect consists in the **electrodynamical model**; for more information the reader is referred to examine Nasdala et al. 2004. An important conclusion that can be obtained from this model is the fact that Raman effect is controlled by the derivative of the polarizability respect to the vibrational coordinate. For a Raman analysis, the sample must be able to change polarisability (molecule capacity to be polarized by an external electrical field) during vibrational motion, so that vibration can propagate in an inelastic fashion. This is the main difference to Infrared (IR)

absorption, where vibrations of light and vibrations of the sample have the same frequency and the interaction depends on the variation in the dipole moment.

Furthermore, for this reason, the kind of molecular bond that can emit a strong Raman signal is the **covalent** one while **ionic substances** are hardly detected and metals cannot be analysed by Raman spectroscopy.

3.3 The Raman spectrum

Raman analysis consists in measuring a signal emitted by the molecules of the sample after their interaction with the incident laser beam. The results of the measurements are graphically depicted as **Raman spectra**. The **intensity** of the scattered light (expressed as *counts*; y-axis) is plotted for each frequency of light (x-axis). The **frequency** is traditionally measured in a unit called *wavenumber* (number of waves per cm, cm^{-1}). The frequency shifts of the scattered light from the laser one are plotted in the x-axis (Fig. 11).

The Rayleigh signal is really intense and located at the Raman Shift 0 value, since it has the same frequency as the incident light beam. Symmetrically to the axis of the ordinates, there are the *Stokes* and *Anti-Stokes lines*; each peak corresponds to a particular **vibrational mode**, to a certain deviation value from the frequency (ν) of the incident light beam:

$$\nu_{\text{vibr}} = \Delta\nu = \nu' - \nu$$

where $\Delta\nu$ is the vibrational energy dissipated (Raman shift), ν is the frequency of the Rayleigh signal (same of the incident light beam) and ν' is the frequency of the scattered Raman signal. Since ν' is independent of ν , the Raman shift is independent of the wavelength of the source.

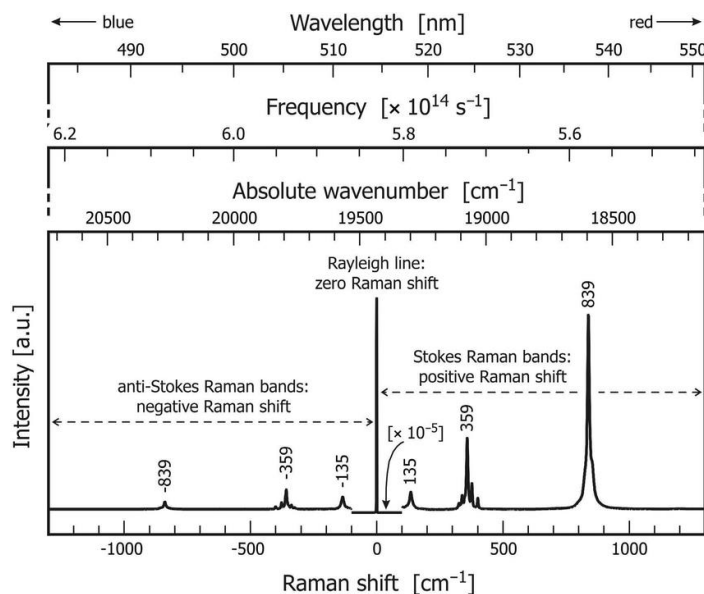


Figure 11 - Comparison of the Stokes ($\nu - \nu_{\text{vibr}}$) and anti-Stokes ($\nu_0 + \nu_{\text{vibr}}$) parts of the Raman spectrum. Spectrum of crocoite (Callenberg, Germany) excited with the Ar^+ 514.5 nm line (which corresponds to 19435 cm^{-1}). Raman bands in the Stokes and anti-Stokes parts of the spectrum have the same Raman shift values (= relative wavenumbers, with 0 cm^{-1} Raman shift set at the Rayleigh line). Note that Stokes bands are always higher in intensity than their anti-Stokes counterparts, with the intensity ratio increasing with increasing Raman shift. Note also that some workers use an opposite convention, with Stokes called negative and anti-Stokes called positive on the grounds that the Stokes Raman bands are actually lower in absolute cm^{-1} than the Rayleigh line. To elucidate the interrelation of absolute and relative wavenumbers, frequencies and wavelengths, the X axis is given with three additional scales at the top. Figure and caption from Nasdala et al. 2004.

Stokes and *anti-Stokes* signals will be shifted at equal distance to 0, at the opposite sides of the Rayleigh scattering. Consequently, the spectrum will be symmetrical, but anti-Stokes peaks will show lower intensity (see Fig. 11).

A complete Raman spectrum includes both Stokes and Anti-Stokes lines but, as already mentioned, since the latter have very low intensity, Raman spectra usually only report the quadrant relative to Stokes scattering. Furthermore, since the Rayleigh signal is not useful for the recognition of the sample chemistry, and its intensity is really strong,

out of scale respect to the Raman peaks, the Rayleigh line should be filtered off and the very low region of the spectrum (0-50/150 cm^{-1} , depending on the filter in use) is usually ignored.

In conclusion, each peak of the spectrum will have an abscissa determined by the difference between the frequency of the incident and the emitted lights and height equal to the **signal intensity**.

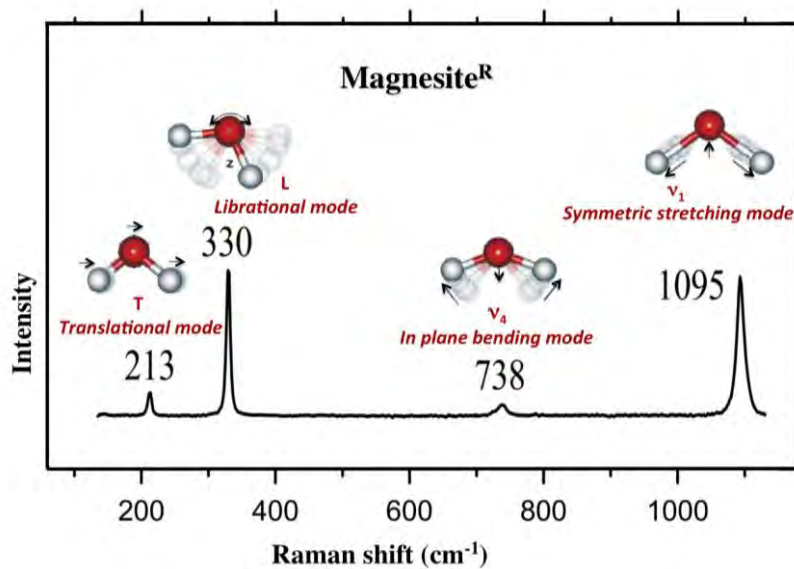


Figure 12 - Magnesite Raman spectrum with its four stronger vibrational modes. T, translational mode; L, librational mode; ν_1 , symmetric stretching mode; ν_4 , in-plane bending mode. This spectrum was collected with the Renishaw InVia spectrometer.

The number of peaks, which represent the vibrational modes (Fig. 12), present in the spectrum depends on the symmetry properties of the molecules and their frequencies depending on the atomic mass of its elements. Every chemical bond type present in every molecule can vibrate in one or more ways, producing one or more vibrational modes. Consequently, the vibrational modes of each intra-molecular and intermolecular bond will be unique and directly dependent on length and strength of the bond: in carbonate minerals for example, the main

peaks represent the CO_3^{2-} vibrational modes which position will be different in calcite (where the bigger Ca^{2+} is present) than in magnesite, since the smaller dimension of Mg^{2+} produces a shorter and stronger bond, and therefore the CO_3^{2-} ion will vibrate differently.

Furthermore, more atoms and bond types are present in a molecule, more peaks will be present in its spectrum: for this reason a spectrum of an element or an oxide, will show less peaks than a more complex molecule as a silicate.

Raman spectrum is, thus, an intrinsic feature of the chemistry, structure, and intermolecular interactions of the sample, like a fingerprint. This characteristic of the Raman effect made this technique so versatile and spread in several research fields (e.g. pharmacy, biology, medicine, gemmology, nano-materials, cultural hermitage). In geology, studying the position and width of the peaks, it is possible to recognize the **chemical composition** and **structural disorder** of the sample, respectively, orientation of the crystal obtaining information about temperature, stress and orientation of the crystal (see Fig. 13).

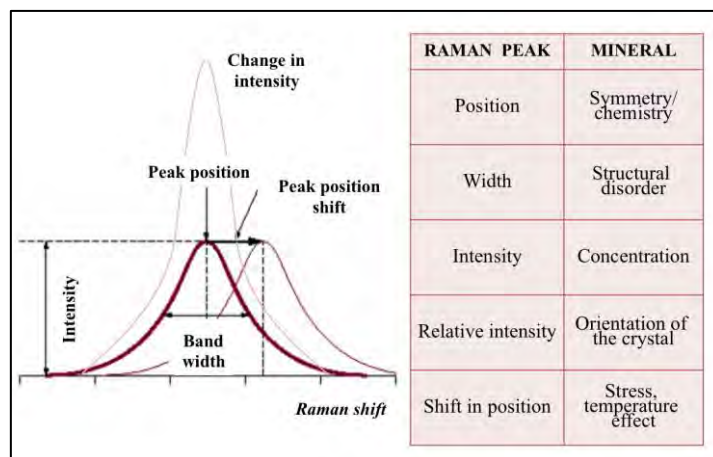


Figure 13 - Studying its Raman spectrum, lots of information can be obtained about a mineral, such as chemistry and symmetry (from the peaks position), structural disorder (from peaks

width), concentration (from peaks intensity), orientation of the crystal (from the relative intensity of a peak in comparison to the other bands present in the spectrum) and sometimes also about the temperature and stress condition of crystallization (from the shift in position respect the ones observed in standard crystals). Modified after Durickovic, 2016.

The quality of the Raman spectra depends on:

- the experimental parameters of the spectrometer (beamsplitter, lens quality, diffraction grating, CCD, etc.);
- confocal hole size;
- magnification of the microscope;
- laser wavelength;
- characteristics of the sample (composition, colour, heterogeneity, smoothness refractive index)

for more information see “3.4 *The Raman spectrometer*” chapter.

3.4 *The Raman spectrometer*

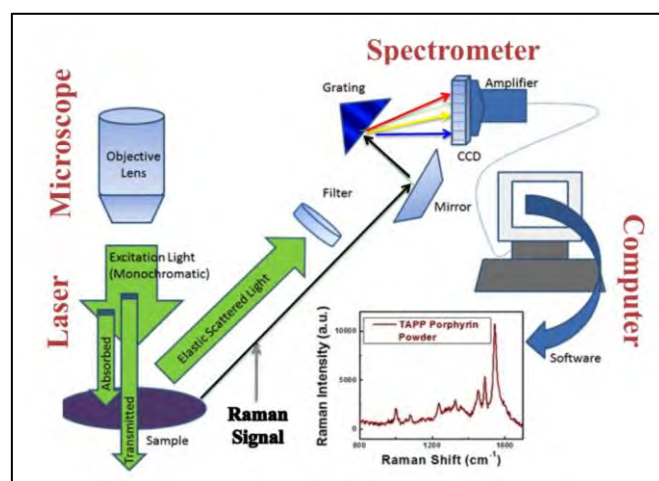


Figure 14 - General scheme of the processes involved in collecting a Raman spectrum. Modified after Murphy et al. 2011.

The primary components to any Raman spectrometer are (Fig.14):

- An excitation source: a monochromatic radiation source (laser);
- An observing apparatus: a microscope;
- A detection system: a spectrometer provided by filters that can isolate the Raman signal from the reflected and scattered radiations and a diffraction grating that can split the light into its constituent colours;
- A computer to control the whole system and display the spectra.

3.4.1 Lasers

Since Raman spectroscopy is based on the shift in wavelength between the source radiation wavelength and the scattered one from the sample, it is crucial to use a monochromatic excitation source of light as lasers (Fig.15), that are characterized by known intensity and frequency, making possible to measure the shift (in cm^{-1}) with the scattered signal. Furthermore, lasers are spot-beams several orders greater in magnitude than other light sources and easy to focus on the sample surface. Not all are suitable for this technique as it is paramount that the frequency is extremely stable.

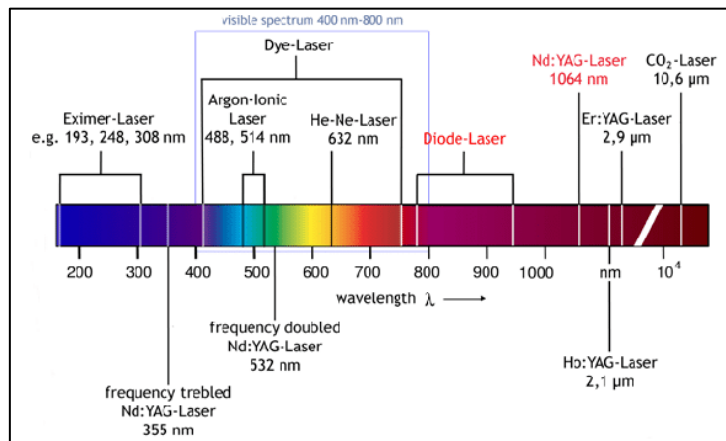


Figure 15 - Different laser lines in use in various scientific fields, with their colour, and wavelength. From Gourzoulidis et al. 2017.

It is important to keep in mind that the spectral resolution is directly influenced by the excitation wavelength. When using the same spectrometer with the same configuration (in particular, the same grating and the same slit), increasing the laser wavelength will produce a better spectral resolution: the intensity of the Raman scattering is proportional to the fourth power of the frequency of the incident light. The shorter the wavelength of the laser, the higher the frequency/energy, the more intense the Raman signal. For example, the intensity of a Raman band at 1000 cm^{-1} measured with the 1064 nm line is only 3.4% of that measured at 488 nm .^(Bersani et al. 2016)

Fig. 16 shows how two different laser lines can produce two different spectra analysing the same sample of aragonite. When the crystal is analysed by a 632.8 nm laser, a higher spectral resolution is achieved, and a doublet is observed.^(Bersani et al. 2016)

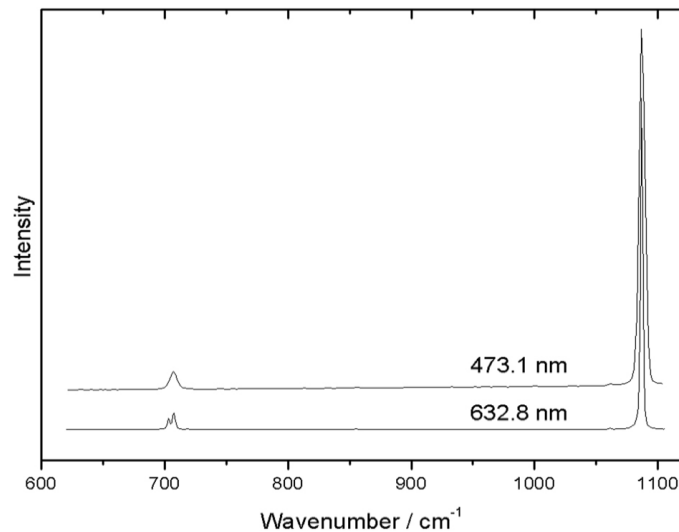


Figure 16 - Raman spectra of the same sample of aragonite, recorded with a different spectral resolution with 632.8 and 473.1 nm excitation wavelengths. Figure and caption from Bersani et al. 2016.

There are several types of lasers (Fig. 15), their wavelengths vary from UV to FT-Raman (Fourier-transform Raman spectroscopy, which uses a 1064 nm laser), and can include solid-state lasers, that use a solid gain medium, rather than a gas one (as the He – Ne red laser). Blue or green lasers can be good for inorganic materials and resonance Raman experiments (e.g., for carbon nanotubes and minerals) and surface enhanced Raman scattering (SERS or TERS). Red or near infrared (660-830 nm) are often good for fluorescence suppression. Ultra-violet lasers are used for resonance Raman on bio-molecules (such as proteins, DNA, and RNA). Furthermore different lasers are more efficient in different regions of the spectrum, consequently to a different efficiency of the CCD: with a short wavelength radiation, as blue, the high region of the spectrum (OH- stretching region) will be a high performing region, instead with a red laser it will be low-performing. ^(Bersani et al. 2016)

During this PhD project both Raman spectrometers were equipped by a green solid state 532 nm line, to the contrary of the TERS one that was equipped with a red 633 nm laser.

Another crucial issue is the effect of **fluorescence**, which can obliterate the weak Raman signal, (see “3.2.1. *Quantum-mechanical model*” chapter). Fluorescence is the emission of light by a substance that has absorbed light or other electromagnetic radiation. It is a form of luminescence. Since the Raman signal is very weak, fluorescence can cover Raman peaks if present.

The frequency of the laser, and therefore the energy irradiated on the sample, decisively influences the Raman spectrum that can be obtained. High-energy lines, such as green or blue ones, have a higher frequency, and for this reason they can easily provoke fluorescence, or burn the sample if it is delicate, as the emission obtainable could be really intense. The energy involved with high-frequency laser can be able to activate unwanted electronic transitions in the sample that can generate

fluorescence phenomena (such as organic materials) and produce difficult-to-read spectra; these phenomena are less evident with less energetic lasers such as NIR (785-1064 nm). One method to avoid fluorescence emission is to select the laser excitation wavelength. For most cases, the choice of a near IR (NIR) or UV laser wavelength can avoid exciting fluorescence, as the IR laser photon does not have enough energy to excite molecular fluorescence. With a UV laser, fluorescence may be excited but the emission is widely separated in energy from the Raman signal so that the Raman spectrum can be recorded without the fluorescence interference. In some cases, however, the detection of a characteristic fluorescence emission while performing Raman measurements can be helpful in the characterization of the material. (Mantovani et al. 2014; Zimmermann et al. 2016)

In conclusion, the **choice of the laser wavelength** is significant, since each laser line can provoke fluorescence in particular samples, and for this reason spectrometers are often equipped by more laser lines. Furthermore, the choice of the laser influences also CCD efficiency, scattering efficiency, resonance, and resolution. (Bersani et al 2016)

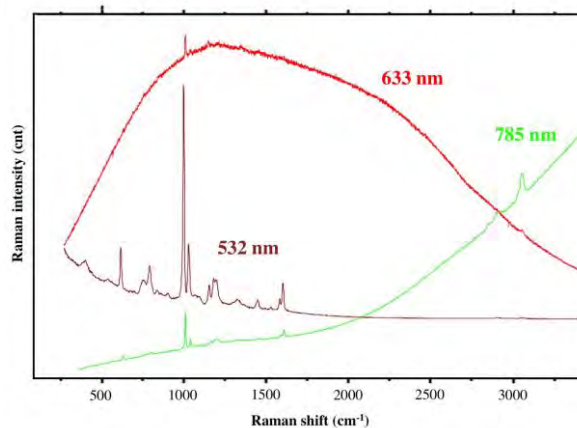


Figure 17 - Three Raman spectra of the same pigment acquired with a 532 nm, a 633 nm and a 785 nm laser lines. Spectra are courtesy of Horiba scientific: Lecture on Raman Scattering and Fluorescence Emission.

An interesting example is given by the characterization of pigments, (Fig. 17) where the choice of the laser wavelength is fundamental for a positive outcome of the analyses. (Gill et al.1970; Burrafato et al.1975; Bersani et al 2016; Rousaki et al. 2016)

In some cases this difference is so marked that some pigments do not provide any spectrum if they are not irradiated with the most appropriate laser.

3.4.2 *The confocal microscope*

Confocal microscopy is an optical imaging technique used to increase optical resolution and to eliminate, in specimens that are thicker than the focal plane, out-of-focus light, in the XY (lateral) and Z (depth) axes (Fig. 18). The spatial resolution is defined principally by the laser wavelength, the closure of the confocal hole, and the magnitude of microscope objective selected. Typical XYZ spatial resolution is in the order of 1 μm at 100x.

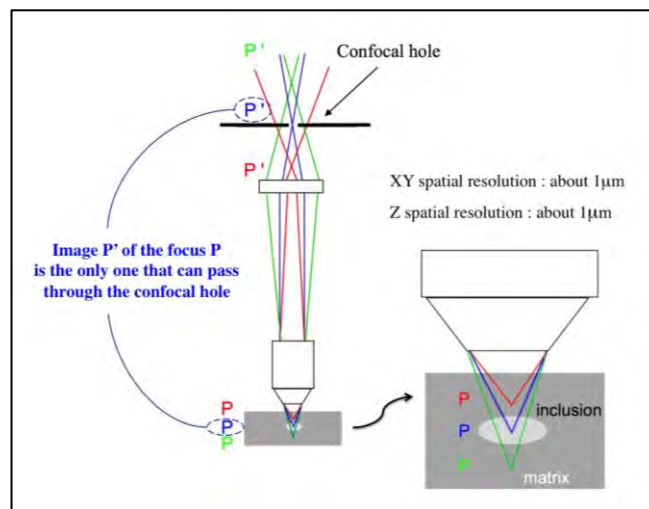


Figure 18 - Simplified schematic diagram of a confocal microscope. The confocal aperture allows all of the in-focus light (in blue) from the sample region of interest to pass through to the detector and avoid that the out-of-focus signal reaches the CCD. As such very little of this light

gets through to the detector. Modified after: Lecture on Photonics and Nanophotonics Trinity College Dublin.

The laser is focused by the **microscope** onto the surface or the inside of the sample. The microscope is provided with lenses and a **confocal hole or diaphragm** (Fig.18), whose aperture selects the fraction of light that will reach the spectrometer, rejecting the scattered rays originated from any out-of-focus points. All the objects out of focus will be suppressed in the spectrum measurement (Fig. 19), thus making internal sample analysis possible, in case of transparent bearing material. A small pinhole (10–25 μm) strongly increases the depth and also the lateral resolution.

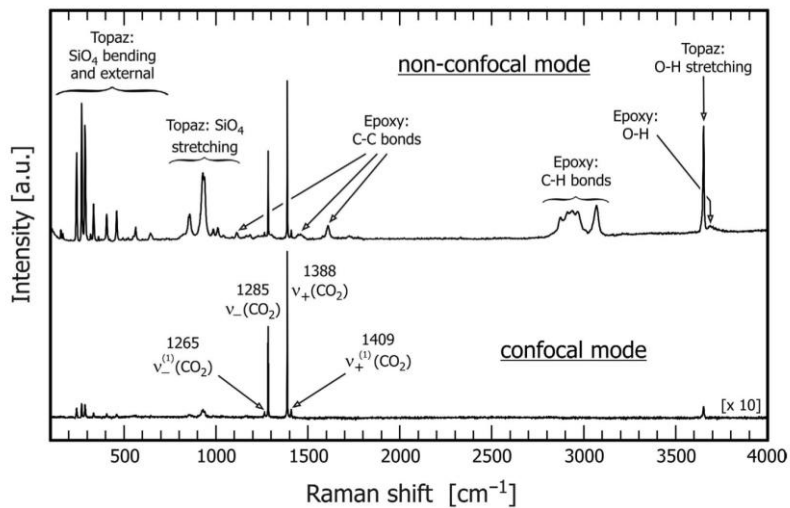


Figure 19 - As a simple example for confocality effects, we present two Raman spectra taken from a carbon dioxide inclusion ($\sim 12 \mu\text{m}$ diameter) inside a topaz grain in a polished rock slice of a greisen from Cinovec, Czech Republic. In the regular, i.e., the non-confocal mode (upper spectrum), a complex Raman spectrum is obtained, which consists of vibrational bands of the included CO_2 gas, the host mineral and also the araldite epoxy used to attach the polished section to a glass slide (about $20 \mu\text{m}$ behind the CO_2 inclusion). With a narrow confocal diaphragm placed in the optical beam path (lower spectrum), internal CO_2 vibrations are clearly obtained whereas topaz bands are largely suppressed and araldite bands are completely suppressed. Figure and caption from Nasdala et al. 2004.

The use of a confocal spectrometer, for example in petrography, permits to investigate solid, liquid or gas inclusions (see Fig. 20).^(Palanza et al. 2008; and Frezzotti et al. 2011; Barone et al. 2016)

Anyway, even if the one described above is the most common, not every spectrometer uses this kind of equipment to perform confocal measurement. The InVia Renisawh spectrometer, for example, uses a combination of two apertures - one physical (the spectrograph entrance slit) and one defined in software (the height of the captured image on the CCD) to spatially filter the scattered light and give a very good depth resolution.

An important concept to point out regards the choice of the enlargement of the microscope: higher is the magnification and higher will be the spatial resolution of the analysis but smaller will be the area (and therefore the number of the molecules) hit by the laser, reducing therefore the intensity of the scattered signal.

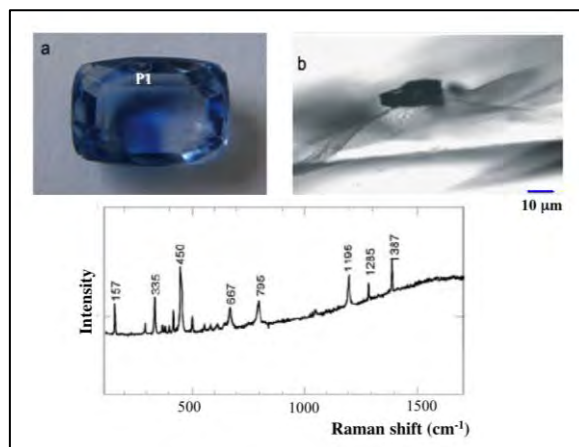


Figure 20 - Sri Lanka Sapphire with an inclusion in P1; b) diaspore and CO₂ inclusions present in P1, whose combined Raman spectrum is shown in panel c). Figure and caption from Palanza et al. 2008

3.4.3 The Raman spectrometer

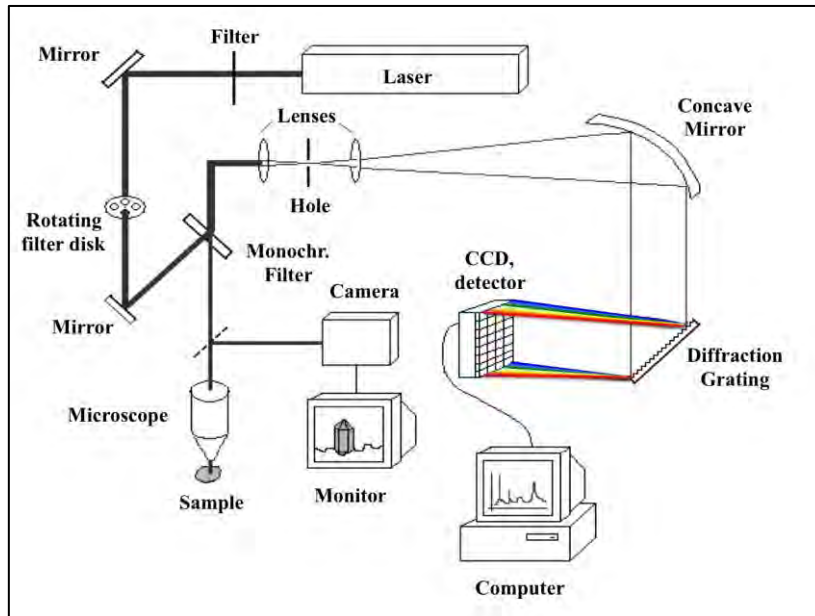


Figure 21 - General scheme of a Raman Spectrometer. Sketch courtesy of Danilo Bersani.

The Raman spectrometer is the detection system, which purpose is to isolate, detect and collect the Raman signal (Fig.21).

At first, the laser beam passes through a filter that eliminates spurious components. Then it is reflected by a mirror towards a rotating disk containing several filters that permit to select its intensity: Raman signal strength is directly proportional to the power of the Raman laser exciting the sample. At a given magnification, the more laser power used, the larger the Raman signal will be. Anyway a drawback to this recommendation is that some substances could burn when exposed to full laser power. Usually, such samples are dark in colour or have an absorption band close to the excitation wavelength.

Afterwards the laser beam is reflected once again and then directed towards a **monochromatic filter**, that separates the Raman signal from the Rayleigh scattering: the more common sre holographic Notch filter (cut off at 70-100 cm^{-1} , Stokes + anti-Stokes) and the Edge, low-pass dielectric filter (cut off at 30-40 cm^{-1} , only Stokes).^(Bersani et al. 2016) The microscope objective allows focusing the beam on the sample and through a beam splitter it is possible to send a part to the camera in order to visualize both laser on the surface and the sample surface if illuminated with a white light source.

After being collected by the confocal microscope, the scattered radiation passes again through the monochromatic filter, probably the most important and tricky step of the entire process. As previously discussed, Raman inelastic scattering is very weak and therefore in some spectrometers a mirror to double its intensity is needed. Then the signal is reflected on a spatial filter, consisting of a pair of lenses and a **hole**, which size is a compromise between resolution and signal throughput: the larger the aperture, the greater the Raman signal admitted into the spectrograph and the higher the signal appears in the spectrum will be. On the one hand the signal should be as high as possible, while on the other hand the spatial resolution should be as good as possible.

Afterwards, the signal reaches the **diffraction grating**, which is used to split the Raman radiation into its monochromatic components, all of which characterized by a different wavelength. The diffraction grating is an array of finely spaced lines on a reflective surface and is used to separate the different wavelengths of Raman scatter and to reduce stray light, which is generated by dispersion in the spectrometer.

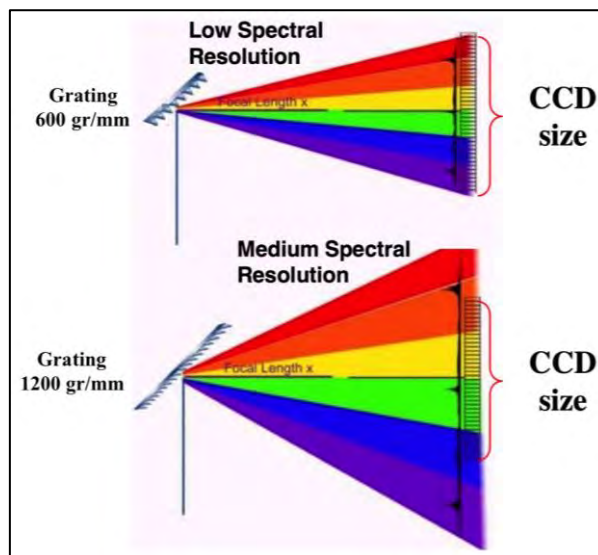


Figure 22 - On the diffraction grating, the inelastic scattering is decomposed into its wavelengths and detected by the CCD, Charge-Coupled-Device. At the same focal distance, a denser grating permits to collect a higher resolution spectrum, but can report, on the other hand, the detection of a limited Raman shifts interval. Modified after A. and B. Adl-Zarrabi, 2016.

An important consideration concerns the **spectral resolution**, which is the ability to solve the different components of the spectrum. There are two ways to increase the spectral resolution. The first option is to increase the focal distance: doubling the focal distance, doubles the spectral resolution, roughly. The second option is to change the grid to disperse the radiation: doubling the lines of the grating it is possible to double the resolution. However, a very dense grating can collect at one time a limited range of Raman shift, while a low resolution grating can collect a spectrum of a wider interval of Raman shift (Fig. 22).

After passing through this complex system of mirrors and lenses, the radiation is detected by the **Charge-Coupled-Device (CCD; Fig 23)**: a sensitive detector that measures the entire Raman spectrum at once. The CCD is made up of photosensitive material (photomultiplier or a network of multichannel photodiodes) and transforms the energy

associated with the photons of the radiation in photoelectrons, which are electric charges. It permits in quickly accumulating a large number of spectra, which amount is decided by the operator. The final spectrum (the one that will be shown by the software and then measured and processed by the operator) is their mathematic sum. This operation permits to improve peaks intensity and to low the signal / noise ratio, since the noise frequencies present in the different spectra are at random and therefore different Raman shifts: for this reason their sum will partly nullify them. On the contrary the sum of the Raman peaks present in each spectrum, that are always in the very same position, will give a higher peak in the final spectrum.

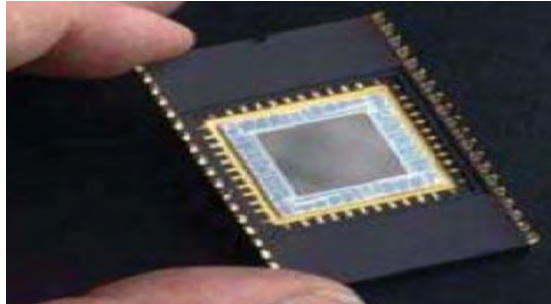


Figure 23 - Photo of a typical CCD detector. From Swaminathan, 2012.

Spectrometer operations are directed by a **computer**, equipped with a dedicated **software** (as Labspec 5) to set up the spectrometer (for example, in terms of range of spectral acquisition, number and duration of the cycles) and archive and process the spectra (for more information see the chapter “5.3 *How to perform an analysis with the Renishaw inVia Reflex confocal Raman microscope*” and “5.5 *Processing of Raman spectra*”).

3.5 Tip-Enhanced Raman Spectroscopy

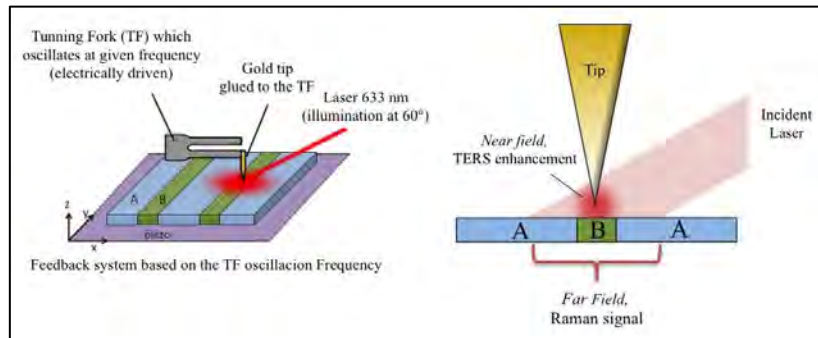


Figure 24 - TERS setup used in the present work, showing a tuning fork (TF) based AFM (Atomic Force Microscopy), scanning a surface composed of two phases, A and B, and a red laser is used at 60° and is focused on the apex of the tip. A near field spectrum would detect only the B component, where the tip is positioned. In case far field is detected, the spectrum would be the sum of the two components spectra (A+B). Figure and caption from Borromeo et al. 2018b.

In the past, new applications in the field of Raman spectroscopy were often the result of technological evolutions, such as innovative developments in Raman instrumentation. Nowadays, in several fields, as bio-sensing or carbon nanotubes, it is quite common to do high performing analyses by enhancing the Raman sensitivity, thanks to exploiting the plasmonic effect occurring in metal nanostructures. Plasmon is a quantum of plasma oscillation and the plasmonic effect is the interaction between free electrons in metal (nano-) particles and incident light. Two techniques derive from this principle: Surface enhanced Raman spectroscopy (SERS)^(Guineau and Guichard 1987; Nie, 1996; Féliidj et al. 2001; Van Elslande et al. 2008; Casadio et al. 2010; Sharma et al 2012; Possi et al. 2016)) and Tip-enhanced Raman Spectroscopy (TERS),^(Pettinger et al. 2004; Picardi et al. 2009; Stadler et al. 2011; Schultz et al. 2014; Toccafondi et al. 2016) the latter of which was used during this PhD project.

TERS instrumentation couples a Raman spectrometer with an Atomic Force Microscope (AFM), a particular type of Scanning Probe

Microscope (SPM), allowing in performing nano-resolved surface mapping while collecting chemical and structure data. Since it involves a scanning probe technique, TERS requires ultra-smooth topography of the samples. In Tip-Enhanced Raman Spectroscopy, the use of a **gold tip**, glued to a **tuning fork** (see Fig. 24), which oscillates at a given frequency (electrically driven), permits to enhance the electric field intensity of the excitation beam. The electric field is enhanced at the top of the tip, where the Raman signal is predominantly generated (*near field*). This enhancement of the Raman signal is close to $(E/E_0)^4$ (where E = enhanced electric field; E_0 = excitation electric field). Unfortunately, this increase is not always guaranteed, since the molecules being excited are less of several orders of magnitude compared to the ones beamed during micro-Raman studies.

When the scattered light is collected by the spectrometer, the Raman signal of the molecules close to the tip apex is enhanced (*near field*, **TERS signal**) but, since the laser spot is larger than the tip, the signal due to the laser directly hitting the sample and scattered from the molecules more far away from the tip (not enhanced by the presence of the tip) is usually still detectable (*far field* signal, **micro-Raman signal**). The collection of the *far field* and *near field* signals happen contemporarily and it will produce a spectrum that is their sum, the superimposition of the two. The example shown in Fig. 24 can clarify this phenomena: when the tip is placed on material B and the laser is beamed, if only *near field* is detected the spectrum will show only B vibrational modes; contrariwise if also *far field* is detected the spectrum collected will show both A and B vibrational modes. Unfortunately, is quite easy that *far field* is collected, since the laser spot (around 1 μm) is larger than the tip size (final width of around 30 nm).

The role of the AFM has been crucial in this PhD project, as it permitted to reach a ~ 20 nm resolution that would have been impossible to achieve with an optical microscope. AFM operates by measuring force between the probe and the sample. Usually, as with

TERS, the probe is a sharp tip. Though the lateral resolution of AFM is lower due to the convolution, the vertical resolution can be up to 0.1nm. To acquire the image resolution, AFMs can generally measure the vertical and lateral deflections of the cantilever (which in TERS is the tuning fork) by using an optical lever. The optical lever operates by reflecting a laser beam off the cantilever. The reflected laser beam strikes a position-sensitive photo-detector consisting of four-segment photo-detector. The differences between the segments of photo-detector of signals indicate the position of the laser spot on the detector and thus the angular deflections of the cantilever.

During this PhD project a first attempt to investigate **minerals** with TERS has been made. The results and challenges will be described further down in the “8. Discussion” chapter.

Until now, TERS has been widely applied only to organic molecules (Fig. 25)^(Pettinger et al. 2004; Schmid et al 2010; Picardi, et al. 2014; Schultz et al. 2014; Toccafondi et al. 2016) and to hard carbon-based materials.^(Stadler et al. 2011) In these research fields it is possible to reach the outstanding detection of single-molecules.^(Pettinger et al. 2004; Schultz et al. 2014)

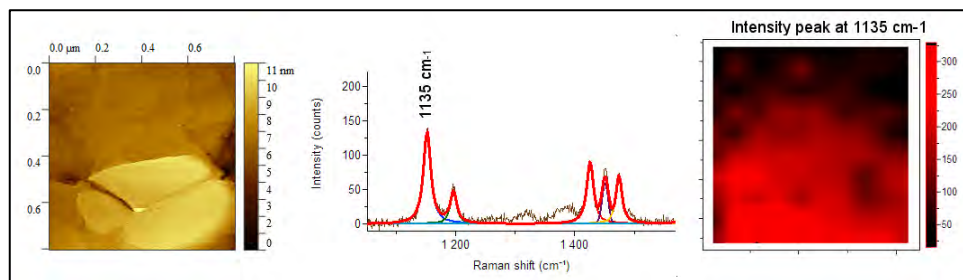


Figure 25 - Example of the capabilities of the TERS instrument: on the left a topographic $1\ \mu\text{m} \times 1\ \mu\text{m}$ image of an azobenzenethiol self-assembled monolayer on gold, in the middle a TERS spectrum acquired in the area showing the peaks characteristic of the molecule and on the right the TERS mapping displaying the $1135\ \text{cm}^{-1}$ peak intensity in the scanned region as a colour scale. It is worth noticing that the molecular monolayer does not give any signal in standard Raman, due to the low amount of material. It is therefore remarkable how the field enhancement due to the tip allows detecting clearly molecular features. Additional details on

these systems can be found in Picardi, et al. (2014) and Toccafondi et al. (2016). Figure and caption from Borromeo et al. 2017b.

When performing analyses on biological samples the best results were reaching in the so-called *gap-mode*, where ultra-thin organic or biological layers) were analysed adsorbed on a metal substrate, which helps in enhancing the Raman scattering.^(Yang et al. 2009; Langelüddeke et al. 2015; Toccafondi et al. 2016) Unfortunately, this mode is not exploitable on minerals, as they are not conducting; therefore the Raman signal enhancement expected in our study is lower than the values described in literature for organic molecules adsorbed on metals.

Even if, theoretically, TERS experiments can be done on any Raman active material, achieving successful TERS measurements is not trivial, and cannot be expected for every possible sample. In particular, chalk analyses turned out to be very challenging, because of its sub-micrometric grain size and its soft and rough texture. A detailed description of the TERS application to chalk samples will be carried out in the Methodology part “5.4 *Additional procedure to perform an analysis with a TERS spectrometer*” chapter.

3.6 Raman spectra of carbonate minerals

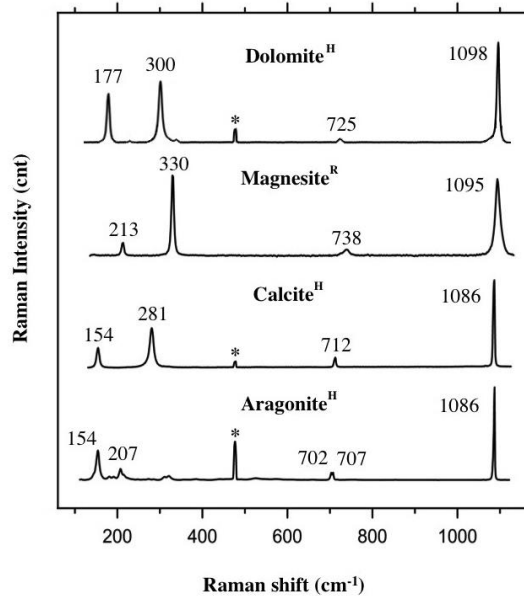


Figure 26 - Raman spectra of calcium and magnesium carbonates: dolomite (UNIMIB standard sample, Selvino, Italy); magnesite (M.A.C. certificated standard); calcite (UNIMIB standard sample, Chihuahua, Mexico, ~ 0 mol% MgCO₃), aragonite (UNIMIB – University of Milano Bicocca – standard sample, Val Formazza, Italy). Spectra with ‘R’ were analysed by the Renishaw inVia confocal Raman microscope and spectra with ‘H’ by Horiba Xplora. Stars represent the neon lamp emission line at 476.8 cm⁻¹ used for calibration with the Horiba XploRA spectrometer. Peak positions are reported without decimals. Figure and caption from Borromeo et al. 2018a.

The first Raman studies on carbonates were carried out by Landsberg and Mandelstam, the two soviet physicist that discover the so called Raman effect one week before the indian colleague (for more information see “3.2 *The discovery of the method*” chapter). (Landsberg and Mandelstam, 1928)

In the last decades, several working groups have carried on with their pioneering work, thanks to the good signal and widespread carbonates diffusion, investigating in detail peaks shifts and widths, and thermodynamic properties. (Porto et al. 1966; Rutt and Nicola, 1974; Frech

et al. 1980; Bischoff et al. 1985; Kuebler et al. 2001; Edwards et al. 2005; Korsakov et al. 2009; Carteret et al. 2013; Sun et al. 2014, Borromeo et al. 2017a)

Raman spectra of carbonates are characterized by four main vibrational modes (see Fig. 26 and Table 1), where the internal vibrations of the $(\text{CO}_3)^{2-}$ group are in the range between 600 and 1700 cm^{-1} : symmetric stretching (600 -1200 cm^{-1}) and by asymmetric stretching (1200 -1700 cm^{-1}). (Bischoff et al. 1085; Borromeo et al. 2017a)

The lattice vibrations - *translation* and *libration* - of the $(\text{CO}_3)^{2-}$ groups relative to the Ca^{+2} or Mg^{+2} lay in the lower region of the spectrum (between 100 and 500 cm^{-1}).

The spectra of carbonate group minerals are quite similar, but the exact position of the peaks is affected by the magnesium content (Bischoff et al. 1085; Borromeo et al. 2017a) as the Mg^{+2} ion is smaller than the Ca^{+2} one, the cation-O bond present in the lattice becomes shorter and therefore stronger when the magnesium ion gets into the crystal structure. As a consequence, $(\text{CO}_3)^{2-}$ group cannot vibrate as before: therefore the positions of the vibrational modes are directly controlled by the amount of magnesium present in the lattice (see Table 1): the higher the magnesium content is, the higher will be the abscissa of the peaks (peaks position). (Bischoff et al. 1085; Borromeo et al. 2017a) The strongest main peak of any carbonate spectra is called ν_1 ($\sim 1090 \text{ cm}^{-1}$) and the secondary peak, the second strongest one, is L (Libration lattice mode, $\sim 300 \text{ cm}^{-1}$). Other important, but weaker, bands are T (translational mode, 150-200 cm^{-1}) and ν_4 (in-plane bending of the $(\text{CO}_3)^{2-}$ group, 700-740 cm^{-1}). During the study on magnesium calcites performed during this PhD project (Borromeo et al. 2017a) ν_1 , ν_4 , and L peaks were used to discriminate between high- and low- magnesium calcite, since they resulted to be the more sensitive to the lattice modification due to the substitution of Ca^{2+}

The **calcite** spectrum (see Fig. 26 and Table 1) is characterized by a ν_1 sharp peak at 1086 cm^{-1} along with other subsidiary bands at 156 cm^{-1} (T), 282 cm^{-1} (L) and 712 cm^{-1} (ν_4). (Krishnan et al. 1945; Krishnamurti et al. 1957; Bischoff et al. 1085; Herman et al. 1987; Kuebler et al. 2001; Dea La Pierre 2014; Borromeo et al. 2017a)

The ν_1 of **aragonite** is also located at 1086 cm^{-1} but its spectrum can be quickly distinguished thanks to three bands in the lowest region (181 , 191 and 207 cm^{-1}) and the presence of a doublet (two very closed peaks) at 702 and 707 cm^{-1} (see Figs. 16 and 26). (French et al. 1980; Herman et al. 1987; Kuebler et al. 2001; Carteret et al. 2013; De La Pierre 2014; Borromeo et al. 2017a) Higher peak positions have been observed in high-pressure and -temperature calcites. (Gillet et al. 1993)

Several investigations on different CaCO_3 polymorphs have been made: Korsakov et al. (2009), Edwards et al. (2005) who compared spectra of mixtures of known aragonite-calcite ratios; Dandeu et al. (2006) who used Raman spectroscopy to study mixtures containing all three polymorphs calcite, aragonite, vaterite to prove that Raman spectroscopy can provide quantitative determination on three polymorphs mixtures.

The **magnesite** spectrum is similar to that of calcite (see Fig. 26 and Table 1), as expected because of their isomorphism. (Krishnamurti 1957; Bischoff et al. 1085; Herman et al. 1987; Gillet et al. 1993; Kuebler et al. 2001; Borromeo et al. 2017a)

Nevertheless, all modes of magnesite are higher because of shorter inter-ionic distances and stronger interionic bonds (as mentioned above).

The layered structure of the **dolomite** lattice induces the presence of another vibrational mode at 335 cm^{-1} . (Bischoff et al. 1085; Herman et al. 1987; Gillet et al. 1993; Kuebler et al. 2001; Sun et al. 2014; Borromeo et al. 2017a) and, together with the ν_1 located at 1097 cm^{-1} , allows its unambiguous differentiation from all other carbonate minerals (see Fig. 26 and Table 1).

Raman spectroscopy

Author	T (cm ⁻¹)				L (cm ⁻¹)				v ₁ (cm ⁻¹)				v ₂ (cm ⁻¹)			
	1	2	3	4	1	2	3	4	1	2	3	4	1	2	3	4
Aragonite ^R	-	150	154	154 ^H	-	205	208	207	-	704	703	702+707	-	1085	1086	1087
Calcite ^R ~0% mol MgCO ₃	154	154	156	154	281	283	282	281	711	714	713	712	1085	1087	1086	1086
Magnesite ^R	213	216	215	213	329	332	332	330	738	738	739	738	1094	1096	1095	1095
Dolomite ^R	175	177	178	177	299	301	302	300	724	729	726	725	1097	1099	1098	1098

Table 1 - Main peaks (T, *translational mode*; L, *librational mode*; v₁, *in plane bending mode*; v₂, *symmetric stretching mode*) of calcium and magnesium carbonates, from the present study and the literature: 1. Bischoff *et al.* 1985; 2. Herman *et al.* 1987; 3. Kuebler *et al.* 2006; 4. Borromeo *et al.* 2017a. To stay in line with literature data, peak positions are reported without decimals. Spectra with “R” were analysed by Renishaw inVia confocal Raman microscope, spectra with “H” were analysed by Horiba Xplora. Table and caption after Borromeo *et al.* 2017a

The complete peaks positions dataset of the magnesian calcite and flooded calk samples, collected during this PhD project, is reported in *Appendix 1* and *Appendix 2*.

3.7 Spectra of non-carbonate minerals

Even if this PhD project has been primarily focused on carbonate group minerals, other species have been encountered and recognised by Raman spectroscopy. As it happens with carbonates, every other mineral can be identified by the comparison of its spectrum with the ones present in databases or manuscripts.

During my Bachelor and Master thesis, I could get deep in the study of detrital minerals, on both (light and heavy fractions), since I developed with Prof. Sergio Andò a method to investigate by Raman spectroscopy Himalayan detrital grains, transported in the suspended load of the Ganga-Brahmaputra rivers system (during the BSc) and then decanted in the Bengal fan (during the MSc).^(Garzanti *et al.* 2011)

The two projects that I have carried out during my PhD beside the carbonates one, were focused as well on detrital minerals (see “7. *Other contributions*” chapter):

- The Lower Cretaceous basinal studies of the Arctic region (LoCrA) Project was concentrated on the Heavy Minerals (HM) present in two cores of the Barents Sea;
- The study of several samples collected on the Cantabrian Mountains (Spain) and then analysed with the optical microscope and with the Raman spectrometer by some students of the University of Stavanger (UiS), under mine and Sergio Andò supervision.

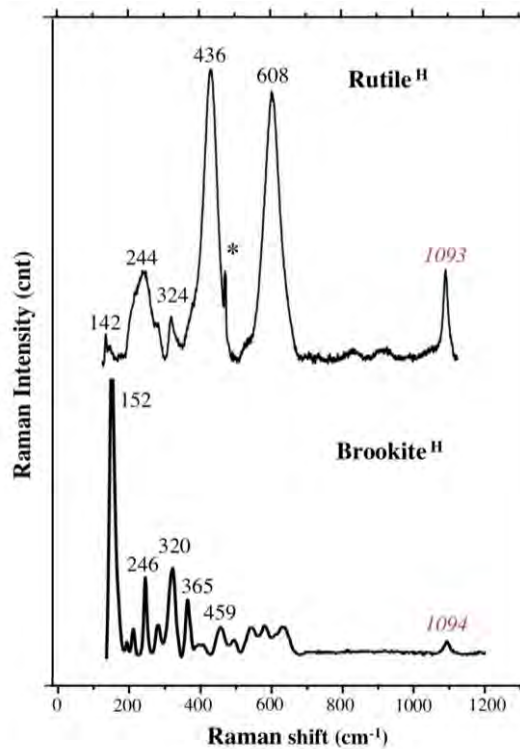


Figure 27 - A brookite spectrum (identified in LT1_p1G) and one of a rutile (identified in LT2_D).The main peak of magnesite (labelled in red) is present in both of them at 1093 and

1094 cm^{-1} , since the two minerals are surrounded by this carbonate, species, which have a strong signal. Both spectra were collected with the Horiba Xplora spectrometer. Stars represent the neon lamp emission line at 476.8 cm^{-1} used for calibration. Peak positions are reported without decimals. Figure and caption from Borromeo et al. 2018a.

Returning to the flooding chalk cores analyses, which represent the main topic of this PhD, analysing LTT and ULTT, only two non-carbonate, minerals were detected: a **brookite** spectrum was collected in LT1_p1G and a **rutile** one in LT2_D (see Fig. 27).

These two minerals show an extremely high Raman signal, and are both polymorphs of the TiO_2 . Rutile is one of the most stable heavy minerals in nature, tetragonal and a common accessory mineral in high-temperature/high-pressure igneous (hornblende-rich plutonic rocks and pegmatites) and metamorphic (schists, gneisses and amphibolites) rocks. Brookite is the orthorhombic polymorph, it is rare compared to the other polymorphs (rutile and anatase), and an accessory mineral of altered igneous rocks, schists, gneisses and hydrothermal veins.

3.8 Advantages and disadvantages of Raman spectroscopy

In conclusion, key advantages and disadvantages of Raman spectroscopy are listed below, with particular attention to its application to the geological research:

Advantages

- No particular sample characteristics needed, since it is possible to analyse: solid, liquid, gas, opaque, transparent, inorganic, and organic substances;
- Minimum or no sample preparation;
- No time consuming: good quality spectrum can be obtained in just a few seconds;

- Non-destructivity: precious sample can be analysed and further investigation (with Raman or other methods) on the very same sample area are possible;
- Resolution down to 1 μm ;
- Chemical and structural characterization of the sample material, also providing information such as, for minerals: crystallinity, chemistry, phase, intrinsic stress/strain and polymorphism;
- 2D and 3D imaging, three-dimensional scanning capability (x-y-z axes);
- Possibility of confocal analyses;
- Vacuum is not necessary;
- Portability, in situ analyses.

Disadvantages

- Cannot analyse metals, problems with ionic substances detection;
- Fluorescence may obscure the Raman signal: changing the laser beam can solve the problem, usually using a laser with higher wavelength and therefore less energy;
- An accurate database is necessary for spectra interpretation, since the identification is achieved through the comparison with a standard spectrum. Sometimes spectra can be difficult to be interpreted, due to the fact that a certain peak position (frequency) can be assigned to more than one substance; moreover, since Raman spectra are sensitive to chemistry and structure, the same peak of different crystals/grains of the same mineral can lie in different positions if the sample material characteristics are a little bit different from the standard mineral ones;
- Can perform semi-quantitative analyses by now, but this is constantly being improved;

Heating from the laser radiation can burn and destroy the sample, but laser power at the sample can be kept sufficiently low to avoid any thermal damage.

3.9 Nowadays Raman spectroscopy technical improvements and applications

The most important and outstanding nowadays achievement in Raman investigations is, for sure, **imaging**. Samples in so many scientific fields can be characterized and visualized, e.g. carbonate materials, tissues and cells of living subject, tablets, imaging their chemical and structural characterization. (Everal et al. 2000; Chuourpa 2005; Šašić, 2007; Keren et al 2008; Ni et al. 2008) In the last decades significant improvements of image quality has been achieved, and new techniques were perfected, obtaining 2D and 3D maps.

The mapping can be arranged in two ways - by scanning the light beam along the sample with a system of oscillating mirrors or by moving the sample itself using an X-Y or X-Y-Z scanning stages. There are a few distinctive geometries of sample mapping:

-X-Y optical sectioning (Surface scan): This simple technique it is usually used on flat samples (such as polished samples, tablets, cut-off or thin-sections) by mapping a thin 2D layer on the sample surface (Fig. 28a).

-X-Z cross-sectioning (Depth profiling): Confocal microscopy can be used as a powerful tool to conduct non-destructive internal investigations of a sample, obtaining a sample's 2D cross-section in X-Z direction (Fig. 28b).

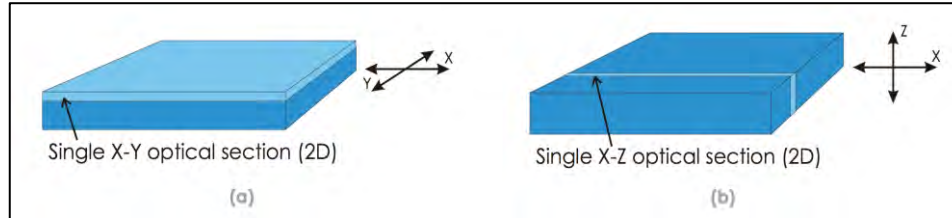


Figure 28 - 2D mapping: single X-Y (a) and X-Z (b) optical sections on a sample. From Princeton Instruments, confocal Raman notes, <http://forum.sci.ccnycunyc.edu/cores/microscopy-imaging/raman/Confocal-raman-note.pdf>

-Z-series (X-Y-Z scan): When a 3D structure of a bulk sample is needed it is possible to take multiple X-Y optical cross-sections along the Z-axis, which is unfortunately, quite time consuming. The technique is useful for analysis of polymers, nano-materials, integrated circuits, pharmaceutical samples and biological objects.

-Surface profiling (Auto-focusing): Another option is to reconstruct a 3D map of a sample from the X-Y-Z scan, using an auto-focusing technique.

Furthermore, there are two types of information that we can get from the imaging: the first one, not that common anymore, is the **multispectral imaging** where each pixel represents n values: the spectrometer captures image data within specific wavelength ranges across the electromagnetic spectrum, measuring light in a small number (typically 3 to 15) of spectral bands.

The second and most common type is the **hyperspectral imaging**, where each pixel of the map represents a spectrum. A different spectrum is captured for each pixel, so that different substances distribution in the sample can be achieved. The collection of spectra taken from multiple spots on the same sample is called a “*Data Cube*” because for a simple 2D X-Y scan the data is represented by a 3D array (cube) where X and Y dimensions hold spatial coordinates and the Z-

needed. For example, a mobile/portable Raman spectrometer will be launched as part of a powerful, rover-based analytical laboratories within the next 6 years for *in situ* analysis on Mars.^(Ellery 2004; Perez et al. 2006)

The potential of these instruments is excellent even if their performances are not comparable to the ones of fixed spectrometers, since resolution and samples stability are often an issue. To obtain a good Raman spectrum, the sample must be placed at the correct focal length from the lens, and holded perfectly still. Using mobile/portable spectrometers, expecially with low weight ones,^(Vandenabeele et al. 2007a) it is possible to move the probe to obtain the correct focus but, however, as the sample is not sympathetic to the instrument, there is a strong possibility that external vibrations will cause loss of focus, undermining the measurement. Unfortunately, mobile/portable spectrometers show a lower resolution than the fixed ones (few tenths of cm^{-1} , versus $0,2\text{-}2 \text{ cm}^{-1}$ for the laboratory spectrometers, depending on the wavelength used)^(Bersani et. al 2016; Borromeo et al. 2017a) but, anyway, the suitability of the technique is well demonstrated.

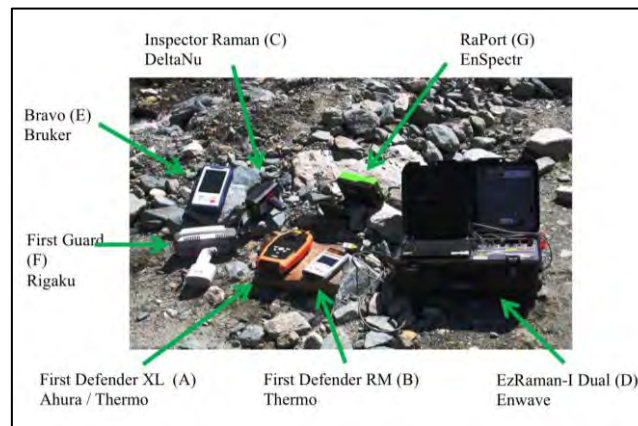


Figure 30 - Some of the most common mobile and portable Raman spectrometers. Photo courtesy of Danilo Bersani, for more information see Jehlička et al. 2014.

As already mentioned, by the use of Raman spectroscopy, it is possible to identify and analyse solids (both transparent and opaque), liquids and gases, organic and non-organic, presented in samples of various sizes and shapes (Fig. 31). These important features have allowed its fertile application in almost all scientific fields. ^(Schmitt and Popp, 2006)



Figure 31 - Raman spectroscopy does not need sample preparation and can be performed directly on minerals, thin sections or cut gems.

That Raman spectroscopy is a very important practical tool for quickly identifying minerals is really well known since Krishnan published his study on crystals in 1929. ^(Krishnan, 1929) In **geological sciences**, beside the recognition of the mineralogical species of the sample, it is possible to obtain much other information. ^(Neuville et al. 2014) In this field portable/mobile equipments open very interesting future prospectives and they may deeply change the everyday approach in geological field trips.

In mineralogy, ^(Aliatis et al. 2015; D'Ippolito, et al. 2015) petrography, ^(Pearson 2014) HT - HP studies, ^(Buob et al. 2006) even *in situ*, ^{(Putnis 1992; Neuville et al. 2014; de Ligny and}

Neuville 2013) and sedimentary petrography^(Ando et al. 2007; 2009; 2011) fields, researchers are developing a series of innovative and complementing applications to the classic analysis, such as microprobes and polarizing microscope. By Raman spectroscopy it is possible to recognize, and in some cases quantify, cations variations and replacement in solid solutions series and minerals group, e.g. olivine,^(Kuebler et al. 2006) garnets,^(Bersani et al. 2009) amphiboles,^(Bersani et al. 2014) and calcites,^(Borromeo et al. 2017a) determine the nature of chemical bonds and recognize lattice defects.

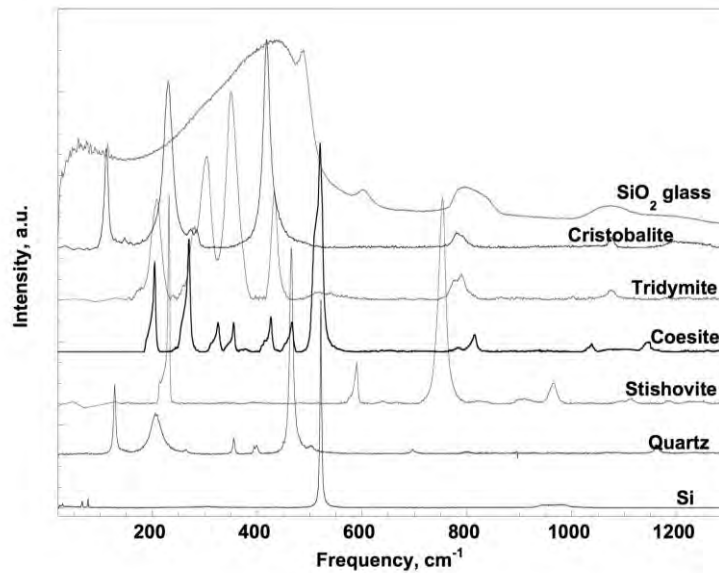


Figure 32 - Raman spectra of silicon and SiO₂ crystalline polymorphs and amorphous states (New Raman spectra made with T64000 Raman spectrometer, with 488 nm excitation line). Figure and caption from Neuville et al. 2014.

There are also other applications in **mineralogy**, such as determination of polymorphs (see Fig. 32),^(She et al. 1971; Dandeu et al. 2006; Neuville et al. 2014) degree of symmetry, structure, order/disorder^(She et al. 1971; Dutta 1988; Balan et al. 2001) chemistry of liquid and gaseous inclusions.^(Palanza et al. Frezzotti et al. 2012, Pearson et al. 2014) Another fundamental application of Raman spectroscopy is in the investigation of the area and conditions of the

crystals formation (crystallography): it is possible to analyse the variations in the position of single peaks that reflect small differences in composition due to particular geodynamic environments (useful for this purpose are, for example, the spikes that reflect the presence of rare earths)^(Moroz et al. 2000) otherwise to analyse the mineralogy and the geochemistry of inclusions,^(Palanza et al. 2008; Barone et al. 2016) which record the chemical-physical changes occurring during the formation of the mineral. An important example consists in the study on diamond inclusions presented in Pearson et al. 2014, where hydrous mantle transition zone is supposed as source, thanks to ringwoodite inclusions (Fig 33).

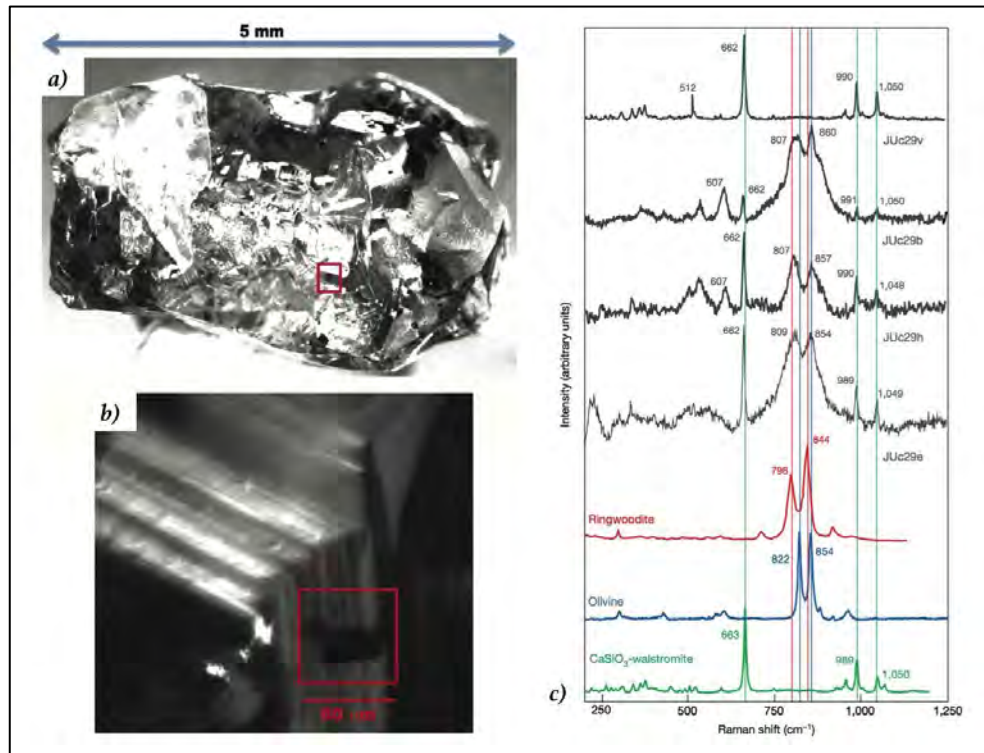


Figure 33 – a) Monochrome image of diamond JUC29 taken under incident light, with the ringwoodite-walstromite inclusion pair highlighted by a red square. The irregular shape and hexagonal pits in the diamond are signs of significant resorption. b) Enlarged view of the area of the host diamond (rotated 90° relative to a) containing the ringwoodite - walstromite

inclusion pair. The shadow behind the rectangular area outlining the inclusion pair is probably a stress fracture in the diamond. c) Raman spectra of ringwoodite and walsstromite inclusions in Juina diamond JUC29. Raman spectra (unsmoothed, background-subtracted, in relative intensity units, stacked for clarity, shown in grey) for two-phase inclusion within JUC29 diamond, Juina. Spectra are complex, displaying SiO_4^{2-} stretching modes for ringwoodite ($[\text{Mg,Fe}]\text{SiO}_4$) that are broadened, probably by disordering induced by incipient retrogression, as well as the characteristic modes for Ca-walsstromite (CaSiO_3). Modified after Pearson et al. 2014.

The Raman spectroscopy has various applications in **gemology** (Kiefert et al. 2000; Palanza et al. 2008; Bersani et al. 2010; 2014; Barone, et al. 2014, 2015, 2016) as a direct consequence of its non-destructivity and portability, fundamental conditions required by the preciousness of the samples. Raman spectroscopy can be used to recognize false or synthetic gems (Bernardino et al. 2009; Barone et al. 2016) (Fig. 34), or treatments made to enhance colour or transparency, (Bersani et al. 2014b; Barone et al. 2016) to valuate the purity, to obtain information about their origin; (Bersani et al. 2014b; Barone et al. 2016) to recognize the composition of solid solutions mineral (important when different end - members have different value). It is possible to analyse mounted and cut gems, amorphous (oxydian and opal), organic (pearls, coral), minerals of any degree of transparency, and even through a transparent containers (Fig. 35).

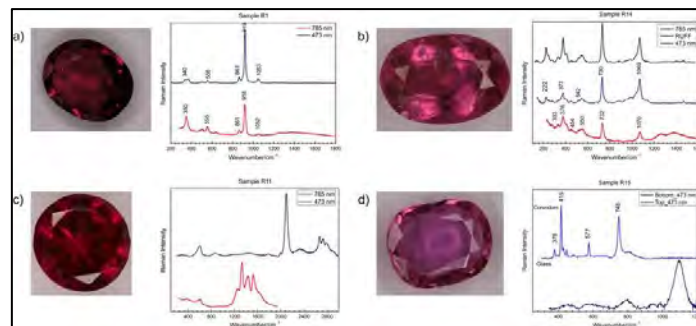


Figure 34 - Pictures and micro-Raman spectra collected with both 785- and 473-nm lines on red gems identified as ruby simulants, as examples. Natural simulants: (a) R1, garnet; (b) R14, tourmaline. Artificial simulant: (c) R10, glass. Composite gem: (d) R15, doublet (data collected with 473-nm line are shown). Figure and caption from Barone et al. 2016.

Raman spectroscopy is a well established approach also in the **preservation of cultural heritage** (Derbyshire et al. 1999; Vandenabeele et al. 2004; 2007b; Edwards and Chalmers, 2005; Bersani et al. 2016; Casadio et al. 2016; Chiriu et al. 2016; Mazzoleni et al., 2016) (Fig. 35), especially to recognize the techniques of execution, falses, and the materials used such as: organic substances (Daher et al. 2014) and mineral phases, (Bersani et al. 2010; Bersani and Lottici, 2016; Barone et al. 2016) in pigments and binders, (Bell et al. 1997; Fremout and Saverwyns, 2012) potteries, (Cantisani et al. 2012; Medeghini et al. 2014; Zimmermann et al. 2016) glass, (Bouchard et al. 2007; Colomban et al. 2007) even their origin, and processes of degradation and corrosion (Hayez et al., 2005; Schutz et al. 2013) in a completely non-destructive way, even through transparent cover (Fig. 35). Studying the origin of raw materials, Raman spectroscopy allows in obtaining information about dating, commercial tracts and habits, helping to develop our historical and social knowledge. (Lofrumento et al. 2012; Rousaki et al. 2015; Bersani et al. 2016)

A noteworthy example, concerns the use of Raman spectroscopy in 2002 when the Shroud Conservation Committee selected the Raman instrumentation to provide an analysis of the Holy Shroud. (Moscardi, 2008)

Moreover, beside micro-Raman spectroscopy, two high-performing spectroscopies are growing and being applied in the archeology field: Surface-Enhanced Raman Spectroscopy (SERS), (Guineau and Guichard 1987; Casadio et al. 2010; Poggi et al. 2016) already mentioned in the “3.5 Tip-Enhanced Raman Spectroscopy” chapter, and the Spatially Offset Raman Spectroscopy (SORS), (Conti et al. 2014, 2016) that overcome the inability of performing confocal analyses on layered turbid substances such as painted layers, usually few tens of micrometres thick.

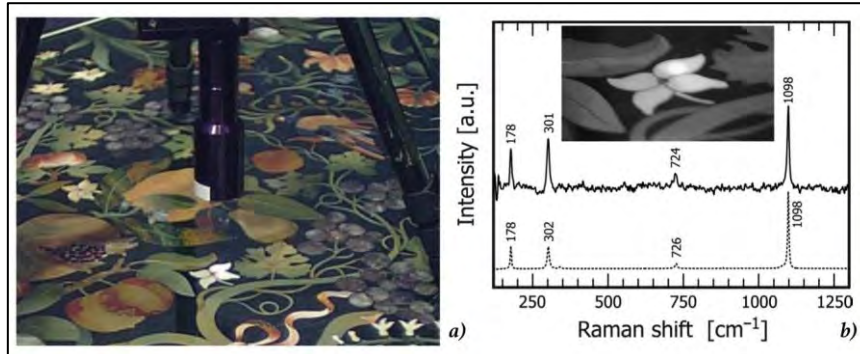


Figure 35 - a) Part of a mobile Raman system sitting on top of a very large precious Florentine black marble table in stone marquetry protected by 1.6 cm thick plate glass (reflections visible). Note the gemstones forming various ornamental designs, especially birds and flowers. Note the tripod suspending the remote head with its long focal length lens (black tube). Verification of the mineral species of a petal of an inlaid flower, using a red 632.8 nm laser beam (spot is seen as bright circle). The collection lens is suspended 7.5 cm above the crystal. b) The Raman spectrum obtained from one of the petals (corrected for background luminescence; solid graph) is shown in comparison with the spectrum of dolomite from Freiberg, Germany (dotted). The obtained spectrum reveals the four principal bands of dolomite. Photographs were taken by D.C. Smith. Pictures and caption modified after Nasdala et al. 2004.

Clear advantages of micro- Raman microscopy assured its proliferation in other several and really different areas of industry and academic research, such as nanoscience,^(Jorio et al. 2012) where characterization of heterogeneous nano-systems continues to grow in importance and impacts key applications in the field of nanotechnology (molecular electronics, nano-sensors, nanotubes and nanowires), material science (phase segregated systems) and catalysis (single site catalysts).^(Schmitt and Popp, 2006) The probably most know application of Raman spectroscopy, TERS and SERS regards the characterization of space distribution of carbon nanotubes (CNT)^(Dresselhaus et al. 2005; Dresselhaus et al. 2010) – the unique nanostructures with remarkable mechanical and electrical properties and significant potential for future innovations. It is important to remark that this type of analysis cannot be done with traditionally used SEM or TEM microscopy.

Bio-science research and pharmaceutical industry constitute another rapidly growing application area for confocal Raman spectroscopy, (Movasaghi et al. 2007; De Veij et al. 2009) TERS and SERS, indicating these instrumentations evolving towards being dedicated tools for biologists. In biological samples, such as tissues and cells, Raman spectra can perform extremely detailed analysis and chemical maps, allowing good specificity for qualitative analysis. (De Gelder et al. 2007) It is amazing to think that today cellular components evolution can be observed during a cell's life cycle, (Xie et al. 2005) and even *in vivo* transcutaneous analyses on murines (Schulmerich et al. 2007) can be performed. Moreover recognition of bacteria (Goeller et al 2007) or diseased/cancerous tissues (Harvard et al. 2005) can be easily achieved. There are other several fields of application of Raman spectroscopy, as the production of degradable and non-degradable polymeric biomaterials for prosthesis, or as indicators of bone quality. (Morris MD and Mandair, 2011)

In pharmaceutical industry confocal Raman has been widely used for the characterization of the structure and distribution of the APIs (Active Pharmaceutical Ingredient) performing high-resolution chemical mapping of commercially distributed pills (Fig. 36). (Wartewigh and Neubert, 2005; Šašić, 2007)

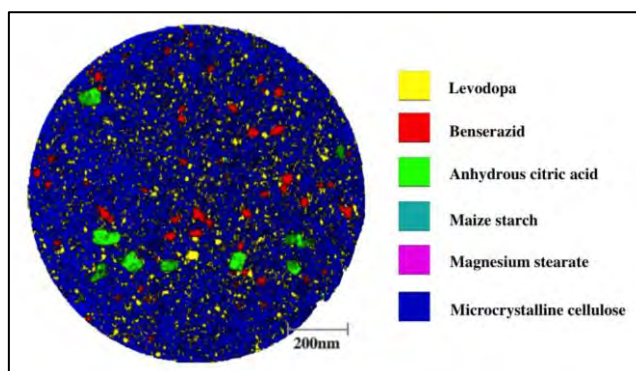


Figure 36 - Raman image of a tablet used for the treatment of Parkinson's disease. It contains two APIs (levodopa – yellow, and benserazid - red) and four excipients (anhydrous citric acid

Raman spectroscopy

– green, maize starch – cyan, magnesium stearate – magenta, and microcrystalline cellulose – blue). Photo courtesy of Renishaw plc.

Furthermore Raman spectroscopy, parallel to SERS,^(Muehlethaler et al. 2015) is applied in **forensic sciences**, where narcotics, polymers, explosives, gunpowder, and biological residues are easily identified, thanks to their strong Raman signal.^(Palenik et al. 2007; Chalmers et al. 2012; Buzzini et al. 2016) The recognition of soil, sand, and rock constituent minerals can also be a source of important evidences for the reconstruction of the facts. Univocal identification of unknown substances is indispensable in this scientific field and must be achieved without compromising the constituent elements in any way, even conducting the analysis through a glass or plastic container.

4 Samples for this research project

During this PhD project, my studies were primarily focused on the carbonate minerals group, with particular attention to calcite, magnesite, and biogenic Mg-calcite. Afterwards, chalk and flooded chalk cores were been deeply analysed by Raman spectroscopy and TERS. Only two non-carbonatic minerals were found in chalk samples: rutile and brookite, two of the three TiO_2 polymorphs (see “3.7 Spectra of non-carbonate minerals”).

Moreover **detrital minerals** were investigated during the Barents Sea cores analyses, where ZTR (zircon, tourmaline, and rutile), garnet, apatite, staurolite, Cr-spinel were the major components. Another chance to study detrital minerals was during the geological fieldwork to the Cantabrian Mountains (Spain) where I’ve been student assistant and during the consequent Sedimentary petrography studies, carried out on the sandstone and shale samples collected there.

4.1 Carbonate minerals



Figure 37 – Calcite (a) and aragonite (b) crystals.

Carbonates are the principal constituents of many sedimentary rocks and are globally wide-spread; these minerals are present in every possible setting (organic, sedimentary, metamorphic, magmatic,

Samples for this research project

extraterrestrial) and represent approximately 30% of the Phanerozoic sedimentary rock record after diagenesis.^(Unvros et al. 1991)

Crystallization of CaCO_3 is a ubiquitous process in nature (limestones, marbles, biominerals, etc.) as well as a prime operation in industry. Carbonates are commonly applied as additive, building materials, fillers, medicines and pills, food, paper, plastics, printing inks.

Calcium carbonate (CaCO_3) can crystallize in three different forms: calcite, aragonite, and vaterite with trigonal, orthorhombic, and hexagonal structure, respectively.

Nucleation and growth of **calcite** crystals normally take place in nature, mostly as a result of biomineralization^(Deer et al. 1992; De la Pierre et al.2014) as calcium carbonate is the major constituent of reefs and oceans seafloor. Calcite (Fig. 37a) is the most stable and abundant polymorph of CaCO_3 as it represents about 4 wt % of the Earth's crust.^(Valenzano et al. 2007) Carbonate rocks are in general soluble in slightly acidic waters and they often have high porosity and permeability, which makes them ideal petroleum reservoirs.

Calcite shows a trigonal system and scalenohedral structure with two molecules per unit cell. Ca^{++} and the carbon atom of the carbonate ion are located on the trigonal axis and the centre of symmetry of the mineral is controlled by the orientations of the two carbonate ions that are staggered relative to each other.^(Sun et al. 2014) The structure of this mineral is particularly interesting because lots of constituents of sedimentary rocks, like magnesium and iron-bearing carbonate, have structures that are similar to the calcite one. In calcite crystals magnesium, iron and manganese impurities are possible.

Calcite structure can accommodate a considerable amount of Mg in its lattice. Magnesium ions are widely present in sedimentary environments where calcite forms or where metastable carbonates recrystallize to low-Mg calcite.^(Goldsmith, 1955; Kats, 1973) Magnesian calcites

Samples for this research project

are common in the Pleistocene and modern carbonates, as they are the major component of marine invertebrates skeletons and cement. (Chave 1954a, 1954b)

The orthorhombic and most unstable CaCO_3 polymorph is **aragonite** (Fig. 37b), which is quite common and can crystallize during biological (coral reefs and shells) and geological processes (hot springs, stalactite and stalagmite cave formations).

Hexagonal **vaterite** is the most rare and least known polymorph. (Gabrielli et al. 2000; Wehrmeister et al. 2010; De La Pierre et al. 2014) It is metastable and mostly present in fresh water biological environments and mineral springs; it forms small micrometric crystals.



Figure 38 - Magnesite (a) and Dolomite (b) minerals.

Magnesite (MgCO_3 ; Fig. 38a) is isomorphous with calcite and shows the same trigonal structure as calcite. It can be found in sedimentary and metamorphic (serpentinites) rocks. Magnesite crystals are often massive and colourless, but euhedral crystals are relatively rare, which makes Raman analysis useful in identification of this mineral.

Another important and common carbonate is **dolomite** ($\text{CaMg}(\text{CO}_3)_2$; Fig. 38b). It is usually formed by diagenesis or hydrothermal metasomatism of limestone. It is quite rare as a primary phase, but

could crystalize in sabkha environments or contact metamorphic rocks, marbles, carbonatites and ultramafic rocks. Its structure is similar to the calcite one but presents an alternation of calcium and magnesium layers that lower the hexagonal symmetry of dolomite.^(Bischoff et al. 1985; Gunasekaran et al. 2006; Sunet al. 2014) The unit cell configuration is similar to that of calcite. Dolomite forms an isomorphic series with the hexagonal ankerite $\text{Ca}(\text{Fe},\text{Mn})(\text{CO}_3)_2$.

Certificated standard samples for magnesite, siderite and ankerite were provided by the M.A.C. Company (Micro-Analysis Consultants). The pure calcite crystal standard was from Chihuahua, Mexico, the aragonite standard from Val Formazza, Italy, and the dolomite standard from Selvino, Italy. The chemistry of all these samples has been checked by microprobe analysis at the SEM-EDS laboratory at Milano-Bicocca University.

4.2 Biological magnesium calcites

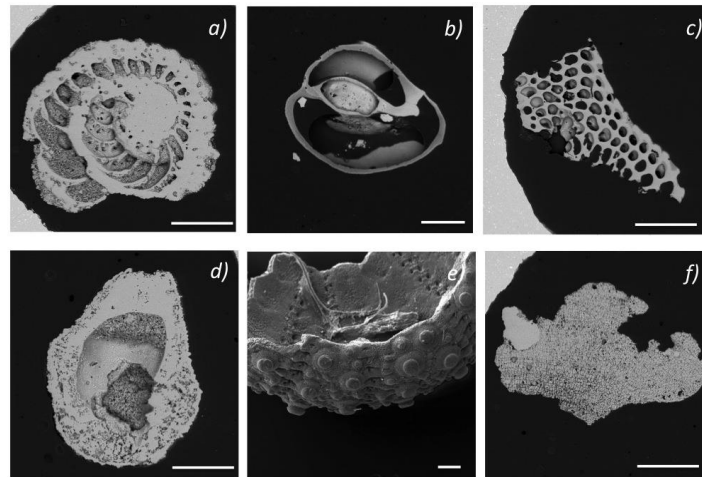


Figure 39 - SEM micrographs of some of the biological Mg-calcite samples analysed during this PhD project, collected at Milano-Bicocca University, Milano. a) Benthic foraminifer (*Elphidium* sp.), Imperia, Italy; b) Benthic foraminifer (Miliolida), Corsica Island, France; c) Benthic foraminifer (*Sorites* sp.), Crete Island, Greece; d) Bryozoan (*Bifissurinella lindembergi*), Rosignano Monferrato, Italy; e) Echinoid, (Echinoidea), Moira Mound,

Samples for this research project

Western Ireland shelf; f) Calcareous red algae (Corallinophycidae), Hvammstangi. Iceland. Bar scale: 200 μ m.

Carbonate sediments are constituted largely or wholly of the skeletons of marine organisms (Fig. 39) mainly foraminifers and algae), which are composed of a variety of Mg and Ca carbonates (calcite, aragonite, and a spectrum of magnesium calcites, rare dolomite).^(Chave 1952)

Goldsmith (1955) studied with X-ray more than one hundred magnesian calcite samples from every possible setting and origin and found that sedimentary and other low temperature calcites are usually very low in Mg. Metamorphic carbonates commonly contain dolomite associated with calcite containing significant amount of MgCO₃ in solid solution, while granulite-facies rocks can bear up to 9 mol per cent of magnesium.^(Goldsmith, 1955)

Chave (1954a, 1954b) and Stehli and Hower (1961) have shown that carbonate skeletal materials of marine organisms are commonly unstable, since aragonite and magnesium calcite are their most common component: pure calcite is the predominate mineral phase only in quite deep water.^(Chave, 1954; Stehli and Hower, 1961)

Phase equilibrium studies of the systems CaCO₃ and MgCO₃ by Jamieson (1953), Harker and Tuttle (1955) Graf and Goldsmith (1955), and others have shown that only low magnesium calcite (i.e., calcite containing less than about 4% MgCO₃ in solid solution) is stable under pressure and temperature conditions at or near the surface of the Earth. Aragonite and calcite containing more than 3 or 4% MgCO₃ in solid solution are unstable, non-equilibrium phases. The dissolution of metastable aragonite and Mg-calcites and the consequent recrystallization of the stable calcite occur during the earliest stages of sedimentation.^(Chave 1962; Land 1967; Hower 2001)

Aragonite → Calcite

Mg Calcite → Calcite + Dolomite

Samples for this research project

Usually textural changes are involved in the substitution of aragonite or magnesium calcite by calcite.^(Sandberg 1975; Towe and Hemleben 1976; Richter 1979, 1984; Manze and Richter 1979; Neugebauer 1979; Brand and Veizer 1980; Blake et al. 1982; Oti and Muller 1985; Turner et al. 1986) Shallow-water magnesian calcites have variable compositions which are related to temperature and dissolved inorganic carbon concentration in seawater during life and precipitation, taxonomy and growth rate of the magnesian calcite-secreting organism.^(Chave 1954a; 1954b; Mackenzie 1983; Mutti et al. 2003)

Biological magnesian calcites samples analysed during this PhD research (reported in Table 2, for more information see Borrromeo et al. 2017a) are recent and fossil foraminifers, coralline red algae, barnacles and sea urchins that were collected from areas situated at different latitudes, depth and depositional environments and characterized by different water temperatures (from 5 to 29.5 °C) and saturations (from 160 ± 20 to 245 ± 15), factors affecting the Mg content in shells of marine organisms.

Taxon	MgCO₃ (mol%)	Age	Location	Average water temperature (°C)
Benthic foraminifer (<i>Ammonia</i> sp.)	0.1	Recent	Imperia. Italy	18.5 ^[44]
Benthic foraminifer (<i>Elphidium</i> sp.)	0.1	Recent	Imperia. Italy	18.5 ^[44]
Benthic foraminifer (Miliolida)	12.4 - 13.3	Recent	Imperia. Italy	18.5 ^[44]
Benthic foraminifer (<i>Elphidium</i> sp.)	0.9 - 2.3	Recent	Corsica Island. France	18.5 ^[44]
Benthic foraminifer (Miliolida)	11.0 - 12.3	Recent	Corsica Island. France	18.5 ^[44]
Benthic foraminifer (<i>Sorites</i> sp.)	11.5 - 11.6	Recent	Corsica Island. France	18.5 ^[44]

Samples for this research project

Benthic foraminifer (<i>Elphidium</i> sp.)	1.9 - 4.0	Recent	Crete Island. Greece	20.5 ^[44]
Benthic foraminifer (Miliolida)	9.3 - 10.7	Recent	Crete Island. Greece	20.5 ^[44]
Benthic foraminifer (<i>Sorites</i> sp.)	11.0 - 11.3	Recent	Crete Island. Greece	20.5 ^[44]
Benthic foraminifer (Miliolida)	13.7	Recent	Sharm el Sheik. Egypt	25.5 ^[44]
Benthic foraminifer (<i>Peneroplis</i> sp.)	13.7	Recent	Sharm el Sheik. Egypt	25.5 ^[44]
Benthic foraminifer (<i>Sorites</i> sp.)	13.6 - 14.4	Recent	Sharm el Sheik. Egypt	25.5 ^[44]
Benthic foraminifer (<i>Elphidium</i> sp.)	0.5 - 1.0	Recent	Kota Kinabalu. Malaysia	30.0 ^[44]
Benthic foraminifer (<i>Sorites</i> sp.)	13.1 - 13.7	Recent	Kota Kinabalu. Malaysia	31.0 ^[44]
Benthic foraminifer (<i>Elphidium</i> sp.)	2.8 - 3.6	Recent	Magoodhoo. Maldives	29.5 ^[44]
Benthic foraminifer (Miliolida)	12.5	Recent	Magoodhoo. Maldives	29.5 ^[44]
Benthic foraminifer (<i>Sorites</i> sp.)	14.4 - 15.5	Recent	Magoodhoo. Maldives	29.5 ^[44]
Benthic foraminifer (<i>Elphidium crispum</i>)	1.2 - 2.0	Miocene	Rosignano Monferrato. Italy	tropical- subtropical ^[45]
Bryozoan (<i>Bifissurinella lindembergi</i>)	2.5 - 2.6	Miocene	Rosignano Monferrato. Italy	tropical- subtropical ^[45]
Calcareous red algae (<i>Neogoniolithon</i>)	16.5 - 17.4	Recent	Magoodhoo. Maldives	29.5 ^[44]
Calcareous red algae (Corallinophycidae)	11.2 - 18.2	Recent	Hvammstangi. Iceland	5.0 ^[44]

Samples for this research project

Calcareous red algae (<i>Porolithon onkodes</i>)	13.4 - 21.3	Recent	Sharm el Sheik. Egypt	25.5 ^[44]
Calcareous red algae (Corallinophycidae)	2.3 - 2.5	Miocene	Rosignano Monferrato. Italy	tropical- subtropical ^[45]
Barnacle (<i>Balanus perforatus</i>)	1.8 - 3.7	Recent	Imperia. Italy	18.5 ^[44]
Barnacle (<i>Balanus</i> sp.)	1.9 - 3.6	Recent	Magoodhoo. Maldives	29.5 ^[44]
Barnacle (<i>Balanus</i> sp.)	1.8 - 2.3	Pliocene	Diano Marina. Italy	18.5 ^[44]
Barnacle (<i>Balanus</i> sp.)	0.6 - 2.3	Miocene	Rosignano Monferrato. Italy	18.5 ^[44]
Echinoid, (Echinoidea)	2.8 - 3.9	Recent	Moirá Mound. Western Ireland shelf	~ 8 ^[46]
Echinoid (<i>Echinocardium fenaxi</i>)	9 - 10.2	Recent	Stromboli. Italy	20.5 ^[44]
Echinoid (<i>Cidaris</i> sp.)	6.3 - 6.4	Recent	La Spezia. Italy	18.5 ^[44]
Echinoid (<i>Paracentrotus lividus</i> sp.)	4.2 - 4.7	Recent	La Spezia. Italy	18.5 ^[44]
Echinoid (Echinoidea)	8.8 - 11.0	Recent	Magoodhoo. Maldives	29.5 ^[44]

Table 2 – List of the biological magnesium calcite samples analysed in this PhD project, with their magnesium content, age, location and water temperature. From Borromeo et al. 2017a.

4.3 Flooded chalk

Fluids injection is one of the most efficacious Improved Oil Recovery (IOR) methods on the Norwegian Continental Shelf.^(Hermansen et al. 2000; Nagel et al. 2001) At reservoir temperatures, seawater weakens the mechanical

Samples for this research project

strength of chalk rocks, directly affecting the oil recovery factor of the fields, since an increase in compaction, and a loss in porosity and permeability do occur.

(Risnes et al. 2003, 2005; Heggheim et al. 2005; Korsnes et al. 2006, 2008a, b; Madland et al. 2006, 2008, 2011; Zangiabadi et al. 2009; Andreassen et al. 2010; Megawati et al. 2012; Hiorth et al. 2013)

The permeability depends on several interdependent material parameters that may change during compaction and dissolution/precipitation, such as change in wettability, specific surface area (S), wettability, the distribution of pore throat diameters, pore size distribution, the tortuosity (τ), the relative permeability arising from capillary forces introduced by surface tension (γ) in the presence of other fluids, and the hydrophobic/hydrophilic (wettability) properties of the mineral surfaces.

(Zimmermann et al 2015)

It is essential to comprehend how brines interact with rocks because textural and chemical/mineralogical changes in the pore space affect also oil+water+rock interaction, such as adsorption and expulsion.

(Austad and Standnes, 2003; Strand et al. 2003;2007; Risnes et al. 2005; Zhang et al. 2006, 2007; Austad et al. 2008; Hiorth et al. 2010; Fathi et al. 2010; Ali et al. 2011; Madland et al. 2011; Megawati et al. 2013).

Several studies were been focused on this important topic, and can be found in literature.

(Korsnes et al. 2006; Zhang et al. 2006; Madland et al. 2011; Andersen et al. 2012; Megawati et al. 2013, 2015; Wang et al. 2016)

Mechanisms such as dissolution, ion exchange, precipitation, adsorption, and desorption are triggered by fluid injection and can interplay at the same time, with different relative significance if close to the injector or to the producer.

With $MgCl_2$, which represent simplified seawater chemistry, the role of Mg^{2+} is investigated. After a long time $MgCl_2$ injection, the calcite coccoliths rings are dissolved, and, after Mg^{2+} has bounded to CO_3^{2-} , a consequent precipitation of rhombohedral magnesite crystals occurs (Fig. 40).

(Risnes et al. 2003, 2005; Korsnes et al. 2006; Hjuler and Fabricius et al. 2007; Hiorth et al, 2010; Madland et al. 2011; Zimmermann et al. 2015a; Minde et al. 2017)

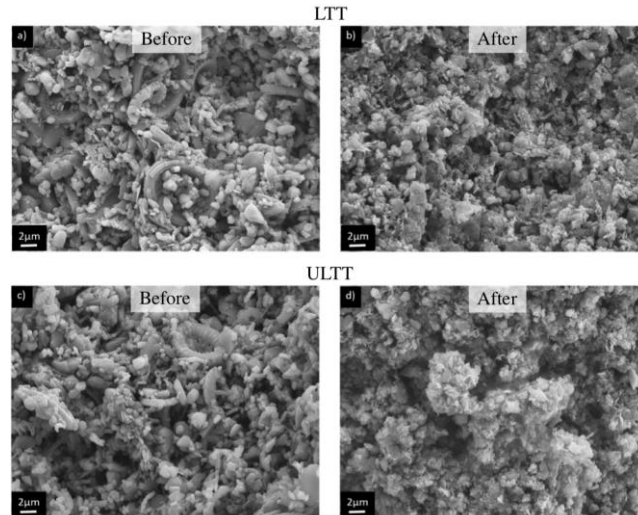


Figure 40 - a) SEM-micrograph of unflooded chalk from the end-piece of the LTT-core (from Zimmermann et al. 2015a). Main components are coccoliths and fragments with a calcitic composition. b) SEM-micrograph of the severely altered part of the flooded core (LTT) towards the inlet of the core (from Zimmermann et al. 2015a). Coccoliths and other fossils are no longer visible, only crystals mainly below 1 μm in size, with high magnesium content. c) SEM-micrograph of unflooded chalk of the ULTT with main components as observed in a). d) SEM-micrograph from slice 5 of the ULTT after flooding with MgCl_2 . Texture and composition is as observed in b). Figure and caption from Borroneo et al. 2018a.

4.3.1 Liège chalk

Chalk is a sedimentary rock known for its very fine-grained texture, with grain size often below 1 micrometre. It is a soft, white/light grey, porous carbonate rock, a pure form of limestone principally composed of calcite (Fig. 41). Chalk forms under reasonably deep and warm marine conditions from the gradual settling of microfossils (Fig. 41) such as coccoliths (plates shed from micro-organisms called coccolithophores). In addition to the coccoliths, the fossil debris includes a variable, but minor, percentage of the fragments of foraminifera, ostracods and mollusks. Also, chert and pyrite (transformed to iron oxides during weathering) nodules could be present. Some chalk carry diagenetic silica-phases like opal-CT (chalk from Aalborg).^(Hjuler and Fabricius, 2009)

On-shore chalk is often used for experiments in relation to hydrocarbon

Samples for this research project

focussed research as off-shore chalk is scarce and extremely expensive. An overview of often used chalk and their compositions can be found in Hjuler and Fabricius (2009).



Figure 41 – a) An example of a chalk rock sample , centimetric scale bar . b) A SEM micrograph of Liège chalk before flooding . Scale bar: 2 micron. From Wang et al. 2016.

The famous White Cliffs of Dover (Fig. 42) are formed of Cretaceous chalk deposits, which do not show clear beddings, at the contrary to other older Carboniferous or Jurassic limestones. This presumably indicates very stable conditions over tens of millions of years. Because chalk is usually deeply jointed it can hold a great amount of ground water, providing a natural reservoir that releases water through dry seasons.



Figure 42 - The most famous chalk cliff, the White cliff, near Dover.

The chalk samples studied in this project were all sampled at the Lixhe

Samples for this research project

outcrop (Gulpen Formation, Campanian - Early Maastrichtian)^(Molenaar and Zijlstra, 1997) near Liège in Belgium, in particular in the Zeven Wegen Member^(Robaszynski et al. 2001) with an age of 75.5–78.0 m.y, and thickness up to 30 m (Fig. 43). This member presents a basal layer of glauconitic zones, with random black, fine-grained flints.^(Robaszynski et al. 2001) The chalk shows clear signs of recrystallization, contact cements, and particles interlocking. Nevertheless, coccolithophores are still well preserved and the rock presents intrafossil porosity.^(Hjuler and Fabricius, 2009)

These Zeven Wegen Member present a clean compositional nature, as its main component is calcite (CaCO₃) together with minor abundances of non-carbonate minerals (between 3-5 wt.% in total)^(Wang et al. 2016; Zimmermann et al 2016) that mainly consist of quartz, smectite/mixed smectite-illite layer, mica, kaolinite, and clinoptilolite and minor quantities of zeolite, apatite, opal, feldspar, pyroxene, pyrites, and titanium oxide.^(Hjuler and Fabricius, 2007; Zimmermann et al. 2015a)



Figure 43 - Chalk cliff at the Hallembaye CPL cave, near Liège in Belgium. 1.Top layer: displaced cover strata; 2. Upper bench: Lanaye (with regular flint layers) and top Lixhe members; 3. Middle bench: Lixhe member (unlayered small flint appearance) and Vijlen member (grey chalk); 4. Lowermost bench: Zeven Wegen Member (with/light grey chalk). After W.M. Felder (1975).

The porosities lies in the range of 40-45 %.^(Felder 1975; Molenaar and Zijlstra 1997; Slimani 2001; Strand et al. 2007; Hjuler and Fabricius 2009 Wang et al. 2016) **More information**

about mineralogy, petrography, and rheological characteristics of the Gulpen Formation can be found in literature. (Felder 1975; Molenaar and Zijlstra 1997; Slimani 2001; Strand et al. 2007; Hjuler and Fabricius 2009)

On shore chalk successions are used as analogues for North Sea reservoir chalk in several flooding studies. (Strand et al. 2007; Austad et al. 2008; Madland et al. 2011; Megawati et al. 2015; Nermoen et al. 2015; Zimmermann et al. 2015; Wang et al. 2016)

4.3.2 Previous studies and characterisation of the sample material

Several high-resolution technologies were applied on the study of the mineralogical alteration in flooded chalk: x-ray diffraction (XRD), (Zimmermann et al. 2015a) whole-rock geochemistry techniques, (Zimmermann et al. 2015a; Minde et al. 2016; Wang et al. 2016) Field Emission Gun Scanning Electron Microscopy– Energy-Dispersive X-Ray Spectroscopy (FEG-SEM-EDS), (Riesnes et al. 2003, 2005; Korsnes et al. 2006; Hjuler and Fabricius et al. 2007; Hiorth et al. 2010; Madland et al. 2011; Zimmermann et al. 2015a; Minde et al. 2016; 2017) X-Ray diffraction (XRD), (Zimmermann et al. 2015a) whole-rock geochemistry techniques, (Zimmermann et al. 2016) Transmission Electron Microscopy (TEM), (Egeland et al. 2017, Minde et al. 2017) Nano Secondary Ion Mass Spectrometry (NanoSIMS 50), (Zimmermann et al. 2015a; Minde et al. 2016) Mineral Liberation Analysis (MLA). (Minde et al. 2017)

A loss of Ca^{2+} and a gain in Mg^{2+} were determined, highlighting Mg-minerals secondary precipitation in the cores (Zimmermann et al. 2015a for the LTT, and Nermoen et al. 2015 for the ULTT). TEM and FEG-SEM could image magnesite crystals with a grain size between 100 nm and 1 μm . (Egeland et al. 2017; Minde et al. 2017)

The Long Term Test was previously studied in detail. Using geochemistry, Zimmermann et al. (2015) could calculate a 20 % mass loss during the 1.5 years long experiment, resulting from dissolution

and compaction: an axial shortening of 18 % (in length) and a porosity reduction of 20% were documented. Applying x-ray diffraction (XRD, see Fig. 44) on the LTT, the same study could detect the presence of magnesite, chrysotile (in slice 1, 2, and 3), tillieyte (only in slice 4), quartz, anthophyllite as well as gypsum (the latter only in the unflooded chalk). Magnesite could only be detected when it was more abundant, pointing out the limits of XRD as a detection method for traces of minerals. Following the geochemical model by Hiorth et al. (2013), talc should precipitate, but this mineral could not be detected by XRD or other mineralogical analyses. NanoSIMS 50 was the only analytical method that could detect and image micron- and sub-micron size magnesite and quartz crystals.^(Zimmermann et al. 2015a) When analysed by MLA, LTT could be imaged, displaying a rather sharp (~1.5 mm) transition between two areas with different mineralogy.^(Minde et al. 2017) All the studies cited above are consistent in showing an almost complete alteration and magnesitisation close to the inlet of the LTT core. Furthest away from the inlet, the mineralogy was still dominated by calcite, with occurrences of magnesite and clay, indicating only partial calcite dissolution opposed to the complete substitution at the inlet.

Samples for this research project

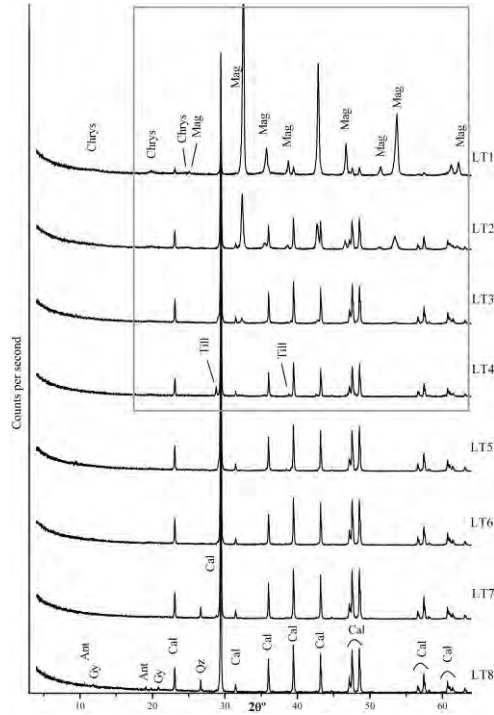


Figure 44 - X-ray diffraction mineralogy of the flooded slices of the core (LT 1–6) and unflooded chalk (LT 7 and LT 8) from Liège. Cal = calcite; Mag = magnesite; Qz = quartz; Ant = anthophyllite; Gy = gypsum; Till = tilleyite; Chrys = chrysotile. Gray rectangle marks the range where most significant changes are observed from slice LT1 to LT4. Figure and caption from Zimmermann et al. 2015a.

The Ultra Long Term Test was deeply studied by Nermoen et al. (2015) where the whole core showed an almost homogeneous composition, dominated by magnesite crystals (see Fig. 45) with the mentioned calcium impurities and clay. Nermoen et al. (2015) described the flooding experiment of the 3-years-test (ULTT) in detail. A porosity decrease from 41.32 % to 40.02 % was measured at the end of the experiment, documenting how compaction significantly altered the solid volume. The solid density increased from 2.68 to 2.90 g/cm³ throughout the experiment, simultaneously to a weight lost of 22.93 g.

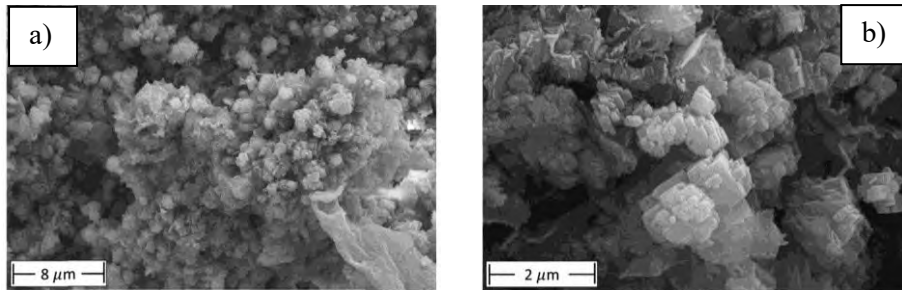


Figure 45 - SEM images of tested core material from slice 2 of the Ultra Long Term Test. Complete reworking of the microstructure and new growth of rhombohedral crystals. Scale bar: 8 μm in a), 2 μm in b). Figures and captions from Nermoen et al. 2015.

Compaction alone could not explain the changes in permeability and porosity over time. During the start of the ULTT experiment, when compaction was the controlling mechanism, permeability and calculated porosity got lower, ^(Nermoen et al. 2015) while throughout the experiment, the permeability and porosity increased again.

This is probably caused by mineralogical transformation: through dissolution of primary and precipitation of secondary minerals. For this reason, the changes in mineralogy are so important factor to both qualify and quantify geomechanical alteration, as also seen in Wang et al. (2016). The additional compaction is a consequence of the dissolution of load-bearing structures, and is due also to the fact that magnesite is denser than calcite. The resulting change in the solid volumes produces a change in wettability, which will impact the recovery factor. ^(Zimmermann et al 2015)

4.3.3 Flooding experiments

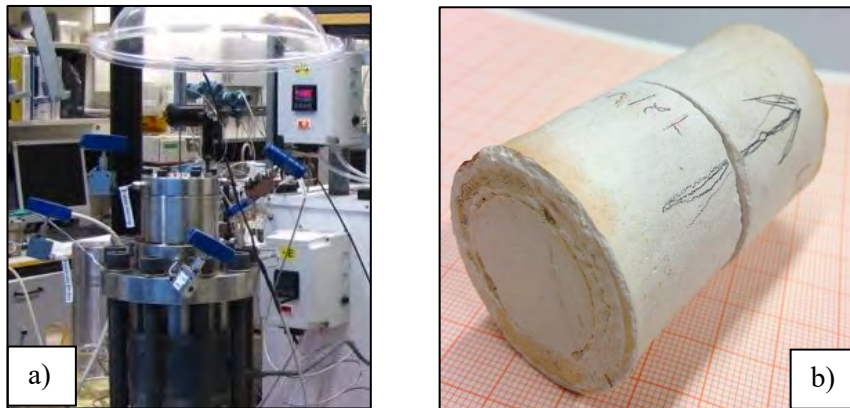


Figure 46 – a) One of the triaxial cells in the laboratory at the University of Stavanger where the rocks were exposed to mechanical compression tests under reservoir conditions. b) Picture of the ULTT core. Arrow indicates flow direction. Photo courtesy of Nina Egeland.

Injection of seawater-like brines is a paramount extraction technique applied on Norwegian Continental Shelf chalk: these fluids increase pressure, helping the oil recovery. The injection supports the pressure of the reservoir, displaces oil, and pushes it towards a well. It is important to understand how fluids interact with chalk because brines tends to weaken it, (Strand et al. 2003; Heggheim et al. 2005; Korsnes et al. 2006, 2008a, 2008b; Madland et al. 2006, 2008; Zangiabadi et al. 2009; Hiorth et al. 2013;) and provoke textural changes in the pore space, affecting the reservoir potential. (Zimmermann et al. 2015a)

During this PhD, to achieve a better knowledge of the mechanisms caused by seawater injection with time (precipitation, dissolution, ion exchange, adsorption, and desorption), three chalk test cores were analysed (Fig. 46b and 47): Long Term Test (516 days, 1.5-year long flooding test, LTT), Medium Long Term Test, (718 days, almost 2-years long flooding test, MLTT), and Ultra Long Term Test core (1072 days, 3-years long flooding test, ULTT).

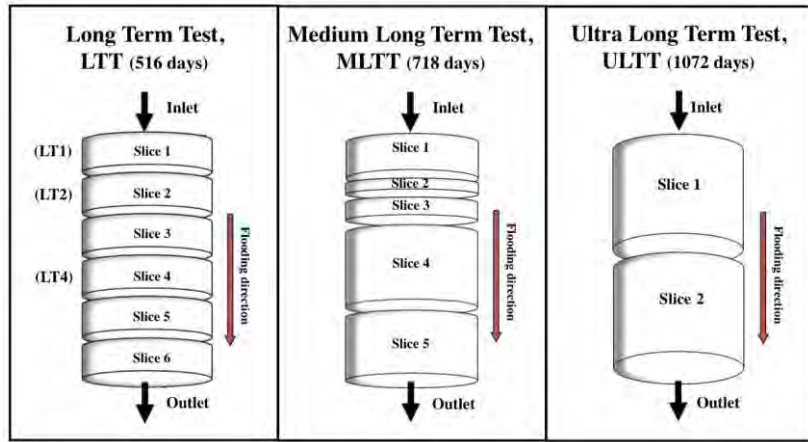


Figure 47 - Schematic drawings of how the three cores were cut after the flooding experiments, from the left to the right: Long Term Test, Medium Long Term Test, and Ultra Long Term Test.

The cores were flooded with fluids, at reservoir condition into triaxial cells (Fig. 46a), allowing measurements of axial and radial strains (for details see Zimmermann et al. (2015), for the LTT, Minde et al. 2017 for the MLTT, and Nermoen et al. (2015) for the ULTT). The cores were 70 mm long and with a diameter of 38 mm. Reactive MgCl_2 was flooded at a rate of 1-3 pore volume (PV) per day, at elevated pressures, stresses, and temperatures (at effective stress 9.5/10.4 MPa, for MLTT and ULTT, respectively, and constant temperature of $130 \pm 0.1^\circ\text{C}$ by a heating jacket and a regulation system).

Only MLTT was flooded for 50 days with a mixture of 0.219 M MgCl_2 and 0.13 M CaCl_2 . To avoid boiling, a pore pressure of 0.7 MPa was applied prior to the heating of the system. While distilled water was injected to ensure a clean pore system and to clean the sample, the confining pressure and pore pressure were simultaneously increased from 0.5 and 0 MPa to 1.2 and 0.7 MPa, respectively, with a constant effective stress equal to 0.5 MPa. (Zimmermann et al. 2015a; Borromeo et al. 2018a) Afterwards the hydrostatic stress was augmented to 12.6 MPa and to

Samples for this research project

11.1 MPa for the LTT and the ULTT, respectively. A 0.219 M MgCl₂ brine was injected with a flooding rate of 1 pore volume per day (1 PV/day) for the LTT and varying between 1-3 PV/day for the ULTT. ^(Nermoen et al. 2015; Zimmermann et al. 2015a; Borromeo et al. 2018a) The flooding rate varied between 33.12 cm³/day and 99.36 cm³/day. The effective stress was 12.6 MPa, 9.5 MPa, and 10.4 MPa for the LTT, MLTT and the ULTT, respectively. ^(Nermoen et al. 2015; Zimmermann et al. 2015a; Borromeo et al. 2018a) When the experiment finished, the tests were dried and cleaned, cut into 10 mm thick slices (see Fig. 46b) and investigated with different methods.

5 Methodology

5.1 Raman Spectroscopy

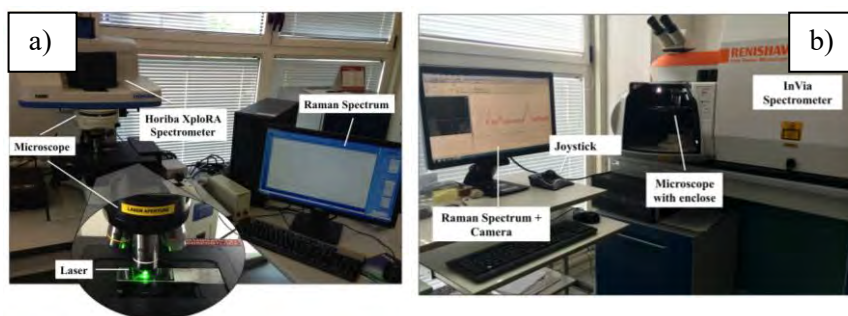


Figure 48 - The Horiba XploRA confocal Raman spectrometer (a) and the Renishaw inVia Reflex (b), both present at the Department of Earth and Environmental Sciences, University of Milano-Bicocca, Milano, Italy.

During this study, two different Raman spectrometers were used to investigate biological magnesium calcite samples and flooded chalk cores. ^(Borromeo et al. 2017a, 2018a)

Most of the spectra in this research (always reported with “H”) were collected with a **Horiba XploRA** set with an Olympus microscope 100x (Fig. 48a). Calibration of spectra was manually achieved by using a silicon wafer (its sharp and only peak is at 520.7 cm^{-1}) as reference and maintained during the analyses with a constant checking of the position of a neon lamp emission line at 476.8 cm^{-1} . A change in the room temperature, for example, can provoke a shift in the position of the peaks, making the analyses less accurate. Because of this it is of utmost importance to maintain the calibration.

Other spectra (always reported with “R”) were acquired using a high-resolution **Renishaw inVia Reflex confocal Raman microscope** (Fig.

Methodology

48b), equipped with an **enclosed Leica DM2500 microscope** (maximum magnification of 100x) and motorized x–y stages.

With both spectrometers, spectra were collected with a green 532 nm line solid-state lasers (10 mW at the sample), laser spot of 1 μm ca., magnification of 100x, spectral resolution of $\pm 1 \text{ cm}^{-1}$, acquisition time of 1-2 minutes.

The spectral region found to be the most important and useful to this study was the low-medium one (100-1200); using a grating of 2400 lines/mm in back-scattering configuration with the XploRA spectrometer, it was possible to collect in the spectral range 100-1200 cm^{-1} ; instead, with the inVia spectrometer grating of 1800 lines/mm was used, collecting in the range of 140-1900 cm^{-1} . Pictures were taken via the optical microscopes for each analysis, both on Mg calcite samples and on flooded chalk ones with a camera.

5.2 *Tip-Enhanced Raman Spectroscopy, TERS*

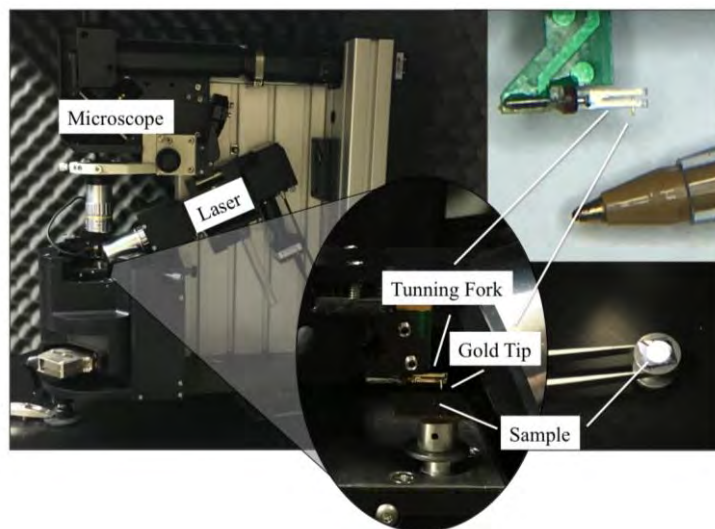


Figure 49 - The TERS system coupling the SPM SmartSPM™-1000 system (AIST) and the confocal Raman spectroscopy Labram HR800 (Horiba) present at the École Polytechnique, Université Paris Saclay. Details of the tuning fork with the gold tip, and of the sample are shown on the right side.

By coupling a confocal Raman spectrometer to a scanning probe microscope, **TERS (*Tip-Enhanced Raman Spectroscopy*)** permits to reach simultaneously both the chemical specificity of Raman spectroscopy and nano-resolved surface mapping of the scanning probe microscope.

During this study, TERS measurements were performed by a tremendous high performing instrumentation consisting of the confocal Raman spectrometer Labram HR800 (Horiba) and the SPM (Scanning Probe Microscopy) SmartSPM™-1000 system (AIST, Advanced Integrated Scanning Tools for Nano Technology), which is an automated scanning probe microscope that permits to reach AFM modes measurements down to 20 nm. The AIST system was used in *non-contact mode*, with the feedback mechanism based on the

Methodology

oscillation of a **tuning fork** (Fig 49).

Gold tips were chemically etched following Ren et al. (2004) and then glued perpendicular to the tuning fork (see Figs. 24 and 49), used as feedback system for the AFM. Since the spatial resolution depends upon the quality of the tip, only tips achieving high (>1000) Q factors were used. Since the thickness of the tip is usually less than 100 nm, the resolution is <100 nm, reaching ~ 20 nm in this PhD project. The tuning fork was operated in the intermittent contact configuration (TF parallel to the surface), with oscillation frequency in air in the 25-28 kHz range, and using a frequency modulated feedback (set-point 3Hz, from Borromeo et al. 2017b, 2018b). A 633 nm red laser was focused at the apex of the gold tip. Surface mapping of areas of different size (maximum $20 \times 20 \mu\text{m}^2$) were acquired. The intrinsic roughness of the samples prevented from scanning larger areas or using high scan rates, which were set at values lower than 0.2 Hz.^(Borromeo et al. 2017b, 2018b) A typical AFM images acquired on these samples are shown in Fig. 50.

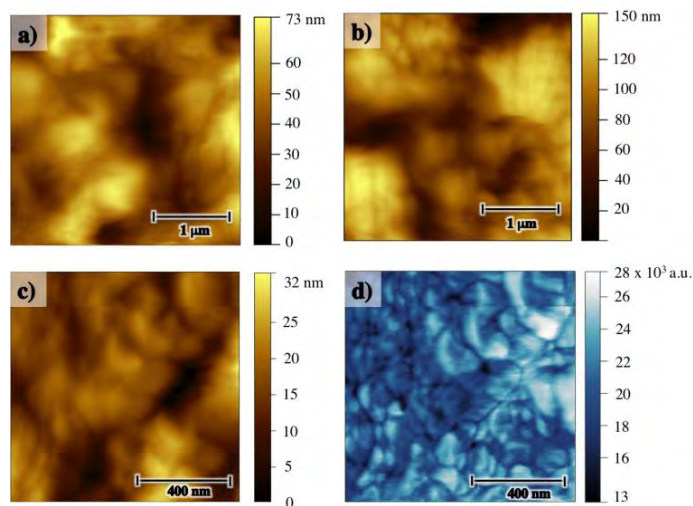


Figure 50 - Examples of AFM images acquired in non-contact mode using a tuning fork oscillator on chalk samples. Panels a) and b) show $3 \mu\text{m} \times 3 \mu\text{m}$ topographic images of an

Methodology

unflooded and a flooded (MLTT) sample, respectively. Panels c) and d) show a $1\ \mu\text{m} \times 1\ \mu\text{m}$ images of a flooded sample acquired detecting the height signal (c) and the oscillation magnitude one (d). Figure and caption from Borromeo et al. 2018b.

The measurements were automatically acquired, using long integration times up to 30 seconds and maximum laser power ($\sim 2\ \text{mW}$), in order to maximize the chalk signal and minimize the background noise. Even though the instrument can virtually acquire for several hours, the tip-laser alignment, which is affected by temperature fluctuations and movements of the optical elements in the path, is not stable enough to guarantee a reliable long acquisition.^(Borromeo et al. 2017b, 2018b) In samples with mixed composition, to better distinguish between magnesite and calcite, a high-resolution grating with 1800 lines/mm was used (see Fig. 51).

A vertical piezoelectric sensor controls the movements of the tip with respect to the sample surface, reaching a movement range of 500 nm: too rough samples may provoke the crash of the tip to the surface. Moreover, the feedback system of tuning fork sensors is quite slow and cannot quickly follow large changes in topography, resulting in blurred images if the sample surface is not smooth enough.^(Borromeo et al. 2017b, 2018b) This is the reason why it is so important to prepare very smooth samples. Chalk is a soft and rough material, as it is final product of the decantation of coccoliths and other foraminifers, and for this it is quite challenging to prepare samples flat enough to be investigated by TERS.

Methodology

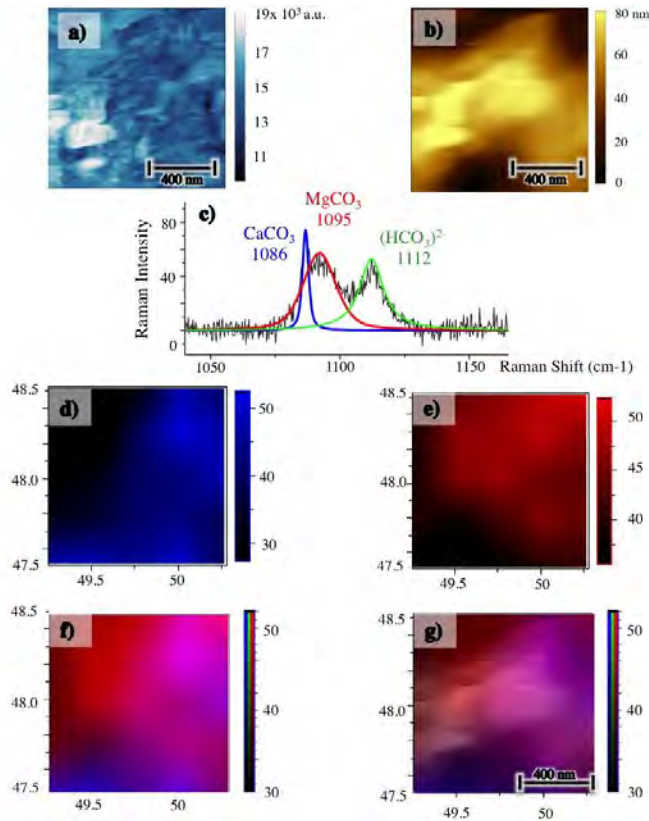


Figure 51 - TERS mapping acquired on Medium Long Term Test (MLTT) chalk sample; a) 1 $\mu\text{m} \times 1 \mu\text{m}$ topography acquired with tuning-fork based AFM; b) Magnitude signal acquired in the same 1 $\mu\text{m} \times 1 \mu\text{m}$ area; c) typical TERS spectrum obtained on a single point, showing peaks at 1086 cm^{-1} (calcite), 1094 cm^{-1} (magnesite) and 1112 cm^{-1} (bicarbonatic ion); d) TERS mapping showing the distribution of the 1086 cm^{-1} calcite ν_1 peak (*symmetric stretching mode*) in the investigated area; e) TERS mapping showing the distribution of the 1094 cm^{-1} magnesite ν_1 peak in the investigated area; f) superimposition of the TERS mappings of calcite and magnesite, following the colour code used in the previous panels; g) superimposition of the TERS mappings of calcite and magnesite and of the topography image in a). Figure and caption from Borromeo et al. 2018b.

After several tries on different kind of chalk sample (as FIB section - *Focused ion beam Scanning Electron Microscopy sections* and $< 2 \mu\text{m}$ mounted powders) the typology of samples that permitted to get the best spectra, were circular thin sections of approximately 3 mm diameter cut by using an ultrasonic drill (Gatan Model 601 Ultrasonic

Methodology

disc cutter) from previously prepared polished thin section inglobated in resin or drill cores. In the drilling process a boron-nitrate grinding powder together with distilled water was used (Fig. 52).^(Borromeo et al. 2017b, 2018b)



Figure 52 - The best way to study chalk samples by TERS is to drill out little disks from cores thin section and carefully polish them.

5.3 How to perform an analysis with a confocal Raman spectrometer

- After switching on the instrumentation (Raman spectrometer, laser generator, computer, monitor), wait 10-20 minutes to warm up the laser generator;
- Perform a **calibration** of the grating and laser in use. Nowadays most of the spectrometers can automatically calibrate by using the 520.70 cm^{-1} sharp peak (Fig. 53) of an internal silicon wafer (as with the Renishaw spectrometer). Otherwise it is possible to use an external silicon sample, as done during this PhD project with the Horiba spectrometer. Due to changes of the ambient conditions (for example room temperature), a displacement of its position of a few

Methodology

cm^{-1} may occur in time; for this reason it is recommended to perform a calibration every 4-5 hours.

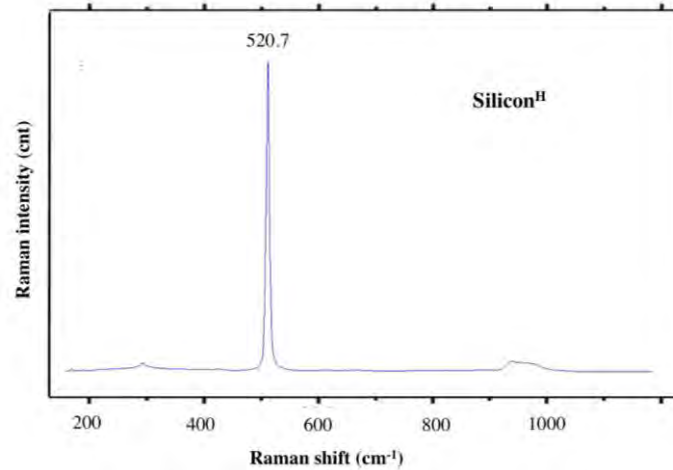


Figure 53 - A spectrum of the silicon wafer used for the calibration.

- Using a low magnification (5-10 x) focus on the sample (mineral, slide of grains, rock sample) and find the spot for analysis;
- Using the 50xL or 100x magnification to focus on the mineral/grain;
- Settle the parameters for the acquisition of the new spectrum, most important of which: length of the collection (seconds x number of cycles), % of the laser power, interval in wavelength to collect);
- Start the acquisition of the spectrum;

Methodology

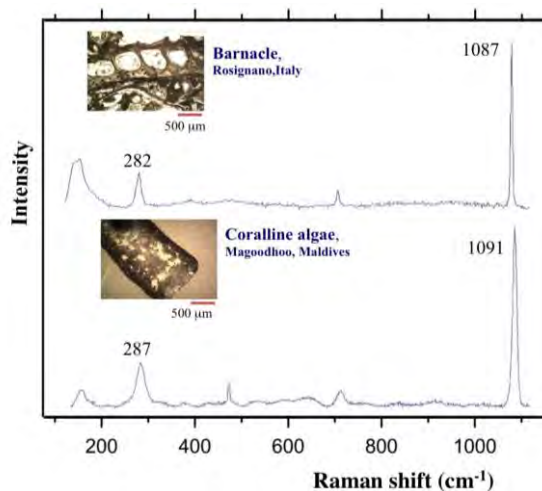


Figure 54 - Two Raman spectra collected on Mg-calcite. Top: spectrum collected on a Barnacles (Rosignano, Italy) bearing 0.38 %MgCO₃ (EDS analysis). Bottom: spectrum collected on a Coralline algae (Magodhoo, Maldives) bearing 6.98 % MgCO₃ (chemical result from EDS analyses). Both spectra were collected with the Horiba XploRA spectrometer. Peaks positions are reported without decimals.

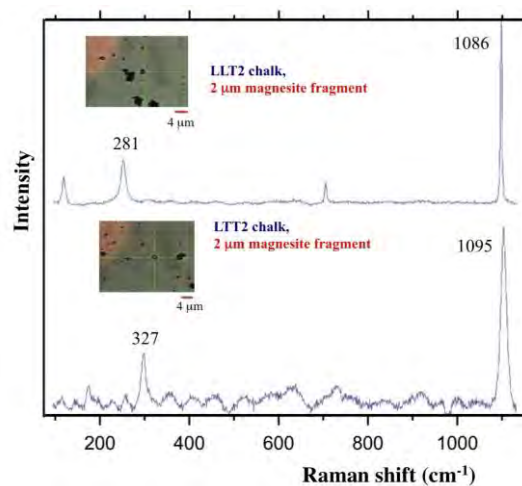


Figure 55 - Two Raman spectra collected on the first slice of the Long Term Test. The occurrence of the original calcite (LT1_p1C_6) and the presence of recrystallized magnesite

Methodology

(LT1_p1B_6) are shown. Both spectra were collected with the Horiba XploRA spectrometer. Peaks positions are reported without decimals.

- Save the spectrum as a text file *.txt*, in order to have the chance to process it in a second phase of the study (Figs. 54 and 55);
- If the sample saturates or shows **fluorescence**, collect a second spectrum in the very same area with a lower laser power or with a shorter acquisition time;
- If the spectrum shows high **background noise** that makes the peaks positions not easily measurable, do a second analysis with a higher number of acquisition cycles;
- Do a last calibration of the machine before to switch off the instrumentation.

The complete peaks positions dataset of the magneisan calcite and flooded calk samples, collected during this PhD project, is reported in *Appendix 1* and *Appendix 2*.

5.4 Additional procedure to perform an analysis with a TERS spectrometer

When carrying out a TERS analysis, the sample surface is first imaged using the AFM. During this PhD, investigations were performed in *non-contact mode*, where the tip does not actually touch the surface, since it is some nanometres away. This approach is usually chosen when the sample surface is not perfectly smooth. The tip, however, is already in the proximity of the surface and therefore it “feels” the atomic forces generated by the nearness of the sample: in these conditions the tip is “*engaged*”. In other words, in free space the tip is oscillating in a free way (the oscillation is due to the tuning fork on which the tip is glued, directly controlled by the operator), while when it approaches the surface the oscillation is being dumped by the

Methodology

interaction with the sample surface. Preliminary maps are collected on large areas, such as $5\ \mu\text{m} \times 5\ \mu\text{m}$, at 10x magnification, in order to select interesting regions to be analysed while verifying their smoothness. Where a flat area is detected, the tuning fork (on which the tip is glued) can be lowered by the operator (tip engaged) the sample and the electromagnetic field between tip and sample surface is obtained: maps can be acquired at higher resolution ($256 \times 256\ \text{px}$) on smaller areas (such as $500 \times 500\ \text{nm}$; see Fig. 56). Afterwards, higher resolution images can be acquired within small areas at higher magnification (the limit in resolution is the size of the tip), since the roughness can prevent from getting a good topography on larger areas at high magnification.

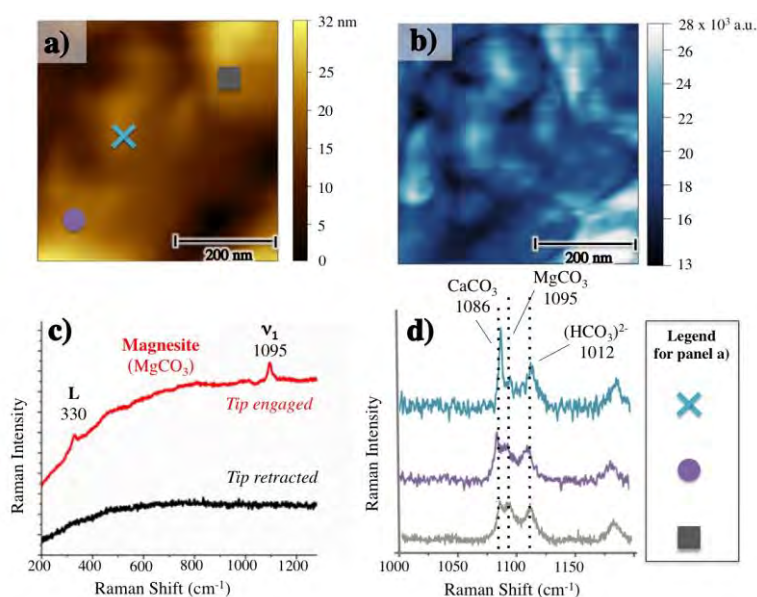


Figure 56 - TERS analysis performed on the MLTT sample. Panels a-b): $500 \times 500\ \text{nm}$ height (a) and oscillation magnitude (b) images. Panel c): magnesite spectra acquired with the tip engaged (red) and retracted (black), demonstrating that the signal measured is actually near field (TERS). Panel d): TERS spectra acquired in 3 different locations in the selected area. Each spectrum (all zoomed in the region $1000\text{-}1200\ \text{cm}^{-1}$) shows the presence of two minerals: calcite (CaCO_3) at $1086\ \text{cm}^{-1}$ and magnesite (MgCO_3) at $1095\ \text{cm}^{-1}$. Also, the presence of the

Methodology

(HCO₃)²⁻ is detected. The locations are identified in panel a) and follow the symbol/colour legend in panel d). Figure and caption from Borromeo et al 2018b.

Shining the laser on the apex of the tip with an inclination of 60°, a TERS spectrum can be acquired. The laser beam is focused through standard microscope objectives, to yield diffraction limited ~ 0.5-1 µm spot size, which is directly dependent on objective and laser wavelength.

The scattered light is collected by the spectrometer. The Raman signal of the molecules close to the tip apex is enhanced (*near field, TERS signal*) but, since the laser spot is larger than the tip, the signal due to the laser directly hitting the sample and scattered from the molecules more far away from the tip (not enhanced by the presence of the tip) is still detectable (*far field signal, Raman signal*). The collection of the *far field* and *near field* signals happen contemporarily and it will produce a spectrum that is their sum, the superimposition of the two (for more information see Fig. 24).

Raman maps can be acquired as presented in Fig. 57 where a TERS mapping measurement performed on the Ultra Long Term Test (ULTT) shows the intensity of the magnesite Raman signal. In panel d) another image shows the superimposing to the topographic map and to the map of the distribution of the bicarbonatic ion (HCO₃)²⁻.

The measurements were automatically acquired, using long integration times up to 30 seconds and maximum laser power (~2 mW) in order to maximize the chalk signal and minimize the background noise.

Methodology

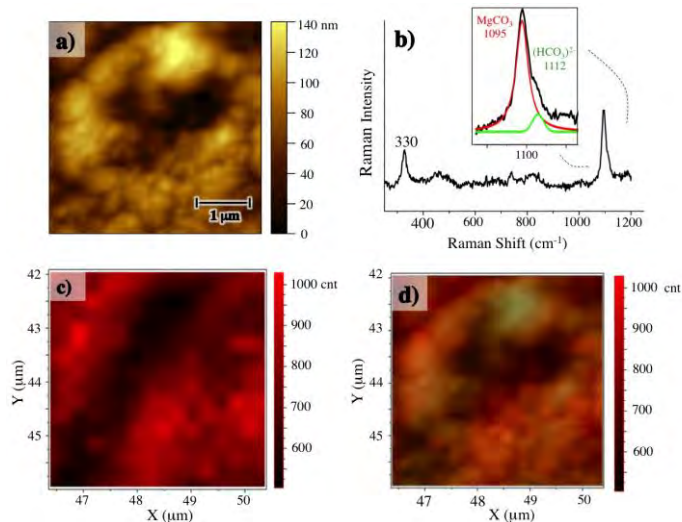


Figure 57- TERS mapping acquired on the Ultra Long Term Test (ULTT) sample: a) 4 μm x 4 μm topography showing a circular structure that may resemble a coccolith; b) a typical TERS spectrum obtained, showing a magnesite vibrational mode at 330 cm⁻¹ (L, *librational mode*) and an asymmetric peak at 1095 cm⁻¹, which is the sum of the high ν_1 (*symmetric stretching mode*) of magnesite and a peak of the bicarbonatic ion (HCO₃)²⁻ present at 1112 cm⁻¹ (Bischoff et al. 1985) that produces a shoulder on the right; c) TERS mapping acquired in the area selected in a) with a step-size of 250 nm and using a red color scale based on the intensity of the 1095 cm⁻¹ peak, according to the color legend; d) if we superimpose the topography to the intensity of magnesite and (HCO₃)²⁻ peaks, we see that magnesite recrystallization is pervasive in the investigated region. On the top-right of d), the bicarbonatic ion Raman signal is present. Figure and caption from Borromeo et al. 2018b.

Even though the instrument can virtually acquire for several hours, the tip-laser alignment, which is affected by temperature fluctuations and movements of the optical elements in the path, is not stable enough to guarantee a reliable long acquisition (Borromeo et al. 2017b, 2018b). For this reason during the PhD was not that trivial to find the right balance between dimension of the map, step-size, and quality of the spectra, considering also the intrinsic roughness of the samples that prevented from scanning larger areas or using high scan rates.

As it happens with Raman analyses, the parameters for spectra/maps acquisition (such as length of the collection, % of the laser power,

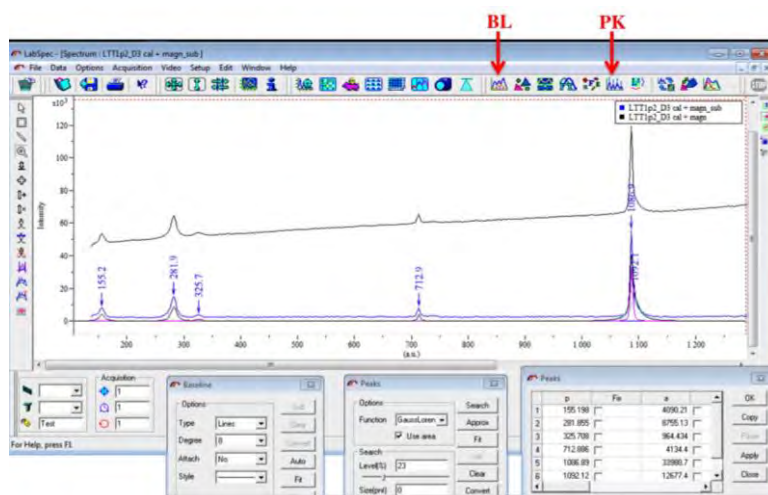
Methodology

interval in wavelength to collect) are settled by the operator. The Raman spectrometers present in TERS equipments are common Raman spectrometers, as the ones used to perform Raman analyses during this PhD, since the TERS enhancement of the signal is reached by its coupling with the AFM. For this reason the collection of the spectra is carried out as described in the previous chapter: “5.3 How to perform an analysis with a confocal Raman spectrometer”. When the acquisition is completed, the map or the spectrum can be saved and processed (see “5.5 Processing of Raman Spectra chapter”).

5.5 Processing of Raman spectra

After the acquisition, spectra are processed and the peaks measured to identify the mineralogy. I recommend keeping an original version of the spectrum.

- Open the spectrum with an appropriate software (in this PhD project I used *Labspec 5*);^(Borromeo et al. 2017a, b, 2018a, 2018b)



Methodology

Figure 58 - Screenshot of the software *Labspec 5*, Horiba. The spectrum LT1_p2_D3 is shown before (black) and after (blue) the *Baseline subtraction correction*. The Baseline button is named “**BL**”, the one to determinate the peaks positions is named “**PK**”. The peaks positions, automatically identified by the deconvolution method, are shown in the Figure (cm^{-1}).

- Do a “**Baseline**” correction (see Fig. 58) to eliminate the eventual natural fluorescence of the sample: the software creates an 8 degree polynomial curve that will be subtracted by a mathematical operation. If the curve proposed by the software does not perfectly fit the spectrum, it can be modified by the operator or another curve can be manually set;
- To determinate the position of the peaks, it is possible to use the “**Peaks**” function that mathematically fits the peaks through the Gaussian - Lorentzian (Pseudo Voight) deconvolution method, with an accuracy of 0.2 cm^{-1} (see Fig. 58). Click at the top of each peak with the cursor and then run the automatic search of the positions: with this function the software can mathematically identify the peaks and their exact position;
- Transcript the positions of the peaks in an Excel file.
The complete peaks positions dataset of the magneisan calcite and flooded calk samples, collected during this PhD project, is reported in *Appendix 1* and *Appendix 2*.

For an operator with experience, the identification of the spectra can often be achieved just by looking at the whole spectrum or by considering the position of the peaks. Otherwise the identification of the sample can be performed running an automatic research of the software in use (as *Labspec 6* or *Crystal Sleuth*, Fig. 59), or by the direct comparison with online databases (*RUFF*, <http://rruff.info>, for example) or on scientific journals. (Frezzotti et al. 2012; Andò and Garzanti, 2013)

Methodology

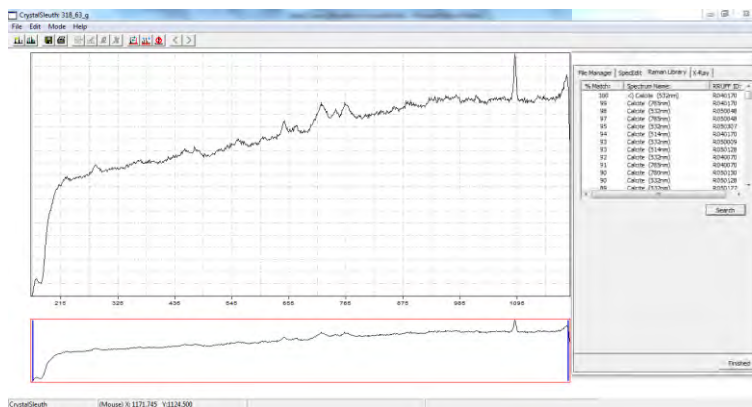


Figure 59 - Screenshot of the *Crystal Sleuth* software, which was used to perform an automatised research of a calcite spectrum.

5.6 EDS - SEM and EMPA - WDS microprobes



Figure 60 - The EDS spectrometer coupled to SEM (Scanning Electron Microscope) present at the Milano-Bicocca University (a) and its sample holder (b).

During my PhD, in particular during the first year, reliable chemical analyses were needed to carry out the study on magnesian calcites. Two different electron microprobes, an EDS (Energy Dispersive Spectroscopy) and a WDS (Wavelength Dispersive Spectrometer)

Methodology

(Figs. 60a and b) were used to measure the Mg^{2+} content in biogenic calcite, in order to compare their chemical content to their Raman spectra.

These two methods perform non-destructive chemical characterization of solids. In contrast to Raman spectroscopy, they cannot directly identify the substance constituting the sample but can identify and quantify its elements composition and transform it into oxides; generally, WDS produces always quantitative data while the EDS needs a very careful set-up to reach such a goal. The interaction of a source of **X-ray excitation** and the sample is used, relying on the fact that each element has a unique atomic structure allowing a unique set of peaks on its electromagnetic **emission spectrum**. During the analysis, the sample is bombarded with an electrons beam, which interacts with the bound electrons of the various elements in the sample, ionizing them. As result, a vacancy in the inner shell is generated and than filled by other electrons with the emission of photons.

The photons are scattered at a characteristic frequency (different for each element), their energy lies in the X-ray region of the electromagnetic spectrum. Since every electron in the periodic system is characterized on specific and unique features, the X-ray lines produced by vacancies in the innermost shells are diagnostic of that electron and subsequently of that element.

The scattered photons are selected and counted by the detector, which counts specific X-ray energy levels (EDS) or wavelengths (WDS) diffracted by the sample, permitting to measure the relative abundance of each element.

These two analytical set ups were used during the PhD project:

- A **Energy Dispersive Spectroscopy (EDS)** uses a solid state semiconductor detector to record simultaneously X-rays of all

Methodology

energies scattered from the sample and produces as output an intensity versus X-ray photon energy plot. EDS requires shorter counting time than WDS, and, to the contrary of WDS, provides reliable results on alkali.

Carbonate biogenic and inorganic samples were analysed at the University of Milano-Bicocca, Italy, (Fig.60a) for their major elements with a Tescan VEGA TS Univac 5136 XM scanning electron microscope coupled with an EDAX Genesis 4000 XMS Imaging 60 SEM-EDS under an electron beam of 20-kV high voltage, with 250-nm spot size and an absorption of current of 190 ± 1 pA, measured in platinum Faraday cup; the quantification of main elements (Ca and Mg) was calibrated on Astimex Scientific standard (Borromeo et al. 2017a). The concentrations of elements from beryllium to plutonium may be measured at levels as low as 0.1%.

- The used **Wavelength Dispersive Spectrometer (WDS)** utilized Bragg diffraction from crystals to select X-ray wavelengths of interest and direct them to gas-flow or sealed proportional detectors. In other words, at the contrary of the EDS, WDS counts only X-rays of a single wavelength at a time, not producing a broad spectrum of all wavelengths, simultaneously. WDS systems contain several standard crystals of known but differing properties (as interplanar spacing), which can be automatically changed depending on the type of sample and on the wavelength of its electrons. This enables to investigate elements from the entire periodic table, with the exception of hydrogen, helium, and lithium, as their atomic numbers are too low to analyse via x-ray methods. The WDS used in this project is the one present at the TU Bergakademie Freiberg, Saxony, Germany, a JEOL Ltd. JXA-8900 RL Electron probe Micro analyzer, with a beam size of 2 μm . As with the EDS, the confidence range was of ± 1 mol% (Fig. 60b).

Methodology

Spectral resolution is better than for the EDS type and the limits of detection are lower (down to 0,001 %). On the other hand, EDS is faster and more convenient to use. X-ray spectrometers attached to SEMs are usually of the EDS type, though sometimes a single multi-crystal WD spectrometer is fitted. Hence, it is a matter of the focus of the study which application shall be used. Moreover, the WDS-EMPA are by far more expensive but normally perfectly set up for quantification of chemical elements. In rare cases quantifying set up are managed to apply to EDS systems and are then very useful to use. If it would be so easy and common to use EDS for quantification purposes WDS systems would not be used anymore.

6 Publications

During the 3 years PhD a fascinating project has been carried on, applying Raman spectroscopy on carbonates. During the first year a study on magnesian calcites has been completed to understand how the identification of magnesite, dolomite, calcite and Mg-rich calcite can be developed in an applied methodology. During this process it was discovered that it is possible to estimate the Mg content by Raman spectroscopy. Then Raman spectroscopy has been applied to flooded chalk samples for mineralogical analyses, to investigate the new growth of magnesite that occurs after MgCl_2 injection into chalk cores. The new grown minerals – mostly carbonates – had different sizes from micron to sub-micron. Finally, in the last part of the PhD, a high-resolution technique as *Tip-Enhanced Raman Spectroscopy* (TERS) was used in combination with an Atomic Force Microscope (AFM) to image and spot one single mineral on sub-micron scale. Most of the electron microscopes can only image but their attached EDS cannot provide sub-micron resolution for a chemical fingerprint. I was hoped that this method could be suitable for the mineralogical characterization studies on chalk samples on a sub-micron scale.

Throughout the PhD, also some clastic rock samples from the Barents Sea and the Cantabrian mountains (Spain) have been analysed using the optical microscope and the Raman spectrometer (for more information see “7. *Other contributions*” chapter).

6.1 Raman Spectroscopy as a tool for magnesium estimation in Mg-calcite; Borromeo et al. 2017a

Raman methodology has been tested in detecting the structural and chemical changes occurring when Mg^{2+} substitutes Ca^{2+} in the calcite lattice and to understand if it was possible to estimate calcite chemical composition examining the position of Raman peaks. Several carbonate samples with variable Mg content (0 - 20 mole % MgCO_3) have been first analysed with a Raman spectrometer (120 spectra) and then studied by SEM-EDS and EMPA-WDS (200 chemical analyses) to determine their chemical composition and allow the correlation between Raman peaks and chemistry. With the exception of some standard minerals (M.A.C., Micro-Analyses Consultant) studied to build a Raman/EDS database, all samples (barnacles, calcareous red algae, foraminifers, bryozoans, echinoids) had a biogenic origin, and were collected all over the world, at different latitude, formed under different water temperatures and calcium carbonate saturation. Those facies parameter affect the skeletons Mg content. (Chave 1954a; 1954b; Mackenzie 1983; Mutti et al. 2003) We determined the position of the four main vibrational modes of several calcite crystals with magnesium content ranging from 0.1 to 19.3 mol% MgCO_3 (Fig. 3): T, *translational mode* (152.0– 160.0 cm^{-1}); L, *librational mode* (278.0–288.7 cm^{-1}); ν_4 , *in-plane bending* (711.6–717.1 cm^{-1}); and ν_1 , *symmetric stretching* (1086.0– 1090.8 cm^{-1}). Our results suggested that Raman shifts follow a one-mode behaviour, increasing with magnesium content in a quite

linear way (Borromeo et al. 2017a, Fig. 3). The regression lines calculated for peak positions (Borromeo et al. 2017a, Fig. 3) indicated that L, ν_4 and ν_1 modes behave approximately linear, with a coefficient of determination R^2 between 0.7 and 0.85 (Borromeo et al. 2017a, Table 3). This implies a linear correlation between Raman peaks position and Mg content. Anyway, the heterogeneity in the distribution of magnesium ions, caused by typically biogenic positional disorder and/or by trace element substitution, provided a consistent uncertainty on the magnesium estimation when a single Raman peak value is used. To obtain a more confident Mg content estimation, two or three peaks were used in combination (Mg content in colour scale), and data were plotted in 2D and 3D plots (Borromeo et al. 2017a, Figs. 5 and 6). In this way, it was possible to detect two different groups of magnesium calcites, one containing from 0 to 5.5 mol% MgCO_3 (low-Mg calcites) and the other one containing from 10.5 to 20 mol% MgCO_3 (high-Mg calcites) (Borromeo et al. 2017a, Fig. 3), from their Raman spectra.

This study has been published in *The Journal of Raman Spectroscopy*, 2017, ISSN: 1097-4555, and edited by John Wiley and Sons.

Raman spectroscopy as a tool for magnesium estimation in Mg-calcite

Laura Borromeo,^{a,b,*} Udo Zimmermann,^{a,b} Sergio Andò,^c Giovanni Coletti,^c Danilo Bersani,^d Daniela Basso,^c Paolo Gentile,^c Bernhard Schulz^e and Eduardo Garzanti^c

Despite their strong Raman scattering and importance in several applications in the geological and biological sciences, Mg-calcites have not been thoroughly investigated by Raman spectroscopy. In this study, we investigated whether Raman spectra of carbonates are sensitive to the structural and chemical changes occurring when Mg²⁺ substitutes Ca²⁺ in the calcite lattice. Different carbonate samples with variable Mg content (from 0 to 20 mol% MgCO₃) of biological and inorganic origin have been first beamed under a Raman spectrometer and then analysed by scanning electron microscopy-energy dispersive spectrometer and electron microprobe analysis-wavelength dispersive spectrometer microprobes to determine their chemistry. The biological samples (foraminifers, algae, barnacles and echinoderms) were collected from areas situated at different latitudes and water temperature and saturation, factors affecting the chemical and isotopic composition of shells in marine organisms. The Raman band positions are directly linked to the amount of magnesium present in the calcite lattice, and all peaks of Mg-calcite spectra show a consistent and linear increase in Raman shifts according to their Mg content, which is a consequence of the decreased inter-atomic distances following the substitution of Ca²⁺ with the smaller Mg²⁺ ion.

This study demonstrates that Raman spectroscopy provides an innovative work perspective in marine biology, provenance studies and oil exploration when estimates of mineralogical and chemical changes are the focus of the study. Raman spectroscopy is even more attractive – for the mentioned fields of research – than many other methods because of the non-destructive nature and its very short analytical time. Copyright © 2017 John Wiley & Sons, Ltd.

Keywords: Mg-calcite; Raman; magnesium; estimation; biogenic calcite

Introduction

Carbonates are abundant in the sedimentary record, and they testify climatic changes since the Archean.^[1] Their isotopic and geochemical composition is a powerful tool in palaeoclimatic research as it reflects the characteristics of the fluids from which they precipitated. Carbonate minerals are present in most depositional environments and geological settings. Classical methods to assess their composition are destructive and time-consuming. Therefore, a more flexible, quick and efficient technique such as Raman spectroscopy is needed to identify the different carbonate types and polymorphs in a simple and reliable way. The method reduces the bias potentially introduced by the operator and allows recognition of single carbonate grains independently on their size, which represents a great improvement for hydrocarbon exploration and provenance^[2] or palaeontological studies. The focus of this contribution is to demonstrate how Raman spectroscopy can be applied to the mentioned fields, representing a powerful tool for anyone interested in carbonate research and its diverse applications particularly for the following: (1) the study of small carbonate grains or crystals in micritic mud and chalk, (2) analyses of shells at micron-scale to monitor changes in skeletal composition related to the variation of water temperature and saturation over time and (3) reliable and fast estimates of the Ca/Mg ratio in carbonates.

Raman spectra of carbonates are sensitive to the structural and chemical changes that occur when Mg²⁺ substitutes Ca²⁺ in the calcite lattice,^[3,4] which allows us to propose an original method

to estimate the Mg content in calcite on the basis of the position of Raman peaks. For this study, we have selected a wide range of different calcite and calcite-bearing samples of both biological (e.g. foraminifers, algae and barnacles) and inorganic origin (mostly certified standards) (Table 1), characterized by different Mg content, provenance, grain size and age. All samples have been first beamed under the Raman spectrometer and subsequently analysed by quantitative scanning electron microscopy-energy dispersive spectrometer (SEM-EDS) analysis and electron microprobe analysis studies on the same spots.

* Correspondence to: Laura Borromeo, Department of Petroleum Engineering, University of Stavanger, Arne Rattedals hus Kjell Arholmsgt. 41, 4036 Stavanger, Norway.
E-mail: laura.borromeo@uis.no

a Department of Petroleum Engineering, University of Stavanger, Stavanger, Norway

b The National IOR Centre of Norway, Stavanger, Norway

c Department of Earth and Environmental Sciences, University of Milano-Bicocca, Milan, Italy

d Department of Physics and Earth Sciences, University of Parma, Parma, Italy

e Institute of Mineralogy, Freiberg University of Mining and Technology, Freiberg, Germany

Table 1. Biogenic magnesian calcite samples and their mol% MgCO ₃ content				
Taxon	MgCO ₃ (mol%)	Age	Location	Average water temperature (°C)
Benthic foraminifer (<i>Ammonia</i> sp.)	0.1	Recent	Imperia, Italy	18.5 ^[53]
Benthic foraminifer (<i>Elphidium</i> sp.)	0.1	Recent	Imperia, Italy	18.5 ^[53]
Benthic foraminifer (<i>Miliolida</i>)	12.4–13.3	Recent	Imperia, Italy	18.5 ^[53]
Benthic foraminifer (<i>Elphidium</i> sp.)	0.9–2.3	Recent	Corsica Island, France	18.5 ^[53]
Benthic foraminifer (<i>Miliolida</i>)	11.0–12.3	Recent	Corsica Island, France	18.5 ^[53]
Benthic foraminifer (<i>Sorites</i> sp.)	11.5–11.6	Recent	Corsica Island, France	18.5 ^[53]
Benthic foraminifer (<i>Elphidium</i> sp.)	1.9–4.0	Recent	Crete Island, Greece	20.5 ^[53]
Benthic foraminifer (<i>Miliolida</i>)	9.3–10.7	Recent	Crete Island, Greece	20.5 ^[53]
Benthic foraminifer (<i>Sorites</i> sp.)	11.0–11.3	Recent	Crete Island, Greece	20.5 ^[53]
Benthic foraminifer (<i>Miliolida</i>)	13.7	Recent	Sharm El Sheik, Egypt	25.5 ^[53]
Benthic foraminifer (<i>Penerosplis</i> sp.)	13.7	Recent	Sharm El Sheik, Egypt	25.5 ^[53]
Benthic foraminifer (<i>Sorites</i> sp.)	13.6–14.4	Recent	Sharm El Sheik, Egypt	25.5 ^[53]
Benthic foraminifer (<i>Elphidium</i> sp.)	0.5–1.0	Recent	Kota Kinabalu, Malaysia	30.0 ^[53]
Benthic foraminifer (<i>Sorites</i> sp.)	13.1–13.7	Recent	Kota Kinabalu, Malaysia	31.0 ^[53]
Benthic foraminifer (<i>Elphidium</i> sp.)	2.8–3.6	Recent	Magoodhoo, Maldives	29.5 ^[53]
Benthic foraminifer (<i>Miliolida</i>)	12.5	Recent	Magoodhoo, Maldives	29.5 ^[53]
Benthic foraminifer (<i>Sorites</i> sp.)	14.4–15.5	Recent	Magoodhoo, Maldives	29.5 ^[53]
Benthic foraminifer (<i>Elphidium crispum</i>)	1.2–2.0	Miocene	Rosignano Monferrato, Italy	Tropical-subtropical ^[54]
Bryozoan (<i>Bifissurinella lindenbergi</i>)	2.5–2.6	Miocene	Rosignano Monferrato, Italy	Tropical-subtropical ^[54]
Calcareous red algae (<i>Neogoniolithon</i>)	16.5–17.4	Recent	Magoodhoo, Maldives	29.5 ^[53]
Calcareous red algae (<i>Corallinophycidae</i>)	11.2–18.2	Recent	Hvammstangi, Iceland	5.0 ^[53]
Calcareous red algae (<i>Porolithon onkodes</i>)	13.4–21.3	Recent	Sharm el Sheik, Egypt	25.5 ^[53]
Calcareous red algae (<i>Corallinophycidae</i>)	2.3–2.5	Miocene	Rosignano Monferrato, Italy	Tropical-subtropical ^[54]
Barnacle (<i>Balanus perforatus</i>)	1.8–3.7	Recent	Imperia, Italy	18.5 ^[53]
Barnacle (<i>Balanus</i> sp.)	1.9–3.6	Recent	Magoodhoo, Maldives	29.5 ^[53]
Barnacle (<i>Balanus</i> sp.)	1.8–2.3	Pliocene	Diano Marina, Italy	18.5 ^[53]
Barnacle (<i>Balanus</i> sp.)	0.6–2.3	Miocene	Rosignano Monferrato, Italy	18.5 ^[53]
Echinoid, (Echinoidea)	2.8–3.9	Recent	Moirá Mound, Western Ireland shelf	~8 ^[55]
Echinoid (<i>Echinocardium fenaxi</i>)	9–10.2	Recent	Stromboli, Italy	20.5 ^[53]
Echinoid (<i>Cidaris</i> sp.)	6.3–6.4	Recent	La Spezia, Italy	18.5 ^[53]
Echinoid (<i>Paracentrotus lividus</i> sp.)	4.2–4.7	Recent	La Spezia, Italy	18.5 ^[53]
Echinoid (<i>Echinoidea</i>)	8.8–11.0	Recent	Magoodhoo, Maldives	29.5 ^[53]

Sea surface temperature of localities, from GIOVANNI N.A.S.A.; Acker J.G. et al.^[53]; inferred palaeotemperatures for the region of Rosignano Monferrato from Mosbrugger et al.^[54]; water temperature in Moira Mound (Western Ireland shelf) is based on CWC Moira Cruise Report.^[55]

Carbonates in the natural environment

CaCO₃ crystallizes in three different forms: calcite, aragonite and vaterite, with trigonal, orthorhombic and hexagonal structure, respectively. The nucleation and growth of calcium carbonate crystals may be controlled by organic or inorganic processes. Calcite shows a trigonal, scalenohedral lattice with two molecules per unit cell. The calcium and the carbon atoms of the carbonate ions are located on the trigonal axis with a centre of symmetry controlled by the orientations of the two carbonate ions that are staggered relative to each other.^[5]

The orthorhombic polymorph is aragonite,^[6,7] a common phase in modern depositional environments but unstable during diagenesis and therefore rarely preserved in carbonate rocks.^[8] Aragonite may be formed by biological (e.g. shells) or inorganic (e.g. speleothems) processes. The rarest and least known polymorph is vaterite,^[9] which forms micrometric and metastable crystals mostly present in freshwater and mineral springs.

Magnesite (MgCO₃), trigonal and isomorphous with calcite, is present in metamorphic,^[10] sedimentary^[11] and magmatic^[12] rocks.

Magnesite generally occurs in colorless crystals that can be distinguished easily from calcite and dolomite by Raman spectroscopy.^[3,13–16]

Dolomite CaMg(CO₃)₂ may form by hydrothermal metasomatism of limestones^[17] or precipitate as a primary phase in hypersaline lakes.^[18] Its occurrence has also been documented in tropical coralline algae.^[19] The alternation of calcium and magnesium layers determines the lower symmetry of dolomite relative to calcite.^[4,5,20] Dolomite forms an isomorphous series with ankerite Ca(Fe,Mn)(CO₃)₂ and siderite (FeCO₃).

Silliman discovered in 1846 that the calcite crystal structure can accommodate a considerable amount of Mg²⁺ ions in its lattice,^[21–25] which prevents a clear definition of Mg-rich carbonates. Magnesian calcite occurs as cement in marine sediments and is common in non-tropical bioclastic sediments.^[26,27] Present-day temperate and cold-water shelf carbonates are dominated by foraminifers, molluscs, bryozoans, echinoids and coralline algae, mainly producing calcite or magnesian calcite. Coralline algae, in particular, may include large amounts of magnesium in their cell walls. Aragonite, contributed mainly from scleractinian corals and calcareous

Raman as a tool for Mg estimation in Mg-calcite

green algae,^[28] dominates instead shallow marine sediments at tropical latitudes. The Mg concentration in biogenic carbonates is strongly affected by water temperature and ocean's saturation state.^[26–28] Alike aragonite, high-Mg calcite is metastable and depletion in Mg usually occurs during meteoric diagenesis,^[6,27,29,30] accompanied by a decrease in Sr and Na and by an increase in Mn, Fe and Zn.^[29]

There is no clear sharp chemical boundary between pure calcite and magnesian calcite. Calcites containing >4 wt% (4 wt% ~ 10 mol%) of MgCO₃ are conventionally defined as high-Mg calcite,^[25,31,32] although this boundary is not universally accepted. For example, Rucker and Carver^[33] and Smith *et al.*^[34] defined three groups: low-Mg calcite (0 to 4 wt% MgCO₃), intermediate-Mg calcite (4 to 8 wt% MgCO₃; 8 wt% ~ 20 mol%) and high-Mg calcite (>8 wt% MgCO₃). Andersson and Mackenzie^[35] suggested 12 wt% MgCO₃ as the boundary between intermediate-Mg and high-Mg calcite,^[36,37] whereas Bøggild^[38] identified a miscibility gap between low-Mg calcite (2–3 mol% MgCO₃) and high-Mg calcite (12–17 mol% MgCO₃).

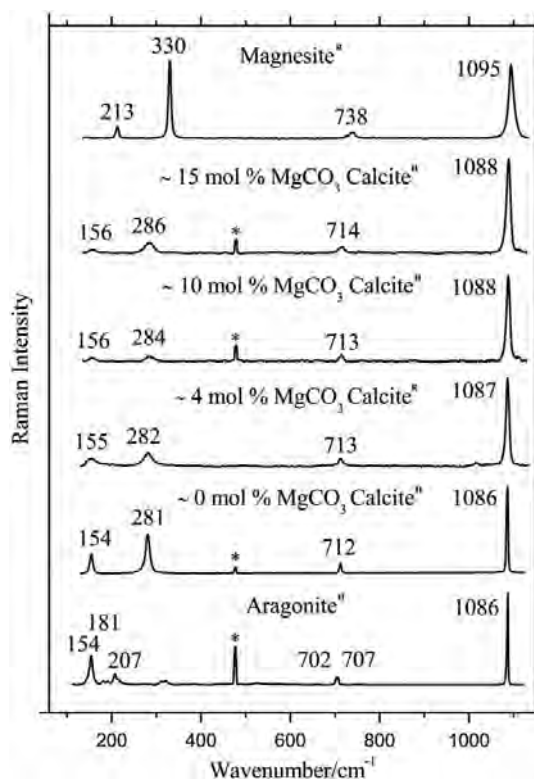


Figure 1. Raman spectra of calcium and magnesium carbonates: aragonite (UNIMIB – University of Milano Bicocca – standard sample, Val Formazza, Italy), calcite (UNIMIB standard sample, Chihuahua, Mexico), a 3.77 mol% MgCO₃ calcite (barnacle, Italy), a 10.15 mol% MgCO₃ calcite (*Paracentrotus lividus*, echinoid, Italy), a 15.01 mol% MgCO₃ calcite (*Cidaris*, echinoid, Italy) and magnesite (M.A.C. certificated standard). Stars represent the neon lamp emission line at 476.8 cm⁻¹ used for calibration with the Horiba XploRA spectrometer. Peak positions are reported without decimals. Spectra with 'R' were analysed by the Renishaw inVia confocal Raman microscope and spectra with 'H' by Horiba XploRA.

Previous Raman spectroscopy studies on magnesian calcites

Despite their importance in several applications in the geological and biological sciences, the crystal chemistry and structure of biogenic and inorganic Mg-calcites have not been investigated thoroughly by Raman spectroscopy. Bischoff *et al.*^[4] pointed out that Raman shifts of synthetic and biogenic high-Mg calcite crystals increase from calcite to magnesite, because of disorder effects generated by Mg substitution (see also Reeder^[39]). Owing to the smaller radius of the Mg²⁺ ion, the Mg–O bond is shorter and therefore stronger than the Ca–O bond. The unit cell volume decreases with increasing Mg concentration,^[4,21,26,40] with a subsequent change in the position of the Raman bands. X-ray powder diffraction studies^[4,24] proved that Mg²⁺ ions are not present preferentially in layers in Mg-calcite crystals, but the substitution of Mg²⁺ for Ca²⁺ is random and disordered, implying no loss in rotational symmetry. Chave^[40] reported a linear correlation between the position of the 1014 diffraction peak of skeletal calcites and their Mg concentration over the range 0–18 mol% MgCO₃. At higher concentrations of Mg²⁺, the relation was observed not to be linear.

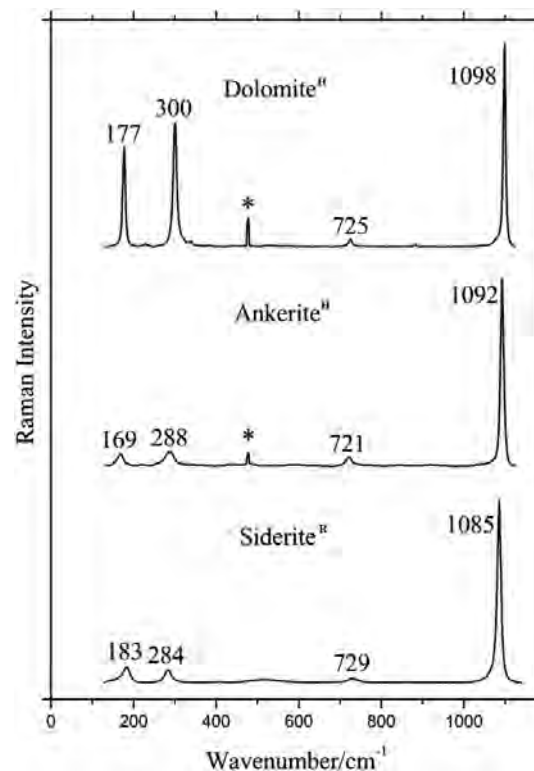


Figure 2. Raman spectra of calcium and iron carbonates: dolomite (UNIMIB standard sample, Selvino, Italy), ankerite (M.A.C. certificated standard) and siderite (M.A.C. certificated standard). Stars represent the neon lamp emission line at 476.8 cm⁻¹ used for calibration with the Horiba XploRA spectrometer. Peak positions are reported without decimals. Spectra with 'R' were analysed by the Renishaw inVia confocal Raman microscope and spectra with 'H' by Horiba XploRA.

By measuring the half-widths of the peaks (width of Raman band measured at half of its intensity) and their Raman shifts, Bischoff *et al.*^[4] showed that positional disorder of carbonate ions [rotation of $(\text{CO}_3)^{2-}$ out of the basal plane] is greater for biogenic calcite than for synthetic calcite, which may explain why Raman peaks for the former are wider. Urmos *et al.*,^[41] instead, ascribed this effect to the smaller crystal size of biogenic Mg-calcite. The greater degree of disorder associated with higher Mg content may be responsible for higher chemical reactivity during diagenesis.^[41] Another interesting study on magnesium calcite^[42] investigated Mg^{2+} incorporation during the growth of synthetic Mg-calcite precipitated from $(\text{Ca}, \text{Mg}) \text{Cl}_2$ solutions characterized by different Mg/Ca ratio; monitoring at high temporal resolution with an *in situ* Raman spectrometer permitted to investigate the formation of amorphous calcium carbonate and its near-instantaneous transformation to a crystalline phase.

Methodology

All carbonate samples were mounted on stubs, incorporated in a bounding resin (DBF Huntsman Araldite), analysed first by Raman spectroscopy, coated with graphite and studied by SEM-EDS. When analysing biogenic samples, we took particular care to beam with the EDS the exact spot already studied with the spectrometer, to avoid inconsistent measurements and inhomogeneities. We could

thus compare and correlate confidently the position of Raman peaks with the chemical measurement of Mg content.

Two different confocal micro-Raman spectrometers have been used for this study. Most spectra (reported with 'H' in Figs 1 and 2 and Tables 2 and S2) were collected with a Horiba XploRA equipped with an Olympus microscope with 100× objective as maximum magnification and motorized x–y stages. Spectra were calibrated using a silicon wafer with a main peak at 520.7 cm^{-1} as reference. During analysis, the calibration was maintained by constantly checking the position of a sharp neon lamp emission line at 476.8 cm^{-1} .

Some spectra (the Italian barnacles, the calcareous algae from the Red Sea, some standard minerals and all reported with 'R' in Figs 1 and 2 and Tables 2 and S2) were collected with a high-resolution Renishaw inVia Reflex confocal Raman microscope, equipped with a Leica DM2500 polarizing microscope with 100× objective as maximum magnification and motorized x–y stages.

Spectra were obtained by 532-nm line, solid-state lasers with a power of approximately 10 mW at the sample, spectral resolution of $\pm 1 \text{ cm}^{-1}$ and acquisition time of 1–2 min.

We decided to focus our attention on the low-medium region of the spectral range and used a grating of 2400 lines/mm in back-scattering configuration with the Explora spectrometer, which allowed us to collect in the range of $100\text{--}1200 \text{ cm}^{-1}$, or a grating of 1800 lines/mm with the inVia spectrometer, which allowed us to collect in the range of $140\text{--}1900 \text{ cm}^{-1}$.

Table 2. Main peaks (T, translational mode; L, librational mode; ν_4 , in-plane bending mode; and ν_1 , symmetric stretching mode) of calcium and magnesium carbonates, from the present study and the literature: 1. Bischoff *et al.*^[4] (0, 3.9, 9.9 and 15.0 mol% MgCO_3 calcites); 2. Herman *et al.*^[21]; 3. Kuebler *et al.*^[22]; 4a. This study, experimental (aragonite, UNIMB standard sample, Val Formazza, Italy; calcite, UNIMB standard sample, Chihuahua, Mexico; a 3.8 mol% MgCO_3 calcite, barnacle, Italy; a 10.2 mol% MgCO_3 calcite, *Paracentrotus lividus*, Echinoid, Italy; a 15.0 mol% MgCO_3 calcite, *Cidaris*, echinoid, Italy; magnesite, M.A.C. certificated standard); 4b. This study, calculated. Regression equations obtained from the experimental data (Fig. 4) and calculated peak positions shown in 4b rows. To conform with literature data, we report peak positions without decimals. Spectra with 'R' were analysed by Renishaw inVia confocal Raman microscope, and spectra with 'H' were analysed by Horiba XploRA.

Vibrational mode	Author	Aragonite ^H	Calcite ^H ~0% mol MgCO_3	Calcite ^R ~4% mol MgCO_3	Calcite ^H ~10% mol MgCO_3	Calcite ^H ~15% mol MgCO_3	Magnesite ^R	Dolomite ^H
T (cm^{-1})	1	—	154	155	157	156	213	175
	2	150	154	—	—	—	216	177
	3	154	156	—	—	—	215	178
	4a	154	154	155	156	156	213	177
	4b	—	155	155	156	156	—	—
				$T = 0.1079 [\text{MgCO}_3] + 154.69; R^2 = 0.3046$				
L (cm^{-1})	1	—	281	281	284	286	329	299
	2	205	283	—	—	—	332	301
	3	208	282	—	—	—	332	302
	4a	207	281	282	284	286	330	300
	4b	—	281	282	283	285	—	—
				$L = 0.2591 [\text{MgCO}_3] + 280.79; R^2 = 0.63257$				
ν_4 (cm^{-1})	1	—	711	712	714	716	738	724
	2	704	714	—	—	—	738	729
	3	703	713	—	—	—	739	726
	4a	702 + 707	712	713	713	714	738	725
	4b	—	712	713	714	715	—	—
				$\nu_4 = 0.1957 [\text{MgCO}_3] + 711.93; R^2 = 0.69127$				
ν_1 (cm^{-1})	1	—	1085	1086	1087	1088	1094	1097
	2	1085	1087	—	—	—	1096	1099
	3	1086	1086	107	—	—	1095	1098
	4a	1087	1086	1087	1088	1088	1095	1098
	4b	—	1086	1087	1088	1088	—	—
				$\nu_1 = 0.1491 [\text{MgCO}_3] + 1086.2; R^2 = 0.69298$				

Raman as a tool for Mg estimation in Mg-calcite

More than one spectrum have been collected for every analysed point, and a picture (provided by the first author on demand) was taken for each beamed point, in order to carry out microprobe analyses exactly in the same area and to correlate the migration of Raman bands with cation composition.

The software LABSPEC 5 was used for baseline subtraction, to eliminate the natural fluorescence of carbonate crystals and to assess the positions of peaks by the Gaussian–Lorentzian (pseudo-Voigt) deconvolution method, which allowed us to determine peak positions with an accuracy of 0.2 cm^{-1} .

Carbonate standards and biogenic samples were analysed for their major elements with a Tescan VEGA TS Univac 5136 XM scanning electron microscope coupled with an EDAX Genesis 4000 XMS Imaging 60 SEM-EDS at the University of Milano-Bicocca, Italy, under an electron beam of 20-kV high voltage, with 250-nm spot size and an absorption of current of $190 \pm 1\text{ pA}$, measured in platinum Faraday cup; the quantification of main elements (Ca and Mg) was calibrated on Astimex Scientific standard.

To test the reliability of the EDS results, chosen samples have been analysed also with the wavelength dispersive spectrometer (WDS) at the TU Bergakademie Freiberg, Saxony, Germany, a JEOL Ltd. JXA-8900 RL electron probe microanalyzer, with a beam size of $2\text{ }\mu\text{m}$. Astimex Scientific standards were used to better evaluate the MgO, CaO, Na_2O , SO_3 , Al_2O_3 (EDS and WDS) and SrO (EDS) molar contents. The Mg content was calculated as mol% $\text{MgO}/(\text{CaO} + \text{MgO} + \text{Na}_2\text{O} + \text{SrO})$ and then transformed in mol% MgCO_3 . The two electron beam instruments provided similar results, with a confidence in the range of $\pm 1\text{ mol}\%$.

Sample description

Certificated standard samples for magnesite, siderite and ankerite were provided by the M.A.C. Company (Micro-Analysis Consultants). The pure calcite crystal is from Chihuahua, Mexico,^[43] the aragonite from Val Formazza, Italy, and the dolomite from Selvino, Italy. The chemistry of all these samples was determined by microprobe analysis.

Biological magnesian calcites from recent and fossil foraminifers, coralline red algae, barnacles and sea urchins (Table 1, complete dataset in Table S1) were collected from areas situated at different latitudes, depth and depositional environments and characterized by different water temperatures (from 5 to $29.5\text{ }^\circ\text{C}$) and saturations (from 160 ± 20 to 245 ± 15), factors affecting the Mg content in shells of marine organisms.

Carbonates Raman spectra

The Raman spectra of carbonates were collected first by Landsberg and Mandelstam^[44] and by Wood,^[45] only few months after CV Raman and his co-worker KS Krishnan had discovered this new radiation. In the last decades, their pioneering work has been carried out by several working groups. Carbonate minerals have been investigated in detail because of their widespread occurrence and good Raman signal, dedicating particular attention to thermodynamic properties and vibrational spectra.^[3,4,13,46–50]

The vibrations can be divided into internal vibrations of the $(\text{CO}_3)^{2-}$ group (range between 600 and 1700 cm^{-1}) and the lattice

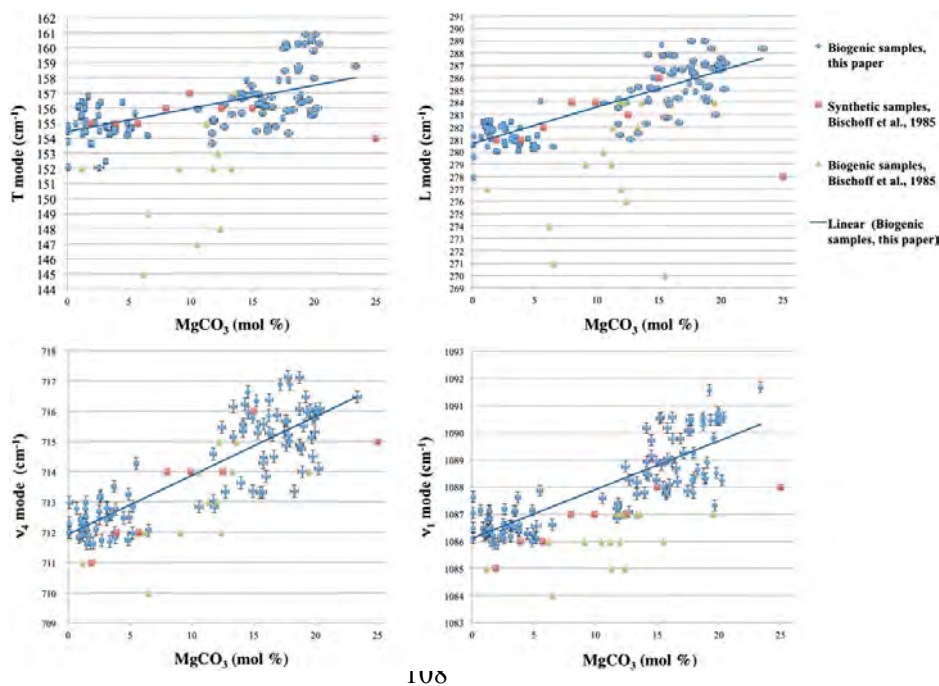


Figure 3. Frequencies of main Raman vibrational modes (T, translational mode; L, librational mode; v_4 , in-plane bending mode; and v_1 , symmetric stretching mode) of biogenic magnesian calcites versus their magnesium content. Data from this study (blue diamonds) are combined with data from Bischoff *et al.*^[4] (biogenic samples as green triangles and synthetic samples as red squares). The integral error in energy dispersive spectrometer and wavelength dispersive spectrometer data and the error in the determination of peak positions are shown. [Colour figure can be viewed at wileyonlinelibrary.com]

vibrations involving translation and libration of the $(\text{CO}_3)^{2-}$ groups relative to the Ca^{2+} or Mg^{2+} ions ($100\text{--}500\text{ cm}^{-1}$). The $(\text{CO}_3)^{2-}$ group vibrational modes are characterized by symmetric stretching (from 600 to 1200 cm^{-1}) and by asymmetric stretching (from 1200 to 1700 cm^{-1}).^[5]

The calcite spectrum (Fig. 1 and Table 2) is characterized by a very sharp peak at 1086 cm^{-1} (ν_1 , symmetric stretching mode of the carbonate ion), along with other subsidiary bands at 156 cm^{-1} (T, translational mode), 282 cm^{-1} (L, librational mode) and 712 cm^{-1} (ν_4 , in-plane bending of the $(\text{CO}_3)^{2-}$ group).^[4,41,47]

The main peak of aragonite is also located at 1086 cm^{-1} (Fig. 1 and Table 2), but its spectrum is easily distinguished on the basis of differing bands in the lowest region (181 , 191 and 207 cm^{-1}) and the presence of a doublet at 702 and 707 cm^{-1} .^[34,48,49]

The magnesite spectrum is similar to that of calcite (Fig. 1 and Table 2), as expected because of their isomorphism.^[3] However, all frequencies of magnesite are higher because of shorter inter-ionic distances and consequent stronger interionic forces.

The layered structure of the dolomite lattice causes the presence of an additional vibrational mode at 335 cm^{-1} , which allows ready distinction from all other carbonate minerals (Fig. 2 and Table 2).^[4]

Results

The Raman shifts observed in different standard minerals (calcite, magnesite, dolomite, aragonite, siderite and ankerite; Figs 1 and 2) agree with the results available in literature, although different authors report values with significant variation (for a comparison, see Table 2). This could be ascribed to the fact that carbonates are solid solutions and their chemical composition greatly influences the Raman modes' positions, and/or to instrumental differences among laboratories.

We determined the position of the four main vibrational modes of several calcite crystals with magnesium content ranging from 0.1 to $19.3\text{ mol}\%$ MgCO_3 (Fig. 3): T, translational mode ($152.0\text{--}160.0\text{ cm}^{-1}$); L, librational mode ($278.0\text{--}288.7\text{ cm}^{-1}$); ν_4 , in-plane bending ($711.6\text{--}717.1\text{ cm}^{-1}$); and ν_1 , symmetric stretching ($1086.0\text{--}1090.8\text{ cm}^{-1}$). Some samples exhibit a band at $1013\text{--}1015\text{ cm}^{-1}$, a peak ascribed to the bicarbonate ion (HCO_3).^[4]

Raman spectra of carbonates are sensitive to the structural and chemical changes occurring when Mg^{2+} ion substitutes the larger Ca^{2+} ion in the calcite lattice, and the position of vibrational modes is directly controlled by the amount of magnesium present in the lattice. Our results (Fig. 3) suggest that Raman shifts follow a one-

mode behaviour, increasing with magnesium content in a quite linear way, in contrast with the dataset presented in Bischoff^[4] on biogenic samples (Fig. 3). Therefore, it is possible to identify a progressive increase in Raman shifts with increasing Mg content in the analysed sample, which reflects the decreased inter-atomic distances following the substitution of Ca^{2+} with the smaller Mg^{2+} ion. The regression lines calculated for peak positions of our biological samples (Fig. 3) indicate that L, ν_4 and ν_1 modes behave approximately linearly, with a coefficient of determination R^2 between 0.7 and 0.85 .

Discussion

As in recent works,^[4,41,42,49] we present our chemical estimates expressed as molar % rather than weight %. The EDS and WDS data showed similar results, with a difference in the range of $\pm 1\text{ mol}\%$, confirming the reliability of the used EDS probe. For the complete WDS and EDS dataset, see Table S2.

Two different groups of magnesium calcites are observed, one containing from 0 to $5.5\text{ mol}\%$ MgCO_3 (low-Mg calcites) and the other one containing from 10.5 to $20\text{ mol}\%$ MgCO_3 (high-Mg calcites) (Fig. 3). Even though ~ 200 chemical analyses were collected on more than 40 samples of diverse taxa from various latitudes and depths, we never found unaltered calcites with $5.5\text{--}10.5\text{ mol}\%$ MgCO_3 (corresponding to $2.5\text{--}4.5\text{ wt}\%$ MgCO_3). We infer that a miscibility gap in magnesium concentration may exist between natural low-Mg calcite and high-Mg calcite,^[38] probably related to the crystal structure of calcite and the smaller size of the Mg^{2+} ion compared with the Ca^{2+} ion. High-Mg calcite is metastable, and marked magnesium depletion may and commonly does occur during diagenetic stabilization with meteoric waters.^[6,29,30] Very few unaltered calcite crystals with $5.5\text{--}10.5\text{ mol}\%$ MgCO_3 have been reported so far, generally with little information about the possible post-depositional alteration.^[4,21,26,27,33] Calcite samples within such an Mg range were described by Budd et al.,^[30] but all of them were altered. Calcites in this chemical range were never found by Bøggild.^[38]

The distinction between low-Mg and high-Mg calcite based on an arbitrary boundary at $\sim 4\text{ wt}\%$ MgCO_3 (a little less than $10.5\text{ mol}\%$ MgCO_3) has been proposed already by previous studies^[24,31,32] and supported by crystallographic, chemical and structural evidence.

A coefficient of determination R^2 of $0.7\text{--}0.85$ for L, ν_4 and ν_1 modes regression indicates a strong linear correlation rather

Table 3. Linear fitting of wavenumbers versus composition for the main Raman peaks (T, translational mode; L, librational mode; ν_4 , in-plane bending mode; and ν_1 , symmetric stretching mode) of biogenic magnesian calcites (blue diamonds in Fig. 3)

Vibrational modes	ν_0 (cm^{-1})	Slope (cm^{-1})	Equations (cm^{-1})	R^2	$\delta\nu$ (cm^{-1})	δMg (mol%)
T	154.4 ± 0.2	0.15 ± 0.02	T = $154.4 + 0.15$ [% mol MgCO_3]	0.38	1.4	5.8
L	280.7 ± 0.2	0.29 ± 0.02		L = $280.7 + 0.29$ [% mol MgCO_3]	0.70	1.5
ν_4	711.9 ± 0.1	0.19 ± 0.01	$\nu_4 = 711.9 + 0.19$ [% mol MgCO_3]	0.85	0.9	3.8
ν_1	1086.1 ± 0.1	0.18 ± 0.01	$\nu_1 = 1086.1 + 0.18$ [% mol MgCO_3]	0.72	0.8	3.9

The $\delta\nu$ column represents the dispersion (root mean square deviation) of the wavenumbers around the regression line. The δMg column shows the dispersion of the MgCO_3 (mol%) values around the regression line obtained from the composition versus wavenumber plot (not shown). It represents the uncertainty on the composition as it is calculated from the value of a single Raman peak.

Raman as a tool for Mg estimation in Mg-calcite

robustly, because more than 100 data points were used in the present study. The R^2 coefficient is instead low (0.38) for T mode regression. The scatter of points around regression lines is significant (error on the wavenumber between 0.8 and 1.5 cm^{-1} , Table 3). On the other hand, this value is lower than the difference in wavenumber provided in the literature for the same peak in

calcites with the same Mg content (Table 2). The observed scatter appears to be an intrinsic characteristic of biogenic magnesian calcites and could be caused by the heterogeneity in the distribution of magnesium ions, by positional disorder and/or by trace element substitution, which are typical of biogenic samples.^[4]

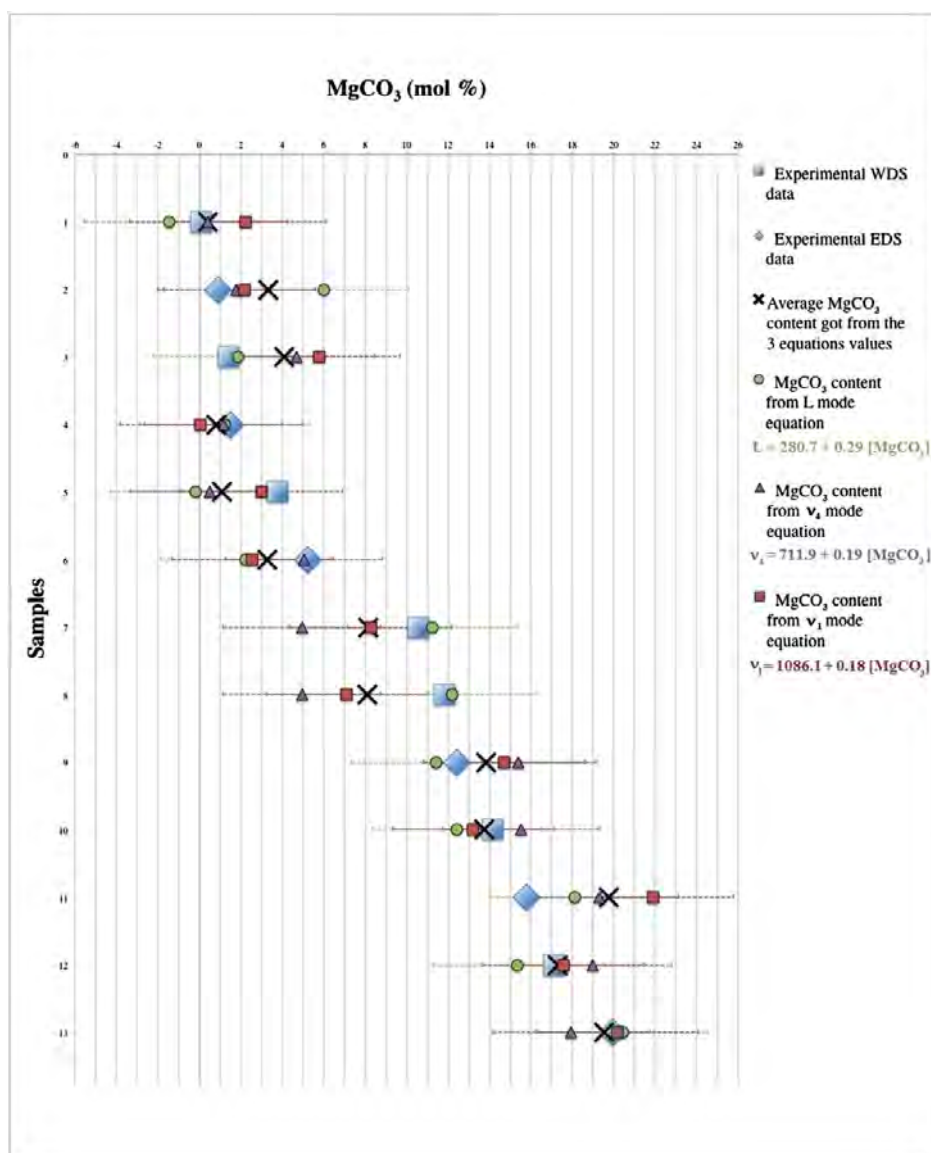


Figure 4. Comparison between theoretical and experimental MgCO_3 values. Theoretical values were obtained using equations for L (*librational mode*, green dots), ν_4 (*in-plane bending mode*, purple triangles) and ν_1 modes (*symmetric stretching mode*, red squares; Tables 3 and 4). The 13 biogenic samples analysed (blue diamonds and squares) were chosen randomly. 1: Benthic foraminifer (*Elphidium* sp.), Italy, WDS; 2: Barnacle (*Balanus* sp.), Italy, energy dispersive spectrometer (EDS); 3: Benthic foraminifer (*Elphidium* sp.), Malaysia, wavelength dispersive spectrometer (WDS); 4: Barnacle (*Balanus* sp.), Italy, EDS; 5: Echinoid, (Echinoidea), Moira Mound, WDS; 6: Barnacle (*Balanus* sp.), Italy, EDS; 7: Echinoid (*Paracentrotus lividus* sp.), Italy, WDS; 8: Echinoid (*P. lividus* sp.), Italy, WDS; 9: Benthic foraminifer (*Milolida*), Greece, EDS; 10: Benthic foraminifer (*Milolida*), Greece, WDS; 11: Calcareous red algae (*Corallinophycidae*), Iceland, EDS; 12: Benthic foraminifer (*Sorites* sp.), Malaysia, WDS; 13: Calcareous red algae (*Porolithon onkodes*), Egypt, EDS. [Colour figure can be viewed at wileyonlinelibrary.com]

Such heterogeneity is quantified by δ Mg values ranging between 3.8 and 5.8 mol% (Table 3), which were obtained by linear fitting of chemical composition versus wavenumber plots. These values represent the uncertainty on the magnesium estimation when a single Raman peak value is used.

To better estimate the reliability of the equations and visualize the discrepancy between theoretical and experimental results, we compared the MgCO_3 content measured from 13 randomly chosen

samples (seven WDS analyses and six EDS analyses; blue squares and diamonds in Fig. 4 and in Table 4) to the compositions obtained using the L , ν_4 and ν_1 modes regression equations (Fig. 4 and Table 3). As expected, the difference between theoretical and experimental data is often significant.

The determination of Mg is thus imprecise when based on a single Raman peak only. When two or three peaks are used in combination, a much better resolution is reached, providing a

Table 4. Comparison between experimental measurements with WDS and EDS probes and calculated compositions based on the L (librational mode), ν_4 (in-plane bending mode) and ν_1 (symmetric stretching mode) equations (Fig. 4)

N° sample	Used probe	[MgCO ₃]: experimental (mol%)	[MgCO ₃]: calculated by L mode equation (mol%)	[MgCO ₃]: calculated by ν_4 mode equation (mol%)	[MgCO ₃]: calculated by ν_1 mode equation (mol%)	[MgCO ₃]: average of L, ν_4 and ν_1 equations results (mol%)	[MgCO ₃]: Δ (experimental – average of L, ν_4 and ν_1 equations results) (mol%)
1	WDS	0.09	-1.45	0.42	2.22	0.40	-0.31
2	EDS	0.89	6.00	1.79	2.17	3.32	-2.43
3	WDS	1.39	1.86	4.68	5.78	4.11	-2.72
4	EDS	1.51	1.21	1.16	0.06	0.81	0.70
5	WDS	3.78	-0.21	0.47	3.00	1.09	2.69
6	EDS	5.21	2.24	5.05	2.56	3.28	1.93
7	WDS	10.58	11.24	4.95	8.28	8.16	2.42
8	WDS	11.82	12.21	4.95	7.11	8.09	3.73
9	EDS	12.43	11.44	15.37	14.72	13.84	-1.41
10	WDS	14.14	12.45	15.53	13.22	13.73	0.41
11	WDS	15.80	18.10	19.32	21.89	19.77	-3.97
12	WDS	17.14	15.34	19.00	17.56	17.30	-0.16
13	EDS	19.93	20.45	17.95	20.17	19.52	0.41

An average of results extrapolated from the three different equations and its difference with experimental measurements are presented in the last columns.

EDS, energy dispersive spectrometer; WDS, wavelength dispersive spectrometer.

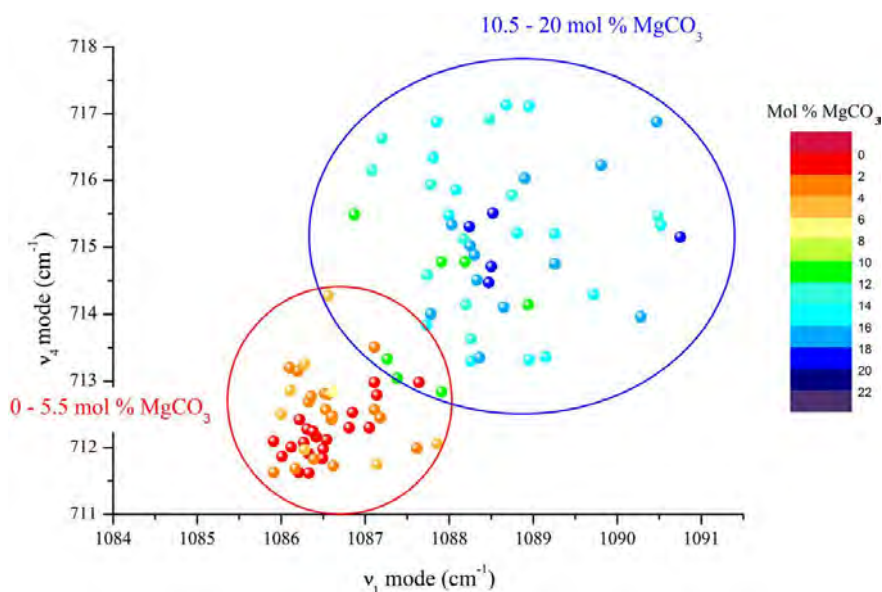


Figure 5. 2D plot of ν_4 (in-plane bending mode) versus ν_1 (symmetric stretching mode). The colour legend indicates magnesium content. [Colour figure can be viewed at wileyonlinelibrary.com]

Raman as a tool for Mg estimation in Mg-calcite

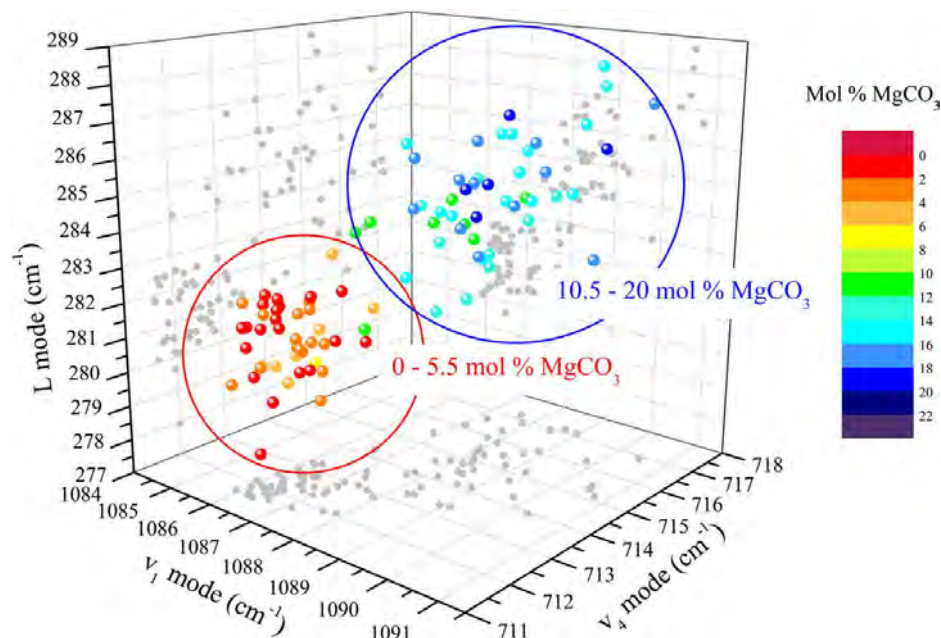


Figure 6. 3D plot of L (librational mode) versus v_4 (in-plane bending mode) versus v_1 (Symmetric stretching mode). The colour legend indicates magnesium content. [Colour figure can be viewed at wileyonlinelibrary.com]

powerful tool to classify magnesian calcites. The two-dimensional plot of Fig. 5 shows the composition of our samples (in colour scale) versus the positions of the v_4 and v_1 peaks (at nearly 1088 and 714 cm^{-1}), which resulted to be the most reliable peaks used to discriminate between low-Mg and high-Mg calcite groups. In the tridimensional plot of Fig. 6, the position of the L peak (around 283 cm^{-1}) is added, showing an even better separation between the two groups. The relations in Fig. 6 can, therefore, be applied with confidence for a classification of calcites on the basis of MgCO_3 content. Within each group, a clear trend between wavenumber and chemical composition is not clearly visible, but the correlation between the position of Raman peaks and microprobe measurements of Mg concentration is evident and linear, in contrast with biogenic calcites studied by Bischoff^[4] (Fig. 3). Extreme caution should thus be used when using the results of Bischoff *et al.* as a reference for the estimation of magnesium content.^[51,52]

Conclusions

We collected nearly 200 chemical analyses and 120 Raman spectra on carbonate samples of both organic and inorganic origin with magnesium content varying from 0 to ~20 mol% MgCO_3 . A miscibility gap in the window between 5.5 and 10.5 mol% MgCO_3 was observed. All peaks in Mg-calcite Raman spectra showed a consistent linear increase in Raman shifts with increasing Mg content, reflecting decreasing inter-atomic distances following the substitution of the Ca^{2+} ion with the smaller Mg^{2+} cation in the calcite lattice. Raman spectra of calcite are thus sufficiently sensitive to chemical and structural changes to allow us to quantify the ratio between Ca and Mg in the solid solution calcite-magnesite. Raman

band positions can be linked directly to the amount of Mg present in the lattice. Two standard graphs that combine Raman shifts and Mg content in calcites are presented. We calculated four equations that link Raman bands to magnesium content, although the heterogeneity of Mg distribution, positional disorder and trace elements substitution limit their effectiveness for biogenic samples. In these samples, most accurate results are obtained by combining two or three Raman peaks rather than a single peak.

This study demonstrates that Raman spectroscopy is a very efficient, user-friendly technique that with a non-destructive sample preparation allows us to obtain, readily and reliably, information about the chemical composition of minerals and to estimate the magnesium content in fossil faunas and floras. This powerful tool opens up new perspectives in provenance, marine biology and palaeontological studies, with direct application to hydrocarbon research.

Acknowledgements

We would like to thank, Giovanni Vezzoli, Alberto Resentini and Agostina Vertino for the precious advice and Nina Egeland for her significant help provided during the study. This work is part of the PhD project of L. B. and was supported by the National IOR Centre of Norway.

The authors acknowledge the Research Council of Norway and the industry partners ConocoPhillips Skandinavia AS, BP Norge AS, Det Norske Oljeselskap ASA, ENI Norge AS, Maersk Oil Norway AS, DONG Energy A/S, Denmark, Statoil Petroleum AS, ENGIE E&P Norge AS, Lundin Norway AS, Halliburton AS, Schlumberger Norge AS and Wintershall Norge AS of The National IOR Centre of Norway for support.

References

- [1] J. Veizer, J. Hoefs, D. R. Lowe, P. C. Thurston, *Geochim. Cosmochim. Acta* **1989**, *53*, 859.
- [2] S. Andò, E. Garzanti, Sediment provenance studies in hydrocarbon exploration and production, in *Geological Society, Special Publications*, London, **2013**, p. 386.
- [3] D. Krishnamurti, *Proceedings of the Indian Academy of Sciences – Section A* **1956**, *43*, 210.
- [4] W. D. Bischoff, S. K. Sharma, F. T. Mackenzie, *Am. Mineral.* **1985**, *70*, 581.
- [5] J. Sun, W. Zeguano, C. Hongfei, *Spectrochim. Acta A* **2014**, *117*, 158.
- [6] U. Brand, *Geol. Soc. Am. Bull.* **1989**, *101*, 377.
- [7] A. Dandeu, B. Humbert, C. Carteret, H. Muhr, E. Plasari, J. M. Bossoutrot, *Chem. Eng. Technol.* **2006**, *29*, 221.
- [8] L. S. Land, *J. Sediment. Petrol.* **1967**, *37*, 914.
- [9] U. Wehrmeister, A. L. Soldati, D. E. Jacob, T. Hager, W. Hofmeister, J. Raman, *Spectroscopy* **2010**, *41*, 193.
- [10] K. Spangenberg, M. Müller, *Heidelberger Beiträge zur Mineralogie und Petrographie* **1949**, *1*, 560.
- [11] F. L. Sayles, W. S. Fyfe, *Geochim. Cosmochim. Acta* **1973**, *37*, 87.
- [12] G. T. Faust, E. Callaghan, *Geol. Soc. Am. Bull.* **1948**, *59*, 11.
- [13] H. N. Rutt, H. Nicola, *J. Phys. C Solid State Phys.* **1974**, *7*, 4522.
- [14] R. G. Herman, C. E. Bogdon, A. J. Sommer, D. R. Simpson, *Appl. Spectrosc.* **1987**, *41*-3, 437.
- [15] K. Kuebler, A. Wang, K. Abbott, L. A. Haskin, *LPS* **2001**, *XXXII*, 1889.
- [16] N. Rividi, M. van Zuilen, P. Philippot, B. Menez, G. Godard, E. Poidatz, *Astrobiology* **2010**, *10*-3, 293.
- [17] E. N. Wilson, L. A. Hardie, O. M. Phillips, *Am. J. Sci.* **1990**, *290*, 741.
- [18] W. M. Last, *Earth Sci. Rev.* **1990**, *27*, 221.
- [19] M. C. Nash, U. Troitzsch, B. N. Opdyke, J. M. Trafford, B. D. Russell, D. I. Kline, *Biogeosciences* **2011**, *8*, 3331.
- [20] S. Gunasekaran, G. Anbalagan, S. Pandi, J. Raman, *Spectroscopy* **2006**, *37*, 892.
- [21] J. R. Goldsmith, D. L. Graf, O. I. Joensuu, *Geochim. Cosmochim. Acta* **1955**, *7*, 212.
- [22] J. R. Goldsmith, D. L. Graf, J. Witters, D. A. Northrop, *J. Geol.* **1962**, *70*, 659.
- [23] A. Katz, *Geochim. Cosmochim. Acta* **1973**, *37*, 1563.
- [24] F. T. Mackenzie, W. D. Bischoff, F. C. Bishop, M. Loijens, J. Schoonmaker, R. Wollast, in *Carbonates: Mineralogy and Chemistry. Reviews in Mineralogy, II* (Ed: R. J. Reeder), Mineralogical Society of America, Washington, **1983**, pp. 97–144.
- [25] D. Basso, *Geodiversitas* **2012**, *34*, 13.
- [26] K. E. Chave, *J. Geol.* **1954a**, *62*, 266.
- [27] K. E. Chave, *J. Geol.* **1954b**, *62*, 587.
- [28] M. Mutti, P. Hallock, *Int. J. Earth Sci.* **2003**, *92*, 465.
- [29] U. Brand, J. Veizer, *J. Sediment. Petrol.* **1980**, *50*-4, 1219.
- [30] D. A. Budd, E. E. Hiatt, *J. Sediment. Petrol.* **1992**, *63*-2, 261.
- [31] M. E. Tucker, V. P. Wright, *Carbonate Sedimentology (Chapter 6)*, Blackwell Publishing Ltd., Oxford, **1990**, pp. 284–313.
- [32] J. B. Ries, A. L. Cohen, D. C. Mc Corkle, *Geology* **2009**, *37*, 1057.
- [33] J. B. Rucker, R. E. Carver, *J. Paleol.* **1969**, *43*, 791.
- [34] A. M. Smith, M. M. Key Jr., P. Gordond, *Earth Sci. Rev.* **2006**, *78*, 287.
- [35] A. J. Andersson, F. T. Mackenzie, *Ecol. Lett.* **2011**, *13*, 1419.
- [36] W. D. Bischoff, F. T. Mackenzie, F. C. Bishop, *Geochim. Cosmochim. Acta* **1987**, *51*, 1413.
- [37] W. D. Bischoff, *Aquat. Geochem.* **1998**, *4*, 321.
- [38] O. B. Bøggild, *Danske Vidensk Selsk Skr.* **1930**, *9*, 235.
- [39] R. J. Reeder, in *Carbonates: Mineralogy and Chemistry* (Ed: R. J. Reeder), Mineralogical Society of America, Chantilly, VA, **1983**, pp. 1–48.
- [40] K. E. Chave, *J. Geol.* **1952**, *60*, 190.
- [41] J. Urmos, S. K. Sharma, T. Mackenzie, *Am. Mineral.* **1991**, *76*, 641.
- [42] B. Purgstaller, V. Mavromatis, M. Dietzel, *EGU General Assembly* **2015**, *2015*, 17.
- [43] J. P. Miller, *Am. J. Sci.* **1952**, *250*, 161.
- [44] G. Landsberg, L. Mandelstam, *Zeit. F. Phys.* **1928**, *50*, 729.
- [45] R. W. Wood, *Philos. Mag.* **1928**, *6*, 729.
- [46] W. P. Griffith, *Nature* **1969**, *224*, 264.
- [47] R. Frech, E. C. Wang, J. B. Bates, *Spectrochim. Acta A* **1980**, *36*, 915.
- [48] J. S. Tribble, R. S. Arvidson, M. Lane III, F. T. Mackenzie, *Sediment. Geol.* **1995**, *95*, 11.
- [49] H. Edwards, S. Villar, J. Jehlicka, T. Munshi, *Spectrochim. Acta A* **2005**, *61*, 2273.
- [50] C. Baita, P. P. Lottici, E. Salvioni-Mariani, P. Vandenebee, M. Librenti, F. Antonelli, D. Bersani, *J. Raman Spectroscopy* **2014**, *45*, 114.
- [51] N. A. Kamenos, H. L. Burdett, E. Aloisio, H. S. Findlay, S. Martin, C. Longbone, J. Dunn, S. Widdicombe, P. Calosi, *Glob. Chang. Biol.* **2013**, *19*, 3621.
- [52] M. Pauly, N. A. Kamenos, P. Donohue, E. LeDrew, *Geology* **2015**, *43*-3, 267.
- [53] J. G. Acker, G. Leptoukh, *Trans. Am. Geophys. Union* **2007**, *88*-2, 14.
- [54] M. Mosbrugger, T. Uterscher, D. L. Dilcher, *Proc. Natl. Acad. Sc. USA* **2005**, *102*-42, 14964.
- [55] S. Spezzaferrri, A. Vertino and the E-CWC Moira cruise scientific party (2012) Cruise No. 2012/16, EUROFLEETS, 2012; *CWC Moira Cruise Report*, 1.

Supporting information

Additional Supporting Information may be found online in the supporting information tab for this article.

6.2 Quick, easy and economic mineralogical studies of flooded chalk for EOR experiments using Raman spectroscopy; Borromeo et al. 2018a

During the first phase of the PhD, it was proved that Raman spectroscopy is a valid method to discriminate between carbonates; during the second phase, instead, it has been tested if this may work on chalk, which, for its softness and micro-grain size, is really challenging to study with traditional methods. Chalk had to be selected, as it is the major target on the Norwegian continental shelf for enhanced oil recovery as the largest hydrocarbon reservoirs are hosted by chalk. The goal was to identify and, if possible, estimate the mineralogical alterations that happen during brine injection, where micron-sized crystals grow in the matrix or on calcite surfaces: these alterations could impact the porosity and permeability of the rocks (Wang et al. 2016).

I applied this grain by grain methodology on two MgCl_2 flooded chalk samples from Liège, Belgium, that have been flooded with MgCl_2 for c. 1.5 (Long Term Test, LTT) and 3 years (Ultra Long Term Test, ULTT) under reservoir conditions, matching important hydrocarbon reservoirs in the North Sea (see “4.3.3 Flooding experiments” chapter or Borromeo et al, 2018a). Raman spectroscopy could identify the presence of recrystallized magnesite along the core of the Long Term Test (1.5-years-test, LTT) up to 4 cm from the injection surface. In the

Publications

Ultra Long Term Test core (3-years-test, ULTT) the growth of MgCO_3 affected nearly the entire core (7 cm). In both samples no dolomite or high-magnesium calcite secondary growth could be detected when spotting $n= 557$ in the LTT and $n= 90$ Raman spectra in the ULTT (Borromeo et al, 2018a).

This paper has been firstly published submitted to Minerals (ISSN 2075-163X), which is published by MDPI (Multidisciplinary Digital Publishing Institute).

1 Article

2 **Quick, Easy and Economic Mineralogical Studies of**
3 **Flooded Chalk for EOR Experiments Using Raman**
4 **Spectroscopy**

5 **Laura Borromeo^{1,2,*}, Nina Egeland^{1,2}, Mona Wettrhus M inde^{1,2}, Udo Zimmermann^{1,2},**

6 **Sergio Andò³, Merete Vadla Madland^{1,2}, Reidar Inge Korsnes^{1,2}**

7 ¹ Department of Energy Resources, University of Stavanger, Norway

8 ² The National IOR Centre of Norway, Stavanger, Norway

9 ³ Department of Earth and Environmental Sciences, University of Milano - Bicocca, Milano, Italy

10 * Correspondence: laura.borromeo@uis.no; Tel.: +39 3386008504

11 **Abstract:** Understanding the chalk-fluid interactions and the associated mineralogical and
12 mechanical alteration at sub-micron scale are major goals in Enhanced Oil Recovery. Mechanical
13 strength, porosity, and permeability of chalk are linked to mineral dissolution that occurs during
14 brine injections, and affect the reservoir potential. This paper presents a novel „single grain“
15 methodology to recognize the varieties of carbonates in rocks and loose sediments: Raman
16 spectroscopy is a non-destructive, quick, and user-friendly technique representing a powerful tool
17 to identify minerals down to 1 µm. An innovative working technique for oil exploration is proposed,
18 as the mineralogy of micron-sized crystals grown in two flooded chalk samples (Liège, Belgium)
19 was successfully investigated by Raman spectroscopy. The drilled chalk cores were flooded with
20 MgCl₂ for c. 1.5 (Long Term Test) and 3 years (Ultra Long Term Test) under North Sea reservoir
21 conditions (Long Term Test: 130°C, 1 PV/day, 9.3 MPa effective stress; Ultra Long Term Test: 130°C,
22 varying between 1-3 PV/day, 10.4 MPa effective stress). Raman spectroscopy was able to identify
23 the presence of recrystallized magnesite along the core of the Long Term Test up to 4 cm from the
24 injection surface, down to the crystal size of 1-2 µm. In the Ultra Long Term Test core the growth of
25 MgCO₃ affected nearly the entire core (7 cm). In both samples, no dolomite or high-magnesium
26 calcite secondary growth could be detected when analysing 557 and 90 Raman spectra on the Long
27 and Ultra Long Term Test, respectively. This study can offer Raman spectroscopy as a breakthrough
28 tool in petroleum exploration of unconventional reservoirs, due to its quickness, spatial resolution,
29 and non-destructive acquisition of data. These characteristics would encourage its use coupled with
30 electron microscopes and energy dispersive systems or even electron microprobe studies.

31 **Keywords:** flooded chalk; Raman spectroscopy; Enhanced Oil Recovery; carbonates; calcite; magnesite.

33 **1. Introduction**

34 Injection of seawater-like brines is one of the most successful Improved Oil Recovery (IOR)
35 methods on the Norwegian Continental Shelf [amongst many others: 1,2]. The mechanical strength
36 of chalk is weakened by seawater at reservoir temperatures, and as a consequence, compaction and
37 loss in porosity occur, affecting the oil recovery factor of carbonate fields [3-10]. It is important to
38 understand how fluids interact with rocks because textural and chemical/mineralogical changes in
39 the pore space affect the way water will adsorb and expel oil from the rock [3, 8, 11-17]. Previous
40 research on fluid injection has been carried out [5, 8, 17-21] and three ions have proven to play
41 important roles when chalk is exposed to seawater at elevated temperatures: Ca²⁺, Mg²⁺, and SO₄²⁻.
42 The injected seawater triggers several mechanisms such as precipitation, dissolution, ion exchange,
43 adsorption, and desorption, to interplay at the same time, with different relative significance
44 depending on the position in the reservoir (nearly to the injector or to the producer). It is therefore

45 beneficial to simplify the system and study each ion individually. With MgCl₂ brines, which represent
46 simplified aqueous chemistry of seawater, the role of Mg²⁺ is specifically studied.

47 The two cores investigated in this study (see Fig. 1), were flooded with MgCl₂ for 1.5 (Long Term
48 Test, LTT) and 3 years (Ultra Long Term Test, ULTT) under reservoir conditions (LTT: 130°C, 1
49 PV/day, 9.3 MPa effective stress, ULTT: 130°C, varying between 1-3 PV/day, 10.4 MPa effective
50 stress), in order to reach a mineralogical insight of the basic processes that happen during long time
51 brine injection.

52 The analyses are carried out by Raman spectroscopy, which is a quick and versatile information-
53 rich technique that can easily be applied to almost all substances (gases, liquids, solids, organic, and
54 inorganic) with the only exception of metals. In the last decades Raman spectroscopy has proven to
55 be an easy way to obtain mineral identification (see Fig. 2) [22-27] as every Raman spectrum is like a
56 fingerprint that can provide various information such as crystallinity, phase, intrinsic stress/strain,
57 and polymorphism [28-31]. Furthermore, mineral phases can be identified down to a few microns
58 [32], a possibility of paramount importance in chalk investigation. By applying Raman to flooded
59 chalk, a „grain by grain“ methodology was developed to obtain a better understanding of its
60 mineralogy.

61 2. Materials and Methods

62 2.1. Samples

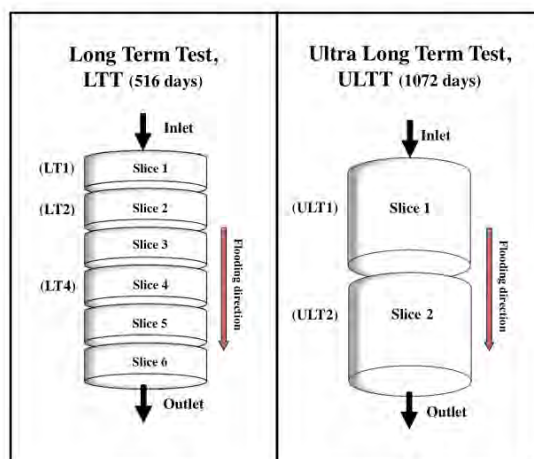
63 The samples studied in this project are all chalk, fine-grained carbonate rocks, built primarily of
64 the skeletal debris of micro- and nano-organisms, mainly coccoliths, shed from coccolithophores (see
65 SEM images in Fig. 3). The cores were sampled at the Lixhe outcrop (Gulpen Formation, Campanian
66 to late early Maastrichtian) [33] near Liège in Belgium, in particular from the Zeven Wegen Member
67 [34] with an age of 75.5–78.0 Ma. The chalk shows clear signs of recrystallization, contact cements,
68 and particle interlocking. Nevertheless, coccoliths are still well preserved and the rock presents
69 intrafossil porosity [35]. The chalk from Liège shows a clean compositional nature, as the main
70 mineral component is calcite (CaCO₃) together with minor abundances of non-carbonate material
71 (between 3-5 wt.% in total) [36, 37] that mainly consists of quartz, smectite/mixed smectite-illite layer,
72 mica, kaolinite, and clinoptilolite, and minor amounts of zeolite, apatite, opal, feldspar, pyroxene,
73 pyrites, and titanium oxide [36, 38].

74 The porosities lie in the range of 40-45 % [21, 35, 39-42]. More information about mineralogy,
75 petrography, and rheological characteristics of these chalk successions can be found in literature [35,
76 39, 40-42]. Onshore chalk successions are used as analogues for North Sea reservoir chalk in several
77 studies [8, 17, 20, 21, 35].

78 2.2. Flooding experiments

79 For this study, two long-term tests were analysed. Both cores were flooded with MgCl₂ at
80 reservoir conditions. The chalk cores (length: ~70 mm, diameter: ~38 mm) were mounted into triaxial
81 cells that allow for measurements of axial strains while flooding of reactive fluids at elevated
82 pressures, stresses, and temperatures. Each triaxial cell was equipped with a heating jacket and a
83 regulation system that kept the temperature constant at 130 ± 0.1°C throughout the experiment. To
84 avoid boiling at temperatures above 100°C, a pore pressure of 0.7 MPa was applied prior to the
85 heating of the system. While distilled water was injected to ensure a clean pore system and to clean
86 the sample, the confining pressure and pore pressure were simultaneously increased from 0.5 and 0
87 MPa to 1.2 and 0.7 MPa, respectively, with a constant effective stress equal to 0.5 MPa. Then, the
88 hydrostatic pressure was increased to 10.0 MPa (LTT) and 11.1 MPa (ULTT). A 0.219 M MgCl₂ brine
89 was injected with a flooding rate of 1 pore volume per day (PV/day) for the LTT and varying between
90 1-3 PV/day for the ULTT. The effective stresses was 9.3 MPa and 10.4 MPa for the LTT and the ULTT,
91 respectively. After the experiment was finished, the cores were cleaned, and after drying, cut into
92 slices with thicknesses of about 10 mm (LTT; to the left in Fig. 1) and of about 35 mm (ULTT; to the
93 right in Fig. 1); the samples were then investigated with different methods. For detailed information

94 of the performed tests, the reader is referred to Zimmermann et al. (2015) [36] for the LTT and
 95 Nermoen et al. (2015) [43] for the ULTT.



96
 97 **Figure 1.** Schematic drawings of how the two cores were cut after the flooding experiment: Long Term
 98 Test (LTT) to the left (modified from Zimmermann et al. 2015 [36]) and Ultra Long Term Test to the
 99 right.

100 2.3. Field Emission Gun-Scanning Electron Microscopy with Energy-Dispersive Spectroscopy

101 Field Emission Gun-Scanning Electron Microscopy with Energy-Dispersive Spectroscopy (FEG-
 102 SEM) analyses were performed at the University of Stavanger using a Zeiss Supra VP 35. Freshly
 103 chipped off pieces of slices from the three core samples were analysed together with chips of
 104 unflooded chalk from the end-pieces of the same cores. The samples were coated with palladium
 105 ensuring a steady flux of electrons. The microscope parameters were set at an acceleration voltage
 106 between 12 to 15kV, 30 μm aperture, and a working distance between 10 and 12 mm. The high current
 107 setting was used. To perform qualitative and semi-quantitative analyses of the chemical composition
 108 of the imaged areas an EDAX energy-dispersive x-ray spectroscopy (EDS) system was used. To
 109 optimize the quantification results, and because the chalk predominantly consists of calcite, an
 110 Iceland spar calcite crystal was used to calibrate the system [36].

111 2.4. Raman spectroscopy

112 During this study, most of the spectra (465 of 557; reported with "H" in figures and Table 1)
 113 were collected with a Horiba XploRA Raman spectrometer equipped with an Olympus microscope
 114 with maximum magnification of 100x, and a motorized x-y stage. Calibration of spectra was obtained
 115 using a silicon wafer with a main peak at 520.7 cm^{-1} as reference and maintained during the analysis
 116 with a constant checking of the position of a sharp neon lamp emission line at 476.8 cm^{-1} . Other
 117 spectra (92 of 557; LTT slice 1: p1_G and I; p2_D and E; slice 4: C and D; reported with "R" in Fig. 2)
 118 were obtained using a high-resolution Renishaw inVia Reflex confocal Raman microscope, equipped
 119 with a Leica DM2500 polarizing microscope (maximum magnification of 100x) and motorized x-y
 120 stages. With both spectrometers, spectra were collected with a 532 nm line, solid-state lasers (10 mW
 121 at the sample), laser spot around 1 μm , spectral resolution of $\pm 1 \text{ cm}^{-1}$, acquisition time of 1-2 minutes,
 122 magnification of 100x. Microscope pictures were taken for each beamed grain or cluster of grains. The
 123 spectral region found to be the most important and convenient to our study was the low-medium
 124 one; setting the XploRA spectrometer with a 2400 lines/mm grating in back-scattering configuration
 125 allowed us to collect in the spectral range 100-1200 cm^{-1} . Using a grating of 1800 lines/mm with the

126 inVia spectrometer instead, allowed us to collect in the range of 140-1900 cm^{-1} . In order to try to detect
127 the occurrence of hydrated silicates, the region between 2900 and 4200 cm^{-1} was investigated
128 collecting 200 spectra with the Renishaw inVia Reflex confocal Raman microscope at 100x of
129 magnification.

130 Determination of the position of the peaks was performed through the Gaussian - Lorentzian
131 (Pseudo Voigt) deconvolution method, with an accuracy of 0.2 cm^{-1} , using the software *Labspec 5*,
132 utilized also for baseline subtraction that helped to eliminate the occasional fluorescence of
133 carbonates. Fluorescence and Raman scattering have similar origins, as both involve the inelastic
134 scattering of photons. Practically, fluorescence represents a strong background noise that can
135 obliterate the Raman signal. To avoid this phenomenon, chalk cores were not analysed directly on
136 the rock surface but as very small amounts of powder that were scraped off with a needle from the
137 rock, placed and spread on a glass slide. As the quantity required is almost negligible, and no specific
138 preparation is needed to perform these analyses, Raman procedure allows for further investigation
139 with other instrumentation if needed.

140 2.5. Raman spectroscopy on carbonates

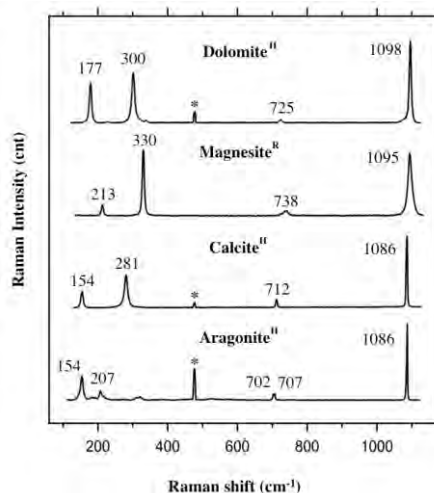
141 For their large diffusion and good Raman signal, carbonates have been investigated in detail,
142 with particular attention to thermodynamic properties and their vibrational spectra (23, 25, 44-49).
143 Their Raman peaks positions are influenced by the magnesium content and crystallographic structure
144 and allow in distinguishing calcite from Mg-calcite, aragonite, magnesite, huntite, and dolomite [32,
145 45, 49-52]. Carbonate minerals show comparable spectra as their structure is quite similar; a consistent
146 increase in Raman shifts according to their Mg content occurs between calcite and magnesite, as a
147 consequence of increased inter-atomic distances following the substitution of Ca^{2+} with the smaller
148 Mg^{2+} ion in the cell [23, 45, 53]. This shift assists in distinguishing between the different carbonates.

149 Carbonate group minerals spectra (see Fig. 2) present four main peaks which can be divided into
150 internal vibrations of the $(\text{CO}_3)^{2-}$ group (symmetric stretching, 600 – 1200 cm^{-1} , and asymmetric
151 stretching, 1200 – 1700 cm^{-1}) [38, 45, 52, 54-56] and into lattice vibrations involving translation and
152 librations of the $(\text{CO}_3)^{2-}$ group relative to the Ca^{2+} or Mg^{2+} ions (100 – 500 cm^{-1}). The strongest and
153 sharpest peak (ν_1 , *symmetric stretching mode* of the carbonate ion) is present around 1086 – 1095 cm^{-1}
154 (calcite – magnesite respectively) along with other subsidiary bands at 150 – 215 cm^{-1} (T, *translational*
155 *mode*), 280 – 330 cm^{-1} (L, *librational mode*), and 712 – 738 cm^{-1} (ν_4 , *in-plane bending* of the $(\text{CO}_3)^{2-}$ group)
156 [45, 57, 58].

157 2.6. Earlier studies and characterisation of the sample material

158 Various high-resolution methods were used to study mineralogical alteration in flooded chalk:
159 field emission gun scanning electron microscopy– energy-dispersive X-ray spectroscopy (FEG-SEM-
160 EDS) [3, 5, 8, 14, 36, 38, 59], nano secondary ion mass spectrometry (NanoSIMS) [36, 50, 60], x-ray
161 diffraction (XRD) [36], whole-rock geochemistry techniques [36, 37, 60], Tip-Enhanced Raman
162 Spectroscopy-Atomic Force Microscopy (TERS-AFM) [61, 62], Transmission Electron Microscopy
163 (TEM) [59, 63], Mineral Liberation Analysis (MLA) [59]. The authors (LTT [36], and ULTT [43])
164 determined a loss of Ca^{2+} and a gain in Mg^{2+} , demonstrating a precipitation of new Mg-minerals in
165 the core. FEG-SEM and TEM images have shown magnesite crystals with a grain size between 100
166 nm and 1 μm [59, 63].

167 Based on geochemical methods, Zimmermann et al. (2015) [36] could calculate that 20 % of the
168 mass of the core had been dissolved during a 1.5 years long experiment. The core experienced axial
169 shortening of 18 % (in length) and a porosity reduction of 20%.



170

171

Figure 2. Raman spectra of calcium and magnesium carbonates: dolomite (UNIMIB standard sample, Selvino, Italy); magnesite (M.A.C. certificated standard); calcite (UNIMIB standard sample, Chihuahua, Mexico, ~0 mol% MgCO₃), aragonite (UNIMIB – University of Milano Bicocca – standard sample, Val Formazza, Italy). Spectra with 'R' were analysed by the Renishaw inVia confocal Raman microscope and spectra with 'H' by Horiba Xplora. Stars represent the neon lamp emission line at 476.8 cm⁻¹ used for calibration with the Horiba XploRA spectrometer. Peak positions are reported without decimals. After Borromeo et al. 2017a [49].

175

176

177

178

179

180

181

182

183

184

185

186

187

188

189

190

191

192

193

194

195

196

197

198

199

200

201

202

203

In the Long Term Test (LTT), using x-ray diffraction (XRD) [36], could detect the presence of magnesite, chrysotile (slice 1-3), tillieyte (only in slice 4), quartz, anthophyllite as well as gypsum (the latter only in the unflooded chalk). Following a geochemical model [14], talc should precipitate, but this mineral could not be detected by XRD or other mineralogical analyses. Furthermore, magnesite could only be detected when it was rather abundant, and showed the limits of XRD as a detection method for traces of minerals. NanoSIMS 50 was the only analytical method that could detect positively with an image proof magnesite and very tiny new grown quartz of micron- and sub-micron sizes [36]. When analysed by MLA, the shorter of the two tests, LTT, displayed a rather sharp (~1.5 mm) transition between two areas with different mineralogy [59]. Closest to the inlet of the core, the rock material is completely altered into magnesite with minor contents of calcium along with clay minerals. In the area furthest away from the inlet, the mineralogy is still dominated by calcite, with occurrences of magnesite and clay, indicating only partial dissolution of calcite and precipitation of magnesite opposed to the complete substitution at the inlet. In the ULTT, the whole core showed similar composition, magnesite with the mentioned calcium impurities and clay.

Nermoen et al. (2015) [43] describes the flooding experiment of the 3-years-test (ULTT) in detail and a porosity decrease from 41.32 % to 40.02 % was observed at the end of the experiment, documenting how dissolution and precipitation of the solid volume may significantly alter the porosity evolution during compaction. The solid density increased from 2.68 to 2.90 g/cm³ throughout the experiment, simultaneously the core has lost 22.93 g, which exemplifies that solid volume changes occur during flooding of MgCl₂ brines.

Common for the two tests is that compaction alone cannot explain the changes in permeability and porosity over time. For the ULTT [43] the permeability and calculated porosity are lowered during the start of the experiment where compaction is the controlling mechanism, while throughout the experiment, the permeability and porosity starts to increase again. This is believed to be caused by processes that involve mineralogical transformation through dissolution of primary and precipitation of secondary minerals. These changes in mineralogy is therefore an important factor to

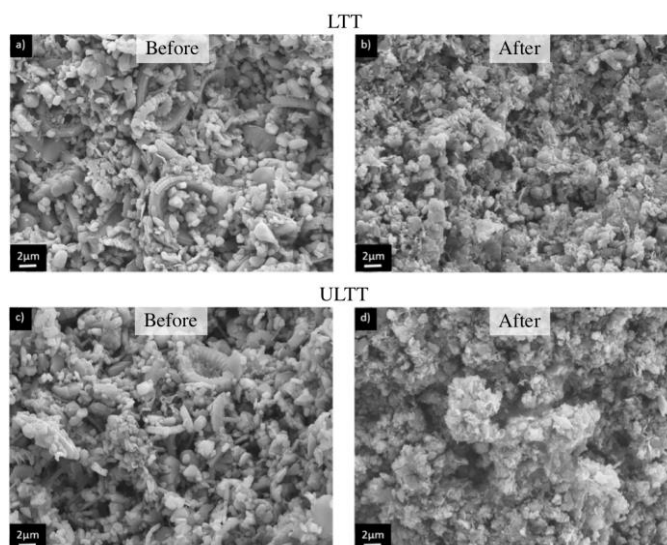
204 both qualify and quantify to understand geomechanical alteration, as also seen in Wang et al. (2016)
205 [37].

206 3. Results

207 3.1. FEG-SEM-EDS

208 The composition of the two cores after flooding has been affected by the nature of the fluid flow
209 paths. This is often only visible at microscale, has a specific geometric form and is composed of
210 several compositional trends [59] and therefore awaits a detailed study and is not of relevance here.
211 Hence, a quick and thorough investigation of the mineralogical composition prior to detailed FEG-
212 SEM-EDS studies or further meticulous electron- and ion-beam-based analyses would be helpful.

213 When studied by FEG-SEM-EDS, both the texture and the chemical composition of the chalk is
214 significantly altered compared to the unflooded material (Fig. 3). The newly precipitated crystals are
215 found in massive parts of the core (inlet part), with a homogenous high-magnesium carbonate
216 composition as well as single crystals within the calcite dominated areas. The grains are no longer
217 rounded, but show a rhombic crystal shape, with grain-size mostly below 1 μm . In the completely
218 altered areas, coccoliths and other micro/nano-fossils are no longer observed, while in parts where
219 the calcite is still present, clear signs of dissolution is visible [36, 59]. Additionally, significant
220 amounts of clay-minerals are present, with main constituents being Mg and Si, which could be
221 interpreted to be talc.



222
223 **Figure 3.** (a) SEM-micrograph of unflooded chalk from the end-piece of the LTT-core (from
224 Zimmermann et al. 2015; [36]). Main components are coccoliths and fragments with a calcitic
225 composition. (b) SEM-micrograph of the severely altered part of the flooded core (LTT) towards the
226 inlet of the core (from Zimmermann et al. 2015 [36]). Coccoliths and other fossils are no longer visible,
227 only crystals mainly below 1 μm in size, with high magnesium content. (c) SEM-micrograph of
228 unflooded chalk of the ULTT with main components as observed in (a). (d) SEM-micrograph from
229 slice 5 of the ULTT after flooding with MgCl_2 . Texture and composition is as observed in (b).

230 3.2. Raman Spectroscopy

231 3.2.1. Generals

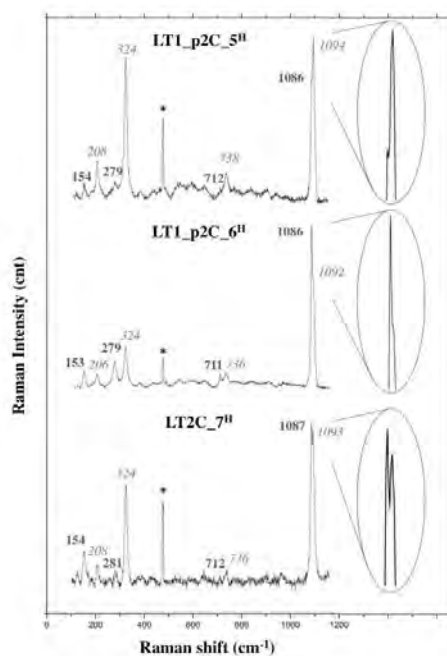
232 Raman spectroscopy has proven to be easy to use, but it requires an experienced operator to
 233 decide the setting of the instrument and how to interpret the spectra (see below). The mineralogical
 234 changes due to fluid injection were quickly evaluated: in few tens of seconds it was possible to
 235 distinguish the carbonate minerals present in the chalk (see Table 1). 647 spectra were collected, of
 236 which only 5 could not be identified, as they were not present in databases or literature. In LTT core
 237 557 low region spectra were collected, 226 in slice 1 (120 in fragment 1, LT1_p1; 106 in fragment 2,
 238 LT1_p2), 220 in slice 2 (LT2), and 111 in slice 4 (LT4). In ULTT 90 spectra were collected in 9 different
 239 areas of the core.

240 In both ULTT and LTT cores no dolomite, aragonite, huntite, or high magnesium-calcite (45, 49)
 241 could be detected. As calcite Raman peaks positions reflect the magnesium content present in its
 242 lattice [49], it is possible to determine that the calcites present in ULTT and LTT always contain a low
 243 magnesium content (0 – 10 mol % \approx 4 w.%; [49]) in the mineral.

244 **Table 1.** Mineral composition of the two cores: amounts and percentages of Raman spectra collected for
 245 each mineral in the Long Term Test (LTT) and in the Ultra Long Term Test (ULTT). When a two
 246 minerals spectrum was found, both components were counted to obtain the calcite/magnesite
 247 percentages.

	CALCITE		MAGNESITE		UNKNOWN		OTHER	
	spectra	%	spectra	%	spectra	%	spectra	%
LT1_p1A	20	77%	6	23%				
LT1_p1B	3	13%	20	87%				
LT1_p1C	20	87%	3	13%				
LT1_p1D	10	31%	20	63%	2	6%		
LT1_p1E	7	26%	20	74%				
LT1_p1F	18	60%	12	40%				
LT1_p1G	0	0%	22	96%			1 Brookite	4%
LT1_p1H	0	0%	25	100%				
LT1_p1I	0	0%	25	100%				
LT1_p2A	18	82%	4	18%				
LT1_p2B	2	10%	18	90%				
LT1_p2C	13	39%	20	61%				
LT1_p2D	16	53%	14	47%				
LT1_p2E	4	82%	16	18%				
LT2_A	71	92%	6	8%				
LT2_B	49	86%	7	12%	1	2%		
LT2_C	48	61%	31	39%				
LT2_D	30	41%	43	58%			1 Rutile	1%
LT4_A	19	79%	5	21%				
LT4_B	18	69%	6	23%	2	8%		
LT4_C	20	100%	0	0%				
LT4_D	20	100%	0	0%				
ULT1_1	3	23%	10	77%				
ULT2_4	1	9%	10	91%				
ULT2_5	0	0%	10	100%				
ULT2_5B	3	23%	10	77%				
ULT2_6	1	9%	10	91%				
ULT2_7	2	17%	10	83%				
ULT2_8	1	9%	10	91%				
ULT1_9	0	0%	9	100%				
ULT1_10	3	8%	10	92%				

249 An important issue regarding the results presented in this study (Table 1) that are shown as a
 250 percentage mineral/total is that we need to consider these % not as weight % or volume %, as the data
 251 express the presence of the signal of a mineral compared to the total of the collected spectra. When
 252 vibrational modes of both calcite and magnesite were detected simultaneously in one spectrum, both
 253 minerals were counted. In fact, occasionally, peaks of both calcite and magnesite were present in the
 254 same spectrum: this can happen when the analyses are performed on overlapped or very closely
 255 spaced fine grains (dimension of 1-2 μm), when the laser beams both grains at the same time and the
 256 laser diameter is too large. In this case, the detector collects photons scattered from the two minerals,
 257 resulting in a spectrum that is the mathematical sum of the two spectra of the two minerals (see Fig.
 258 4). Consequently, the strong and sharp ν_1 peak (*symmetric stretching mode* of the carbonate ion) of both
 259 calcite and magnesite is present in one spectrum, respectively around 1086 and around 1095 cm^{-1} (25,
 260 45, 46, 49) depending on the intensity, sharpness, and nearness of these two peaks, shoulders
 261 (asymmetric peaks) or double peaks (peaks with two edges) can be present (examples in Fig. 4).
 262 However, of importance is the fact that this can be detected. Another clear result of the simultaneous
 263 presence of calcite and magnesite signals in the same spectrum is given by the occurrence of the L
 264 (*librational mode*) peaks of the two carbonates at 280 and 330 cm^{-1} respectively. When a two minerals
 265 spectrum was found, both components were counted to obtain the calcite/magnesite percentages for
 266 each slice (see Table 1). It is important to point out that, as Raman spectroscopy can differentiate
 267 between the carbonate species, the spectrum collected in cases as the one described above (a
 268 magnesite and a calcite beamed at the same time, resulting in a combined spectrum) would be
 269 different from high Mg-calcite [49] or a dolomite spectrum (compare spectra shown in Fig. 2 and the
 270 ones presented in Fig. 4).

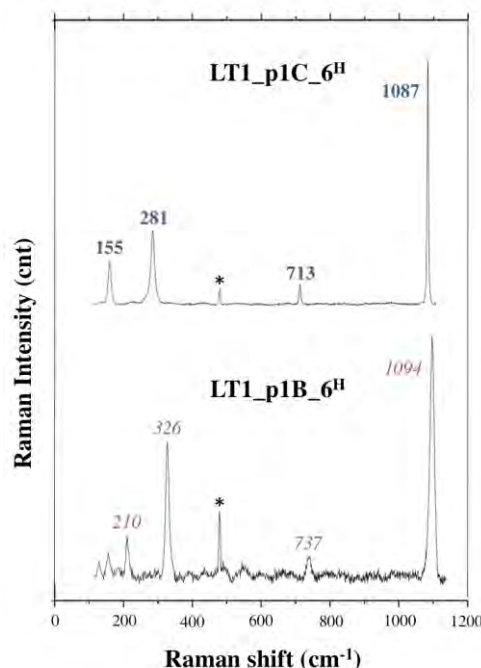


271
 272 **Figure 4.** Raman spectra showing magnesite and calcite peaks in the same spectrum. This will happen
 273 when grains of 1-2 μm in size and different mineralogy are overlapped or placed very close: the laser
 274 beams both grains at the same time and as a consequence, the instrumentation detects the vibrational
 275 modes of both minerals. In LT1_p2C_5 the signal from magnesite is stronger than the calcite one, in
 276 LT1_p2C_6 it is weaker. The main peaks (ν_1 , *symmetric stretching mode* of the carbonate ion) of the two

277 minerals are very close, generating a high peak with a “shoulder”. In the third example shown,
 278 LT2C_7, the ν_1 of the two grains is so sharp and strong that a double peak is present. Calcite peaks
 279 are reported in blue/**bold**, magnesite peaks in red/*italic*. All the spectra were collected with the Horiba
 280 XploRA spectrometer, stars represent the neon lamp emission line at 476.8 cm^{-1} used for calibration.
 281 Peak positions are reported without decimals.

282 In order to detect the occurrence of hydrated silicates, the presence of diagnostic vibrational
 283 modes in the high frequencies region ($2900\text{--}4200 \text{ cm}^{-1}$) of the Raman spectra was used, where the
 284 (OH)- vibrational modes are located [25, 64, 65]. The signal of phyllosilicates is quite weak and, in the
 285 $0\text{--}1200 \text{ cm}^{-1}$ region, it is easily covered by the calcite and magnesite stronger intensity. As these two
 286 carbonates are anhydrous, they do not show peaks in the high region of the spectra. More than 200
 287 high region spectra were collected in slice one, LT1_p2_B where an intense recrystallization of
 288 magnesite was already registered by Raman spectroscopy. The platy and very thin habit of
 289 phyllosilicates and clay minerals makes them really challenging to be detected, as it is very difficult
 290 to focus the laser inside their crystals and distinguish their weak scattering. Also, camera resolution
 291 and laser wavelength limit the analysis, and can lower the capability of focusing on the sample
 292 surface (under $1\text{--}2 \mu\text{m}$ in size).

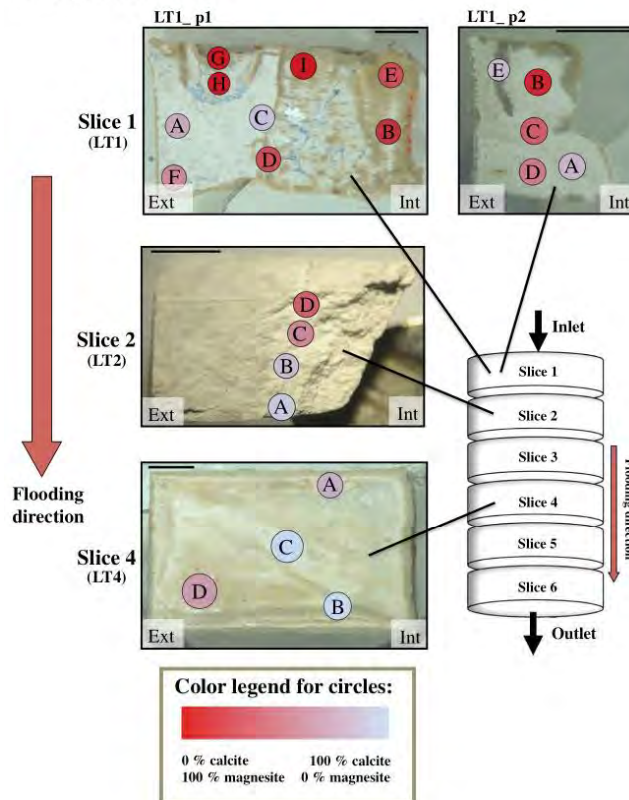
293 3.2.2. Long Term Test



294
 295 **Figure 5.** Raman spectra collected on the first slice of the Long Term Test. Raman showing the
 296 occurrence of the original calcite (LT1_p1C_6) and the presence of recrystallized magnesite
 297 (LT1_p1B_6). Calcite peaks are reported in blue/**bold**, magnesite peaks in red/*bold*. All the spectra
 298 were collected with the Horiba XploRA spectrometer, stars represent the neon lamp emission line at
 299 476.8 cm^{-1} used for calibration with the Horiba XploRA spectrometer. Peak positions are reported
 300 without decimals.

301 Raman spectroscopy could identify the presence of recrystallized magnesite along the core of the
 302 Long Term Test up to 4 cm from the injection surface (see Figs. 5 and 6), which is also supported
 303 by Zimmermann et al. (2015) [36]. As predictable, the average alteration of the core is more pervasive
 304 close to the inlet surface, showing a decreasing amount of newly grown minerals with flooding
 305 direction (60 % of magnesite in slice 1-LT1; 30 % in in slice 2-LT2; and 10 % in slice 4-LT4; see Table 1
 306 and Fig. 6). In Zimmermann et al. (2015) [36] positive XRD proof for magnesite could not be given in
 307 slice 4, but, however, geochemical data highlighted c. 3.9 % of MgO present in this slice, in
 308 comparison to 0.3 % of MgO in the unflooded material. In this study, only two non-carbonate crystals
 309 out of 647 Raman spectra were detected in LTT: brookite in LT1_p1_G and rutile in LT2_D (see Table
 310 1 and Fig. 7).

Long Term Test



311
 312 **Figure 6.** Mineralogical composition of the LTT core: 10 to 70 spectra have been collected in each of
 313 the area shown (9 areas in LT1_p1, 4 in LT1_p2, 4 in LT2, and 4 in LT4). Colour legend reflects the
 314 percentage of calcite and magnesite spectra collected in each area of the sample. See Table 1 for calcite
 315 and magnesite amounts and percentages obtained for each area. Flooding direction is indicated. Inner
 316 (core) end external (rim) parts of the samples are marked. The scales represent 0.25 cm. A schematic
 317 drawing (modified from Zimmermann et al. 2015 [36]) of how the cores were cut after the flooding
 318 experiment is shown to the right.

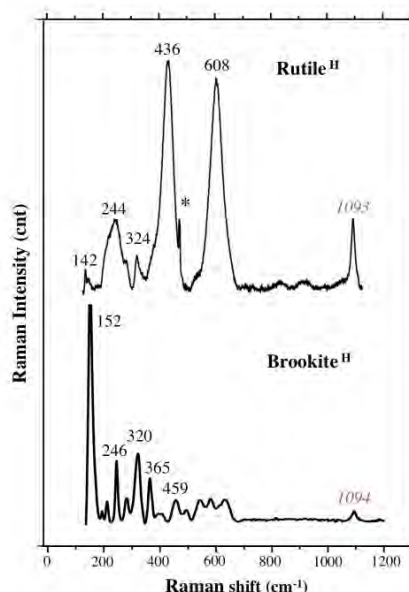
125

319 Two pieces of Slice 1 (LT1_p1 and LT1_p2, LTT; see Fig. 6) were analysed, with a total of 14
 320 areas, and 226 Raman spectra (Table 1; Figs. 5 and 6).

321 In fragment 1 (LT1_p1) an intense magnesite regrowth is present in the inner portion of the core
 322 (LT1_p1 E and B 74, and 87 %, respectively, see Table 1 and Fig. 6), which becomes less pervasive
 323 close to the external rims (LT1_p1 A, F: 23, 40 %, respectively). In LT1_p1 a brown/ocre flow semi-
 324 circular structure is present and clearly visible to naked eye in the external part of the core; here a
 325 complete recrystallization to magnesite is present, reaching 100 % (LT1_p1 G and H, see Fig. 6).
 326 However, in this region, also a crystal of brookite (TiO₂) was detected (see Table 1 and Fig. 7). The
 327 average recrystallization of LT1_p2 is 47 %, and another textural element has been observed, a grey
 328 vein of calcite (CaCO₃ 82 %, LT1_p2 E, see Fig. 6). In order to try to detect hydrated minerals in
 329 LT1_p2, 210 high region spectra were collected. Unfortunately, no signal of clay minerals or talc was
 330 registered in any of them.

331 In Slice 2 (LT2; LTT) a longitudinal gradient in Mg content is perfectly detectable along flooding
 332 direction with a major magnesite recrystallization in the nearest areas to the inlet surface (from 58 (in
 333 LT2_D) to 8 (in LT2_A) %, see Table 1 and Fig. 6). Four areas were investigated in slice 2, with a total
 334 amount of 220 Raman spectra. A rutile spectrum was collected in LT2_D (see Table 1 and Fig. 7).

335 In Slice 4 (LT4; LTT) the recrystallization is less pervasive in the core than in the others (LT1 and
 336 LT2, LTT), as is the furthest from the inlet surface (Table 1; Fig. 6). A diagonal deep and pale grey
 337 structure crosses the LT4 slice (see Fig. 6) with a pure calcitic composition (111 spectra, 100 % of
 338 CaCO₃ no magnesite spectra were detected in this area). Some MgCO₃ spectra have been collected in
 339 a brownish area near the rim of the core (23 % of magnesite).

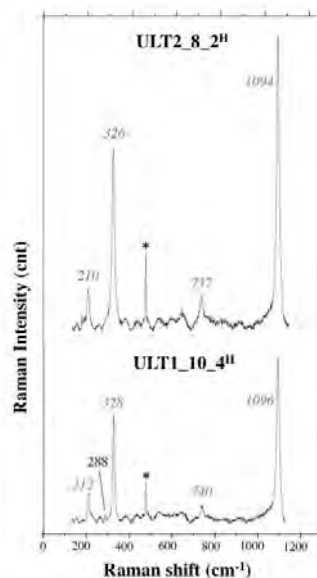


340
 341 **Figure 7.** A brookite spectrum (identified in LT1_p1G) and one for rutile as identified in LT2_D (see
 342 Table 1). The main peak of magnesite (labelled in red) is present in both of them at 1093 and 1094 cm⁻¹,
 343 since the two minerals are surrounded by carbonates, which have a strong signal. Both spectra were
 344 collected with the Horiba Xplora spectrometer, the star represents the neon lamp emission line at
 345 476.8 cm⁻¹ used for calibration. Peak positions are reported without decimals.

346 3.2.3. Ultra Long Term Test

126

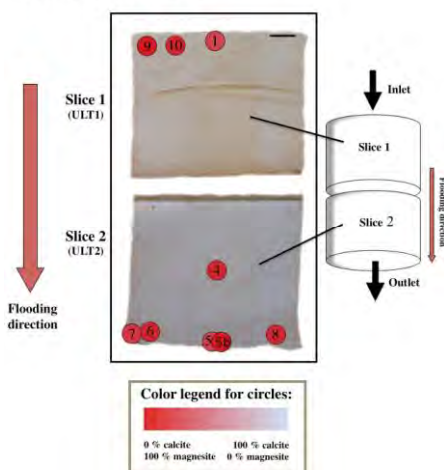
347 The Ultra Long Term Test presents a widespread recrystallization of magnesite (MgCO₃) in the
 348 range of 77-100 % (see Table 1 and Figs. 8 and 9) along the entire core, and no alteration front was
 349 detectable anymore with Raman spectroscopy [43, 66].



350
351
352
353
354
355
356

Figure 8. Raman spectra collected on the Ultra Long Term Test Raman showing the presence of recrystallized magnesite. The spectrum at the bottom of the figure (ULTT_10_4) shows the presence of a peak of calcite at 288 cm⁻¹ (*L*, librational mode). Calcite peaks are reported in blue/bold, magnesite peaks in red/italic. Both spectra were collected with the Horiba XploRA spectrometer, stars represent the neon lamp emission line at 476.8 cm⁻¹ used for calibration with the Horiba XploRA spectrometer. Peak positions are reported without decimals.

Ultra Long Term Test



357
358
359
360
361
362

Figure 9. Mineralogical composition of the ULTT core: 10 spectra have been collected in each of the 9 areas shown. Colour legend reflects the percentage of calcite and magnesite spectra collected in each area of the sample. See Table 1 for calcite and magnesite amounts and percentages obtained for each area. Flooding direction is indicated. The scale represents 0.5 cm. A schematic drawing of how the cores were cut after the flooding experiment is shown to the right.

363 Raman spectra were collected in 9 different areas situated along the 7 cm core (90 spectra in total,
364 see Table 1 and Fig. 9). No structures or patterns are visible to the naked eye and the core seems to
365 be quite mineralogically homogeneous. Another study [60] made using ICP-MS (induced coupled
366 plasma mass spectrometry) confirmed our data as average of 4 % of CaO was detected on the bulk
367 sample, with no great difference in composition in the different portions of the sample.

368 4. Discussion

369 This study represents the first attempt to apply Raman spectroscopy to chalk mineralogy with a
370 single grain approach on micron scale. The very fine-grained and soft texture of this sedimentary
371 rock made detailed analysis quite challenging with common methods, and for this reason in the last
372 years several high performing techniques have been included in Enhanced Oil Recovery (EOR)
373 research. Raman spectroscopy, thanks to its quickness, low cost, and micrometric resolution, turned
374 out to be very suitable for these studies as, in few seconds and without any sample preparation, a
375 mineralogical identification can be provided. It is perfectly complementary to methods such as SEM-
376 EDS.

377 The major alteration front in LTT was previously suggested between LT3 and LT4 [36], however
378 by the use of Raman spectroscopy, it was possible to detect magnesite even in slice 4 (Table 1; Fig. 6),
379 when XRD studies could not be positive in this regard [36]. The calcite dissolution and magnesite
380 recrystallization were massive in the first 2 cm of the core (slice 1 and 2 of LTT; Fig. 6). LTT5 and
381 LTT6 were not studied in this investigation as in a previous study [36], these slices were found to be
382 the least altered slices by the flooding unable to provide further information when applying the used
383 methods. Raman spectroscopy confirmed that such an alteration front was no longer present within
384 the ULTT, which means that in three years of MgCl₂ injection, a sufficient quantity of Mg²⁺ was
385 flooded into the core [43], permitting the substitution of almost all the Ca²⁺ to take place (92 % of
386 magnesite Raman spectra; see Table 1 and Fig. 9).

387 As already seen with other techniques (SEM, XRD) applied in a previous study [36] it was not
388 possible to identify clay-minerals in the two cores using Raman spectroscopy. It is very difficult to
389 find a technique that could provide a resolution high enough to spot <1 μm crystals and
390 simultaneously have the capability to cover a portion of the sample wide enough to detect a ≤ 5 %
391 component, in a quick way, and image it at the same time. A principle technique would be a Mineral
392 Liberation Analyser (MLA) with a nanometre-small spot size, which is still technically challenging
393 using electron-beams on such small scales, or a Nano-scale Secondary Ion Mass Spectrometer (nano-
394 SIMS) [36] or nanoRaman (TERS, Tip Enhanced Raman Spectroscopy) [61,62], application coupled
395 with an Atomic Force Microscope (AFM). In the LTT sample nano-crystals of quartz has been
396 detected only by nano-SIMS [36], which is a very time-consuming and destructive methodology,
397 extraordinarily expensive and not quantitative. Another technique would be TEM-EDS
398 (Transmission Electron Microscopy) with the same critique points besides that the latter reveals
399 quantitative data along with mineral-identification through diffraction analysis [63]. Raman
400 spectroscopy could be the tool to use but with the known limits of 1-2 micron spotsizes and the
401 impossibility to image the analysed area with an optical microscope. An advance would be to scan
402 an area, which is still a technical issue. A very low abundance of a mineral may be challenging to
403 detect unless collecting a really huge number of spectra, which in turn would be time consuming.
404 Furthermore, the identification of small and thin hydrated minerals is quite difficult to achieve in the
405 0-1200 cm⁻¹ region of the Raman spectra, since their signal is weak and easily covered by the higher
406 carbonate peaks. For this reason, we tried to detect them with a different setting of the
407 instrumentation, moving the analyses to the high region of the Raman spectra, around 3500 cm⁻¹,
408 where the OH⁻ vibrational modes are present. Anhydrous minerals such as calcite and magnesite do
409 not show peaks in this region. Unfortunately, no signal from phyllosilicates has been detected,
410 possibly as a consequence of these technical difficulties.

411 Despite the impossibility to recognise so low-concentrated and platy minerals, since the set-up
412 is relatively economical and rapid the authors think that Raman spectroscopy represents a very
413 helpful methodology that could and should be used on hydrocarbon drilling rigs, possibly even as a

414 drilling steering tool, because carefully investigations could show that positive and useful results
415 were generated. This can lead to well-developed methodologies in the future for different
416 approaches, like the petroleum industry.

417 5. Conclusions

418 The mineralogical and textural changes that follow dissolution, precipitation and compaction in
419 brine-injected chalk affect the permeability, porosity, reservoir potential, and the oil flow pathways
420 (e.g. 8, 21, 36, 59). For this reason, a deep investigation of secondary mineral recrystallization is of
421 paramount importance in EOR research.

422 This study demonstrates that Raman spectroscopy is a robust, cheap, user-friendly point-
423 analysis technique that with a non-destructive sample preparation allows to quickly obtain semi-
424 quantitative mineralogical and chemical information. This method has been applied to micron-sized
425 chalk samples, giving an advantage in comparison to time consuming methods like SEM, thin section
426 studies, nano-Raman or EMPA, and ion-probe analysis. An estimation of the magnesite
427 recrystallization could be performed on two chalk cores that were flooded under reservoir conditions
428 with MgCl₂: Long Term Test (1.5-years-test, LTT) and Ultra Long Term Test (3-years-test, ULTT). In
429 the LTT the average recrystallization is more pervasive close to the inlet surface and varies with
430 flooding direction from c. 60 % (slice 1) to c. 10 % (slice 4). ULTT is, on the other hand, quite
431 homogeneous, as the alteration front is no longer visible and the whole core is predominantly
432 consisting of magnesite (92 %).

433 However, not all reservoir rocks do contain minerals and/or phases as small as those in chalk,
434 which would make the here shown methodology very attractive. Raman spectroscopy can, together
435 with other research methods, provide a full range of information on flooded chalk cores for a broader
436 understanding of chemical and mineralogical changes in those samples during the mentioned EOR
437 experiments.

438 Until today Raman spectroscopy has been only occasionally applied in the oil industry [67- 70]
439 and it is time for it to become a routine analysis.

440 **Acknowledgments:** The authors acknowledge the Research Council of Norway and the
441 industry partners; ConocoPhillips Skandinavia AS, Aker BP ASA, Eni Norge AS, Maersk Oil Norway AS, Statoil
442 Petroleum AS, ENGIE E&P NORGE AS, Lundin Norway AS, Halliburton AS, Schlumberger Norge AS,
443 Wintershall Norge AS, DEA Norge AS of The National IOR Centre of Norway for support.

444 This study is a central part of the PhD thesis of LB who thanks the NIOR Centre of Norway for a grant to carry
445 out the research, Eduardo Garzanti and the group of Provenance Studies (University of Milano – Bicocca) for
446 their advices.

447 **Author Contributions:** L.B. made a substantial contribution to every step of the study, such as acquisition (with
448 the fundamental help of N.E.) and interpretation of the data and writing of the paper. U.Z., L.B, MW.M. and S.A.
449 contributed to design and conception of the present publication. M.V.M. and R.I.K. designed and performed the
450 long-term tests on the chalk cores. All the co-authors performed a critical revision of the intellectual content of
451 the paper.

452 **Conflicts of Interest:** The authors declare no conflict of interest. The founding sponsors had no role in the design
453 of the study; in the collection, analyses, or interpretation of data; in the writing of the manuscript, and in the
454 decision to publish the results.

455 References

- 456 1. Hermansen, H; Landa, G. H.; Sylte, J. E.; Thomas, L. K. Experiences after 10 years of waterflooding the
457 Ekofisk Field, Norway. *J. Pet. Sci. Eng.* **2000**, *26*,1, 11-18.
- 458 2. Nagel, N. B. Compaction and subsidence issues within the petroleum industry: from Wilmington to Ekofisk
459 and beyond. *Phys. Chem. Earth A.* **2001**, *26*, 3-14.
- 460 3. Risnes, R.; Madland M. V.; Hole M.; Kwabiah N. K. Water weakening of chalk – Mechanical effects of water-
461 glycol mixtures, *J. Pet. Sci. Eng.* **2005**, *48*, 21-36.

- 462 4. Heggheim, T.; Madland, M. V.; Risnes, R.; Austad, T. A chemical induced enhanced weakening of chalk by
463 seawater. *J. Pet. Sci. Eng.* **2005**, *46*(3), 171-184.
- 464 5. Korsnes, R. I.; Strand S.; Hoff Ø.; Pedersen T.; Madland M. V.; Austad T. Does the chemical interaction
465 between seawater and chalk affect the mechanical properties of chalk? In *Multiphysics coupling and long term*
466 *behaviour in rock mechanics*; Cotthem; A. V.; Charlier R.; Thimus J. F. and Tshibangu J. P. Eds.; Taylor &
467 Francis: London, England, **2006**; pp. 427-434.
- 468 6. Korsnes, R. I.; Madland, M. V.; Austad, T.; Haver, S.; Rosland, G. The effects of temperature on the water
469 weakening of chalk by seawater. *J. Pet. Sci. Eng.* **2008a**, *60*, 183- 193.
- 470 7. Madland, M. V.; Midtgarden, K.; Manafov, R.; Korsnes, R. I.; Kristiansen, T.; Hiorth, A. The Effect of
471 Temperature and Brine Composition on the Mechanical Strength of Kansas Chalk. *International Symposium*
472 *of the Society of Core Analysts*, Abu Dhabi, **2008**, 6.
- 473 8. Madland, M.V.; Hiorth, A.; Omdal E.; Megawati M.; Hildebrand-Habel T.; Korsnes I. R.; Evje S.; Cathles M.
474 L. Chemical alterations induced by rock-fluid interactions when injecting brines in high porosity chalks,
475 *Transp. Porous Med.* **2011**, *87*, 679-702.
- 476 9. Zangiabadi, B.; Korsnes, R. I.; Hildebrand-Habel, T.; Hiorth, A.; Surtarjana, I. K.; Lian, A.; Madland, M. V.
477 Chemical water weakening of various outcrop chalks at elevated temperature. In *Poromechanics IV*, Ling H.
478 I., Smyth A., and Betti, R., Eds. DEStech Publications, Inc., Lancaster, England, **2009**; pp. 543-548.
- 479 10. Andreassen, K.A. and Fabricius, I. L. Biot critical frequency applied to description of failure and yield of
480 highly porous chalk with different pore fluids, *Geophysics*, **2010**, *75*(6), E205-E213.
- 481 11. Zhang, P.; Tveheyo, M.T.; Austad T.; Wettability alteration and improved oil recovery by spontaneous
482 imbibition of seawater into chalk: impact of the potential determining ions Ca²⁺, Mg²⁺, and SO₄²⁻, *Colloids*
483 *Surf. A Physicochem. Eng. Aspects*, **2007**, *301*, 199–208.
- 484 12. Strand, S.; Hjulær, M. L.; Torsvik, R.; Pedersen, J. I.; Madland, M. V.; Austad, T. Wettability of chalk: impact
485 of silica, clay content and mechanical properties. *Petroleum Geoscience*, **2007**, *13*(1), 69-80.
- 486 13. Austad, T.; Strand, S.; Madland, M.V.; Puntervold, T.; Korsnes, R.I. Seawater in chalk: An EOR and
487 compaction fluid, *SPE Reservoir Evaluation and Engineering*, **2008**, *11*(4), 648-654.
- 488 14. Hiorth, A.; Cathles, L.; Madland, M. The Impact of Pore Water Chemistry on Carbonate Surface Charge
489 and Oil Wettability, *Transp. Porous Med.* **2010**, *85*(1), 1–21.
- 490 15. Fathi, S.J.; Austad, T.; Strand, S. "Smart Water" as a Wettability Modifier in Chalk: The Effect of Salinity
491 and Ionic Composition, *Energy & fuels*, **2010**, *24*, 2514-2519.
- 492 16. Ali, A.Y., Salah Hamad, A.S., Abdulaziz, A.K.; Mohammed Saleh, A.J., Laboratory Investigation of the
493 Impact of Injection Water Salinity and Ionic Content on Oil Recovery From Carbonate Reservoirs, *SPE*
494 *Reservoir Evaluation & Engineering*, **2011**.
- 495 17. Megawati, M.; Hiorth, A.; Madland, M. V. The impact of surface charge on the mechanical behavior of
496 high-porosity chalk. *Rock Mech. Rock Eng.* **2013**, *46.5*, 1073-1090.
- 497 18. Zhang, P.; Tveheyo, M. T.; Austad, T. Wettability Alteration and Improved Oil Recovery in Chalk: The
498 Effect of Calcium in the Presence of Sulfate. *Energy & Fuels*, **2006**, *20*(5), 2056-2062.
- 499 19. Andersen, P.Ø., Evje, S., Madland, M.V.; Hiorth, A., A geochemical model for interpretation of chalk core
500 flooding experiments, *Chem. Eng. Sci.* **2012**, *84*, 218-241.
- 501 20. Megawati, M.; Madland, M. V.; Hiorth, A. Mechanical and physical behavior of high-porosity chalks
502 exposed to chemical perturbation: *J. Pet. Sci. Eng.* **2015**, *133*, 313-327.
- 503 21. Wang, W.; Madland, M. V.; Zimmermann, U.; Nermoen, A.; Reidar, I.; Korsnes, R.; Bertolino, S. R. A.;
504 Hildebrand-Habel, T. Evaluation of porosity change during chemo-mechanical compaction in flooding
505 experiments on Liege outcrop chalk. In *Reservoir Quality of Clastic and Carbonate Rocks: Analysis, Modelling*
506 *and Prediction*. Armitage, P. J.; Butcher, A. R.; Churchill, J. M.; Csoma, A. E.; Hollis, C.; Lander, R. H.; Omma,
507 J. E. & Worden, R. H. Eds.; Geological Society: London, England, **2016**, Special Publications, 435.
- 508 22. Raman, C.V. A new radiation. *Indian J. Phys.* **1928**, *2*, 387–398.
- 509 23. Krishnamurti, D. Raman spectrum of magnesite. *Proceedings of the Indian Academy of Sciences – Section A*
510 **1956**, *43*, 210.
- 511 24. Griffith, W.P., Raman spectroscopy of minerals. *Nature* **1969**, *224*, 264–266.
- 512 25. Kuebler, K.; Wang A.; Abbott, K.; Haskin, L. A. Can we detect carbonate and sulfate minerals on the surface
513 of Mars by Raman spectroscopy? *Lunar and Planetary Science XXXII* **2001**, n. 1889.

- 514 26. Downs, R. T. "The RRUFF Project: an integrated study of the chemistry, crystallography, Raman and
515 infrared spectroscopy of minerals." In *Program and Abstracts of the 19th General Meeting of the International*
516 *Mineralogical Association in Kobe, Japan, 2006*. 2006.
- 517 27. Andò, S. and Garzanti, E. Raman spectroscopy in heavy-mineral studies. In *Sediment Provenance Studies in*
518 *Hydrocarbon Exploration and Production* Scott, R. A., Smyth, H. R., Morton, A. C. & Richardson, N. Eds.
519 Geological Society: London, England, Special Publications, 2013, 386.
- 520 28. Gillet, P.; Biellmann, C.; Reynard, B.; McMillan, P. Raman spectroscopic studies of carbonates Part I: High-
521 pressure and high-temperature behaviour of calcite, magnesite, dolomite and aragonite. *Phys. Chem.*
522 *Minerals*, **1993**; *20* (1), 1-18.
- 523 29. Bendel, V. and Schmidt, B. C. Raman spectroscopic characterisation of disordered alkali feldspars along
524 the join KAlSi_3O_8 - $\text{NaAlSi}_3\text{O}_8$: application to natural sanidine and anorthoclase. *Eur. J. Mineral.* **2008**, *20*,
525 1055-1065.
- 526 30. Noguchi, N.; Abduriyim, A.; Shimizu, I.; Kamegata, N.; Otake, S.; Kagi, H. Imaging of internal stress
527 around a mineral inclusion in a sapphire crystal: application of micro-Raman and photoluminescence
528 spectroscopy. *JRS.* **2013**, *44*(1), 147-154.
- 529 31. De La Pierre, M.; Carteret, C.; Maschio, L.; André, E.; Orlando, R.; Dovesi, R. The Raman spectrum of CaCO_3
530 polymorphs calcite and aragonite: a combined experimental and computational study. *J. Chem. Phys.* **2014**,
531 *140*(16), 164509.
- 532 32. Del Monte, B.; Paleari, C. I.; Andò, S.; Garzanti, E.; Andersson, P. S.; Petit, J. R.; Crosta, X.; Narcisi, B.; Baroni,
533 C.; Salvatore, M. C.; Baccolo, G.; Maggi V. Causes of dust size variability in central East Antarctica (Dome
534 B): Atmospheric transport from expanded South American sources during Marine Isotope Stage 2. *Quat.*
535 *Sci. Rev.* **2017**, *168*, 55-68.
- 536 33. Molenaar, N. and Zijlstra, J. J. P. Differential early diagenetic low-Mg calcite cementation and rhythmic
537 hardground development in Campanian-Maastrichtian chalk. *Sediment. Geol.*, **1997**, *109*(3-4), 261-281.
- 538 34. Robaszynski, F.; Dhondt, A. V.; John, W. M. Cretaceous lithostratigraphic units (Belgium). *Geol. Belg.* **2001**,
539 *4* 1-2, 121-134.
- 540 35. Hjuler, M.L.; Fabricius, I.L. Engineering properties of chalk related to diagenetic variations of Upper
541 Cretaceous onshore and offshore chalk in the North Sea area. *J. Pet. Sci. Eng.* **2009**, *68*, 151-170. DOI:
542 10.1016/j.petro.2009.06.005.
- 543 36. Zimmermann, U.; Madland, M. V.; Nermoen, A.; Hildebrand-Habel, T.; Bertolino, S. A. R.; Hiorth, A.;
544 Korsnes, R. I.; Audinot, J. N.; Grysan P. Evaluation of the compositional changes during flooding of reactive
545 fluids using scanning electron microscopy, nano-secondary ion mass spectroscopy, x-ray diffraction, and
546 whole-rock geochemistry: *AAPG. Bulletin*, **2015**, *99*, 791-805.
- 547 37. Wang, W., Madland, M.V., Zimmermann, U., Nermoen, A., Korsnes, R.I., Bertolino, S.R.A., Hildebrand-
548 Habel, T. Evaluation of porosity change during chemo-mechanical compaction in flooding experiments on
549 Liège outcrop chalk. *Geol. Soc. Spec. Publ.* **2016**; DOI: 10.1144/SP435.10
- 550 38. Hjuler, M. L., and Fabricius, I. L. Diagenesis of upper cretaceous onshore and offshore chalk from the North
551 Sea area. Technical University of Denmark, Department of Civil Engineering, Arctic Technology Centre,
552 ARTEK, **2007**.
- 553 39. Felder, R. M.; Spence, R. D.; Ferrell, J. K. A method for the dynamic measurement of diffusivities of gases
554 in polymers. *J. Polym. Sci.* **1975**. *19*(12), 3193-3200.
- 555 40. Molenaar, N., and Zijlstra, J. J. P. Differential early diagenetic low-Mg calcite cementation and rhythmic
556 hardground development in Campanian-Maastrichtian chalk. *Sediment. Geol.* **1997**, *109*(3-4), 261-281.
- 557 41. Slimani, H. New species of dinoflagellate cysts from the Campanian-Danian chalks at Hallembaye and
558 Turnhout (Belgium) and at Beutenaken (the Netherlands), *J. Micropalaeontol.* **2001**, *20* (1), p. 1-11,
559 DOI:10.1144/jm .20.1.1.
- 560 42. Strand, S.; Hjuler, M. L.; Torsvik, R.; Pedersen, J. I.; Madland, M. V.; Austad, T. Wettability of chalk: impact
561 of silica, clay content and mechanical properties. *Petrol. Geosc.* **2007**, *13*(1), 69-80.
- 562 43. Nermoen, A.; Korsnes, R. I.; Hiorth, A.; Madland, M. V. Porosity and permeability development in
563 compacting chalks during flooding of nonequilibrium brines: Insights from long-term experiment. *JGR:*
564 *Solid Earth* **2015**, *120*(5), 2935-2960.
- 565 44. Rutt, H. N. and Nicola, H. J. Raman spectra of carbonates of calcite structure. *Phys. C: Solid State Phys.* **1974**,
566 *7*, 4522.

- 567 45. Bischoff, W. D.; Sharma, S. K.; MacKenzie, F. T. Carbonate ion disorder in synthetic and biogenic magnesian
568 calcites: a Raman spectral study. *Am. Mineral.* **1985**, *70*(5-6), 581-589.
- 569 46. Herman, R. G.; Bogdan, C. E.; Sommer, A. J.; Simpson, D. R. Discrimination among carbonate minerals by
570 Raman spectroscopy using the laser microprobe. *Appl. Spectrosc.* **1987**, *41*(3), 437-440.
- 571 47. Edwards, H.; Villar, S.; Jehlicka, J.; Munshi, T. FT-Raman spectroscopic study of calcium-rich and
572 magnesium-rich carbonate minerals. *Spectrochim. Acta A*, **2005**; *61*, 2273.
- 573 48. Korsakov, A.; De Gussem, K.; Zhukov, V. P.; Perraki, M.; Vandenabeele, P.; Golovin, A. V. Aragonite-
574 calcite-dolomite relationships in UHPM polycrystalline carbonate inclusions from the Kokchetav Massif,
575 northern Kazakhstan. *Eur. J. Mineral.* **2009**, *21*, 1301.
- 576 49. Borromeo, L.; Zimmermann, U.; Andò, S.; Coletti, G.; Bersani, D.; Basso, D.; Gentile, P.; Schulz, B. and
577 Garzanti, E. Raman spectroscopy as a tool for magnesium estimation in Mg-calcite. *JRS.* **2017a**, *48*(7), 983-
578 992.
- 579 50. Dandeu, A.; Humbert, B.; Carteret, C.; Muhr, H.; Plasari, E.; Bossoutrot, J. M. Raman Spectroscopy – A
580 Powerful Tool for the Quantitative Determination of the Composition of Polymorph Mixtures: Application
581 to CaCO₃ Polymorph Mixtures. *Chem. Eng. Technol.* **2006**; *29*, 221.
- 582 51. Carteret, C.; De La Pierre, M.; Dossot, M.; Pascale, F.; Erba, A.; Dovesi, R. The vibrational spectrum of
583 CaCO₃ aragonite: A combined experimental and quantum-mechanical investigation. *J. Chem. Phys.* **2013**;
584 *138*, 014201.
- 585 52. Sun, J.; Zeguang, W.; Hongfei, C. A Raman spectroscopic comparison of calcite and dolomite, *Spectrochim.*
586 *Acta A*, **2014**; *117*, 158.
- 587 53. Purgstaller, B.; Mavromatis, V.; Immenhauser, A.; Dietzel, M. Transformation of Mg-bearing amorphous
588 calcium carbonate to Mg-calcite – In situ monitoring. *Geoch. Et Cosmoch. Acta*, **2016**, *174*, 180–195.
- 589 54. Krishnan, R. S. Proc. Math. Sci. **1945**; Part. I: Calcite, 182.
- 590 55. White, W.B., In *Infrared Spectra of Minerals*, V.C. Farmer Eds. Mineralogical Society Monograph 4,
591 Mineralogical Society, London, England, **1974a**, pp 87–110.
- 592 56. White, W.B., In *Infrared Spectra of Minerals*, V.C. Farmer Eds. Mineralogical Society Monograph 4,
593 Mineralogical Society, London, England, **1974b**, pp 227–284.
- 594 57. Gillet, P.; Biellmann, C.; Reynard, B.; McMillan, P. Raman spectroscopic studies of carbonates Part I: High-
595 pressure and high-temperature behaviour of calcite, magnesite, dolomite and aragonite. *Phys. Chem.*
596 *Minerals* **1993**; *20* (1), 1-18.
- 597 58. Urmos, J.; Sharma, S. K.; Mackenzie, T. Characterization of some biogenic carbonates with Raman
598 spectroscopy, *Am. Mineral.* **1991**; *76*, 641.
- 599 59. Minde, M. W.; Haser, S.; Korsnes, R. I.; Zimmermann, U.; Madland, M. V. Comparative Studies of
600 Mineralogical Alterations of Three Ultra-long-term Tests of Onshore Chalk at Reservoir Conditions. In *IOR*
601 *2017-19th European Symposium on Improved Oil Recovery 2017*, **2017**.
- 602 60. Minde, M. W.; Zimmermann, U.; Madland, M. V., Korsnes, R. I. Submicron investigations –What can we
603 learn? IOR Norway 2016, Stavanger, **2016**.
- 604 61. Borromeo, L.; Minde, M.; Toccafondi, C.; Zimmermann, U.; Andò, S.; Ossikovski R. A New Frontier
605 Technique for Nano-analysis on Flooded Chalk-TERS (Tip Enhanced Raman Spectroscopy). In *IOR 2017-
606 19th European Symposium on Improved Oil Recovery. 2017b*.
- 607 62. Borromeo, L.; Toccafondi, C.; Minde, M.; Zimmermann, U.; Andò, S.; Madland, M. V., Korsnes, R. I.
608 Ossikovski R. Application of Tip Enhanced Raman Spectroscopy in the nanoscale characterization of
609 flooded chalk. Submitted to Minerals, January **2018**;
- 610 63. Egeland, N.; Minde, M.W.; Kobayashi, K.; Ota, T.; Nakamura, E.; Zimmermann, U.; Madland, M.W. and
611 Korsnes, R.I. Quantification of Mineralogical Changes in Flooded Carbonate under Reservoir Conditions.
612 In *IOR 2017-19th European Symposium on Improved Oil Recovery. 2017*.
- 613 64. Frezzotti, M. L.; Tecce, F.; Casagli, A. Raman spectroscopy for fluid inclusion analysis, *J Geochem Explor.*
614 **2012**, *112*, 1–20;
- 615 65. Wang, A.; Freeman, J. J.; Jolliff, B. L. Understanding the Raman spectral features of phyllosilicates, *JRS,*
616 **2015**, *46*, 829–845.
- 617 66. Egeland, N. Raman Spectroscopy Applied to Enhanced Oil Recovery. University of Stavanger, unpublished
618 MSc thesis, **2015**.
- 619 67. Gorelik, V. S.; Chervyakov, A. V.; Koltsova, L. V.; Veryaskin, S. S. Raman Spectra of Saturated
620 Hydrocarbons and Gasolines. *J. Russ. Laser Res.* **2000**, *21*, 323-334.

Publications

Preprints (www.preprints.org) | NOT PEER-REVIEWED | Posted: 27 February 2018

doi:10.20944/preprints201802.0173.v1

18 of 18

- 621 68. Costa, J. C. S.; Sant'Ana, A. C.; Corio P; Temperini, M. L. A. Chemical analysis of polycyclic aromatic
622 hydrocarbons by surface-enhanced Raman spectroscopy. *Talanta* **2006**, *70*, 1011-1016.
- 623 69. Sebek, J.; Pele, L.; Potma, E. O.; Gerber, R. B. Raman spectra of long chain hydrocarbons: anharmonic
624 calculations, experiment and implications for imaging of biomembranes. *PCCP*, **2011**, *13*, 12724-12733.
- 625 70. Andrews, A. B.; Wang D.; Marzec, K. M.; Mullins, O. C.; Crozier, K. B. Surface enhanced Raman
626 spectroscopy of polycyclic aromatic hydrocarbons and molecular asphaltenes. *Chem. Phys. Lett.* **2015**, *620*,
627 139-143.

6.3 Application of Tio-Enhanced Raman Spectroscopy for the nanoscale characterization of flooded chalk; Borromeo et al 2017b, 2018b

During the LTT and ULTT studies with Raman spectroscopy it was not possible to clearly focus camera and laser on single grains, as they were extremely small and often overlapped. As consequence, it was not possible to discriminate between the magnesite newly grown minerals, often far below 1 micron (50-600 nm; e.g. Zimmermann et al. 2015) and the primary calcite in form of coccolithophores or their fragments and other micro-fossils debris. Exceptional spatial resolution (<100 nm) for imaging and chemical analyses was achieved using TERS (Tip Enhanced Raman Spectroscopy), which combines Raman Spectroscopy with Atomic Force Microscopy (AFM). Also for this study we have analysed the ULTT, to which we have added the Medium Long Term Test, MLTT, flooded for 718 days at the same reservoir condition, with MgCl₂, and CaCl₂ (for more technical information see Borromeo et al. 2018b).

TERS requires ultra-smooth topography, since it involves a scanning probe technique, and cannot quickly follow large changes in topography. For this reason a specific sample preparation was developed and it turned out that the nano-scale analyses were quite time consuming.

Singular Raman spectra (see Figs. 3,4,5 in Borromeo et al. 2018b), AFM (topography; see Figs. 2, 3, 4, 5 in Borromeo et al. 2018b) and

Raman (mineralogy; see Figs. 4, 5 in Borromeo et al. 2018b) maps were acquired on unflooded (mono-component, calcite) and flooded (bi-components, calcite + magnesite). Parallel to TERS analyses, some TEM-EDS data were acquired on MLTT and ULTT (see Fig. 6 in Borromeo et al. 2018b)

This paper has been firstly published as extended abstract in IOR 2017-19th European Symposium on Improved Oil Recovery, EAGE conference (see Borromeo et al 2017b) and then submitted to the journal *First break* (Borromeo et al. 2018b).

Application of Tip Enhanced Raman Spectroscopy for the nanoscale characterization of flooded chalk

Laura Borromeo^{1,2,*}, Chiara Toccafondi³, Mona Wettrhus Minde^{1,2},
Udo Zimmermann^{1,2}, Sergio Andò⁴,
Merete Vadla Madland^{1,2}, Reidar Inge Korsnes^{1,2}

Razvigor Ossikovski³

¹Department of Energy Resources, University of Stavanger, Norway

²The National IOR Centre of Norway, Stavanger, Norway *laura.borromeo@uis.no

³LPICM, CNRS, Ecole Polytechnique, Université Paris Saclay, 91128, Palaiseau,
France

⁴Department of Earth and Environmental Sciences, University of Milano-Bicocca,
Milan, Italy

Abstract

One of the most challenging goals of flooded chalk analyses used in Enhanced Oil Recovery is to reach high-resolution mineralogical data, in order to detect the composition of new crystals grown after brine injections. Magnesite formation is the most pervasive process when MgCl_2 is injected into chalk and it can affect porosity and permeability. The sub-micrometric grain size of the new minerals requires a high performing imaging technique and a new approach: in our study, we present the first attempt of applying Tip Enhanced Raman Spectroscopy (TERS) to minerals. It is a new frontier technique that couples Raman Spectroscopy with Atomic Force Microscopy, allowing impressively high-resolution topography and mineralogical maps (~ 20 nm), even if time consuming.

Two long-term (1072 and 718 days) flooded chalk experiments were investigated. First analyses identified an almost pure magnesite composition in the first one and a less pervasive secondary growth of magnesite in the second one. Transmission electron microscopy (TEM) has been employed to confirm the results of TERS and add dark and bright field grain-imaging to the investigations.

This confirms the need for high-resolution methodology such as TERS and TEM to fully understand EOR effects at sub-micron scale.

Introduction

Enhanced oil recovery (EOR) permits to increment the amount of hydrocarbons that can be extracted, through flooding by fluids into reservoir rocks (e.g. Strand et al. 2007; Madland et al. 2009, 2011). The effects of such flooding include changes in geo-mechanical parameters enhancing compaction (Risnes et al 2005; Heggheim et al. 2005; Hiorth et al. 2013; Korsnes et al. 2006, 2008; Madland et al. 2006, 2011; Zangiabadi et al. 2009) of the reservoir, along with changes in wettability of the rock (Strand et al. 2003, 2007; Zhang et al. 2006;). In EOR studies brine injection is often used and the impact of flooding processes on the mineralogical and chemical properties of onshore chalk are investigated. The most common fluid is $MgCl_2$ and after its injection in chalk rocks, calcite ($CaCO_3$) dissolution occurs and Mg^{++} ions bond with the carbonate ion with a consequential sub-microscopic magnesite ($MgCO_3$) crystal precipitation (Madland et al. 2011; Wang et al. 2016). The grain size of these crystals can vary between 50 and 1000 nm range (Egeland et al. 2017; Minde et al. 2017). This new growth has been studied by several researchers, using Nano-scale Secondary Ion Mass

Spectrometry (nanoSIMS; Zimmermann et al. 2015), geomechanic studies (Madland et al. 2011), Mineral Liberation Analyzer (MLA; Minde et al. 2017) or Transmission Electron Microscopes with Coupled Energy-Dispersive Spectroscopy (TEM-EDS; Egeland et al. 2017). However, the aim is to apply a methodology which delivers a clear image of the analysed areas together with a determination tool for the identification of minerals at nano-scale. This is only possible with TEM-EDS techniques and the here presented approach by TERS. All other mentioned analytical methods either cannot image the minerals or the identification tool has a too large spot-size, hence is not able to provide detailed chemical data (Zimmermann et al. 2015, 2017; Egeland et al. 2017; Minde et al. 2017).

The interaction with fluids at reservoir conditions induces a mechanical weakening of chalk and a reduction in porosity, affecting the oil recovery rate (e.g. Strand et al. 2007; Madland et al. 2011). The change in the mechanical and permeability properties of chalk is related to calcite dissolution during brine injections and the secondary formation of new minerals such as magnesite. Due to the nano-metric grain size of the new grown minerals, it is necessary to use investigation techniques with high spatial resolution and extraordinary sensitivity.

In this paper, we propose the use of Tip-Enhanced Raman Spectroscopy (TERS) as a tool to investigate the mineralogical content of flooded chalk samples at nanoscale. This study represents the first attempt to use this methodology to investigate rocks or minerals. Until now, enhancing the Raman sensitivity thanks to the exploiting of the plasmonic effect occurring at the edge of a metal tip, TERS was mainly applied to organic molecules (Pettinger et al. 2004; Picardi et al. 2009; Stadler et al. 2011; Schultz et al. 2014; Toccafondi et al. 2016). Furthermore, TERS was also been utilized

successfully applied to carbon-based materials (Stadler et al. 2011), and to semiconductor structures (Vanacore et al. 2013).. TERS is a recent high performing technique, which couples Raman spectroscopy (Raman, 1928; Griffith, 1969; Andò & Garzanti, 2013) with Atomic Force Microscopy (AFM; Park et al. 2010), resulting in a very high-resolution type of Scanning Probe Microscopy (SPM) that performs surface mapping on nano-scale while collecting chemical and crystallographic information. Raman spectroscopy provides these data by detecting the vibrational mode peaks: each mineralogical species shows a spectrum that is unique and diagnostic, like a fingerprint. In particular, Raman spectroscopy can easily distinguish amongst different carbonate minerals (calcite, aragonite, magnesite, dolomite, high Mg-calcite; Krishanmurti, 1956; Rutt and Nicola, 1974; Bischoff et al. 1985; Herman et al. 1987; Unvros et al. 1991; Kuebler et al. 2001; Edwards et al. 2005; Dandeu et al. 2006; De La Pierre et al. 2014; Sun et al. 2014; Purgstaller et al. 2016; Borromeo et al. 2017), which are often difficult to classify using electron microprobes or geochemical methods. However the resolution of Raman spectroscopy is limited by the diffraction limit, therefore it can hardly go beyond the micrometer scale (Zimmermann et al. 2017; Borromeo et al. 2018). In TERS, however, the laser light is focused at the apex of a gold tip, which is glued to a tuning fork (see Fig. 1). Here, a strong enhancement of the electromagnetic field occurs (*near field*), due to the excitation of localized surface plasmons (Ossikovski et al. 2007; Bailo and Deckert, 2008; Picardi et al. 2009; Schultz et al. 2014). The plasmonic effect occurring at the apex of the TERS metal tip determines an increased sensitivity down to single-molecule detection and a spatial resolution far below the diffraction limit (Pettinger et al. 2004; Schultz et al. 2014). The signal, due to the laser hitting directly the sample and scattered from its molecules further away from the tip (not enhanced), is still detectable (*far*

field signal, Raman signal; Fig. 1). If, in *far field*, a different substance is present, its signal may be detected and may interfere with the *near field* (TERS). Impressive results in terms of high sensitivity and spatial resolution can be achieved using a metal tip and analyzing ultra-thin organic or biological layers adsorbed on a metal substrate, in the so-called *gap-mode* (Yang et al. 2009; Langelüddecke et al. 2015; Toccafondi et al. 2016). Unfortunately, this mode is not exploitable on minerals; therefore the enhancement expected in our study is lower than the values described in literature for organic molecules adsorbed on metals.

TERS single measurements and mappings were acquired on both unflooded samples and long-term flooding experiments of chalk at reservoir conditions typical for carbonate hydrocarbon deposits at the Norwegian Continental Shelf (details see below). The results were compared with those obtained by Transmission Electron Microscopy (TEM) and with Raman spectroscopy.

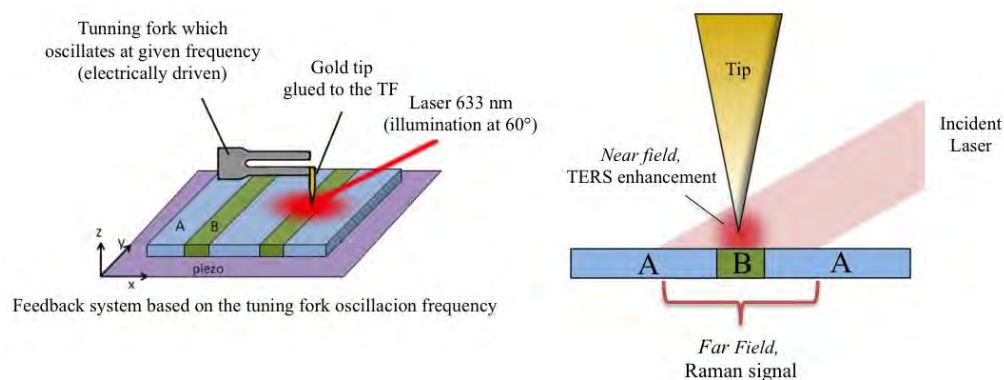


Figure 1: TERS setup used in the present work, showing a tuning fork (TF) based AFM, scanning a surface composed of two phases, A and B, and a red laser is used at 60° and is focused on the apex of the tip. A *near field* spectrum would detect only the B component, where the tip is positioned. In case *far field* is detected, the spectrum would be the sum of the two components spectra (A+B).

Materials and Method

Sampling and flooding of chalk

Chalk is a very fine-grained sedimentary rock, with grain sizes often straddling 1 micrometer. It is a soft, white, porous carbonate rock, a pure limestone principally composed of calcite, with only minor occurrences of non-carbonate minerals. Chalk forms from the gradual settling of microfossils such as coccoliths (plates shed from micro-organisms called coccolithophores) beside a minor occurrence of foraminifera, ostracods and mollusks fragments and is therefore a deep marine sedimentary rock. The chalk samples investigated in this study have been collected near Liège in Belgium (Lixhe outcrop, Late Campanian in age, Molenaar and Zijlstra, 1997; Robaszynski et al. 2001; Slimani, 2001; Strand et al. 2007; Hjuler and Fabricius, 2007) and contains (before flooding) ~5 weight % of non-carbonate minerals as phyllosilicates, quartz, feldspars and occurrences of heavy minerals, together with a porosity in the range of 40-45% (see geological compilation in Zimmermann et al. 2015). On-shore quarry samples have been drilled with a diameter of ~38 mm and a length of ~70 mm. The first core, the Medium Long Term Test, MLTT, was flooded for 718 days, and the second one, the Ultra Long Term Test, ULTT, for 1072 days. Both samples were flooded at similar conditions to North Sea chalk reservoirs in triaxial cells, at 130 °C. The MLTT was flooded with 0.219 M MgCl₂, at a rate of one pore volume (PV) per day, at effective stress 9.5 MPa. Moreover, the core was flooded for 50 days with a mixture of 0.219 M MgCl₂ and 0.13 M CaCl₂. The pH was varied during the flooding period by adding either citric acid to result in a pH of 2.7, or NaOH to reach a pH of 9. During other intervals, the pH was held closer to neutral (5.7) (Minde et al. 2017). Similar procedures were applied during ULTT brine injection test, which was flooded with 0,219 M

MgCl₂ with rates of 1-3 PV per day, a hydrostatic pressure of 11,1 MPa, at 10.4 MPa effective stress and 130°C (for details see Nermoen et al. 2015).

Tip-Enhanced Raman Spectroscopy

TERS experiments were performed by coupling of a Scanning Probe Microscope (SPM) SmartSPM-1000 system (AIST) with a confocal Raman spectroscopy setup (Labram HR800 from Horiba Jobin Yvon). The AIST system was used as an Atomic Force Microscope (AFM) in non-contact mode, with the feedback mechanism based on the oscillation of a tuning fork. The tuning fork is operated in the intermittent contact configuration (tuning fork parallel to the surface and a metal tip glued perpendicularly to the lower arm, Fig.1). Gold tips (final width of around 30 nm) were chemically etched following a recipe reported in (Ren et al. 2004) and were then cut and glued to the tuning fork. The measurements were acquired in frequency modulation mode, with typical oscillation frequencies in the 25-28 kHz range and the feedback set at 3 Hz. Due to the high roughness of chalk samples, the topographical images (maximum 20x20 μm²) were obtained by using very low scan rates (0.1-0.2 Hz).

TERS requires ultra-smooth topography of the samples, since it involves a scanning probe technique. In this instrument, the vertical piezoelectric sensor, which controls the movements of the tip with respect to the sample, has a movement range of 500 nm and if this limit is exceeded, the tip may collide with the sample surface. Moreover, the feedback system of tuning fork sensors is quite slow and cannot quickly follow large changes in topography, resulting in blurred images if the sample surface is irregular. Therefore, chalk samples, which are very rough, cannot be used without preparation. Here, circular disks of approximately 3 mm diameter from highly polished thin

sections were cut using an ultrasonic drill (Gatan Model 601 Ultrasonic disc cutter). In the drilling process a boron-nitrate grinding powder together with distilled water has been used.

When performing TERS measurements, a red laser ($\lambda = 633$ nm) was focused at the apex of the gold tip. Measurements were acquired using long integration times (up to 30 seconds) and maximum laser power (2 mW) to maximize the low number of counts. In samples with mixed composition, in order to better distinguish between magnesite and calcite peaks in the 1080-1100 cm^{-1} region, a high-resolution grating with 1800 lines/mm was used, instead of the usual 600 lines/mm.

Transmission Electron Microscopy (TEM)

TEM analyses were performed in order to confirm the results of TERS investigations and to evaluate their feasibility. Chalk is a brittle material and TEM analysis requires extremely thin samples, in the range of 100 nm. A Focused Ion Beam (FIB) technique was therefore used in a Scanning Electron Microscope (FIB-SEM) in order to produce such samples. Thin wafers of approximately 20 by 10 μm were milled from larger rock fragments or thin sections of chalk using a gallium (Ga) ion-beam and tilting the sample at different angles with respect to the beam. The sample slice was then attached to a manipulator, cut loose by the ion-beam, and welded to a copper grid. A final thinning and cleaning of the sample was performed with the ion-beam, yielding a sample of approximately 100 nm thickness.

The TEM microscope (Jeol JEM-2100) was operated at 200kV acceleration voltage. High-resolution images of chalk samples were acquired together with spot analyses showing the elemental composition, obtained using energy

dispersive X-ray spectroscopy (EDS, by EDAX). From this composition, the mineralogy of the sample can be reconstructed.

Results

Tip-Enhanced Raman Spectroscopy

TERS spectra were acquired on both flooded and unflooded chalk samples from Liège. First, the samples were imaged using the AFM in non-contact mode only, in order to verify their smoothness and to select interesting regions to be analyzed with TERS. Images were acquired within small areas ($< 5 \mu\text{m} \times 5 \mu\text{m}$), since the roughness prevented the AFM from getting a good topography images on larger areas, which is a major challenge (Fig. 2).

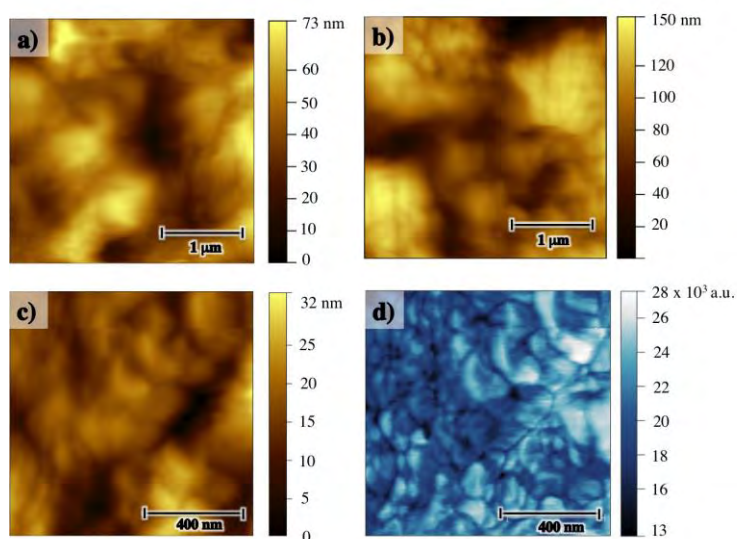


Figure 2: AFM images acquired in non-contact mode using a tuning fork oscillator on chalk samples. Panels a) and b) show $3 \mu\text{m} \times 3 \mu\text{m}$ topographic images of an unflooded and a flooded (MLTT) sample, respectively. Panels c) and d) show a $1 \mu\text{m} \times 1 \mu\text{m}$ images of a flooded sample acquired detecting the height signal (c) and the oscillation magnitude one (d).

Typical AFM images obtained on an unflooded and on a flooded (Medium Long Term Test, MLTT) sample are presented in Fig. 2. The yellow

topographical images in panels a-c) clearly show the rough nature of the samples, even when prepared as a ultra-polished thin section samples. Circular particles smaller than 1 μm are still visible after the fluid injection and resemble coccoliths. Since the samples are rough and many nanocrystals are packed in a small area, the topographical images may not be very clear due to topographical artefacts, common to all the SPM techniques. The width of the surface features derives from the convolution of the tip shape with the surface, resulting in larger “mountains” and smaller “valleys” in the topography. It is sometimes helpful to revise the magnitude signal (Fig. 2d), providing an image that reflects the change in magnitude of the tuning fork frequency modulated oscillation. In fact, the oscillation magnitude image also carries information and can better identify the grain boundaries. This is quite evident if we compare panel c) and d) of Fig. 2, showing images of the height and magnitude signals, respectively.

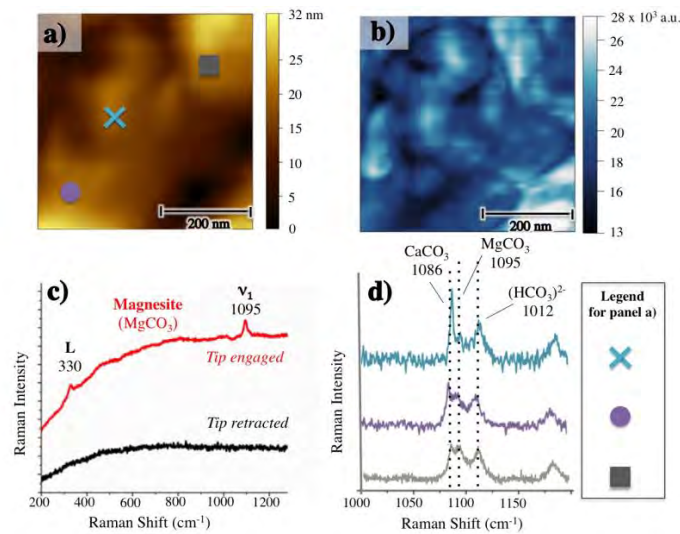


Figure 3: TERS analysis performed on the MLTT sample. Panels a-b): 500x500 nm height (a) and oscillation magnitude (b) images. Panel c): magnesite spectra acquired with the tip engaged (red) and retracted (black), demonstrating that the signal measured is actually *near field* (TERS). Panel d): TERS

spectra acquired in 3 different locations in the selected area. Each spectrum (all zoomed in the region 1000-1200 cm^{-1}) shows the presence of two minerals: calcite (CaCO_3) at 1086 cm^{-1} and magnesite (MgCO_3) at 1095 cm^{-1} . Also, the presence of the $(\text{HCO}_3)^{2-}$ is detected. The locations are identified in panel a) and follow the symbol/color legend in panel d).

Fig. 3 shows TERS spectra acquired in different locations within a selected area of 500 x 500 nm in a MLTT sample. The AFM images of the area are presented in Figs. 3a, b, and show the height and the magnitude channel, respectively. The oscillation magnitude image helps here to identify a circular structure. Shining the laser on the apex of the tip, a TERS spectrum can be acquired: a typical one is presented in Fig. 3c as a red line, and its peak position provides the mineralogical identification of a magnesite crystal (first identify by Krishnamurti, 1956). The corresponding spectrum in the same location but with the tip retracted is also presented in the same panel as a black curve. In this case, no peaks appear, proving that no *far field* signal is detected and that the signal we acquire with the tip engaged is actually a *near field* (TERS) signal, scattered by the area very close to the gold tip, and not by the surrounding sample surface (*far field*, see also Fig. 1). The number of counts is not influencing the result, since there is a fluorescence background. However, the significant difference is the presence of the peaks when the tip is in contact, proving that the Raman signal is actually enhanced by the presence of the tip. In Fig. 3d, moreover, TERS spectra acquired in three different positions in the chosen area are presented. In all spectra we can identify the main peak of calcite (at 1086 cm^{-1}), and of magnesite at (1095 cm^{-1}), named in literature ν_1 , *symmetric stretching mode peak* (Bischoff et al 1985; Herman et al. 1987; Kuebler et al. 2001, Borromeo et al. 2017). Furthermore, in Fig. 3c, the strongest secondary peak of magnesite (L, *librational mode*) is also detectable at 330 cm^{-1} . At 1112 cm^{-1} another peak is

detected and attributed to the bicarbonate ion $(\text{HCO}_3)^{2-}$ (according to Bischoff et al. 1985).

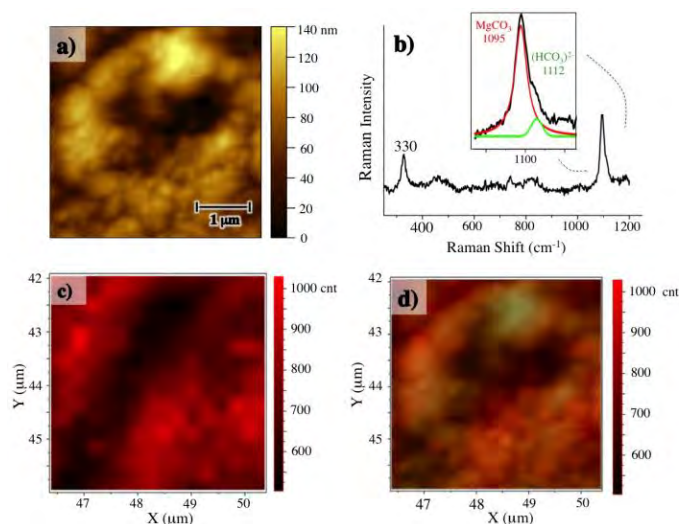


Figure 4: TERS mapping acquired on the Ultra Long Term Test (ULTT) sample: a) $4 \mu\text{m} \times 4 \mu\text{m}$ topography showing a circular structure that may resemble a coccolith; b) a typical TERS spectrum obtained, showing a magnesite vibrational mode at 330 cm^{-1} (L, *librational mode*) and an asymmetric peak at 1095 cm^{-1} , which is the sum of the high ν_1 (*symmetric stretching mode*) of magnesite and a peak of the bicarbonatic ion $(\text{HCO}_3)^{2-}$ present at 1112 cm^{-1} (Bischoff et al. 1985) that produces a shoulder on the right; c) TERS mapping acquired in the area selected in a) with a step-size of 250 nm and using a red color scale based on the intensity of the 1095 cm^{-1} peak, according to the color legend; d) if we superimpose the topography to the intensity of magnesite and $(\text{HCO}_3)^{2-}$ peaks, we see that magnesite recrystallization is pervasive in the investigated region. On the top-right of d), the bicarbonatic ion Raman signal is present.

In Fig. 4, the TERS mapping measurements performed on the Ultra Long Term Test (ULTT) chalk sample are presented. The almost pure magnesite composition of this flooded core has already been documented in a previous study by Raman spectroscopy (Borromeo et al. 2018). Such measurements were not only used as a feasibility test for the TERS mapping, but also as a control in view of the measurements on the samples with mixed composition. In Fig. 4a the topographic image ($4 \mu\text{m} \times 4 \mu\text{m}$) acquired on the sample is

shown. A typical single-point TERS spectrum, presented on the top right in Fig. 4b, shows two peaks at 330 and 1095 cm^{-1} , diagnostic of magnesite. In Fig. 4c, a TERS mapping acquired in the area selected in Fig. 4a is displayed by using a red color scale based on the intensity of the 1095 cm^{-1} peak, according to the color legend. When the topography is superimposed to the TERS mapping, we obtain the image shown in Fig. 4d and the distribution of the magnesite in the investigated region can be imaged. Here, the distribution is constant almost everywhere but decreases in the central hole of the circular structure and in the particle at the top.

The most interesting samples investigated and imaged in the studies are the one characterized by a bi-components nature, as the Medium Long Term Test (MLTT), where both original calcite and recrystallized magnesite are present.

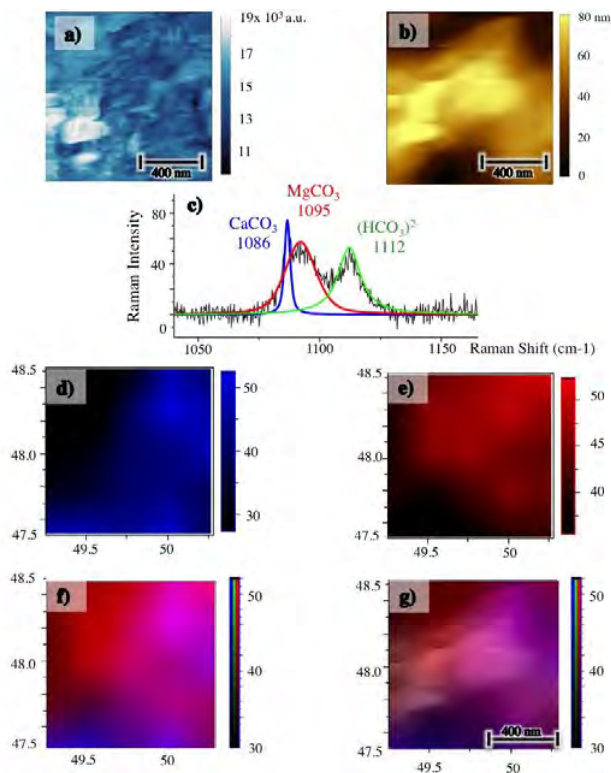


Figure 5 – TERS mapping acquired on Medium Long Term Test (MLTT) chalk sample; a) $1\ \mu\text{m} \times 1\ \mu\text{m}$ topography acquired with tuning-fork based AFM; b) Magnitude signal acquired in the same $1\ \mu\text{m} \times 1\ \mu\text{m}$ area; c) typical TERS spectrum obtained on a single point, showing peaks at $1086\ \text{cm}^{-1}$ (calcite), $1094\ \text{cm}^{-1}$ (magnesite) and $1112\ \text{cm}^{-1}$ (bicarbonatic ion); d) TERS mapping showing the distribution of the $1086\ \text{cm}^{-1}$ calcite ν_1 peak (*symmetric stretching mode*) in the investigated area; e) TERS mapping showing the distribution of the $1094\ \text{cm}^{-1}$ magnesite ν_1 peak in the investigated area; f) superimposition of the TERS mappings of calcite and magnesite, following the color code used in the previous panels; g) superimposition of the TERS mappings of calcite and magnesite and of the topography image in a).

Fig. 5 displays the results of a TERS mapping measurement acquired on the MLTT sample, showing mixed calcite-magnesite composition. In this experiment, a smaller area ($1\ \mu\text{m} \times 1\ \mu\text{m}$) was investigated, because of the need to use a high-resolution grating (1800 lines/mm) to separate calcite and magnesite peaks more efficiently. This results in longer acquisition times for each spectrum, therefore a compromise has been chosen, in order to limit the

total measurement time to four hours. Figures 5a and b show the topography (height) signal and the oscillation magnitude signal, respectively.

In Fig. 5c, a zoomed view of a typical TERS spectrum acquired on this sample is reported, showing a region where both magnesite and calcite are present. It is possible to identify the calcite ν_1 peak at 1086 cm^{-1} and the magnesite one at 1094 cm^{-1} ; at 1112 cm^{-1} another vibrational mode is present and attributed to the bicarbonate ion $(\text{HCO}_3)^{2-}$ (according to Bischoff et al. 1985). The colored lines are the curves resulting from the fitting of the spectrum, performed by the software Labspec 6 (Horiba), using Gaussian-Lorentzian functions and attributed, to calcite (blue), magnesite (red), and bicarbonate ion (green). The distribution of the calcite and magnesite fitting peaks is presented in Figs. 5d and e, respectively, following the color code in Fig. 5c. Therefore, the blue map in Fig. 5d represents the calcite main peak distribution in the area, which is concentrated in the right side of the image. In contrast, the red map represents the magnesite peak distribution, which is located in the center and top of Fig. 5e. The two maps can be superimposed, presented in Fig. 5f, disclosing regions where almost pure calcite (blue, at the bottom of the picture), or pure magnesite (red, on the left) compositions are detected. Purple areas are characterized by the simultaneous presence of calcite + magnesite Raman signals. In Fig. 5g, the topography information has been added, showing that the large grain in the center-right of the image is actually of mixed mineral composition.

Transmission Electron Microscopy (TEM)

FIB-lamellas from both the ULTT and the MLTT were analysed by TEM-EDS. The resulting images and elemental composition that were found during these analyses, match the finding of TERS measurements. In the sample from

the ULTT core, only magnesium-phases were found, where the majority of the analysed crystals have a composition matching high magnesium carbonate or magnesite. Homogenously distributed, minor (<4 wt %) impurities of calcium are observed within the magnesite crystals. Additionally, phases containing high amounts of silicon together with the magnesium were observed, interpreted as clay-minerals. In the MLTT similar magnesium-dominated phases as found in the ULTT were found, however, this sample also contains calcium carbonate (calcite) (Fig 6). The crystal shape and diffraction when imaged in TEM differs significantly between the original calcite grains (white arrows and point 1 in Fig 6) and the new-formed magnesite (e.g. point 2 in Fig 6). The magnesite grains, seen to the lower left corner of Fig. 6, are smaller and more angular and present a coarser internal structure in TEM bright field (BF) images compared to the more rounded and smoother calcite grains (white arrows, Fig 6).

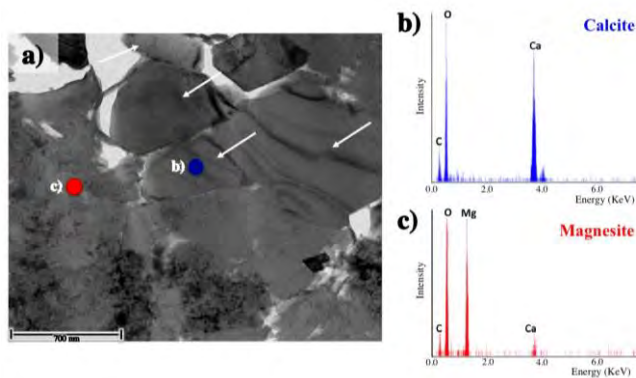


Figure 6: a) TEM bright field image from the FIB-lamella of the MLTT. White arrows pointing to original calcite grains, including spot b). Spot c) and the coarser structure to the lower left are newly formed magnesite grains. EDS spectra collected in spot b (calcite) and spot c (magnesite), respectively are reported in panels b) c).

Unfortunately, the two methods TERS and TEM cannot use the same sample material as FIB-SEM samples for TEM analyses cannot be used for TERS (the material is not rigid enough, and it is positioned in a grid to which the tip can be destroyed), and the drilled polished thin sections cannot be inserted into the TEM, as the glass plate inhibit transmission analysis.

Discussion

This study presents a first application of the new, high-resolution technique, TERS, on mineralogical material (rocks or minerals). In particular we tested its potential and limits on flooded chalk samples (please see the explanation of the experiment in chapter *Sampling and flooding of chalk*), which are challenging to investigate because of the submicron grain size of new minerals, grown after injection of non-equilibrium brines. TERS could produce two kinds of imaging at the nanoscale, representing the height signal (topography) and the oscillation magnitude one, helping to define topography and grains boundaries. Furthermore spectra and Raman maps could be obtained and superimposed onto these maps.

Sample preparation turned out to be tough and fundamental for a positive outcome of the analyses, since the instrumentation is extremely sensitive to roughness, and a perfectly smooth surface is impossible to obtain with such a soft material like chalk. For this reason, before collecting Raman maps, the samples were imaged using the AFM in non-contact mode, in order to select smooth regions to be analyzed with TERS. Moreover, images were acquired within small areas ($< 5\mu\text{m} \times 5\mu\text{m}$) in order minimize the effects of the surface-roughness. Despite this procedure to optimize the AFM maps, the result on chalk were not at the level of the ones obtained with TERS on organic and biological samples (*Pyne et al. 2014*), but, anyway, even if time

consuming, images with an unachievable resolution for a “normal” Raman spectrometer were collected.

Afterwards, TERS spectra were acquired of both, flooded and unflooded chalk. As expected, unflooded material showed a calcite composition, whereas in the MLTT sample, even in small areas ($1\ \mu\text{m} \times 1\ \mu\text{m}$), it was possible to distinguish zones with different calcite and magnesite contents in the MLTT sample, as shown for instance, in Fig. 3d. The spectrum acquired on the turquoise cross reflects a higher content of calcite while this amount decreases in the area marked by the grey square, where a stronger magnesite concentration is present. A first Raman map has been collected on the ULTT, characterized by an already confirmed almost pure magnesitic composition (Nermoen et al. 2015; Borromeo et al. 2018). In Fig. 4 it is evident that a strong magnesite signal occurs everywhere in the mapped region and therefore the differences in intensities of the ν_1 peak cannot be attributed to a change in composition, but only to a change in topography or crystallinity. In MLTT, where calcite and magnesite appear together (Minde et al. 2017), spectra were acquired with the highest resolution grating (1800 lines/mm) to be able to separate magnesite from calcite signals, as their main peaks are close at $1095\ \text{cm}^{-1}$ and at $1086\ \text{cm}^{-1}$, respectively.

To obtain the best possible TERS maps, an optimized compromise between high spectral resolution, high signal intensity and reasonable acquisition time has been chosen. During the analyses the TERS enhancement of the Raman signal has been registered, as demonstrated by the curves in Fig. 3c. The magnitude of the enhancement was limited by the impossibility to investigate in *non-gap mode* and by the necessity to use a higher resolution grating to better separate the different contributions. Therefore, to improve the intensity of the signal, the spectra were collected with quite long acquisition times (up to 60 sec). This poses a severe limitation in terms of time and the capability of

measuring large TERS maps with low spatial resolution. In fact, even though the instrument can acquire for several hours, the tip-laser alignment, which is really sensitive and affected by temperature fluctuations and movements of the optical elements, is not stable enough to guarantee a long acquisition.

The identification of mixed composition (primary calcite and secondary magnesite) in this kind of samples is in accordance with TEM-EDS observation and proves that it is possible to detect and image chemical changes in bulk samples at the nanoscale. However, the imaging is related to the roughness of the sample and for this reason cannot reach the quality expected. This lies in the nature of chalk, which cannot be easily polished on that scale compared to hard minerals or metals. The tested FIB-SEM samples (not shown here) or other sample preparations could not deliver the necessary smoothness of perfect images and results have been discarded. Additional TEM-analyses show the presence of high magnesium carbonate together with calcite at pore-scale. Formerly, analytical application (like Scanning Electron Microscopy or Mineral Liberation analyzer (MLA) with lower resolution spot-sizes (c. 1 μm ; Minde et al. 2017) pointed to a dolomitic composition, which was not the case. TERS can confirm the results from previous studies (Minde et al. 2017) that dolomite is not an existing phase but an intermingled occurrence of magnesite and calcite (see Fig. 5). This result is of utmost importance for the modeling of the fluid-rock interaction during EOR experiments (Nermoen et al. 2015; Zimmermann et al. 2015; Andersen et al. 2017).

In a precedent work, Raman spectroscopy has proved to be reliable and fast in recognizing minerals down to few microns in size (Borromeo et al. 2018). However, the restrictions imposed by the diffraction limit, did prevent from distinguishing the secondary grown crystals from the coccolithophore rings or

fragments. This is related to impossibility of visualization of sub-micrometric grains in chalk with an optical microscope. TERS methodology, with its outstanding resolution, could map the topography and the composition of the samples reaching nano-scale. Unfortunately, the unfeasibility to use the so-called *gap-mode* precluded to reach a very good quality of the maps. To sum up, it is possible to state that of the here mentioned techniques, there are two, TERS and TEM-EDS that can both identify chalk mineralogy and add a sufficient informative image. Raman spectroscopy on micron scale is able in determining the mineralogy but cannot provide images, while MLA and High-Resolution Field Emission SEM (FEG-SEM) can image the minerals but not identify the grain by grain mineralogy because the spotsize is too large. However, both, TEM and TERS are time consuming and expensive methods. Routine measurements on FEG-SEM can be rather quick and may be used complementary to Raman spectroscopy as a first quick investigation of the mineralogy and texture.

Conclusions

The composition of flooded chalk samples has been investigated down to the nanoscale with one dominant carbonate mineral (magnesite, ULTT) and two abundant carbonate minerals (calcite and magnesite, MLTT), using TERS. We proved the possibility of performing TERS measurements on these samples, being able to detect a *near-field* signal from different carbonate phases. This result is very interesting because it stands out for being obtained on non-conductive samples, therefore not in *gap mode*. Results obtained from mapping chalk with sub-micron sized particles were shown, identifying compositional variations at nanoscale, in accordance with other techniques like TEM-EDS. These results qualify TERS as an interesting investigation

tool in this field, even if the required sample preparation and the long acquisition times prevent its massive use as characterization tool. However, it is a very feasible tool for the study of chalk composition or other small-grained rock samples besides its usual use for organic and metal sample. The best way to exploit TERS potentiality in this field would be, to investigate selected key samples, from which more general information can be gathered. Nevertheless, we have demonstrated the feasibility of TERS investigations of chalk samples, and subsequently of other small-grained rock samples, besides its usual use for organic and inorganic thin layers. The most important achievement is the simultaneous information of image and composition at nanoscale, only otherwise provided by TEM-EDS.

Acknowledgements

The authors acknowledge the Research Council of Norway and the industry partners; ConocoPhillips Skandinavia AS, Aker BP ASA, Eni Norge AS, Maersk Oil Norway AS, , Statoil Petroleum AS, ENGIE E&P NORGE AS, Lundin Norway AS, Halliburton AS, Schlumberger Norge AS, Wintershall Norge AS, DEA Norge AS of The National IOR Centre of Norway for support. This study is a central part of the PhD thesis of LB who thanks the National IOR Centre of Norway for a grant to carry out the research and Eduardo Garzanti and the group of Provenance Studies (University of Milano – Bicocca). CT gratefully acknowledges financial support from the Chaire de Recherche CAP sponsored by TOTAL at the Ecole Polytechnique. Data for TEM-EDS analyses are part of the PhD thesis by MM. UZ likes to thank the École Polytechnique for the extraordinary kind and efficient cooperation and the interest in this topic.

References

1. Andersen, P.Ø., Wang, W., Madland, M.V., Zimmermann, U., Korsnes, R.I., Bertolino, S.R.A., Minde, M., Schulz, B. and Gilbricht, S. [2017] Comparative study of five outcrop chalks flooded at reservoir conditions: chemo-mechanical behaviour and profiles of compositional alteration. *Transport in Porous Media*, 1-47.
2. Andò, S. and Garzanti, E. [2013] Raman spectroscopy in heavy-mineral studies. In *Sediment Provenance Studies in Hydrocarbon Exploration and Production* Scott, R. A., Smyth, H. R., Morton, A. C. & Richardson, N. Eds. Geological Society: London, England, Special Publications, 386.
3. Bailo, E. and Deckert, V. [2008] Tip-enhanced Raman scattering, *Chemical Society Reviews*. **37**, 921-930.
4. Bischoff, W. D., Sharma, S. K. and MacKenzie, F. T. [1985] Carbonate ion disorder in synthetic and biogenic magnesian calcites: a Raman spectral study. *American Mineralogist*, **70**(5-6), 581-589.
5. Borromeo, L., Zimmermann, U., Andò, S., Coletti, G., Bersani, D., Basso, D., Gentile, P., Schulz, B. and Garzanti, E. [2017] Raman spectroscopy as a tool for magnesium estimation in Mg-calcite. *Journal of Raman Spectroscopy*, **48**(7), 983-992.
6. Borromeo, L., Egeland N., Minde, M. W., Zimmermann, U., Andò, S., Madland, M. V. and Korsnes, R. I. [2018] Quick, easy and economic mineralogical studies of flooded chalk for EOR experiments using Raman spectroscopy. Submitted to *Minerlas*, January 2018.
7. Dandeu, A., Humbert, B., Carteret, C., Muhr, H., Plasari, E. and Bossoutrot, J. M. [2006] Raman spectroscopy—a powerful tool for the quantitative determination of the composition of polymorph mixtures: application to CaCO₃ polymorph mixtures. *Chemical engineering & technology*, **29**(2), 221-225.
8. De La Pierre, M., Carteret, C., Maschio, L., André, E., Orlando, R. and Dovesi, R. [2014] The Raman spectrum of CaCO₃ polymorphs calcite and

Publications

- aragonite: a combined experimental and computational study. *The Journal of Chemical Physics*, **140**(16), 164509.
9. Edwards, H., Villar, S., Jehlicka, J. and Munshi, T. [2005] FT-Raman spectroscopic study of calcium-rich and magnesium-rich carbonate minerals. *Spectrochimica Acta A*, **61**, 2273.
 10. Egeland, N., Minde, M.W., Kobayashi, K., Ota, T., Nakamura, E., Zimmermann, U., Madland, M.W. and Korsnes, R.I. [2017] Quantification of Mineralogical Changes in Flooded Carbonate under Reservoir Conditions. In *IOR 2017-19th European Symposium on Improved Oil Recovery*.
 11. Griffith, W.P. [1969] Raman spectroscopy of minerals. *Nature*, **224**, 264–266.
 12. Herman, R. G., Bogdan, C. E., Sommer, A. J. and Simpson, D. R. [1987] Discrimination among carbonate minerals by Raman spectroscopy using the laser microprobe. *Applied Spectroscopy*, **41**(3), 437-440.
 13. Heggheim, T., Madland, M. V., Risnes, R. and Austad, T. [2005] A chemical induced enhanced weakening of chalk by seawater. *Journal of Petroleum Science and Engineering*, **46**(3), 171-184.
 14. Hiorth A., Jettestuen E., Lawrence C. M. and Madland M. V. [2013] Precipitation, dissolution, and ion exchange processes coupled with a lattice Boltzmann advection diffusion solver. *Geochimica et Cosmochimica Acta* **104**, 99-110.
 15. Hjuler, M. L. and Fabricius, I. L. [2009] Engineering properties of chalk related to diagenetic variations of Upper Cretaceous onshore and offshore chalk in the North Sea area. *Journal of Petroleum Science and Engineering*, **68**(3), 151-170.
 16. Korsnes R. I., Strand S., Hoff Ø., Pedersen T., Madland M. V. and Austad T. [2006] Does the chemical interaction between seawater and chalk affect the mechanical properties of chalk. *Multiphysics coupling and long term behaviour in rock mechanics*, 427-434.
 17. Korsnes R. I., Madland M. V., Austad T., Haver S. and Rosland G. [2008] The effects of temperature on the water weakening of chalk by seawater.

- Journal of Petroleum Science and Engineering*, **60**, 183- 193.
18. Korsnes, R. I., Madland, M. V., Zimmermann, U., Haser, S., Audinot, J. N., Gysan, P., Schulz, B., Gutzmer, J. and Hiorth, A. [2013]. Neoformed Dolomite in Flooded Chalk for EOR Processes. In *75th EAGE Conference & Exhibition incorporating SPE EUROPEC 2013*.
 19. Krishnamurti, D. [1956] Raman spectrum of magnesite. *Proceedings of the Indian Academy of Sciences – Section A*, **43**, 210-212.
 20. Kuebler, K., Wang A., Abbott, K. and Haskin, L. A. [2001] Can we detect carbonate and sulfate minerals on the surface of Mars by Raman spectroscopy? *Lunar and Planetary Science XXXII* n. 1889.
 21. Langelüddecke, L., Singh, P. and Deckert, V. [2015] Exploring the nanoscale: fifteen years of tip-enhanced Raman spectroscopy. *Applied Spectroscopy OA*, **69**(12), 1357-1371.
 22. Madland, M. V., Finsnes, A., Alkafadgi, A., Risnes, R. and Austad, T. [2006] The influence of CO₂ gas and carbonate water on the mechanical stability of chalk. *Journal of Petroleum Science and Engineering*, **51**, 149-168.
 23. Madland, M. V., Midtgarden, K., Manafov, R., Korsnes, R. I., Kristiansen, T., Hiorth, [2008] A. The Effect of Temperature and Brine Composition on the Mechanical Strength of Kansas Chalk. *International Symposium of the Society of Core Analysts*, Abu Dhabi, United Arab Emirates 2008, 1-6.
 24. Madland, M. V. [2009] Rock-Fluid interactions in chalk exposed to seawater, MgCl₂, and NaCl brines with equal ionic strength. In *15th European Symposium on Improved Oil Recovery-Paris, France*, 27-29.
 25. Madland, M.V., Hiorth, A., Omdal E., Megawati M., Hildebrand-Habel T., Korsnes I. R., Evje S., Cathles M. L. [2011] Chemical alterations induced by rock-fluid interactions when injecting brines in high porosity chalks. *Transport in Porous Media*, **87**, 679-702.
 26. Minde, M. W., Haser, S., Korsnes, R. I., Zimmermann, U. and Madland, M. V. [2017] Comparative Studies of Mineralogical Alterations of Three Ultra-long-term Tests of Onshore Chalk at Reservoir Conditions. In *IOR 2017-*

Publications

19th European Symposium on Improved Oil Recovery 2017.

27. Molenaar, N. and Zijlstra, J. J. P. [1997] Differential early diagenetic low-Mg calcite cementation and rhythmic hardground development in Campanian-Maastrichtian chalk. *Sedimentary Geology*, **109**(3-4), 261-281.
28. Nerموen, A., Korsnes, R. I., Hiorth, A. and Madland, M. V. [2015] Porosity and permeability development in compacting chalks during flooding of nonequilibrium brines: Insights from long-term experiment. *Journal of Geophysical Research: Solid Earth*, **120**(5), 2935-2960.
29. Ossikovski, R., Nguyen, Q. and Picardi, G. [2007] Simple model for the polarization effects in tip-enhanced Raman spectroscopy. *Physical Review B*, **75**(4), 045412.
30. Park, J. Y., Maier, S., Hendriksen, B. and Salmeron, M. [2010] Sensing current and forces with SPM, *Materials Today*, **13** (10), 38-45.
31. Pettinger, B., Ren, B., Picardi, G., Schuster, R. and Ertl, G. [2004] Nanoscale probing of adsorbed species by tip-enhanced Raman spectroscopy. *Physical review letters*, **92**(9), 096101.
32. Picardi, G., Chaigneau, M., Ossikovski, R., Licitra, C. and De La Pierre, G. [2009] Tip enhanced Raman spectroscopy on azobenzene thiol self-assembled monolayers on Au (111). *Journal of Raman Spectroscopy*, **40**(10), 1407-1412.
33. Purgstaller, B., Mavromatis, V., Immenhauser, A. and Dietzel, M. [2016] Transformation of Mg-bearing amorphous calcium carbonate to Mg-calcite – In situ monitoring. *Geochimica et Cosmochimica Acta*, **174**, 180–195.
34. Pyne A., Thompson, R., Leung, C., Roy, D. and Hoogenboom, B. W. [2014] Single-Molecule Reconstruction of Oligonucleotide Secondary Structure by Atomic Force Microscopy. *Small*, **10** (16), 3257-3261.
35. Raman, C.V. A new radiation [1928] *Indian Journal of Physics*, **2**, 387–398.
36. Ren, B., Picardi, G. and Pettinger, B. [2004] Preparation of Gold Tips Suitable for Tip-Enhanced Raman Spectroscopy and Light Emission by Electrochemical Etching. *Review of Scientific Instruments*. **75**, 837-841.

37. Risnes, R., Madland M. V., Hole M. and Kwabiah N. K. [2005] Water weakening of chalk – Mechanical effects of water-glycol mixtures, *Journal of Petroleum Science and Engineering*, **48**, 21-36.
38. Robaszynski, F., Dhondt, A. V. and John, W. M. [2001] Cretaceous lithostratigraphic units (Belgium). *Geologica Belgica*, **4** (1-2), 121-134.
39. Rutt, H. N. and Nicola, J. H. [1974] Raman spectra of carbonates of calcite structure. *Journal of Physics C: Solid State Physics*, **7**(24), 4522-4528.
40. Schultz, Z. D., Marr, J. M. and Wang, H. [2014] Tip enhanced Raman scattering: plasmonic enhancements for nanoscale chemical analysis. *Nanophotonics*, **3**(1-2), 91-104.
41. Slimani, H. [2001] New species of dinoflagellate cysts from the Campanian-Danian chalks at Hallembaye and Turnhout (Belgium) and at Beutenaken (the Netherlands), *Journal of Micropalaeontology*, **20** (1), 1–11, DOI:10.1144/jm .20.1.1.
42. Stadler, J., Schmid, T. and Zenobi, R. [2011] Nanoscale chemical imaging of single-layer graphene. *ACS Nano* **5**(10), 8442-8448.
43. Strand, S., Standnes, D. C. and Austad, T. [2003] Spontaneous imbibition of aqueous surfactant solutions into neutral to oil-wet carbonate cores: Effects of brine salinity and composition. *Energy & fuels*, **17**(5), 1133-1144.
44. Strand, S., Hjuler, M. L., Torsvik, R., Pedersen, J. I., Madland, M. V. and Austad, T. [2007] Wettability of chalk: impact of silica, clay content and mechanical properties. *Petroleum Geoscience*, **13**(1), 69-80.
45. Sun, J., Wu, Z., Cheng, H., Zhang, Z. and Frost, R. L. [2014] A Raman spectroscopic comparison of calcite and dolomite. *Spectrochimica Acta Part A: Molecular and Biomolecular Spectroscopy*, **117**, 158-162.
46. Toccafondi, C., Picardi, G. and Ossikovski, R. [2016] Molecular Bending at the Nanoscale Evidenced by Tip-Enhanced Raman Spectroscopy in Tunneling Mode on Thiol Self-Assembled Monolayers. *The Journal of Physical Chemistry C*, **120**(32), 18209-18219.
47. Unvros, J., Sharma, S. and Mackenzie, F. [199] Characterization of some biogenic carbonates with Raman spectroscopy. *American Mineralogist*, **76**,

- 641-646.
48. Vanacore, G. M., Chaigneau, M., Barrett, N., Bollani, M., Boioli, F., Salvalaglio, M., Montalenti, F., Manini, N., Caramella, L., Biagioni, P., Chrastina, D., Isella, G., Renault, O., Zani, M., Sordan, R., Onida, G., Ossikovski, R., Drouhin, H.-J. and Tagliaferri, A. [2013] Hydrostatic strain enhancement in laterally confined SiGe nano-stripes, *Physical Review.B*, **88**, 115309.
 49. Yang, Z., Aizpurua, J. and Xu, H. [2009] Electromagnetic field enhancement in TERS configurations. *Journal of Raman Spectroscopy*, **40**(10), 1343-1348.
 50. Wang, W., Madland, M. V., Zimmermann, U., Nerموen, A., Reidar, I., Korsnes, R., Bertolino, S. R. A. and Hildebrand-Habel, T. [2016] Evaluation of porosity change during chemo-mechanical compaction in flooding experiments on Liege outcrop chalk. In *Reservoir Quality of Clastic and Carbonate Rocks: Analysis, Modelling and Prediction*. Armitage, P. J., Butcher, A. R., Churchill, J. M., Csoma, A. E., Hollis, C., Lander, R. H., Omma, J. E. & Worden, R. H. Eds., Geological Society: London, England, Special Publications, 435-10.
 51. Zangiabadi, B., Korsnes, R. I., Hildebrand-Habel, T., Hiorth, A., Surtarjana, I. K., Lian, A. and Madland, M. V. [2009] Chemical water weakening of various outcrop chalks at elevated temperature. In *Poromechanics IV*, Ling H. I., Smyth A. and Betti, R. Eds. DEStech Publications, Inc., Lancaster, England, 543-548.
 52. Zimmermann, U., Madland, M. V., Nerموen, A., Hildebrand-Habel, T., Bertolino, S. A. R., Hiorth, A., Korsnes, R. I., Audinot, J. N. and Grysan P. [2015] Evaluation of the compositional changes during flooding of reactive fluids using scanning electron microscopy, nano-secondary ion mass spectroscopy, x-ray diffraction, and whole-rock geochemistry: *American Association of Petroleum Geologists Bulletin*, **99**, 791-805.
 53. Zimmermann, U., Madland, M., Minde, M., Borromeo, L. and Egeland, N. [2017] Tools to Determine and Quantify Mineralogical Changes During

Publications

- EOR Flooding Experiments on Chalk. *SPE Abu Dhabi International Petroleum Exhibition & Conference. Society of Petroleum Engineers.*
54. Zhang, P., Tweheyo, M. T. and Austad, T. [2006] Wettability Alteration and Improved Oil Recovery in Chalk: The Effect of Calcium in the Presence of Sulfate. *Energy & Fuels*, **20**(5), 2056-2062.

7 Other contributions

During this PhD project, other activities have been carried out, throughout the three years:

- CONFERENCES
- FIELDWORK and LABORATORY WORK as STUDENT ASSISTANT.

7.1 Conferences

Beside the three papers presented above, the results obtained on the investigation on carbonate group minerals were presented in several international and national congresses and conferences, listed below. Throughout the PhD supporting research has been carried out on other projects and the dissemination of results was performed.

Here, contributions are listed which I wrote during the PhD research project:

- *Contributions on carbonate minerals and flooded chalk analyses with Raman spectroscopy and TERS:*
 - Borromeo L., Zimmermann U., Andò S., Coletti G., Garzanti E.; Raman spectroscopy: an “unconventional” and innovative tool to identify the mineralogy of chalk and other fine-grained rocks applicable to IOR research. Abstracts and Proceedings, *Vinterkonferansen 2015, Winter conference*, Stavanger, Norway, **2014**, 12.-14.1. 2015;
 - Borromeo L., Zimmermann U., Andò S., Coletti G., Bersani D., Basso D., Gentile P., Garzanti E.; Raman Spectroscopy as a tool for magnesium estimation in Mg- calcite. *Periodico di Mineralogia, ECMS, European Conference on Mineralogy and Spectroscopy*, Rome, Italy, **2015**, 84, 2, 35-36;

- Borromeo L., Egeland N., Minde M., Zimmermann U., Andò S., Toccafondi C., Ossikovski R.; Micro- and Nano- Raman analyses of chalk. *IOR Conference*, Stavanger, Norway, **2016**;
 - Borromeo L., Zimmermann U., Andò S., Coletti G., Bersani D., Egeland N., Basso D., Gentile P., Garzanti E.; Raman Spectroscopy as a tool for magnesium estimation in Mg-calcite. *Goldschmidt Conference*, Yokohama, Japon, **2016**;
 - Borromeo L., Minde M., Zimmermann U., Andò S., Toccafondi C., Ossikovski R.; A new frontier technique for nano-analysis on flooded chalk: TERS (Tip-Enhanced Raman Spectroscopy). *IOR-EAGE*, Stavanger, Norway, **2017**;
 - Borromeo L., Zimmermann U., Andò S., Minde M., Egeland N., Toccafondi C., Ossikovski R.; Micro-Raman spectroscopy and TERS (Tip-Enhanced Raman Spectroscopy) applied to Enhanced Oil Recovery. *Nano Innovation conference*, Rome, Italy, **2017**;
 - Borromeo L., Zimmermann U., Andò S., Raman spectroscopy applied to mineralogical analyses of flooded chalk. *IOR Conference*, Stavanger, Norway, **2018**;
 - Egeland, Nina; Zimmermann, Udo; Borromeo, Laura; Andò, Sergio; Madland, Merete Vadla; Minde, Mona Wethrus; Korsnes, Reidar Inge. **2016**. Raman spectroscopy applied to Enhanced Oil Recovery research. *Goldschmidt 2016*;
 - Zimmermann, U.; Madland, M.V.; Minde, M.; Borromeo, L.; Egeland, N.; Tools to determine and quantify mineralogical changes during EOR flooding experiments on chalk. *S.P.E. International* **2017**.
- *Contributions concentrated on the identification and concentration estimation of the heavy minerals (HM) in the major types of source areas for Mesozoic rocks in the Barents Sea.* The HM population of two cores was deeply investigated by optical microscope and Raman Spectroscopy in order to recognise the provenance

fingerprint of the samples. **Lower Cretaceous basinal studies of the Arctic region (LoCrA) Project:**

- Matthews, N.E., Zimmermann, U., Støle, L., Ruud, C., Mostafa, E., Borromeo, L., Andò, S., Magnaghi, M., Lapen, T.J. A multi-technique approach for provenance studies of Mesozoic clastic rocks in the Barents Sea. AGU Fall meeting, V025: Novel high-resolution approaches to deciphering source-to-sink linkages between tectonic hinterland and basin evolution Session ID#: 9154, V53D-3148. **2015**.

➤ *Contributions related to the heavy minerals (HM) identification and concentration in various detrital rocks collected to the **Cantabrian Mountains (Spain)**:*

- Birkeland, H., Malde, P.-K., Oppedal, E., Østensen, O.C., Zimmermann, U., Andò, S., Borromeo, L. Correlation of quartz-rich Ordovician successions in the Cantabrian Mountains using high-resolution heavy mineral analysis and Raman spectroscopy. NGF Abstracts and Proceedings, Vinterkonferansen **2015**, 12.-14.1. 2015 Stavanger, 11-12.
- Grønberg, A., Røynestad, L.M., Zimmermann, U., Andò, S., Borromeo, L., Garzanti, E. Provenance signals from coarse-grained sandstones, siltstones and shales in the Middle to Upper Cambrian Oville Formation - a test using whole-rock geochemistry and high-resolution heavy mineral analysis. NGF Abstracts and Proceedings, Vinterkonferansen 2015., 12.-14.1. **2015**, Stavanger, 35-36.
- Kristiansdottir, M., Zimmermann, U., Andò, S., Borromeo, L. Test for dependence of provenance signals in varying facies of the same rock formation: a study of Lower Cambrian rocks deposited in northern Spain. NGF Abstracts and Proceedings, Vinterkonferansen **2015**, 12.-14.1. 2015 Stavanger, 54.
- Kristiansen, K., Myhre, A., Zimmermann, U., Andò, S., Borromeo, L. Correlation of the Precambrian-Cambrian

boundary in siliciclastic rocks using high-resolution heavy mineral analysis in the Cantabrian Mountains. NGF Abstracts and Proceedings, Vinterkonferansen 2015, 12-14.1. **2015**, Stavanger, 54-55.

- Mostafa, E., Ruud, C., Støle, L., Matthews, N., Zimmermann, U., Andò, S., Borromeo, L. 2015. High resolution heavy mineral studies of Mesozoic rocks of the Hammerfest basin. NGF Abstracts and Proceedings, Vinterkonferansen 2015, 12-14.1. **2015** Stavanger, 67.

➤ *Contribution related to the heavy minerals (HM) quantitative mineralogical analysis performed in modern sands and in coastal deposits with the aim to investigate erosive events and hydraulic sorting during big storms (Calabria, Italy):*

- Årlebrand, A., Hope, B., Andò, S., Zimmermann, U., Vezzoli, G., Borromeo, L. After and before the storm: effect of erosion during heavy mineral climate events on the composition of sediments, a comparison of provenance information. NGF Abstracts and Proceedings, Vinterkonferansen 2015, 12.-14.1. **2015**, Stavanger, 107-108.

7.2 Fieldwork and Laboratory work as student assistant

In July 2015 I have accompanied Prof. Udo Zimmermann on a field trip in the Cantabrian mountains (Spain), as student assistant studying different approaches (mineralogy, sedimentology, applied stratigraphy, petrography, geochronology, structural geology, and geomorphology). Afterwards laboratory work has been carried out at University of Milano-Bicocca, Department of Earth and Environmental Sciences, DISAT, in the Laboratory for Provenance Studies, by several students, under Sergio Andò and mine supervision, on the rock sample collected

Other contributions

in the field. Each sample was separated into low-density ($<2.90 \text{ g/cm}^3$) and high-density fractions (HM; $>2.90 \text{ g/cm}^3$) and recovered. Mineralogical data were obtained on the HM fraction by identifying at least 100 grains on each slide by optical microscope.

8 Discussion

This project has been focused on the application of Raman spectroscopy^(Borromeo et al. 2017b) and Tip-Enhanced Raman spectroscopy^(Borromeo et al. 2017b, 2018b) in the oil research field, and in particular on the investigation of carbonatic reservoir, representing the first attempt to apply Raman spectroscopy on chalk and to investigate rocks by TERS.

Raman spectroscopic analyses allow the recognition of minerals down to 1 μ m in size,^(Delmonte et al. 2017, Borromeo et al. 2018a) it is non-destructive, rapid, economic and can be performed directly on any sample. For its characteristics this method has been commonly used in other disciplines, and not yet truly considered as a routine analysis by oil companies and only few studies on hydrocarbon molecules have been completed.^(Gorelik et al. 2000; Costa et al. 2006; Sebek et al. 2011; Andrews et al. 2015) During the first stage of this PhD, after studying several calcite samples with variable Mg content (0 - 20 mole % MgCO₃), Raman has been confirmed to be sensitive to structural and chemical changes occurring when Mg²⁺ substitutes Ca²⁺ in the calcite lattice (Borromeo et al. 2017a). The correlation between their peaks positions and their chemical composition has found to be not perfectly linear, fact probably caused by some heterogeneities due to their biogenic origin. With a simple and quick measure of their peaks position it is now possible to rapidly estimate their magnesium content, dividing them into low-Mg (0 - 5.5 mol% MgCO₃), and high-Mg calcites (10.5 - 20 mol% MgCO₃), opening up interesting potentialities in several fields as marine biology.^(Borromeo et al. 2017a) With this method, on Quaternary fossils, where diagenetic substitution of Mg calcite has not taken place yet, it would be now possible to obtain quick information about species (e. g. foraminifers, algae, barnacles and echinoderms), their habits and paleoecological conditions (as water saturation and water temperature). This study demonstrates, also, that Raman spectroscopy could provide

an innovative work perspective also in provenance studies and oil exploration when estimates of mineralogical and chemical changes are the focus of the study, and moreover, in marine geology and biology fields. Raman spectroscopy is even more attractive – for the mentioned fields of research – than many other methods because of the non-destructive nature and its very short analytical time.

Afterwards, knowing that Raman spectroscopy was a valid method to discriminate between carbonates, I tried to get deeper in the EOR research field, applying Raman and Tip-Enhanced Raman spectroscopies to flooded and unflooded chalk cores, since the most important and common reservoirs in the Norwegian continental shelf are hosted in this kind of sedimentary rock. Both techniques could demonstrate that dolomite is not an existing phase but an intermingled occurrence of magnesite and calcite. This result is of utmost importance for the modeling of the fluid-rock interaction during EOR experiments.^(Nermoen et al. 2015; Zimmermann et al. 2015a; Andersen et al. 2017)

Furthermore, with both methods, it was possible to confidently distinguish primary calcite to the after-flooding grown magnesite crystals down to the micrometric (Raman) and nanometric (TERS) scales, since by these two techniques is possible to obtain mineralogical and chemical information. The very fine-grained and soft texture of this sedimentary rock made its analysis quite challenging with common methods, and for this reason in the last years several high performing techniques were included in Enhanced Oil Recovery (EOR) research. Three cores were tested, one named Long Term Test, LTT, studied by Raman, another one named Middle Long Term test, MLTT, studied by TERS, and the last one named Ultra Long Term Test, ULTT, analysed with both spectroscopies.

Raman spectroscopy permitted to obtain a quick evaluation of the LTT and ULTT composition in some days of work, thanks to the quickness of the analyses.^(Borromeo et al 2018a) It was possible to detect magnesite down to slice 4 of the core, adding new information to a previous study

made on the same core, by Zimmermann et al. (2015), where the major alteration front was suggested between LT3 and LT4. Furthermore Raman spectroscopy could also confirm that the alteration front was no longer present within the ULTT, which means that in three years of MgCl_2 injection, a sufficient quantity of Mg^{2+} was flooded into the core,^(Nerموen et al. 2015) permitting the substitution of almost all the Ca^{2+} to take place. As already seen with other techniques (SEM, XRD) applied in the same previous study,^(Zimmermann et al. 2015a) it was not possible to detect silicates in the two cores using Raman spectroscopy or Tip-Enhanced Raman spectroscopy. In fact, it is very difficult to find a technique that could provide a resolution high enough to spot $<1 \mu\text{m}$ crystals and simultaneously have the capability to cover a portion of the sample wide enough to detect a $\leq 5 \%$ component, in a quick way, and image it at the same time. In the LTT sample nano-crystals of quartz has been detected only by nano-SIMS,^(Zimmermann et al. 2015a) which is a very time-consuming and destructive methodology, extraordinarily expensive and not quantitative. Raman spectroscopy could be the tool to use, since is less time consuming than TERS, but the scanning process, is still a technical issue. A very low abundance of a mineral, in fact, may be challenging to detect unless collecting a really huge number of spectra, which in turn would be time consuming with Raman and extremely time consuming with TERS. Furthermore, the identification of small and so thin hydrated minerals is quite difficult to achieve in the $0\text{-}1200 \text{ cm}^{-1}$ region of the Raman spectra, since their signal is weak and easily covered by the higher carbonate peaks. For this reason, we tried to detect them, by Raman spectroscopy, with a different setting of the instrumentation, moving the analyses to the high region of the Raman spectra, around 3500 cm^{-1} , where the OH vibrational modes are present. Unfortunately, no signal from phyllosilicates has been detected.

In order to exceed the resolution limit of the Raman spectroscopy we tried to apply Tip-Enhanced Raman spectroscopy to flooded chalk

cores, since the major issue with Raman spectroscopy on chalk is that the very little grain-size of the coccoliths and the secondary grown crystals make not possible to achieve a satisfactory imaging of the spotted area.^(Borromeo et al. 2017b; 2018b) As mentioned above, to the contrary of Raman, TERS requires considerable expertise and sample preparation, but provides an outstanding spatial resolution (~ 20 nm), even if really time consuming.

Tip-Enhanced Raman Spectroscopy could produce two kinds of imaging at the nanoscale, representing the height signal (topography) and the oscillation magnitude one, helping to define topography and grains boundaries.^(Borromeo et al. 2017b; 2018b) Furthermore spectra and Raman maps could be obtained and superimposed to these maps.

Sample preparation turned out to be tough and fundamental for a positive outcome of the analyses, since the instrumentation is extremely sensitive to roughness, and a perfectly smooth surface is impossible to be obtained with such a soft material like chalk. For this reason, before collecting Raman maps, the samples were imaged using the AFM in non-contact mode, in order to select smooth regions to be analysed with TERS. Moreover, images were acquired within small areas ($< 5\mu\text{m} \times 5\mu\text{m}$) in order minimize the effects of the surface-roughness. Despite this procedure to optimize the AFM maps, the result on chalk were not at the level of the ones obtained with TERS on organic and biological samples,^(Pyne et al. 2014) but, anyway, even if time consuming, images with an unachievable resolution for a Raman spectrometer were collected.

The magnitude of the enhancement was limited by the impossibility to investigate in *non-gap mode* therefore, to improve the intensity of the signal, the spectra were collected with quite long acquisition times (up to 60 sec). This poses a severe limitation in terms of time to the capability of measuring large TERS mappings with low spatial resolution. In fact, even though the instrument can virtually acquire for several hours, the tip-laser alignment, which is really sensitive and affected by temperature fluctuations and movements of the optical

elements, is not stable enough to guarantee a long acquisition. However, the imaging is related to the roughness of the sample and for this reason cannot reach the quality expected. This lies in the nature of, chalk, which cannot be easily polished on that scale compared to hard minerals or metals.

At the end of this three years research it appears that a direct comparison between Raman spectroscopy and TERS is needed to be carried out (Fig. 61).

Raman Vs TERS

Quick	Time consuming
Micro scale resolution	Nano scale resolution
No sample preparation	Long/difficult sample prep.
No topography	Topography
Cheap	Expensive

Figure 61 - Comparison between pros and cons of Raman and Tip-Enhanced Raman spectroscopies.

Raman spectroscopy, thanks to its quickness, low cost, and micrometric resolution, turned out to be very suitable for these studies as, in few seconds and without any sample preparation, a mineralogical identification can be provided. It is perfectly complementary to methods such as SEM-EDS and in few days of work permits to estimate the mineral composition and calcite/magnesite % present a chalk core, and to investigate mineralogical changes occurring along

the sample. However, the restrictions imposed by the diffraction limit did not allow in distinguishing the secondary grown crystals from the coccolithophore rings or fragments. This is related to the impossibility of visualization of sub-micrometric grains in chalk with an optical microscope.

TERS methodology, with its outstanding resolution, could map the topography and the composition of the samples reaching the nano-scale. Unfortunately, as mentioned above, the impossibility to use the so-called *gap-mode* precluded reaching a very good quality of the maps and this method turned out to be very time consuming on chalk, since it requires a particular sample preparation and the analyses are quite challenging.

To sum up, it is possible to state that there are two techniques, Raman and TERS that can both identify chalk mineralogy and add a sufficient informative image. Raman spectroscopy represents a very helpful methodology that could and should be used on hydrocarbon drilling rigs, possibly even as a drilling steering tool, because this study could show that positive and useful results were generated.^(Borromeo et al. 2018a)

This can lead to well-developed methodologies in the future for different approaches, like the petroleum industry.

This PhD study demonstrated the feasibility of TERS investigations of chalk samples, and subsequently of other small-grained rock samples, besides its usual use for organic and inorganic thin layers, and it qualifies TERS as an interesting investigation tool in oil research field, even if the required sample preparation and the long acquisition times prevent its massive use as characterization tool. The best way to exploit TERS potentiality in this field would be, to investigate selected key samples, from which more general information can be gathered.

The subsequent step is comparing the used techniques with other already applied in EOR. Raman spectroscopy on micron scale is able in determining the mineralogy but cannot provide images, while Mineral Liberation Analysis (MLA)^(Minde et al. 2017) and high-resolution field

emission scanning electron microscope coupled with energy dispersive spectrometer (FEG-SEM-EDS)^(Riesnes et al. 2003, 2005; Korsnes et al. 2006; Hjuler and Fabricius, 2007; Hiorth et al. 2010; Madland et al. 2011; Zimmermann et al. 2015a; Minde et al. 2017)

can image the minerals but not determine via the chemistry the mineralogy because the spot-size of the EDS is too large. Routine measurements on FEG-SEM can be rather quick and may be used – depending on the equipment of the laboratories – complementary to Raman spectroscopy as a first quick investigation of the mineralogy and texture. Chemical analyses with a resolution comparable to TERS one, are transmission electron microscope (TEM)^(Egeland et al. 2017; Minde et al. 2017; Borromeo et al. 2018b) which, as TERS, is time consuming and expensive and cannot perform mineralogical analyses but just chemical ones. Another comparable new frontier technique is the Nanoscale Secondary Ion Mass Spectrometry (SIMS), which, however, cannot image well the spot-area, only when coupled with electron microscopes (nanoSIMS)^(Zimmermann et al. 2015a; Minde et al. 2016) or Focused ion beam-scanning electron microscope technique (FIB-SEM),^(Minde et al. 2017) very problematic and time consuming.

During this PhD thesis also clastic rocks have been analysed by Raman spectroscopy, which, one more time again, demonstrated how useful this tool is to solve doubts that can easily rise while studying silt or sand sized heavy and light minerals by optical microscope, preventing the operator to introduce a bias in quantitative counting. However, this application is well known known^(Raman, 1928; Krishnamurti, 1956; Griffith, 1969; Kuebler et al. 2001; Downs, 2006; Bersani et al. 2009; Andò and Garzanti, 2013; Delmonte et al. 2017)

and lies out of the main focus of this study here. Nevertheless it is of importance to mention that these studies as well have been carried out during this thesis project.

9 Conclusions

Raman spectroscopy is a very efficient, user-friendly technique that permits to obtain, readily, feasible and reliable, information about the chemical composition of minerals.

In the last decades, Raman spectroscopy has already proved to be sensitive to chemical and structural changes in minerals.^(Kuebler et al. 2006; Bersani et al. 2009; Bersani et al. 2014; Aliatis et al. 2015) This PhD study demonstrates that this technique is sufficiently sensitive to chemical and structural changes in calcites, allowing estimating the ratio between Ca^{2+} and Mg^{2+} in the solid solution calcite-magnesite and estimating the magnesium content in fossil faunas and floras, which in turn can provide information about habits and habitat of the organisms. This powerful tool opens up new perspectives in provenance, marine biology, and palaeontological studies.

During this project, Raman spectroscopy and TERS were been used to investigate the mineralogical changes that follow dissolution and compaction in brine-injected chalk, which affect the permeability, porosity, reservoir potential, and the oil flow pathways.^(Madland et al. 2011; Zimmermann et al. 2015a; Wang et al. 2016; Minde et al. 2017) For this reason, a deep investigation of secondary minerals recrystallization is of paramount importance in EOR research. Raman spectroscopy and TERS could, together with other research methods used in the project (FEG-SEM-EDS, WDS, TEM), provide a full range of information on three flooded chalk cores for a broader understanding of the after flooding chemical and mineralogical changes.

With both methods, chalk turned out to be a very challenging material to analyse (as already seen with other methods as MLA, nano-SIMS; FIB-SEM), especially for its sub-micron scale + fluorescence (with Raman spectroscopy) and its softness + roughness (with TERS). For these reasons the quality of the results were not at the height of the ones

obtain on other materials or minerals, but more interesting than the ones obtained on the same material with other techniques. However, not all reservoir rocks do contain minerals or phases with chalk characteristics, which would make the here shown methodology very attractive.

This project proved, once again, that Raman spectroscopy is a robust, cheap, quick, user-friendly point-analysis technique that with a non-destructive and no time consuming sample preparation allows to quickly obtain semi-quantitative mineralogical and chemical information, down to the micrometric scale.

Confocal Raman microscopy has proven to be an extremely popular analytical technique with the set of unique advantages such as:

- No preparation of the sample required.
- Great spatial resolution.
- Clear image quality
- Outstanding chemical differentiation.
- Ability to perform 3D mapping of bulk samples.

For its characteristics, in the future, Raman spectroscopy could be used as a breakthrough tool in petroleum exploration of conventional and unconventional reservoirs, as siltstones, sandstones or chalk. Until today Raman spectroscopy has been only occasionally applied in the oil industry^(Gorelik et al. 2000; Costa et al. 2006; Sebek et al. 2011; Andrews et al. 2015) and it is time for it to become a routine analysis, on-shore and off-shore, where mineral and chemical characterization of rocks is needed. In particular, I would like to promote its use in pilot projects, as the ones that will incorporate EOR flooding in clastic at the NIOR centre of Norway.

Furthermore, the feasibility of performing TERS measurements on chalk has been investigated and proved. This result is very interesting because it stands out for being obtained on non-conductive samples, therefore not in *gap made*. These results qualify TERS as an interesting

Conclusions

investigation tool in this field, even if it is quite expensive and the required sample preparation and the long acquisition times prevent its massive use as characterization tool. The best way to exploit TERS potentiality in this field would be, to investigate selected key samples, where nano scale information are needed.

10 References

- 11 Ali, A.Y.; Salah Hamad, A.S.; Abdulaziz, A.K.; Mohammed Saleh, A.J.; Laboratory Investigation of the Impact of Injection Water Salinity and Ionic Content on Oil Recovery From Carbonate Reservoirs, **2011**. *SPE Reservoir Evaluation and Engineering*;
- 12 Aliatis, I.; Lambruschi, E.; Mantovani, L.; Benisek, A.; Bersani, D.; Carpenter, M.; Gatta, G.; Tribaudino, M. and Lottici, P.; Characterization of plagioclase solid solution by Raman spectroscopy: a procedure for the determination of the chemical composition,. *Periodico Di Mineralogia*, **2015**, 17-18;
- 13 Andersen, P.Ø.; Evje, S.; Madland, M.V.; Hiorth, A.; A geochemical model for interpretation of chalk core flooding experiments. *Chem. Eng. Sci.*; **2012**, *84*, 218-241;
- 14 Andersen, P.Ø.; Wang, W.; Madland, M.V.; Zimmermann, U.; Korsnes, R.I.; Bertolino, S.R.A.; Minde, M.; Schulz, B.; Gilbricht, S.; Comparative Study of Five Outcrop Chalks Flooded at Reservoir Conditions: Chemo-mechanical Behaviour and Profiles of Compositional Alteration. *Transport in Porous Media*, **2017**, 1-47. doi: <https://doi.org/10.1007/s11242-017-0953-6>;
- 15 Andò S. and Garzanti E.; In: Heavy minerals in use, (Vol. 58). Mange, M. A.; and Wright, D. T. Eds.. Elsevier **2007**;
- 16 Andò S. and Garzanti E.; Raman spectroscopy in heavy-mineral studies. From: Scott, R. A.; Smyth, H. R.; Morton, A. C. and Richardson, N. (eds) *Sediment Provenance Studies in Hydrocarbon Exploration and Production. Geological Society, London, Special Publications*, **2013**, 386;
- 17 Andò S.; Vignola P.; Garzanti E.; Raman counting: a new method to determine provenance of silt. *Rendiconti Lincei*, **2011**, *22* (4) 327-347;
- 18 Andò, S.; Bersani, D.; Vignola, P.; Garzanti E.; *Spectrochimica Acta Part A: Molecular and Biomolecular Spectroscopy*, **2009**, *73*, 450-455;
- 19 Andreassen, K.A. and Fabricius, I. L.; Biot critical frequency applied to description of failure and yield of highly porous chalk with different pore fluids, *Geophysics*, **2010**, *75*(6), E205-E213;
- 20 Andrews, A. B.; Wang D.; Marzec, K. M.; Mullins, O. C.; Crozier, K. B. Surface enhanced Raman spectroscopy of polycyclic aromatic hydrocarbons and molecular asphaltenes. *Chem. Phys. Lett.* **2015**, *620*, 139-143;
- 21 Årlebrand, A.; Hope, B.; Andò, S.; Zimmermann, U.; Vezzoli, G.; Borromeo, L.; After and before the storm: effect of erosion during heavy mineral climate events on the composition of sediments, a comparison of provenance information. *NGF Abstracts and Proceedings, Vinterkonferansen 2015*, **2015**, Stavanger, 107-108;

References

- 22 Austad, T. and Standnes, D. C. Spontaneous imbibition of water into oil-wet carbonates. *J Pet Sci Eng.* **2003**, *39*, 363-376;
- 23 Austad, T.; Strand, S.; Madland, M.V.; Puntervold, T.; Korsnes, R.I.; Seawater in chalk: An EOR and compaction fluid. *SPE Reservoir Evaluation and Engineering*, **2008**, *11*(4), 648-654;
- 24 Bailo, E. and Deckert, V.; Tip-enhanced Raman scattering, *Chemical Society Reviews.*; **2008**, *37*, 921-930;
- 25 Balan E., Neuville DR., Trocellier P., Fritsch E., Muller JP., Calas G.; Zircon metamictization, zircon stability and zirconium mobility. *Am Mineral* *86*:1025-1033;
- 26 Barone, G.; Bersani, D.; Crupi, V.; Longo, F.; Longobardo, U.; Lottici, P.P.; Aliatis, I.; Majolino, D.; Mazzoleni, P.; Raneri, S. and Venuti, V.; **2014**. A portable versus micro-Raman equipment comparison for gemmological purposes: the case of sapphires and their imitations. *Journal of Raman Spectroscopy*, *45*(11-12), pp.1309-1317;
- 27 Barone, G.; Bersani, D.; Jehlička, J.; Lottici, P. P.; Mazzoleni, P.; Raneri, S.; Vandenebeele, P.; Di Giacomo, C.; and Larinà. G.; Nondestructive investigation on the 17-18th centuries Sicilian jewelry collection at the Messina regional museum using mobile Raman equipment. *Journal of Raman Spectroscopy* , **2015** ,*46*, 10 989-995;
- 28 Barone, G.; Bersani, D.; Lottici, P. P.; Mazzoleni, P.; Raneri, S.; & Longobardo, U.; Red gemstone characterization by micro-Raman spectroscopy: the case of rubies and their imitations. *Journal of Raman Spectroscopy*, **2016**, *47*(12), 1534-1539;
- 29 Bell, I.M.; Clark, R.J. and Gibbs, P.J.; Raman spectroscopic library of natural and synthetic pigments (pre- \approx 1850 AD). *Spectrochimica Acta Part A: Molecular and Biomolecular Spectroscopy*, **1997**. *53*(12), pp.2159-2179.
- 30 Bernardino, D. E. N.; Izumi, C. MS; and de Faria, D. LA.; Fake turquoises: an example of Raman Microscopy applied to gemology. *Forensic Science International* *262*, **2016**, 196-200;
- 31 Bersani D. and Lottici P.P.; Applications of Raman spectroscopy to gemology. *Anal. Bioanal. Chem.* **2010**, *397*, 2631–2646;
- 32 Bersani, D. and Lottici, P.P.; Raman spectroscopy of minerals and mineral pigments in archaeometry. *Journal of Raman Spectroscopy*, **2016**, *47*(5), pp.499-530;
- 33 Bersani, D.; Andò, S.; Scrocco, L.; Gentile, P.; Salvioli-Mariani E.; and Lottici, P. P.; Study of the composition of amphiboles in the tremolite - ferroactinolite series by micro-raman and sem-edxs. *11th GeoRaman International Conference*, **2014b**, St. Louis, Missouri, USA;

References

- 34 Bersani, D.; Andò, S.; Vignola, P.; Moltifiori, G.; Marino, I. G.; Lottici, P. P.; and Diella, V.; Raman spectroscopy as a routine tool for garnet analysis. *Spectrochim.*; **2009**, *73*, 484-491;
- 35 Bersani, D.; Azzi, G.; Lambruschi, E.; Barone, G.; Mazzoleni, P.; Raneri, S.; Longobardo, U.; and Lottici, P.P.; Characterization of emeralds by micro-Raman spectroscopy. *Journal of Raman Spectroscopy* *45*, **2014a**, 11-12, 1293-1300;
- 36 Bersani, D.; Conti, C.; Matousek, P.; Pozzi, F.; and Vandenabeele, P.; Methodological evolutions of Raman spectroscopy in art and archaeology. *Analytical Methods*, **2016**, *8*(48), 8395-8409;
- 37 Birkeland, H.; Malde, P.-K.; Oppedal, E.; Østensen, O.C.; Zimmermann, U.; Andò, S.; Borromeo, L. Correlation of quartz-rich Ordovician successions in the Cantabrian Mountains using high-resolution heavy mineral analysis and Raman spectroscopy. *NGF Abstracts and Proceedings, Vinterkonferansen 2015*, **2015**, Stavanger, 11-12;
- 38 Bischoff, W.D.; Sharma, S.K.; Mackenzie, F.T.; Carbonate ion disorder in synthetic and biogenic magnesian calcites: a Raman spectral study. *Am. Mineral.* **1985**, *70*, 581–589;
- 39 Borromeo L.; Zimmermann U.; Andò S.; Coletti G.; Bersani D.; Basso D.; Gentile P.; Garzanti E.; Raman Spectroscopy as a tool for magnesium estimation in Mg- calcite. *Periodico di Mineralogia, ECMS, European Conference on Mineralogy and Spectroscopy*, **2015**, Rome, Italy, *84*, *2*, 35-36;
- 40 Borromeo L.; Zimmermann U.; Andò S.; Coletti G.; Garzanti E.; Raman spectroscopy: an unconventional and innovative tool to identify the mineralogy of chalk and other fine-grained rocks applicable to IOR research. *Abstracts and Proceedings, Vinterkonferansen 2015*, **2015**, Stavanger;
- 41 Borromeo L.; Egeland N.; Minde M.; Zimmermann U.; Andò S.; Toccafondi C.; Ossikovski R.; Micro- and Nano- Raman analyses of chalk. *IOR Conference*, **2016**, Stavanger, Norway;
- 42 Borromeo L.; Zimmermann U.; Andò S.; Coletti G.; Bersani D.; Egeland N.; Basso D.; Gentile P.; Garzanti E.; Raman Spectroscopy as a tool for magnesium estimation in Mg-calcite. *Goldschmidt Conference*, **2016**, Yokohama, Japan;
- 43 Borromeo, L.; Zimmermann, U.; Andò, S.; Coletti, G.; Bersani, D.; Basso, D.; Gentile, P.; Schulz, B. and Garzanti, E. Raman spectroscopy as a tool for magnesium estimation in Mg-calcite. *JRS*. **2017a**, *48*(7), 983-992.
- 44 Borromeo, L.; Minde, M.; Toccafondi, C.; Zimmermann, U.; Andò, S.; Ossikovski R. A New Frontier Technique for Nano-analysis on Flooded Chalk-TERS (Tip-Enhanced Raman Spectroscopy). In *IOR 2017-19th European Symposium on Improved Oil Recovery*. **2017b**.

References

- 45 Borromeo L.; Zimmermann U.; Andò S.; Minde M.; Egeland N.; Toccafondi C.; Ossikovski R.; Micro-Raman spectroscopy and TERS (Tip-Enhanced Raman Spectroscopy) applied to Enhanced Oil Recovery. *Nano Innovation conference*, **2017**, Rome, Italy;
- 46 Borromeo, L.; Egeland N.; Minde, M. W.; Zimmermann, U.; Andò, S.; Madland, M. V. and Korsnes, R. I.; Quick, easy and economic mineralogical studies of flooded chalk for EOR experiments using Raman spectroscopy. Submitted to *Minerlas*, **2018a** (doi: 10.20944/preprints201802.0173.v1).
- 47 Borromeo, L.; Toccafondi, C.; Minde, M.; Zimmermann, U.; Andò, S.; Madland, M. V.; Korsnes, R. I. Ossikovski R. Application of Tip-Enhanced Raman Spectroscopy in the nanoscale characterization of flooded chalk. Submitted to *First Break*, **2018b**;
- 48 Borromeo, L.; Zimmermann, U.; Andò, S.; Raman spectroscopy applied to mineralogical analyses of flooded chalk. *IOR Conference*, Stavanger, Norway, **2018**;
- 49 Bouchard, M.; Smith, D.C. and Carabatos-Nédelec, C.; An investigation of the feasibility of applying Raman microscopy for exploring stained glass. *Spectrochimica Acta Part A: Molecular and Biomolecular Spectroscopy*, **2007**, 68(4), pp.1101-1113.
- 50 Buzzini, P. and Suzuki, E.; Forensic applications of Raman spectroscopy for the in situ analyses of pigments and dyes in ink and paint evidence. *Journal of Raman Spectroscopy*, **2016**, 47(1),16-27;
- 51 C. Carteret, M. De la Pierre, M. Dossot, F. Pascale, A. Erba, and R. Dovesi, The vibrational spectrum of CaCO₃ aragonite: A combined experimental and quantum-mechanical investigation, *J. Chem. Phys.* **2013**, 138, 014201;
- 52 Cantisani, E.; Cavalieri, M.; Lofrumento, C.; Pecchioni, E. and Ricci, M.; 2012. Ceramic findings from the archaeological site at Aiano-Torraccia di Chiusi (Siena, Italy): a multi-analytical approach. *Archaeological and Anthropological Sciences*, 4(1), 29-4;
- 53 Casadio, F.; Daher, C. and Bellot-Gurlet, L.; Raman spectroscopy of cultural heritage materials: overview of applications and new frontiers in instrumentation, sampling modalities, and data processing. *Topics in Current Chemistry*, **2016**, 374(5), 62;
- 54 Casadio, F.; Leona, M.; Lombardi, J.R. and Van Duyne, R.; Identification of organic colorants in fibers, paints, and glazes by surface enhanced Raman spectroscopy. *Accounts of chemical research*, **2010**, 43(6), 782-791;
- 55 Chalmers, J. M.; Edwards, H. G.; and Hargreaves, M. D. Eds. *Infrared and Raman spectroscopy in forensic science*. John Wiley and Sons; **2012**;
- 56 Chave, K. E.; Aspects of the biogeochemistry of magnesium. 1. Calcareous marine organisms. *Journal of Geology*, **1954a**, 62,266-283;

References

- 57 Chave, K. E. A solid solution between calcite and dolomite. *Journal of Geology*, **1952**, *60*, 190-192;
- 58 Chave, K. E.; Aspects of the biogeochemistry of magnesium. 2. Calcareous sediments and rocks. *Journal of Geology*, **1954b** *62*, 587-599;
- 59 Chiriu, D.; Ricci, P.C.; Carbonaro, C.M.; Nadali, D.; Polcaro, A. and Mocci, F.; Drying oil detected in mid-third Millennium BC Mesopotamian clay artifacts: Raman spectroscopy and DFT simulation study. *Microchemical Journal*, **2016**, *124*, pp.386-395;
- 60 Chourpa, I.; Douziech-Eyrolles, L.; Ngaboni-Okassa, L.; Fouquenot, J. F.; Cohen-Jonathan, S.; Soucé, M. and Dubois, P. Molecular composition of iron oxide nanoparticles, precursors for magnetic drug targeting, as characterized by confocal Raman microspectroscopy. *Analyst*, **2005**, *130*(10), 1395-1403;
- 61 Colomban, P. and Tournié, A.; On-site Raman identification and dating of ancient/modern stained glasses at the Sainte-Chapelle, Paris. *Journal of Cultural Heritage*, **2007**, *8*(3), pp.242-256;
- 62 Conti, C.; Colombo, C.; Realini, M.; Zerbi, G. and Matousek, P.; Subsurface Raman analysis of thin painted layers. *Applied spectroscopy*, **2014**, *68*(6), pp.686-691;
- 63 Conti, C.; M. Realini, C. Colombo, A. Botteon, and P. Matousek. "Contrasting confocal with defocusing microscale spatially offset Raman spectroscopy." *Journal of Raman Spectroscopy* **2016**, *47*, 565-570;
- 64 Costa, J. C. S.; Sant'Ana, A. C.; Corio P; Temperini, M. L. A.; Chemical analysis of polycyclic aromatic hydrocarbons by surface-enhanced Raman spectroscopy. *Talanta* **2006**, *70*, 1011-1016;
- 65D. Krishanmurti, The Raman spectrum of calcite and its interpretation, *Proceedings of the Indian Academy of Sciences - Section A*, **1957**; *46*, 3, 183;
- 66 D'Ippolito, V.; Andreozzi, G. B.; Bersani, D.; and Lottici, P. P. Raman fingerprint of chromate, aluminate and ferrite spinels. *J. Raman Spectrosc.*; **2015**, *46*, 1255–1264. doi: 10.1002/jrs.4764;
- 67 Daher, C.; Drieu, L.; Bellot- Gurlet, L.; Percot, A.; Paris, C. and Le Hô, A.S.; Combined approach of FT- Raman, SERS and IR micro- ATR spectroscopies to enlighten ancient technologies of painted and varnished works of art. *Journal of Raman Spectroscopy*, **2014**. *45*(11-12), 1207-1214;
- 68 Dandeu, A.; Humbert, B.; Carteret, C.; Muhr, H.; Plasari, E.; and Bossoutrot, J.-M.; Raman spectroscopy—A powerful tool for the quantitative determination of the composition of polymorph mixtures: Application to CaCO₃ polymorph mixtures. *Chem. Eng. Technol.*; **2006**, *29*, 221–225;
- 69 De Gelder, J.; Gussem, K.; Vandenebee, P.; and Moens, L.; Reference database of Raman spectra of biological molecules. *Journal of Raman spectroscopy* **38**, **2007**, *9*, 1133-1147;

References

- 70 De La Pierre M.; Carteret C.; Maschio L.; André E.; Orlando R. and Dovesi R.; The Raman spectrum of CaCO₃ polymorphs calcite and aragonite: A combined experimental and computational study. *The Journal Of Chemical Physics*, **2014**, *140*, 164509;
- 71 De Ligny D, Neuville DR La spectrométrie Raman: un outil de choix pour l'étude des mécanismes de nucléation et de croissance cristalline. In: Du verre au Cristal: Nucléation, Croissance et Démixtion, de la Recherche aux Applications. Neuville DR, Cormier L, Caurant D, Montagne L (eds) EDP-Sciences, **2013**; 285-309;
- 72 De Veij, M.; Vandenabeele, P.; De Beer, T.; Remon, J. P.; and Moens, L.; Reference database of Raman spectra of pharmaceutical excipients. *Journal of Raman Spectroscopy* **40**, **2009**, *3*, 297-307;
- 73 Deer W. A.; Howie R. A.; and Zussman J.; An Introduction to the Rock-Forming Minerals. **1992**, Eds. Longman Group, England;
- 74 Delmonte, B.; Paleari, C. I.; Andò, S.; Garzanti, E.; Andersson, P. S.; Petit, J. R.; Crosta, X.; Narcisi, B.; Baroni, C.; Salvatore, M. C.; Baccolo, G.; Maggi, V.; Causes of dust size variability in central East Antarctica (Dome B): Atmospheric transport from expanded South American sources during Marine Isotope Stage 2. *Quaternary Science Review*, **2017**, *168*, 55-68;
- 75 Derbyshire, A. and Withnall, R.; Pigment analysis of portrait miniatures using Raman microscopy. *Journal of Raman Spectroscopy*, **1999**, *30*(3), 185-188;
- 76 Downs R.T.; The RUFF Project: an integrated study of the chemistry, crystallography, Raman and infrared spectroscopy of minerals. *19th General Meeting of the International Mineralogical Association*, Kobe, **2006**. Japan, 03-13;
- 77 Dresselhaus, M.S.; Dresselhaus, G.; Saito, R. and Jorio, A.; Raman spectroscopy of carbon nanotubes. *Physics reports*, **2005**, *409*(2), pp.47-99;
- 78 Dresselhaus, M.S.; Jorio, A.; Hofmann, M.; Dresselhaus, G. and Saito, R.; Perspectives on carbon nanotubes and graphene Raman spectroscopy. *Nano letters*, **2010**. *10*(3), 751-758;
- 79 Durickovic, I.; Using Raman Spectroscopy for Characterization of Aqueous Media and Quantification of Species in Aqueous Solution. In *Applications of Molecular Spectroscopy to Current Research in the Chemical and Biological Sciences*, InTech, **2016**;
- 80 Dutta, P. K.; Shieh, D. C.; and Puri, M. Correlation of framework Raman bands of zeolites with structure. *Zeolites*, **1988**, *8*(4), 306-309;
- 81 Edwards, H.; Villar, S.; Jehlicka, J.; Munshi, T. FT-Raman spectroscopic study of calcium-rich and magnesium-rich carbonate minerals. *Spectrochim. Acta A*, **2005**; *61*, 2273;
- 82 Egeland, N. Raman Spectroscopy Applied to Enhanced Oil Recovery.

References

- University of Stavanger, unpublished MSc thesis, **2015**.
- 83 Egeland, N.; Minde, M.W.; Kobayashi, K.; Ota, T.; Nakamura, E.; Zimmermann, U.; Madland, M.W. and Korsnes, R.I. Quantification of Mineralogical Changes in Flooded Carbonate under Reservoir Conditions. In *IOR 2017-19th European Symposium on Improved Oil Recovery*. **2017**.
- 84 Egeland, N.; Zimmermann, U.; Borromeo, L.; Andò, S.; Madland, M. V.; Minde, M. W.; Korsnes, R. I.; Raman spectroscopy applied to Enhanced Oil Recovery research. *Goldschmidt*, **2016**;
- 85 Ellery, A.; and Wynn-Williams, D.. Why Raman spectroscopy on Mars? - A case of the right tool for the right job. *Astrobiology*, **2003**, 3(3), 565-579.
- 86 Everall, N. J.; Modeling and measuring the effect of refraction on the depth resolution of confocal Raman microscopy. *Applied Spectroscopy*, **2000**, 54(6), 773-782;
- 87 Fathi, S.J.; Austad, T.; Strand, S. "Smart Water" as a Wettability Modifier in Chalk: The Effect of Salinity and Ionic Composition, *Energy and fuels*, **2010**, 24, 2514-2519.
- 88 Felder, R. M.; Spence, R. D.; Ferrell, J. K. A method for the dynamic measurement of diffusivities of gases in polymers. *J. Polym. Sci.* **1975**. 19(12), 3193-3200.
- 89 Félidj, N.; J. Aubard, G. Lévi, J. R. Krenn, M. Salerno, G. Schider, B. Lamprecht, A. Leitner, and F. R. Aussenegg. Controlling the optical response of regular arrays of gold particles for surface-enhanced Raman scattering. *Physical Review B* 65, **2002**, 7, 075419.
- 90 Freeman J. J. and Wang, A et al. Characterization of natural feldspars by Raman spectroscopy for future planetary exploration. *The Canadian Mineralogist*, **2008**, 46, 1477-1500;
- 91 Fremout, W. and Saverwyns, S.; Identification of synthetic organic pigments: the role of a comprehensive digital Raman spectral library. *Journal of Raman Spectroscopy*, **2012**. 43(11), pp.1536-1544.
- 92 Frezzotti M. L.; Francesca Tecce, Alessio Casagli, Raman spectroscopy for fluid inclusion analysis. *Journal of Geochemical Exploration*, **2012**, 112, 1–20;
- 93 G. A. Gourzoulidis I. Tsilikas, A. Serafetinides, I. Sianoudis, P. Stasinopoulou, A. Achtipis, C. Kappa and Makropoulou M.; The Identification Of Occupational Exposure To Laser Radiation In Greece; **2017**, 5, 12, 1-18;
- 94 Gabrielli, C. Jaouhari, R. Joiret S. and G. Maurin In situ Raman spectroscopy applied to electrochemical scaling. Determination of the structure of vaterite. *J. Raman Spectrosc.* **2000**, 31, 497–501;
- 95 Garzanti, Eduardo, Sergio Andó, Christian France-Lanord, Paolo Censi, Pietro Vignola, Valier Galy, and Maarten Lupker. Mineralogical and chemical

References

- variability of fluvial sediments 2. Suspended-load silt (Ganga–Brahmaputra, Bangladesh). *Earth and Planetary Science Letters* 302, **2011**, 1-2, 107-120;
- 96 Gill, D.; Kilponen, R.G. and Rimai, L.; Resonance Raman scattering of laser radiation by vibrational modes of carotenoid pigment molecules in intact plant tissues. **1970**, *Nature*, 227(5259), 743;
- 97 Gillet, P.; Biellmann, C.; Reynard, B.; McMillan, P. Raman Spectroscopic studies of carbonates part I: high-pressure and high-temperature behaviour of calcite, magnesite, dolomite and aragonite. *Phys. Chem. Minerals*, **1993**, 20, 1–18;
- 98 Goeller, Lindsay J.; and Mark R. Riley. "Discrimination of bacteria and bacteriophages by Raman spectroscopy and surface-enhanced Raman spectroscopy." *Applied spectroscopy*, **2007**, 61.7, 679-685.
- 99 Goldsmith, J.R.; Graf, D.L.; Joensuu, O.I.; The occurrence of magnesian calcites in nature. *Geochimica et Cosmochimica Acta*, **1955**, 7, 212-230;
- 100 Gorelik, V. S.; Chervyakov, A. V.; Kol'tsova, L. V.; Veryaskin, S. S. Raman Spectra of Saturated Hydrocarbons and Gasolines. *J. Russ. Laser Res.* **2000**, 21, 323-334;
- 101 Griffith W.P.; Raman spectroscopy of minerals. *Nature*, **1969**, 224, 264–266;
- 102 Grønberg, A.; Røynestad, L.M.; Zimmermann, U.; Andò, S.; Borromeo, L.; Garzanti, E. Provenance signals from coarse-grained sandstones, siltstones and shales in the Middle to Upper Cambrian Oville Formation - a test using whole-rock geochemistry and high-resolution heavy mineral analysis. NGF Abstracts and Proceedings, Vinterkonferansen 2015.; 12.-14.1. **2015**, Stavanger, 35-36;
- 103 Guineau B.; and Guichard, V.; ICOM Committee for Conservation: 8th Triennial Meeting, *Preprints, The Getty Conservation Institute, Marina del Rey, CA*, **1987**, 2, p659;
- 104 Guineau, B.; & Guichard, V. Identification de colorants organiques naturels par microspectrométrie Raman de résonance et par effet Raman exalté de surface (SERS). In *ICOM committee for conservation: 8th triennial meeting, Sydney, Australia, 1987. Preprints* (Vol. 2, pp. 659-666). The Getty Conservation Institute;
- 105 H. J. Butler, Lorna Ashton, Benjamin Bird, Gianfelice Cinque, Kelly Curtis, Jennifer Dorney, Karen Esmonde-White, Nigel J Fullwood, Benjamin Gardner, Pierre L Martin-Hirsch, Michael J Walsh, Martin R McAinsh, Nicholas Stone and Francis L Martin. Using Raman spectroscopy to characterize biological materials; *Nature Protocols* **2016**, 11, 664–687 (2016) doi:10.1038/nprot.2016.036;
- 106 Haka, A.S.; Shafer-Peltier, K.E.; Fitzmaurice, M.; Crowe, J.; Dasari, R.R. and Feld, M.S.; Diagnosing breast cancer by using Raman spectroscopy.

References

- Proceedings of the National Academy of Sciences of the United States of America*, **2005**, *102*(35), 12371-12376;
- 107 Hayez, V.; Costa, V.; Guillaume, J.; Terryn, H. and Hubin, A.; Micro Raman spectroscopy used for the study of corrosion products on copper alloys: study of the chemical composition of artificial patinas used for restoration purposes. *Analyst*, **2005**, *130*(4), 550-556;
- 108 Heggheim, T.; Madland, M. V.; Risnes, R.; Austad, T. A chemical induced enhanced weakening of chalk by seawater. *J. Pet. Sci. Eng.* **2005**, *46*(3), 171-184;
- 109 Herman, R. G.; Bogdan, C. E.; Sommer, A. J. and Simpson, D. R. Discrimination among carbonate minerals by Raman spectroscopy using the laser microprobe. *Applied Spectroscopy*, **1987**, *41*(3), 437-440;
- 110 Hermansen, H; Landa, G. H.; Sylte, J. E.; Thomas, L. K. Experiences after 10 years of waterflooding the Ekofisk Field, Norway. *J. Pet. Sci. Eng.* **2000**, *26.1*, 11-18;
- 111 Hiorth, A.; Cathles, L.; Madland, M. The Impact of Pore Water Chemistry on Carbonate Surface Charge and Oil Wettability, *Transp. Porous Med.* **2010**, *85*(1), 1–21;
- 112 Hiorth, A.; Jettestuen, E.; Lawrence, C. M.; Madland M. V. Precipitation, dissolution, and ion exchange processes coupled with a lattice Boltzmann advection diffusion solver. *Geochimica et Cosmochimica Acta*, **2013**, *104*, 99-110.
- 113 Hjuler, M. L. and Fabricius, I. L. Engineering properties of chalk related to diagenetic variations of Upper Cretaceous onshore and offshore chalk in the North Sea area. *Journal of Petroleum Science and Engineering*, **2009**, *68*(3), 151-170.
- 114 Hjuler, M. L.; and Fabricius, I. L. Diagenesis of upper cretaceous onshore and offshore chalk from the North Sea area. Technical University of Denmark Danmarks Tekniske Universitet, Department of Civil Engineering Institut for Byggeri og Anlæg, Arctic Technology Centre, ARTEK Center for Arktisk Teknologi, ARTEK, **2007**.
- 115 Hover, V.C.; Walter, L.M. and Peacor, D.R.; Early marine diagenesis of biogenic aragonite and Mg-calcite: new constraints from high-resolution STEM and AEM analyses of modern platform carbonates. *Chemical Geology*, **2001**, *175*(3-4), pp.221-248;
- 116 Jamieson, J. C. Phase Equilibrium in the System Calcite-Aragonite. *The Journal of Chemical Physics*, **1953**, *21*(8), 1385-1390.
- 117 Jehlička, J.; Culka, A.; Bersani, D.; Vandenabeele, P.; Comparison of seven portable Raman spectrometers: beryl as a case study, *J. Raman Spectroscopy*, **2017**, DOI 10.1002/jrs.5214;

References

- 118 Jehlička, J.; Vitek, P.; Edwards, H. G. M.; Hargreaves, M. D.; and Čapoun, T. Fast detection of sulphate minerals (gypsum, anglesite, baryte) by a portable Raman spectrometer. *Journal of Raman Spectroscopy*, **2009**, *40*(8), 1082-1086;
- 119 Jensen, T. B.; K. J. Harpole, and A. Østhus. EOR screening for Ekofisk. In *SPE European Petroleum Conference*. Society of Petroleum Engineers, **2000**.
- 120 Johnson, J. P.; D. W. Rhett, and W. T. Siemers. Rock mechanics of the Ekofisk reservoir in the evaluation of subsidence. In *Offshore Technology Conference*. Offshore Technology Conference, 1988.
- 121 Jorio, A.; Raman spectroscopy in graphene-based systems: prototypes for nanoscience and nanometrology. *ISRN Nanotechnology*, **2012**.
- 122 Kakavand A. and Adl-Zarrabi B.; Introduction of possible inspection methods for evaluating thermal aging status of existing pre-insulated district heating systems Prepared for Department of Civil and Environmental Engineering Division of Building Technology Chalmers University of Technology Gothenburg, Sweden, **2016**;
- 123 Katz. A. The interaction of magnesium with calcite during crystal growth at 25-90°C and one atmosphere. *Geochimica et cosmochimica Acta*, **1973**, *37*. 1563 to 1586;
- 124 Keren, S.; Zavaleta, C.; Cheng, Z.; de La Zerda, A.; Gheysens, O.; and Gambhir, S. S.; Noninvasive molecular imaging of small living subjects using Raman spectroscopy. *Proceedings of the National Academy of Sciences*, **2008**, *105*(15), 5844-5849;
- 125 Kiefert, L.; Haenni, H.A. and Chalain, J.P.; September. Identification of gemstone treatments with Raman Spectroscopy. In *Optical Devices and Diagnostics in Materials Science* **2000**, 4098, 241-252). International Society for Optics and Photonics;
- 126 Korsakov A.; De Gussem K.; Zhukov V. P.; Perraki M.; Vandenabeele P. and Golovin A. V.; 2009. Aragonite-calcite-dolomite relationships in UHPM polycrystalline carbonate inclusions from the Kokchetav Massif, northern Kazakhstan. *Eur. J. Mineral.* **2009**, *21*, 1301;
- 127 Korsnes R. I.; Madland M. V.; Austad T.; Haver S.; and Rosland G. The effects of temperature on the water weakening of chalk by seawater. *Journal of Petroleum Science and Engineering*, **2008a**, *60*, 183- 193.
- 128 Korsnes, R. I.; Strand S.; Hoff Ø.; Pedersen T.; Madland M. V.; Austad T. Does the chemical interaction between seawater and chalk affect the mechanical properties of chalk? In *Multiphysics coupling and long term behaviour in rock mechanics*; Cotthem; A. V.; Charlier R.; Thimus J. F. and Tshibangu J. P. Eds.; Taylor and Francis: London, England, **2006**; pp. 427-

References

- 434;
- 129 Korsnes, R. I.; Wersland, E.; Madland, M. V.; Austad, T. Anisotropy in chalk studied by rock mechanics. *J. Pet. Sci. Eng.* **2008b**, *62*, 28-35.
- 130 Krishnamurti, D. Raman spectrum of magnesite. *Proceedings of the Indian Academy of Sciences – Section A*, **1956**, *43*, 210-212.
- 131 Krishnan K.S. The Raman Spectra of Crystals. *Proc. Roy. Soc.; A*, **1929**, *122*, p. 23;
- 132 Krishnan, R. S.; and Shankar, R. K. Raman effect: History of the discovery. *Journal of Raman Spectroscopy*, **1981** *10*(1), 1-8;
- 133 Kristiansdottir, M.; Zimmermann, U.; Andò, S.; Borromeo, L. Test for dependence of provenance signals in varying facies of the same rock formation: a study of Lower Cambrian rocks deposited in northern Spain. NGF Abstracts and Proceedings, Vinterkonferansen **2015**, 12.-14.1. 2015 Stavanger, 54.
- 134 Kristiansen, K.; Myhre, A.; Zimmermann, U.; Andò, S.; Borromeo, L. Correlation of the Precambrian-Cambrian boundary in siliciclastic rocks using high-resolution heavy mineral analysis in the Cantabrian Mountains. NGF Abstracts and Proceedings, Vinterkonferansen 2015, 12-14.1. **2015**, Stavanger, 54-55.
- 135 Kubler K. E. Et al. Extracting olivine (Fo-Fa) compositions from Raman spectral peak positions. *Geochim. Cosmochim.* **2006**, *70*, 6201-6222;
- 136 Kuebler K.; Wang A.; Abbott K.; Haskin L. A.;. Can we detect carbonate and sulfate minerals on the surface of Mars by Raman spectroscopy? *Lunar and Planetary Science XXXII*, **2001**, n. 1889.
- 137 L. Mantovani, M. Tribaudino, I. Aliatis, E. Lambruschi, P. P. Lottici and D. Bersani, *Phys. Chem. Miner.*; 2014, *42*,179;
- 138 L. Valenzano · Y. Noël · R. Orlando · C. M. Zicovich-Wilson · M. Ferrero · R. Dovesi 2007. Ab initio vibrational spectra and dielectric properties of carbonates: magnesite, calcite and dolomite. *Theor Chem Acc* (2007) 117:991–1000
- 139 Land, L. S. Diagenesis of skeletal carbonates. *Journal of Sedimentary Petrology*, **1967** *37*, 914-930.
- 140 Landsberg G. and Mandelstam L.; *Über die Lichtzerstreuung in Kristallen, Zeit. F. Phys.* **1928**; *50*, 729;
- 141 Langelüddecke, L.; Singh, P. and Deckert, V. Exploring the nanoscale: fifteen years of Tip-Enhanced Raman Spectroscopy. *Applied Spectroscopy OA*, **2015**, *69*(12), 1357-1371.
- 142 Lauwers, D.; Hutado, A. G.; Tanevska, V.; Moens, L.; Bersani, D.; and Vandenabeele, P. Characterisation of a portable Raman spectrometer for in situ

References

- analysis of art objects. *Spectrochimica Acta Part A: Molecular and Biomolecular Spectroscopy*, **2014**, *118*, 294-301;
- 143 Lofrumento, C.; Ricci, M.; Bachechi, L.; De Feo, D.; & Castellucci, E. M. The first spectroscopic analysis of Ethiopian prehistoric rock painting. *Journal of Raman Spectroscopy*, **2012**, *43*(6), 809-816;
- 144 Lommel, E.. Theorie der normalen und anomalen Dispersion. *Annalen der Physik*, **1878**, *239*(3), 339-356.
- 145 Long, D.A.; The Raman effect: a unified treatment of the theory of Raman scattering by molecules. *West Sussex* **2002**;
- 146 Mackenzie, F. T.; Bischoff, W. D.; Bishop, F. C.; Loijens, Michele, Schoonmaker Jane, and Wollast, Roland Magnesian calcites: Low-temperature occurrence, solubility, and solid solution behavior. In R. J. Reeder, Ed.; *Carbonates: Mineralogy and Chemistry. Reviews in Mineralogy*, Mineralogical Society of America, Washington, **1983**, *11*, 97-144;
- 147 Madland M.V.; Hiorth A.; Omdal E.; Megawati M.; Hildebrand-Habel T.; Korsnes R.I.; Evje S.; Cathles L.M.; Chemical Alterations Induced by Rock–Fluid Interactions When Injecting Brines in High Porosity Chalks. *Transport in Porous Media*, **2011**, *87*, 679–702.
- 148 Madland, M. V.; Finsnes, A.; Alkafadgi, A.; Risnes, R.; Austad, T. The influence of CO₂ gas and carbonate water on the mechanical stability of chalk. *J. Pet. Sci. Eng.* **2006**, *51*, 149-168.
- 149 Madland, M. V.; Midtgarden, K.; Manafov, R.; Korsnes, R. I.; Kristiansen, T.; Hiorth, A. The Effect of Temperature and Brine Composition on the Mechanical Strength of Kansas Chalk. *International Symposium of the Society of Core Analysts*, Abu Dhabi, **2008**, 6.
- 150 Matthews, N.E.; Zimmermann, U.; Støle, L.; Ruud, C.; Mostafa, E.; Borromeo, L.; Andò, S.; Magnaghi, M.; Lapen, T.J. A multi-technique approach for provenance studies of Mesozoic clastic rocks in the Barents Sea. AGU Fall meeting, V025: Novel high-resolution approaches to deciphering source-to-sink linkages between tectonic hinterland and basin evolution Session ID#: 9154, V53D-3148. **2015**.
- 151 Mazzoleni, P Barone, G.; Raneri, S.; Aquilia, E.; Bersani, D.; and Cirrincione, R. Application of micro-Raman spectroscopy for the identification of unclassified minerals preserved in old Museum collections. *PLINIUS* *42* (2016): 112-124. Megawati, M.; Madland, M.V.; Hiorth, A.; Probing pore characteristics of deformed chalk by NMR relaxation, *J. Pet. Sci. Eng.* **2012**, *100*, 123– 130.
- 152 Medeghini, L.; Lottici, P.P.; De Vito, C.; Mignardi, S. and Bersani, D.; Micro-Raman spectroscopy and ancient ceramics: applications and problems. *Journal of Raman Spectroscopy*, **2014**, *45*(11-12), pp.1244-1250;

References

- 153 Megawati, M.; Hiorth, A.; Madland, M. V. The impact of surface charge on the mechanical behavior of high-porosity chalk. *Rock Mech. Rock Eng.* **2013**, *46.5*, 1073-1090.
- 154 Megawati, M.; Madland, M. V.; Hiorth, A. Mechanical and physical behavior of high-porosity chalks exposed to chemical perturbation: *J. Pet. Sci. Eng.* **2015**, *133*, 313-327.
- 155 Minde, M. W.; Haser, S.; Korsnes, R. I.; Zimmermann, U. and Madland, M. V. Comparative Studies of Mineralogical Alterations of Three Ultra-long-term Tests of Onshore Chalk at Reservoir Conditions. In *IOR 2017-19th European Symposium on Improved Oil Recovery 2017*.
- 156 Minde, M. W.; Zimmermann, U.; Madland, M. V.; Korsnes, R. I. Submicron investigations –What can we learn? IOR Norway 2016, Stavanger, **2016**.
- 157 Molenaar, N. and Zijlstra, J. J. P. [1997] Differential early diagenetic low-Mg calcite cementation and rhythmic hardground development in Campanian-Maastrichtian chalk. *Sedimentary Geology*, **109**(3-4), 261-281;
- 158 Moroz I. Et al. Raman microspectroscopy and fluorescence of emeralds from various deposits. *Journal of Raman Spectroscopy*. **2000** ,31: 485-490;
- 159 Morris, M. D.; and Mandair, G. S. (2011). Raman assessment of bone quality. *Clinical Orthopaedics and Related Research*®, *469*(8), 2160-2169;
- 160 Morris, M.D. and Mandair G.S. Raman assessment of bone quality. *Clinical Orthopaedics and Related Research*®. **2011**, 1; 469(8):2160-9;
- 161 Moscardi, G. (2008, August). Analysis by Raman Microscopy of Powder Samples Drawn from the Turin Shroud. In *Shroud Science Group International Conference, Columbus, Ohio*.
- 162 Mostafa, E.; Ruud, C.; Støle, L.; Matthews, N.; Zimmermann, U.; Andò, S.; Borromeo, L. 2015. High resolution heavy mineral studies of Mesozoic rocks of the Hammerfest basin. NGF Abstracts and Proceedings, Vinterkonferansen 2015, 12-14.1. **2015** Stavanger, 67.
- 163 Movasaghi Z, Rehman S, Rehman IU. Raman spectroscopy of biological tissues. *Applied Spectroscopy Reviews*. **2007**; *42*(5) 493-541;
- 164 Muehlethaler, C.; Leona, M. and Lombardi, J.R.; Review of surface enhanced Raman scattering applications in forensic science. *Analytical chemistry*, **2015**, *88*(1), 152-169;
- 165 Muehlethaler, C.; Leona, M.; and Lombardi, J. R. Review of surface enhanced Raman scattering applications in forensic science. *Analytical chemistry*, **2015**, *88*(1), 152-169.
- 166 Murphy, S.; Huang, L.; and Kamat, P. V. (). Charge-transfer complexation and excited-state interactions in porphyrin-silver nanoparticle hybrid structures. *The Journal of Physical Chemistry C*, **2011**, *115*(46), 22761-22769;

References

- 167 Mutti, M.; and Hallock, P. Carbonate systems along nutrient and temperature gradients: some sedimentological and geochemical constraints. *International Journal of Earth Sciences* 92, **2003**, 4, 465-475;
- 168 Nagel, N. B. Compaction and subsidence issues within the petroleum industry: from Wilmington to Ekofisk and beyond. *Phys. Chem. Earth A*. **2001**, 26, 3-14.
- 169 Nasdsala L. et al. Raman spectroscopy: analytical perspectives in mineralogical research. In : Beran, A.; and Libowitzy E. (Eds), *Spectroscopic methods in mineralogy. Eur. Mineral. Union Notes in Mineralogy* 6, Eotovos Univ. Press, Budapest, **2004**, 281-343;
- 170 Nerموen, A.; Korsnes, R. I.; Hiorth, A. and Madland, M. V. Porosity and permeability development in compacting chalks during flooding of nonequilibrium brines: Insights from long-term experiment. *Journal of Geophysical Research: Solid Earth*, **2015** 120(5), 2935-2960;
- 171 Neuville, D. R.; de Ligny, D.; and Henderson, G. S. Advances in Raman spectroscopy applied to earth and material sciences. *Reviews in Mineralogy and Geochemistry*, **2014**, 78(1), 509-541;
- 172 Neuville, D.R.; De Ligny, D. and Henderson, G.S.; Advances in Raman spectroscopy applied to earth and material sciences. *Reviews in Mineralogy and Geochemistry*, **2014**, 78(1), 509-541;
- 173 Ni, Z.; Wang, Y.; Yu, T.; and Shen, Z.; Raman spectroscopy and imaging of graphene. *Nano Research*, 1(4), **2008**, 273-291;
- 174 Nie, S. Probing Single Molecules and Single Nanoparticles by Surface-Enhanced Raman Scattering. *Science* (80), 1997, 275 (5303), 1102–1106;
- 175 Palanza V. et al. , Raman spectroscopy applied to the study of inclusions within sapphire. *Journal of Raman spectroscopy*, **2008**, 39, 1007-1011;
- 176 Palenik, S. In *Heavy Minerals in Use*; Mange, M.A.; Wright, D.T.; Eds.; Developments in Sedimentology, Vol. 58; Elsevier: New York, **2007**, 937-961
- 177 Pearson, D. G.; Brenker, F. E.; Nestola, F.; McNeill, J.; Nasdala, L.; Hutchison, M. T.; ... and Vekemans, B. Hydrous mantle transition zone indicated by ringwoodite included within diamond. *Nature*, **2014** 507(7491), 221-224;
- 178 Pearson, D. G.; F. E. Brenker, F. Nestola, J. McNeill, L. Nasdala, M. T. Hutchison, S. Matveev et al. "Hydrous mantle transition zone indicated by ringwoodite included within diamond." *Nature* 507, **2014**, 7491, 221;
- 179 Pérez, F. R.; and Martinez-Frias, J. Raman spectroscopy goes to Mars. *Spectroscopy Europe*, **2006**, 18(1), 18-21;
- 180 Pettinger, B.; Ren, B.; Picardi, G.; Schuster, R. and Ertl, G. Nanoscale probing of adsorbed species by Tip-Enhanced Raman Spectroscopy. *Physical review letters*, **2004**, 92(9), 096101;

References

- 181 Picardi, G.; Chaigneau, M.; Ossikovski, R.; Licitra, C. and De La Pierre, G. Tip-Enhanced Raman spectroscopy on azobenzene thiol self-assembled monolayers on Au (111). *Journal of Raman Spectroscopy*, **2009**, *40*(10), 1407-1412;
- 182 Pozzi, F. and Leona, M.; Surface-enhanced Raman spectroscopy in art and archaeology. *Journal of Raman Spectroscopy*, **2016**, *47*(1), 67-77;
- 183 Purgstaller, B.; Mavromatis, V.; Immenhauser, A.; Dietzel, M. Transformation of Mg-bearing amorphous calcium carbonate to Mg-calcite – In situ monitoring. *Geoch. Et Cosmoch. Acta*, **2016**, *174*, 180–195.
- 184 Putnis, A.; Introduction to mineral science. Cambridge University Press **1992**;
- 185 Pyne A.; Thompson, R.; Leung, C.; Roy, D. and Hoogenboom, B. W. *Single-Molecule Reconstruction of Oligonucleotide Secondary Structure by Atomic Force Microscopy. Small*, **2014**, *10* (16), 3257-3261.
- 186 R. French, E. C. Wang, and J. B. Bates, The i.r. and Raman spectra of CaCO₃ (aragonite), *Spectrochim. Acta A* **36**, 915–919 **1980**
- 187 Krishnan, R. S. *Part. I: Calcite, Proc Ind. Acad. Sci.* **1945**, *22A*, 182.
- 188 Raman, C. V.; LXX. Photographs of vibration curves. The London, Edinburgh, and Dublin Philosophical Magazine and Journal of Science, **1911** *21*(125), 615-618;
- 189 Raman Spectroscopy in Archaeology and Art History, ed. H. G. M. Edwards and J. M. Chalmers, Royal Society of Chemistry, Cambridge, **2005**;
- 190 Raman, C. V.; A new radiation. *Indian Journal of Physics*, *2*, **1928**, 387–398;
- 191 Raman, C. V.; and K.S. Khrishnan, Production of New Radiations by Light Scattering, *Proc. Roy. Soc.* **1929**; *122*, 23;
- 192 Raman, C. V.; and K.S. Khrishnan, The optical Analogue of Compton effect, *Nature*, **1928b**, *121*, 711;
- 193 Raman, C. V.; and Krishnan, K. S.. A new type of secondary radiation. *Nature*, **1928a**, *121* (3048), 501.
- 194 Raman, C. V.; On the molecular scattering of light in water and the colour of the sea. *Proceedings of the Royal Society of London. Series A, Containing Papers of a Mathematical and Physical Character*, **1922**, *101*, 708, 64-80;
- 195 Raman, C. V.; Unsymmetrical diffraction-bands due to a rectangular aperture. *The London, Edinburgh, and Dublin Philosophical Magazine and Journal of Science* *12.71* **1906**: 494-498.
- 196 Rayleigh, Lord. XLII. On the scattering of light by a cloud of similar small particles of any shape and oriented at random. *The London, Edinburgh, and Dublin Philosophical Magazine and Journal of Science* **1918**, *35.209*: 373-381;

References

- 197 Ren, B.; Picardi, G. and Pettinger, B. Preparation of Gold Tips Suitable for Tip-Enhanced Raman Spectroscopy and Light Emission by Electrochemical Etching. *Review of Scientific Instruments*. **2004**, *75*, 837-841;
- 198 Risnes, R.; Haghghi, H.; Korsnes, R.I.; Natvik, O. Chalk–fluid interactions with glycol and brines, *Tectonophysics*, **2003**, *370*, 213– 226;
- 199 Risnes, R.; Madland M. V.; Hole M.; Kwabiah N. K. Water weakening of chalk – Mechanical effects of water-glycol mixtures, *J. Pet. Sci. Eng.* **2005**, *48*, 21-36;
- 200 Robaszynski, F.; Dhondt, A. V. and John, W. M. Cretaceous lithostratigraphic units (Belgium). *Geologica Belgica*, **2001**, *4* (1-2), 121-134;
- 201 Rousaki, A.; Bellelli, C.; Carballido Calatayud, M.; Aldazabal, V.; Custo, G.; Moens, L.; Vandenabeele, P. and Vazquez, C.; Micro-Raman analysis of pigments from hunter–gatherer archaeological sites of North Patagonia (Argentina). *Journal of Raman Spectroscopy*, **2015**, *46*(10), 1016-1024;
- 202 Rutt, H. N. and Nicola, H. J. Raman spectra of carbonates of calcite structure. *Phys. C: Solid State Phys.* **1974**, *7*, 4522;
- 203 S. P. S. Porto, J. A. Giordmaine, and T. C. Damen, Depolarization of ra-man scattering in calcite, *Phys. Rev.* **1966**, *147*, 608–611;
- 204 Šašić, S. Raman mapping of low-content API pharmaceutical formulations. I. Mapping of alprazolam in alprazolam/xanax tablets. *Pharmaceutical research*, **2007**, *24*(1), 58-65.
- 205 Schmitt M. and J. Popp; Raman spectroscopy at the beginning of the twenty-first century *J. Raman Spectrosc.* **2006**; *37*: 20–28;
- 206 Schulmerich, M.V.; Dooley, K.A.; Vanasse, T.M.; Goldstein, S.A. and Morris, M.D.; Subsurface and transcutaneous Raman spectroscopy and mapping using concentric illumination rings and collection with a circular fiber-optic array. *Applied spectroscopy*, **2007**, *61*(7), 671-678;
- 207 Schultz, Z. D.; Marr, J. M. and Wang, H. Tip-Enhanced Raman scattering: plasmonic enhancements for nanoscale chemical analysis. *Nanophotonics*, 2014 , *3*(1-2), 91-104;
- 208 Schütz, R.; Bertinetti, L.; Rabin, I.; Fratzi, P. and Masic, A.; Quantifying degradation of collagen in ancient manuscripts: the case of the Dead Sea Temple Scroll. *Analyst*, **2013**, *138*(19), 5594-5599.
- 209 Sebek, J.; Pele, L.; Potma, E. O.; Gerber, R. B. Raman spectra of long chain hydrocarbons: anharmonic calculations, experiment and implications for imaging of biomembranes. *PCCP*, **2011**, *13*, 12724-12733;
- 210 Sharma, B.; Frontiera, R.R.; Henry, A.I.; Ringe, E. and Van Duyne, R.P.; SERS: Materials, applications, and the future. *Materials today*, **2012**. *15*(1-2), 16-25;
- 211 She Y.; Masso JD.; Edwards, DF.; Raman scattering by polarization waves in

References

- uniaxial crystals. *J Phys Chem Solids*, **1971**, *32*, 1887-1900;
- 212 Slimani, H. New species of dinoflagellate cysts from the Campanian-Danian chinks at Hallembaye and Turnhout (Belgium) and at Beutenaken (the Netherlands), *J. Micropalaeontol.* **2001**, *20* (1), p. 1–11, DOI:10.1144/jm.20.1.1;
- 213 Smekal, A. Zur quantentheorie der dispersion. *Naturwissenschaften*, **1923** *11*(43), 873-875;
- 214 Smith, E.M.; Shirey, S.B.; Nestola, F.; Bullock, E.S.; Wang, J.; Richardson, S.H. and Wang, W.; 2016. Large gem diamonds from metallic liquid in Earth's deep mantle. *Science*, *354*(6318), 1403-1405;
- 215 Stadler, J.; Schmid, T.; Zenobi, R.; Graphene, S.; Stadler, J.; Schmid, T. and Zenobi, R. Nanoscale chemical imaging of single-layer graphene. *ACS Nano* **2011**, *5*(10), 8442-8448;
- 216 Stehli, F. G.; and Hower, J. Mineralogy and early diagenesis of carbonate sediments. *Journal of Sedimentary Research*, **1961**, *31*(3).
- 217 Strand, S.; Standnes, D. C.; Austad, T. Spontaneous imbibition of aqueous surfactant solutions into neutral to oil-wet carbonate cores: Effects of brine salinity and composition. *Energy and fuels* **2003**, *17*(5), 1133-1144;
- 218 Strand, S.; Hjuler, M. L.; Torsvik, R.; Pedersen, J. I.; Madland, M. V.; Austad, T. Wettability of chalk: impact of silica, clay content and mechanical properties. *Petroleum Geoscience*, **2007**, *13*(1), 69-80;
- 219 Sun, J.; Zeguang, W.; Hongfei, C. A Raman spectroscopic comparison of calcite and dolomite, *Spectrochim. Acta A*, **2014**; *117*, 158;
- 220 Swaminathan, P.; Raman Spectroscopy, Ppt presentation on <https://www.slideshare.net> , **2012**;
- 221 Teufel, Lawrence W.; Douglas W. Rhett, and Helen E. Farrell. Effect of reservoir depletion and pore pressure drawdown on in situ stress and deformation in the Ekofisk field, North Sea. In *The 32nd US Symposium on Rock Mechanics (USRMS)*. American Rock Mechanics Association, **1991**.
- 222 Toccafondi, C.; Picardi, G. and Ossikovski, R. Molecular Bending at the Nanoscale Evidenced by Tip-Enhanced Raman Spectroscopy in Tunneling Mode on Thiol Self-Assembled Monolayers. *The Journal of Physical Chemistry C*, **2016**, *120*(32), 18209-18219;
- 223 Towe, K.M. and Hemleben, C.; Diagenesis of magnesian calcite: evidence from miliolacean foraminifera. *Geology*, **1976**, *4*(6), pp.337-339;
- 224 Unvros, J.; Sharma, S. K.; Mackenzie, T. Characterization of some biogenic carbonates with Raman spectroscopy, *American Mineralogist* **1991**; *76*, 641.
- 225 Valenzano, L.; Torres, F. J.; Doll, K.; Pascale, F.; Zicovich-Wilson, C. M.; and Dovesi, R.; *Ab Initio* study of the vibrational spectrum and related properties

References

- of crystalline compounds: The case of CaCO₃ calcite, *Z. Phys. Chem.* **2006**, *220*, 893–912;
- 226 Van Elslande, E.; Lecomte, S. and Le Hô, A.S.; Micro-Raman spectroscopy (MRS) and surface-enhanced Raman scattering (SERS) on organic colourants in archaeological pigments. *Journal of Raman Spectroscopy*, **2008**, *39*(8), 1001-1006;
- 227 Vandenabeele, P.; Raman spectroscopy in art and archaeology. *Journal of Raman spectroscopy*, **2004**, *35*, 8-9, 607-609;
- 228 Vandenabeele, P.; Castro, K.; Hargreaves, M.; Moens, L.; Madariaga, J.M. and Edwards, H.G.M.; Comparative study of mobile Raman instrumentation for art analysis. *Analytica Chimica Acta*, **2007a**, *588*(1), 108-116.;
- 229 Vandenabeele, P.; Edwards, H. G. M. and Moens L.; A decade of Raman spectroscopy in art and archaeology. *Chemical reviews*, **2007b**, *107*, no. 3, 675-686;
- 230 Vandenabeele, Peter, H. G. M. Edwards, and J. Jehlička. The role of mobile instrumentation in novel applications of Raman spectroscopy: archaeometry, geosciences, and forensics. *Chemical Society Reviews*, **2014**, *43*, 8. 2628-2649;
- 231 Vítek, P.; Ali, E.M.; Edwards, H.G.; Jehlička, J.; Cox, R. and Page, K.; Evaluation of portable Raman spectrometer with 1064 nm excitation for geological and forensic applications. *Spectrochimica Acta Part A: Molecular and Biomolecular Spectroscopy*, **2012**, *86*, 320-327;
- 232 Wang, A.; Freeman, J. J.; Jolliff, B. L. Understanding the Raman spectral features of phyllosilicates, *JRS*, **2015**, *46*, 829–845.
- 233 Wang, W.; Madland, M. V.; Zimmermann, U.; Neramoen, A.; Korsnes, R. I.; Bertolino, S. R. A.; and Hildebrand-Habel, T. Evaluation of porosity change during chemo-mechanical compaction in flooding experiments on Liège outcrop chalk. In: Armitage, P. J.; Butcher, A. R.; Churchill, J. M.; Csoma, A. E.; Hollis, C.; Lander, R. H.; Omma, J. E. and Worden, R. H. (eds) Reservoir Quality of Clastic and Carbonate Rocks: Analysis, Modelling and Prediction. Geological Society, London, Special Publications, **2016**, 435, doi.org/10.1144/SP435.10;
- 234 Wartewig, S.; and Neubert, R. H. Pharmaceutical applications of Mid-IR and Raman spectroscopy. *Advanced drug delivery reviews*, **2005**, *57*(8), 1144-1170;
- 235 Wehrmeister, U.; Soldati, A. L.; Jacob, D. E.; Häger, T.; and Hofmeister, W.; Raman spectroscopy of synthetic, geological and biological vaterite: a Raman spectroscopic study. *Journal of Raman Spectroscopy*, **2010**, *41*, 193–201;
- 236 Wilson, E.B.; Decius, J.C. and Cross, P.C.; *Molecular vibrations: the theory of infrared and Raman vibrational spectra*. Courier Corporation. **1955**;
- 237 Xie, T.; S. R. Shieh, and G. R. Osinski. Raman Study of Shock Effects in

References

- Lunar Anorthite from the Apollo Missions. In *Lunar and Planetary Science Conference*, **2017**, 48;
- 238 Yang, Z.; Aizpurua, J. and Xu, H. Electromagnetic field enhancement in TERS configurations. *Journal of Raman Spectroscopy*, **2009** 40(10), 1343-1348;
- 239 Zangiabadi, B.; Korsnes, R. I.; Hildebrand-Habel, T.; Hiorth, A.; Surtarjana, I. K.; Lian, A.; Madland, M. V. Chemical water weakening of various outcrop chalks at elevated temperature. In *Poromechanics IV*, Ling H. I.; Smyth A.; and Betti, R.; Eds. DEStech Publications, Inc.; Lancaster, England, **2009**; pp. 543-548;
- 240 Zhang, P.; Tweheyo, M. T.; Austad, T. Wettability Alteration and Improved Oil Recovery in Chalk: The Effect of Calcium in the Presence of Sulfate. *Energy and Fuels*, **2006**, 20(5), 2056-2062;
- 241 Zhang, P.; Tweheyo, M.T.; Austad T.; Wettability alteration and improved oil recovery by spontaneous imbibition of seawater into chalk: impact of the potential determining ions Ca^{2+} , Mg^{2+} , and SO_4^{2-} , *Colloids Surf. A Physicochem. Eng. Aspects*, **2007**, 301, 199–208;
- 242 Zhang, X. Kirkwood, W.J.; Walz, P.M.; Peltzer, E.T. and Brewer, P.G.; A review of advances in deep-ocean Raman spectroscopy. *Applied spectroscopy*, **2012**. 66(3), pp.237-249;
- 243 Zimmermann, U.; Madland, M. V.; Nermoen, A.; Hildebrand-Habel, T.; Bertolino, S. A. R.; Hiorth, A.; Korsnes, R. I.; Audinot, J. N.; Gysan P. Evaluation of the compositional changes during flooding of reactive fluids using scanning electron microscopy, nano-secondary ion mass spectroscopy, x-ray diffraction, and whole-rock geochemistry: *AAPG. Bulletin*, **2015**, 99, 791-805;
- 244 Zimmermann, U.; Kristoffersen, E.S.; Fredriksen, P.D.; Bertolino, S.A.; Andò, S. and Bersani, D.; Provenance and composition of unusually chrome and nickel-rich bucket-shaped pottery from Rogaland (southwestern Norway). *Sedimentary geology*, **2016**. 336, 183-196;
- 245 Zimmermann, U.; Madland, M.; Minde, M.; Borromeo, L. and Egeland, N.; Tools to Determine and Quantify Mineralogical Changes During EOR Flooding Experiments on Chalk. *SPE Abu Dhabi International Petroleum Exhibition and Conference. Society of Petroleum Engineers*, **2017**.

Appendices

Appendix 1 – Peaks position of the Mg-calcite spectra

Appendices

Sample	WDS	EDS	Average WDS EDS	D WDS - EDS	EDS	EDS	EDS	Raman vibrational modes			
	MgO (weigh %t)	MgO (weight %)	(weight %)	(weigh %t)	Mg (mol %)	Integr. Err. %	T	L	n ₄	(HCO ₃) ⁻	n ₁
Alga Egypt 1 1		8.30			19.93	1.50	159.77	287.17	715.77		1090.5
Alga Egypt 1 1a		8.07			19.78	1.52	160.47	286.97	715.77		1090.5
Alga Egypt 1 2		7.03			17.52	1.64	160.0	286.87	715.67		1090.1
Alga Egypt 1 2a		7.28			17.70	1.64	160.27	286.47	715.67		1090.1
Alga Egypt 1 3		8.06			19.30	1.51	160.87	286.77	716.0		1090.5
Alga Egypt 1 3a		8.56			20.08	1.49	160.87	286.77	716.0		1090.5
Alga Egypt 1 4		7.73			18.71	1.55	160.27	287.17	716.07		1090.6
Alga Egypt 1 4a		8.74			20.38	1.46	160.27	287.17	716.07		1090.6
Alga Egypt 2 1		16.14			34.39	0.99	160.37	287.57	716.07		1090.7
Alga Egypt 2 1a		8.62			19.99	1.44	157.97	287.57	716.07		1090.7
Alga Egypt 2 2		5.69			14.14	1.86	155.67	287.87	715.57		1090.2
Alga Egypt 2 2a		6.66			15.80	1.73	155.67	287.87	715.57		1090.2
Alga Egypt 2 3		6.68			16.25	1.71	154.77	286.67	716.37		1089.8
Alga Egypt 2 3a		7.05			16.87	1.69	154.77	286.67	715.87		1089.8
Alga Egypt 2 4		6.53			16.22	1.74	154.47	287.77	715.27		1090.6
Alga Egypt 2 4a		6.40			15.32	1.80	154.47	287.77	715.27		1090.6
Alga Egypt 3 1		8.10			19.21	1.53	160.27	288.37	716.47		1091.6
Alga Egypt 3 1a		9.54			23.35	1.39	158.77	288.37	716.47		1091.7
Alga Egypt 3 2		6.97			17.62	1.68	158.47	289.0	714.87		1090.5
Alga Egypt 3 2a		7.81			18.69	1.57	158.47	289.0	714.87		1090.5
Alga M aldives 1 1		7.46			17.77	1.50	160.0	287.37	717.13		1090.5
Alga M aldives 2 1		7.38			18.71	1.53	158.72	287.0	717.11		1090.3
Alga Egypt 4 1		8.65			18.73	1.65	156.66	284.4	714.88		1088.5
Alga Egypt 4 2		8.80			19.78	1.65	155.51	287.01	714.51		1088.5
Alga Egypt 4 3		9.06			19.93	1.60	155.57	286.63	715.31		1090.8

Appendices

Alga Iceland summer 2 1	7.81	19.03	1.56	156.38	285.37	715.51	1088.9
Alga Iceland summer 2 2	5.76	14.13	1.92	156.6	284.1	715.34	1088.9
Alga Iceland summer 2 3	8.17	19.56	1.52	156.52	283.0	716.0	1089.8
Alga Iceland summer 2 6	6.63	16.62	1.75	156.06	282.36	714.5	1088.2
Alga Iceland summer 2 7	6.34	15.80	1.79	156.54	283.8	714.47	1089.0
Alga Iceland summer 2 4	8.20	19.68	1.51	155.8		715.12	1087.3
Alga Iceland winter 2 1	5.13	13.35	1.91	156.67	285.28	715.15	1088.2
Alga Iceland winter 2 2	5.74	14.28	1.89	156.87	285.23	716.23	1088.4
Barnades italy 4A p1 1 R	0.62	1.43	10.61		282.39	712.24	1086.4
Barnades italy 4A p2 1 R	0.43	0.99	14.69		282.06	712.42	1086.2
Barnades italy 4A p3 1 R	0.99	2.25	6.83	155.0	282.04	712.1	1086.2
Barnades italy 4B p4 2 R	0.51	1.19	12.46	155.61	281.67	711.91	1086.3
Barnades italy 4B p4 3 R	0.51	1.18	12.47	155.61	281.67	711.91	1086.3
Barnades italy 4B p4 1 R	0.51	1.18	12.45	155.61	281.67	711.91	1086.3
Barnades italy 4B p5 1 R	0.38	0.89	17.56	156.1	282.44	711.84	1086.5
Barnades italy 4B p5 2 R	0.38	0.89	17.56	156.1	282.44	711.84	1086.5
Barnades italy 4B p5 3 R	0.38	0.89	17.56	156.1	282.44	711.84	1086.5
Barnades italy 4B p6 1 R	0.47	1.10	13.93	155.44	282.0	712.28	1086.3
Barnades italy 4B p6 2 R	0.47	1.10	13.94	155.44	282.0	712.28	1086.3
Barnades italy 4B p6 3 R	0.47	1.10	13.95	155.44	282.0	712.28	1086.3
Barnades italy 1Aa p1 R	0.64	1.52	10.39	155.17	281.85	711.62	1086.3
Barnades italy 1Aa p2 R	0.50	1.17	13.14	156.42	282.53	712.08	1086.3
Barnades italy 1Ab p10 R	0.60	1.42	10.77	156.0	282.55	713.0	1087.1
Barnades italy 1Ab p11 R	0.61	1.44	11.02	156.32	282.48	712.53	1086.9
Barnades italy 1Ba p3 R	0.71	1.70	9.54	156.76	281.79	711.87	1086.2
Barnades italy 1Bb p7 R	0.64	1.50	10.72		281.68		1086.5
Barnades italy 1Bb p8 R	0.55	1.31	11.40		281.87	712.16	1086.4
Barnades italy 1Bb p9 R	0.64	1.51	10.08	154.41	281.05	712.12	1086.01
Bernace Maldives 1 1	1.96	4.87	3.80	155.0	280.55	713.25	1016.0
Bernace Maldives 1 2	1.49	3.70	4.63	154.925	280.135	713.505	1015.7
Bernace Maldives 2 1	1.05	2.63	6.15	154.479	280.558	713.199	1017.5
Barnades italy 5 p6 R	1.07	2.51	6.39	156.133	282.24	712.69	1086.6

Appendices

Barnacles Italy 5 p7 R	1.34			3.11	5.12	152.47	282.44	712.42	1086.2
Barnacles Italy 5 p8 R	1.16			2.71	6.16	156.36	281.91	711.73	1086.5
Barnacles Italy 6 p1 R	2.01			4.95	4.03	154.5	280.58	712.5	1013.1
Barnacles Italy 6 p2 R	2.19			5.21	3.83	154.69	281.35	712.86	1086.6
Barnacles Italy 6 p3 R	1.06			2.54	6.73	155.51	280.83	712.45	1086.3
Barnacles Italy 6 p4 R	1.89			4.47	3.77	156.37	281.06	712.47	1013.0
Barnacles Italy 6 p5 R	1.63			3.83	4.59	154.68	281.96	712.77	1015.9
Echino M ardives 1_3	5.23			12.75	2.35	156.23	285		1088.3
Echino M ardives 1_4	4.34	4.43	-0.82	10.55	N.A.	155.29	280.8	712.97	1086.2
Echino M ardives 1_6	4.80	4.79	0.18	11.14	N.A.	155.2	283.3	713.13	1087.7
Echino M ardives 1_7	5.83			11.73	2.16	153.65	282.28	714.58	1087.2
Echino M ardives 5_1	5.01			12.71	2.38	154.74	281.02	713.33	1087.1
Echino fenauxi Italy_1	5.35			13.34	2.27	155.596	281.51	716.15	1087.7
Echino fenauxi Italy_2	4.71			11.87	2.45	155.234	281.374	-0.726	1087.3
Echino Cidaris Italy_1	6.27			15.76	2.04	156.22	284.18	714.29	1087.8
Echino Cidaris Italy_2	6.44			15.98	1.97	156.13	286.32	713.84	1088.1
Echino Cidaris Italy_3	6.31			15.71	2.00	156.23	282.79	713.32	1087.7
Echino Paracentrotus lividus Italy_1	3.36	3.77	-0.82	10.58	2.68	155.91	284.0	712.84	1087.6
Echino Paracentrotus lividus Italy_2	3.49	4.11	-1.24	11.73	2.44	154.33	283.56	713.04	1086.9
Echino Paracentrotus lividus Italy_3	4.05	4.38	-0.65	11.82	2.47	155.13	284.24	712.84	1087.4
Echino M ora Mounds 1	1.82	2.03	-0.43	5.52	4.29	154.65	280.51	711.9	1086.3
Echino M ora Mounds 2	1.63	1.83	-0.40	5.19	4.74	154.69	280.4	712.0	1086.1
Echino M ora Mounds 3	0.95	1.22	-0.55	3.78	5.83	154.61	280.64	712.0	1086.4
Foram Elphidium M ardives 1	1.97			4.86	4.26	154.19	280.23	711.75	1086.0
Foram Elphidium M ardives 2	2.6			6.50	3.85	154.18	280.42	712.06	1086.6
Foram Elphidium M ardives 3	1.5			3.80	6.10	154.41	280.66	711.83	1086.4
Foram M iliolida M ardive 7x5 1	4.53	4.67	-0.29	11.85	2.26	155.98	284.23	714.85	1088.4
Foram M iliolida M ardive 7x5 2	5.27	6.04	-1.53	16.52	1.92	156.72	284.36	715.21	1088.7
Foram M iliolida Egypt_2	0.15	0.33	-0.37	1.24	15.04	151.55		703.13	1085.1
Foram M iliolida Egypt_3	5.31	6.44	-2.25	17.98	1.80	156.85	285.0	714.0	1088.4
Foram Peneroplis Egypt_1	5.62	6.62	-2.00	17.92	1.78	154.32	286.06	715.0	1087.8
Foram Soritides Egypt_1	8.02			18.86	1.71	156.35	285.25	714.75	1088.3

Appendices

Foram Soritides Egypt_2						17.83	1.81	155.81	286.37	715.2	1088.3
Foram Soritides Egypt_3						18.28	1.74	155.87	285.64	713.35	1088.7
Foram Soritides Maldives_1						20.24	1.66	156.0	285.08	714.1	1088.2
Foram Soritides Maldives_3						18.93	1.73	156.87	284.1	714.0	1088.3
Foram Ammonia Italy_1						0.09	7.26	154.81	281.31	713.0	1087.6
Foram Ammonia Italy_2						0.08	8.06	154.44	280.61	712.3	1087.1
Foram Mililida Greece_2						14.14	2.03	157.0	284.3	715.49	1088.5
Foram Mililida Greece_3						12.43	1.72	156.14	284.0	715.46	1088.8
Foram Elphidium Greece_1						2.58	5.91	153.0	282.83	714.15	1086.1
Foram Elphidium Greece_2						5.50	6.98	155.65	284.14	714.27	1087.9
Foram Elphidium Italy Miocene_1						1.83	6.98	153.63	280.07	711.63	1085.9
Foram Elphidium Italy Miocene_2						2.03	7.11	153.63	280.07	711.63	1085.9
Alga Italy Miocene_7x5_1						3.37	4.74	154.27	280.88	711.69	1086.5
Alga Italy Miocene_7x5_2						3.18	5.03	154.73	281.27	712.8	1086.6
Bryozoa Italy Miocene_1						3.51	4.62	154.31	281.25	712.57	1087.1
Bryozoa Italy Miocene_2						3.39	4.51	154.31	281.25	712.57	1087.1
Foram Elphidium Italy_1						0.09	7.78	152.08	277.94	712.0	1086.1
Foram Elphidium Italy_2						0.09	7.69	153.78	279.63	712.0	1086.5
Foram Mililida Italy_1						17.46	1.61	155.33	285.53	715.33	1087.9
Foram Mililida Italy_2						16.11	1.71	155.86	282.93	714.71	1088.0
Foram Soritides France_1						15.21	1.72	156.94	288.67	716.34	1090.5
Foram Soritides France_2						15.34	1.63	156.24	286.62	715.48	1088.8
Foram Mililida France_1						14.53	1.79	156.79	285.0	715.94	1089.2
Foram Mililida France_2						16.20	1.67	156.12	286.47	715.86	1089.0
Foram Elphidium France_1						1.23	12.61	154.29	280.45	712.3	1086.8
Foram Elphidium France_2						3.08	5.05	154.81	281.0	712.81	1086.6
Foram Soritides Malaysia_1						17.14	1.57	157.85	284.89	716.88	1089.3
Foram Soritides Malaysia_2						17.93	1.53	157.85	284.89	716.88	1089.3
Foram Elphidium Malaysia_1						1.39	10.73	155.0	281.24	712.79	1087.1
Foram Elphidium Malaysia_2						0.69	22.78	155.0	281.24	712.79	1087.1
Foram Soritides France_1						14.92	1.72	157.11	285.1	715.78	1089.0
Foram Soritides France_2						14.53	1.78	157.84	286.0	716.63	1089.7

Appendix 2 – Peaks position of the flooded chalk spectra

Appendices

Name	T	L	n ₄	n ₁
LTT1_p1A_10x5_100%_11	280,8	715,2	1086,4	
LTT1_p1A_10x5_100%_7	280,9	712,6	1086,4	
LTT1_p1A_10x5_100%_3	281,0	712,3	1086,5	
LTT1_p1A_10x5_100%_6	280,5	712,5	1086,5	
LTT1_p1A_10x5_100%_17	280,1	712,5	1086,5	
LTT1_p1A_10x5_100%_15	280,9	712,7	1086,6	
LTT1_p1A_10x5_100%_16	280,1	712,5	1086,7	
LTT1_p1A_10x5_100%_19	280,5	712,3	1086,7	
LTT1_p1A_10x5_100%_8	280,3	712,7	1086,8	
LTT1_p1A_10x5_100%_20			1086,8	
LTT1_p1A_10x5_100%_10	280,8	713,2	1086,8	
LTT1_p1A_10x5_100%_2	281,1	712,8	1086,9	
LTT1_p1A_10x5_100%_5	281,7	713,3	1087,0	
LTT1_p1A_10x5_100%_18	280,6	713,3	1087,0	
LTT1_p1A_10x5_100%_14	280,9	713,0	1087,2	
LTT1_p1A_10x5_100%_12	281,4	713,2	1087,3	
LTT1_p1A_10x5_100%_4	281,6	713,3	1087,5	
LTT1_p1A_10x5_100%_13	280,4	712,1	1087,6	
LTT1_p1A_10x5_100%_9	282,0	713,1	1087,6	
LTT1_p1A_10x5_100%_1start	281,3	713,3	1087,6	
LTT1_p1A_10x5_100%_11	325,0	736,4	1093,9	Magn
LTT1_p1A_10x5_100%_7	324,9	736,1	1093,9	Magn
LTT1_p1A_10x5_100%_20	326,0	737,6	1094,0	Magn
LTT1_p1A_10x5_100%_13	324,8	736,3	1094,2	Magn
LTT1_p1A_10x5_100%_10	324,5	736,7	1094,5	Magn
LTT1_p1A_10x5_100%_16	325,1		1095,6	Magn
LTT1_p1B_10x5_100%_4			1085,4	
LTT1_p1B_10x5_100%_10			1085,8	
LTT1_p1B_10x5_100%_16			1087,1	
LTT1_p1B_10x5_100%_10	324,4		1092,2	Magn
LTT1_p1B_10x5_100%_13	325,4		1093,1	Magn
LTT1_p1B_10x5_100%_2	321,8		1093,5	Magn
LTT1_p1B_10x5_100%_17	326,4	736,4	1093,5	Magn
LTT1_p1B_10x5_100%_8	324,6		1093,7	Magn
LTT1_p1B_10x5_100%_14	323,0		1093,7	Magn
LTT1_p1B_10x5_100%_19	327,0	738,7	1094,0	Magn
LTT1_p1B_10x5_100%_7	327,0		1094,1	Magn
LTT1_p1B_10x5_100%_6	325,5	737,1	1094,2	Magn
LTT1_p1B_10x5_100%_9	329,0		1094,4	Magn
LTT1_p1B_10x5_100%_1	325,5		1094,4	Magn
LTT1_p1B_10x5_100%_12	327,0		1094,4	Magn
LTT1_p1B_10x5_100%_11	327,0		1094,6	Magn
LTT1_p1B_10x5_100%_4	327,3	737,1	1094,6	Magn
LTT1_p1B_10x5_100%_16	325,9		1094,6	Magn
LTT1_p1B_10x5_100%_18	326,2	738,3	1094,7	Magn
LTT1_p1B_10x5_100%_3	328,3	738,5	1094,8	Magn

Appendices

LTT1_p1B_10x5_100%_20	328,2		1094,9	Magn
LTT1_p1B_10x5_100%_5	325,5		1094,9	Magn
LTT1_p1B_10x5_100%_15	326,5		1094,9	Magn
LTT1_p1C_10x5_100%_1	283,1	713,6	1087,1	
LTT1_p1C_10x5_100%_12	279,2	711,9	1086,1	
LTT1_p1C_10x5_100%_11	279,9	712,5	1086,3	
LTT1_p1C_10x5_100%_3	281,3	711,8	1086,5	
LTT1_p1C_10x5_100%_8	280,6	712,1	1086,6	
LTT1_p1C_10x5_100%_20	280,4	712,7	1086,6	
LTT1_p1C_10x5_100%_2	280,2	712,8	1086,7	
LTT1_p1C_10x5_100%_18	281,0	712,7	1086,7	
LTT1_p1C_10x5_100%_13	277,4	712,7	1086,7	
LTT1_p1C_10x5_100%_7	280,9	712,9	1086,7	
LTT1_p1C_10x5_100%_4	280,8	712,6	1086,8	
LTT1_p1C_10x5_100%_17	281,3	712,9	1086,9	
LTT1_p1C_10x5_100%_5	282,5	712,1	1086,9	
LTT1_p1C_10x5_100%_6_cal	281,1	712,8	1086,9	
LTT1_p1C_10x5_100%_10	280,1	712,9	1086,9	
LTT1_p1C_10x5_100%_15	280,3	712,6	1087,0	
LTT1_p1C_10x5_100%_14	280,8	712,8	1087,0	
LTT1_p1C_10x5_100%_19	280,4	712,8	1087,1	
LTT1_p1C_10x5_100%_9	280,6	713,2	1087,3	
LTT1_p1C_10x5_100%_16	280,9	713,4	1087,4	
LTT1_p1C_10x5_100%_5	326,1	736,5	1093,8	Magn
LTT1_p1C_10x5_100%_3	325,2		1094,3	Magn
LTT1_p1C_10x5_100%_4	325,0	736,5	1094,6	Magn
LTT1_p1D_10x5_100%_4	318,0		1094,7	Magn
LTT1_p1D_10x5_100%_1	326,4	736,5	1094,4	Magn
LTT1_p1D_10x5_100%_16	326,1	736,2	1094,4	Magn
LTT1_p1D_10x5_100%_12	325,9	737,0	1094,4	Magn
LTT1_p1D_10x5_100%_19	325,1	737,0	1094,2	Magn
LTT1_p1D_10x5_100%_11	324,8	738,1	1093,9	Magn
LTT1_p1D_10x5_100%_13	324,7	735,1	1093,8	Magn
LTT1_p1D_10x5_100%_3	326,9	734,9	1093,8	Magn
LTT1_p1D_10x5_100%_20	324,0	735,7	1093,6	Magn
LTT1_p1D_10x5_100%_15	323,9		1093,6	Magn
LTT1_p1D_10x5_100%_14	325,5	736,6	1093,5	Magn
LTT1_p1D_10x5_100%_7	325,9	735,5	1093,5	Magn
LTT1_p1D_10x5_100%_18	322,9		1093,4	Magn
LTT1_p1D_15x5_100%_9			1093,2	Magn
LTT1_p1D_10x5_100%_8	322,9		1093,1	Magn
LTT1_p1D_10x5_100%_2	326,2		1093,1	Magn
LTT1_p1D_10x5_100%_17	323,4		1092,7	Magn
LTT1_p1D_10x5_100%_6	205		1092,3	Magn
LTT1_p1D_10x5_100%_5			1091,5	Magn
LTT1_p1D_10x5_100%_13			1089,0	

Appendices

LTT1_p1D_10x5_100%_4			1088,7	
LTT1_p1D_10x5_100%_15	288,9	743,1	1087,2	
LTT1_p1D_10x5_100%_20			1087,0	
LTT1_p1D_10x5_100%_3			1085,8	
LTT1_p1D_10x5_100%_11	288,0			
LTT1_p1D_10x5_100%_18	287,7			
LTT1_p1D_10x5_100%_2	289,7			
LTT1_p1D_10x5_100%_16	287,7			
LTT1_p1D_10x5_100%_17	288,7			
LTT1_p1E_10x5_100%_7	288,9			
LTT1_p1E_10x5_100%_8	287,4			
LTT1_p1E_10x5_100%_1			1084,5	
LTT1_p1E_10x5_100%_3			1085,6	
LTT1_p1E_10x5_100%_6			1085,8	
LTT1_p1E_10x5_100%_20			1086,3	
LTT1_p1E_10x5_100%_12			1086,3	
LTT1_p1E_10x5_100%_11	323,2		1092,6	Magn
LTT1_p1E_10x5_100%_9	328,0		1092,9	Magn
LTT1_p1E_10x5_100%_2	319,3		1092,9	Magn
LTT1_p1E_10x5_100%_10	324,1	740,2	1093,2	Magn
LTT1_p1E_10x5_100%_8	324,4		1093,4	Magn
LTT1_p1E_10x5_100%_15	327,2		1093,6	Magn
LTT1_p1E_10x5_100%_14	328,3		1093,7	Magn
LTT1_p1E_10x5_100%_3	325,9	737,2	1093,7	Magn
LTT1_p1E_10x5_100%_7	327,5		1093,9	Magn
LTT1_p1E_10x5_100%_19			1094,0	Magn
LTT1_p1E_10x5_100%_12	327,1		1094,0	Magn
LTT1_p1E_10x5_100%_17	326,0	737,5	1094,3	Magn
LTT1_p1E_10x5_100%_13	326,2		1094,3	Magn
LTT1_p1E_10x5_100%_4	327,2	737,2	1094,5	Magn
LTT1_p1E_10x5_100%_18	325,1		1094,5	Magn
LTT1_p1E_10x5_100%_6	327,6		1094,6	Magn
LTT1_p1E_10x5_100%_20	326,7		1094,7	Magn
LTT1_p1E_10x5_100%_16	327,3	737,9	1094,8	Magn
LTT1_p1E_10x5_100%_5	325,9	739,7	1094,9	Magn
LTT1_p1E_10x5_100%_1	322,3	738,7	1095,3	Magn
LTT1_p1F_10x5_100%_2			1084,6	
LTT1_p1F_10x5_100%_13	280,1	712,7	1085,6	
LTT1_p1F_10x5_100%_12	280,1	711,5	1085,7	
LTT1_p1F_10x5_100%_4	280,1	712,0	1085,8	
LTT1_p1F_10x5_100%_15	278,7	712,6	1085,9	
LTT1_p1F_10x5_100%_5	279,2	711,7	1086,0	
LTT1_p1F_10x5_100%_17	280,0	712,1	1086,1	
LTT1_p1F_10x5_100%_18	280,0	711,9	1086,2	
LTT1_p1F_10x5_100%_10	278,1	712,8	1086,3	
LTT1_p1F_10x5_100%_20	280,3	712,0	1086,4	

Appendices

LTT1_p1F_10x5_100%_14	280,0	712,5	1086,4	
LTT1_p1F_10x5_100%_8	280,4	712,5	1086,4	
LTT1_p1F_10x5_100%_9	280,5	712,5	1086,4	
LTT1_p1F_10x5_100%_3	279,8	712,0	1086,5	
LTT1_p1F_10x5_100%_11	280,9	712,8	1086,8	
LTT1_p1F_10x5_100%_16	281,4	712,5	1086,9	
LTT1_p1F_10x5_100%_6	279,8	712,9	1086,9	
LTT1_p1F_10x5_100%_19	280,4	712,6	1087,0	
LTT1_p1F_10x5_100%_16	325,2		1090,1	Magn
LTT1_p1F_10x5_100%_14	325,9		1091,3	Magn
LTT1_p1F_10x5_100%_20	324,2		1091,5	Magn
LTT1_p1F_10x5_100%_19	323,7	735,6	1092,9	Magn
LTT1_p1F_10x5_100%_13	325,9		1092,9	Magn
LTT1_p1F_10x5_100%_5	324,8		1093,4	Magn
LTT1_p1F_10x5_100%_1	327,3		1093,5	Magn
LTT1_p1F_10x5_100%_7	325,2	736,3	1094,1	Magn
LTT1_p1F_10x5_100%_12	325,7		1094,6	Magn
LTT1_p1F_10x5_100%_10	324,6		1094,6	Magn
LTT1_p1F_10x5_100%_8	326,9		1095,2	Magn
LTT1_p1F_10x5_100%_4			1095,5	Magn
LTT1_p2A_10x5_100%_6	280,0	711,8	1085,9	
LTT1_p2A_10x5_100%_9	279,9	711,6	1086,0	
LTT1_p2A_10x5_100%_10	280,8	712,8	1086,4	
LTT1_p2A_10x5_100%_13	281,5	712,5	1086,4	
LTT1_p2A_10x5_100%_14	280,7	712,4	1086,5	
LTT1_p2A_10x5_100%_5	279,9	712,8	1086,6	
LTT1_p2A_10x5_100%_3	281,7	712,7	1086,8	
LTT1_p2A_10x5_100%_16	281,8	712,3	1086,8	
LTT1_p2A_10x5_100%_17	281,2	712,7	1086,8	
LTT1_p2A_10x5_100%_8	282,8	712,5	1086,9	
LTT1_p2A_10x5_100%_7	282,1	712,8	1086,9	
LTT1_p2A_10x5_100%_11	281,7	712,3	1086,9	
LTT1_p2A_10x5_100%_20	280,9	712,3	1086,9	
LTT1_p2A_10x5_100%_4	281,4	712,8	1087,0	
LTT1_p2A_10x5_100%_18	280,8	713,0	1087,0	
LTT1_p2A_10x5_100%_12	281,8	713,7	1087,0	
LTT1_p2A_10x5_100%_2	282,3	713,5	1087,3	
LTT1_p2A_10x5_100%_15	281,9	713,2	1087,5	
LTT1_p2A_10x5_100%_20	324,9	736,5	1094,2	Magn
LTT1_p2A_10x5_100%_11	326,4	736,5	1094,6	Magn
LTT1_p2A_10x5_100%_10			1095,0	Magn
LTT1_p2A_10x5_100%_6			1095,1	Magn
LTT1_p2B_10x5_100%_5			1085,4	
LTT1_p2B_10x5_100%_6	207	704,2	1085,6	
LTT1_p2B_10x5_100%_3	328,7		1093,1	Magn
LTT1_p2B_10x5_100%_11	327,7	737,0	1093,5	Magn

Appendices

LTT1_p2C_10x5_100%_3	324,8	738,0	1095,2	Magn
LTT1_p2C_15x5_100%_7_sar	325,0	736,8	1095,3	Magn
LTT2_p1A_5x4_100%_1	281,4		1086,5	
LTT2_p1A_5x4_100%_2	282,8	711,9	1086,2	
LTT2_p1A_5x4_100%_3	283,3		1085,3	
LTT2_p1A_5x4_100%_4	278,9		1085,9	
LTT2_p1A_5x4_100%_5	276,7	713,0	1086,3	
LTT2_p1A_5x4_100%_6	279,5	711,5	1086,1	
LTT2_p1A_5x4_100%_7	278,9	711,9	1086,1	
LTT2_p1A_5x4_100%_8	283,9	774,3	1084,8	
LTT2_p1A_5x4_100%_9			1085,9	
LTT2_p1A_5x15_100%_10	282,2		1086,2	
LTT2_p1A_5x4_100%_11	283,4		1085,3	
LTT2_p1A_5x4_100%_12	282,7		1085,2	
LTT2_p1A_5x4_100%_13	278,1	712,2	1086,0	
LTT2_p1A_5x4_100%_14	280,0	712,6	1087,1	
LTT2_p1A_5x4_100%_15	280,7	712,0	1085,7	
LTT2_p1A_5x4_100%_16			1085,9	
LTT2_p1A_5x4_100%_17	280,3	712,7	1086,6	
LTT2_p1A_5x15_100%_17	281,0	713,0	1087,2	
LTT2_p1A_5x15_100%_18	280,6	712,3	1086,1	
LTT2_p1A_5x15_100%_19	280,0	712,0	1086,3	
LTT2_p1A_5x4_100%_20	282,0		1087,1	
LTT2_p1A_5x4_100%_21	281,1	712,5	1086,2	
LTT2_p1A_5x4_100%_22	280,8	712,3	1086,8	
LTT2_p1A_5x4_100%_23	281,9	712,8	1087,0	
LTT2_p1A_5x4_100%_24	281,8	712,9	1086,8	
LTT2_p1A_5x4_100%_25	281,0	712,4	1086,6	
LTT2_p1A_5x4_100%_26	281,1	711,0	1086,4	
LTT2_p1A_5x4_100%_27	281,3	712,9	1087,1	
LTT2_p1A_5x4_100%_28	281,5	713,0	1087,1	
LTT2_p1A_5x4_100%_29	281,1	712,4	1086,6	
LTT2_p1A_5x4_100%_30	280,8	712,6	1086,1	
LTT2_p1A_5x15_100%_31			1086,1	
LTT2_p1A_5x4_100%_32	282,5	713,8	1087,6	
LTT2_p1A_5x4_100%_32	325,8		1093,3	Magn
LTT2_p1A_5x4_100%_33	279,3	712,1	1085,5	
LTT2_p1A_5x4_100%_33	324,4			Magn
LTT2_p1A_5x4_100%_34	280,2	711,9	1086,3	
LTT2_p1A_5x4_100%_34	323,2			Magn
LTT2_p1A_5x4_100%_35	280,6	712,3	1086,7	
LTT2_p1A_5x4_100%_36	280,6	712,8	1086,7	
LTT2_p1A_5x4_100%_37	281,3	713,2	1087,3	
LTT2_p1A_5x4_100%_38	276,1	711,9	1085,0	
LTT2_p1A_5x4_100%_39	280,0	711,9	1086,1	
LTT2_p1A_5x4_100%_40	281,0	713,5	1086,7	
LTT2_p1A_5x4_100%_41	279,8	712,4	1086,9	
LTT2_p1A_5x4_100%_42	280,8	711,9	1087,2	

Appendices

LTT2_p1A_5x4_100%_43	280,1	712,5	1086,2	
LTT2_p1A_5x4_100%_44	280,9	712,1	1086,1	
LTT2_p1A_5x4_100%_45	283,0		1087,3	
LTT2_p1A_5x4_100%_45MA	385,6			Magn
LTT2_p1A_5x4_100%_46	280,5	712,0	1086,2	
LTT2_p1A_5x4_100%_47	280,7	712,2	1086,7	
LTT2_p1A_5x4_100%_48	281,8	713,0	1087,1	
LTT2_p1A_5x15_100%_49			1086,1	
LTT2_p1A_5x4_100%_50	280,6	712,0	1086,9	
LTT2_p1A_5x4_100%_51	279,5	711,5	1085,9	
LTT2_p1A_5x4_100%_52	280,7	712,5	1086,5	
LTT2_p1A_5x4_100%_53	283,1		1087,1	
LTT2_p1A_5x4_100%_54	279,0	711,4	1085,6	
LTT2_p1A_5x4_100%_55	282,6		1087,1	
LTT2_p1A_5x4_100%_56	280,7		1086,7	
LTT2_p1A_5x4_100%_56	325,8		1093,0	Magn
LTT2_p1A_5x4_100%_57	281,2	712,4	1086,4	
LTT2_p1A_5x4_100%_58	281,0	712,7	1086,6	
LTT2_p1A_5x4_100%_58MA	328,0		1094,5	Magn
LTT2_p1A_5x4_100%_59	280,7	712,5	1086,5	
LTT2_p1A_5x4_100%_60	279,7	712,4	1086,4	
LTT2_p1A_5x4_100%_61	280,0	712,0	1086,5	
LTT2_p1A_5x4_100%_62	282,9		1087,2	
LTT2_p1A_5x4_100%_63	280,2	712,2	1086,7	
LTT2_p1A_5x4_100%_64	280,9	712,4	1087,0	
LTT2_p1A_5x4_100%_65	280,9	712,0	1086,9	
LTT2_p1A_5x4_100%_66			1086,9	
LTT2_p1A_5x4_100%_67	279,7	712,1	1086,1	
LTT2_p1A_5x15_100%_68	281,4	712,9	1086,4	
LTT2_p1A_5x4_100%_69	280,0	712,1	1085,6	
LTT2_p1A_5x4_100%_70	280,5	712,4	1086,4	
LTT2_p1B_5x4_100%_1	281,8	713,4	1087,2	
LTT2_p1B_5x15_100%_3	286,4		1087,3	
LTT2_p1B_5x15_100%_4	280,1	713	1087,6	
LTT2_p1B_5x15_100%_4MA	323,6		1093,2	Magn
LTT2_p1B_5x4_100%_5	280,6	713	1085,6	
LTT2_p1B_5x4_100%_6	281,8		1087,1	
LTT2_p1B_5x4_100%_7	278,8	712,1	1085,6	
LTT2_p1B_5x4_100%_8	280,7	712,7	1086,1	
LTT2_p1B_5x4_100%_9	279,9	712,1	1086,2	
LTT2_p1B_5x4_100%_10	282,5	712,2	1086	
LTT2_p1B_5x4_100%_11	281,3	712,4	1086,8	
LTT2_p1B_5x4_100%_12	288,0		1088,2	
LTT2_p1B_5x15_100%_12MA	326,1		1094,6	Magn
LTT2_p1B_5x4_100%_13	280,3	713,0	1086,5	
LTT2_p1B_5x4_100%_14	280,1	713,4	1086,9	

Appendices

LTT2_p1B_5x4_100%_15	281,1	712,6	1086,4	
LTT2_p1B_5x4_100%_16	280,1		1086,2	
LTT2_p1B_5x4_100%_17	279,8	712,0	1086,3	
LTT2_p1B_5x4_100%_18	280,8	712,5	1086,7	
LTT2_p1B_5x15_100%_19			1086,5	
LTT2_p1B_5x4_100%_20	280,9	713,1	1087,4	
LTT2_p1B_5x4_100%_21	281,0	712,4	1087,5	
LTT2_p1B_5x4_100%_22	280,8	711,8	1086,0	
LTT2_p1B_5x4_100%_23	281,2	711,9	1085,7	
LTT2_p1B_5x15_100%_23M	325,1		1093,4	Magn
LTT2_p1B_5x4_100%_24	281,2	712,7	1086,9	
LTT2_p1B_5x4_100%_25	280,4	712,0	1085,9	
LTT2_p1B_5x4_100%_26	281,0	712,5	1086,4	
LTT2_p1B_5x4_100%_27	280,7	712,1	1086,4	
LTT2_p1B_5x4_100%_28	281,3	711,7	1087,0	
LTT2_p1B_5x4_100%_29	281,0	713,3	1086,3	
LTT2_p1B_5x4_100%_30	280,2	712,7	1086,5	
LTT2_p1B_5x4_100%_31			1084,7	
LTT2_p1B_5x4_100%_32	280,7	712,3	1086,1	
LTT2_p1B_5x4_100%_33	281,0	711,8	1086,5	
LTT2_p1B_5x4_100%_34	281,3	713,0	1087,0	
LTT2_p1B_5x4_100%_35	280,4	712,1	1085,4	
LTT2_p1B_5x4_100%_36	280,1	712,0	1086,1	
LTT2_p1B_5x15_100%_36M	324,6		1093,7	Magn
LTT2_p1B_5x4_100%_37	280,0	712,1	1086,2	
LTT2_p1B_5x15_100%_37M	323,7		1093,8	Magn
LTT2_p1B_5x4_100%_38	281,0	712,3	1086,6	
LTT2_p1B_5x4_100%_39	280,1	712,8	1086,1	
LTT2_p1B_5x4_100%_40	280,4	712,8	1086,2	
LTT2_p1B_5x4_100%_41	280,0	712,6	1086,4	
LTT2_p1B_5x15_100%_42	280,4	712,0	1086,3	
LTT2_p1B_5x4_100%_43	281,1	711,9	1085,6	
LTT2_p1B_5x4_100%_44	280,7	712,9	1087,1	
LTT2_p1B_5x4_100%_45	280,6	711,5	1086,1	
LTT2_p1B_5x4_100%_46	280,6	713,2	1086,8	
LTT2_p1B_5x4_100%_47	280,7	712,9	1087,0	
LTT2_p1B_5x4_100%_48	279,9	712,5	1086,2	
LTT2_p1B_5x15_100%_48M	324,9		1091,5	Magn
LTT2_p1B_5x15_100%_49	281,0	713,2	1087,0	
LTT2_p1B_5x15_100%_49M	324,0		1093,8	Magn
LTT2_p1B_5x15_100%_50			1086,5	
LTT2_p1B_5x15_100%_50_U	258,2	389,0	688,6	ufo
LTT2_p1C_5x4_100%_1	281,8	712,8	1086,8	
LTT2_p1C_5x15_100%_2	284,1	712,0	1085,8	
LTT2_p1C_5x15_100%_2M	323,7		1092,7	Magn
LTT2_p1C_5x15_100%_3	280,5	713,4	1085,8	
LTT2_p1C_5x15_100%_3M			1093,9	Magn

Appendices

LTT2_p1C_5x4_100%_4	279,3	712,1	1085,6	
LTT2_p1C_5x15_100%_4MA	322,0		1093,8	Magn
LTT2_p1C_5x15_100%_5MA	325,1	736,6	1094,0	Magn
LTT2_p1C_5x15_100%_6	281,4	711,8	1086,0	
LTT2_p1C_5x15_100%_6MA	325,1		1091,8	Magn
LTT2_p1C_5x15_100%_7	283,4	712,7	1086,0	
LTT2_p1C_5x15_100%_7MA	324,8	735,9	1093,1	Magn
LTT2_p1C_5x4_100%_8	280,7	711,9	1086,4	
LTT2_p1C_5x4_100%_9	281,8	713,2	1086,9	
LTT2_p1C_5x15_100%_9MA	325,4	736,1	1093,3	Magn
LTT2_p1C_5x4_100%_10	279,3	712,2	1085,9	
LTT2_p1C_5x15_100%_10MA	323,8		1094,2	Magn
LTT2_p1C_5x4_100%_11	280,5	713,0	1086,7	
LTT2_p1C_5x4_100%_12	281,2	712,2	1086,8	
LTT2_p1C_5x15_100%_12MA	325,5	735,4	1094,9	Magn
LTT2_p1C_5x4_100%_13	283,7		1087,4	
LTT2_p1C_5x15_100%_13MA	325,9		1094,7	Magn
LTT2_p1C_5x15_100%_14	281,4	711,5	1086,7	
LTT2_p1C_5x4_100%_15	280,2	712,2	1086,4	
LTT2_p1C_5x15_100%_15MA	324,0	736,6	1092,6	Magn
LTT2_p1C_5x4_100%_16	281,4	712,3	1086,7	
LTT2_p1C_5x15_100%_16MA	325,7	736,7	1093,6	Magn
LTT2_p1C_5x15_100%_17	280,4	711,9	1085,8	
LTT2_p1C_5x15_100%_17MA	323,7	735,9	1093,5	Magn
LTT2_p1C_5x15_100%_18	325,3	738,1	1087,1	
LTT2_p1C_5x15_100%_18MA	283,1	712,5	1094,3	Magn
LTT2_p1C_5x4_100%_20	279,3	711,5	1085,2	
LTT2_p1C_5x15_100%_21	280,9	712,0	1086,0	
LTT2_p1C_5x15_100%_21MA	324,9	735,3	1094,4	Magn
LTT2_p1C_5x4_100%_22	280,4	712,7	1086,1	
LTT2_p1C_5x4_100%_23	279,4	711,2	1085,4	
LTT2_p1C_5x4_100%_24	323,9	735,6	1086,9	
LTT2_p1C_5x15_100%_24MA	283,0	712,9	1094,3	Magn
LTT2_p1C_5x4_100%_25	280,6	712,4	1086,6	
LTT2_p1C_5x15_100%_25MA	324,8		1093,9	Magn
LTT2_p1C_5x4_100%_26	280,4		1086,5	
LTT2_p1C_5x4_100%_27	278,4	712,7	1086,4	
LTT2_p1C_5x4_100%_28	280,2	711,5	1085,5	
LTT2_p1C_5x4_100%_29	280,6	712,1	1086,4	
LTT2_p1C_5x15_100%_29MA	325,0		1094,1	Magn
LTT2_p1C_5x4_100%_30	282,1		1086,5	
LTT2_p1C_5x15_100%_29MA	324,9	736,9	1094,8	Magn
LTT2_p1C_5x4_100%_31	279,9	712,6	1086,0	
LTT2_p1C_5x4_100%_32	280,5	712,3	1086,0	
LTT2_p1C_5x15_100%_32MA	324,6			Magn
LTT2_p1C_5x4_100%_33	280,8	712,1	1086,3	
LTT2_p1C_5x15_100%_33MA	324,6		1093,6	Magn
LTT2_p1C_5x4_100%_34	280,1	712,4	1086,5	

Appendices

LTT2_p1C_5x15_100%_34	323,1		1095,2	Magn
LTT2_p1C_5x4_100%_35	280,3	711,6	1086,0	
LTT2_p1C_5x4_100%_36	283,0		1085,6	
LTT2_p1C_5x4_100%_37	281,9	712,9	1086,9	
LTT2_p1C_5x15_100%_37	325,6		1094,3	Magn
LTT2_p1C_5x4_100%_38	281,2	712,3	1086,1	
LTT2_p1C_5x15_100%_38	324,8	734,6	1094,0	Magn
LTT2_p1C_5x15_100%_39	282,7		1086,1	
LTT2_p1C_5x15_100%_39	323,1		1093,7	Magn
LTT2_p1C_5x4_100%_40	282,1		1085,8	
LTT2_p1C_5x15_100%_40				Magn
LTT2_p1C_5x4_100%_41	279,5	713,2	1086,5	
LTT2_p1C_5x15_100%_41	324,8		1095,4	Magn
LTT2_p1C_5x4_100%_42	287,2	711,0	1084,7	
LTT2_p1C_5x4_100%_43	278,9	712,3	1085,8	
LTT2_p1C_5x15_100%_43	324,1		1093,7	Magn
LTT2_p1C_5x4_100%_44	281,1	713,0	1086,9	
LTT2_p1C_5x4_100%_45	279,3	712,0	1085,8	
LTT2_p1C_5x15_100%_45	323,4		1094,1	Magn
LTT2_p1C_5x4_100%_46			1086,5	
LTT2_p1C_5x15_100%_47	281,7	712,7	1086,1	
LTT2_p1C_5x15_100%_47	325,5		1094,6	Magn
LTT2_p1C_5x4_100%_48	280,6	713,2	1085,6	
LTT2_p1C_5x4_100%_49	284,8	713,7	1085,7	
LTT2_p1C_5x4_100%_50	281,4		1086,6	
LTT2_p1C_5x15_100%_50	324,9	735,4	1093,3	Magn
LTT2_p1D_5x4_100%_1	283,6	711,5	1086,8	
LTT2_p1D_5x4_100%_30	279,5	711,3	1085,3	
LTT2_p1D_5x4_100%_15	287,0		1085,9	
LTT2_p1D_5x4_100%_21	280,0	712,0	1086,1	
LTT2_p1D_5x4_100%_2	279,0	712,1	1086,1	
LTT2_p1D_5x4_100%_34	283,5		1086,2	
LTT2_p1D_5x4_100%_18	280,5	712,0	1086,2	
LTT2_p1D_5x4_100%_38	286,0		1086,2	
LTT2_p1D_5x4_100%_22	281,5	712,3	1086,3	
LTT2_p1D_5x4_100%_13_UF	281,6	711,9	1086,3	
LTT2_p1D_5x4_100%_14	280,6	712,6	1086,3	
LTT2_p1D_5x4_100%_17	280,7	712,4	1086,4	
LTT2_p1D_5x4_100%_39	282,7	712,3	1086,4	
LTT2_p1D_5x4_100%_29	280,3	713,1	1086,4	
LTT2_p1D_5x4_100%_19	281,0	712,4	1086,5	
LTT2_p1D_5x4_100%_20	281,7	711,6	1086,6	
LTT2_p1D_5x4_100%_37	279,8	712,3	1086,7	
LTT2_p1D_5x4_100%_28	280,6	712,7	1086,9	
LTT2_p1D_5x4_100%_33	212		1087,0	
LTT2_p1D_5x4_100%_16	281,4	712,6	1087,2	
LTT2_p1D_5x4_100%_41		714,1	1087,7	

Appendices

LTT2_p1D_5x15_100%_50	281,1	712,5	1089,3	
LTT2_p1D_5x15_100%_49	279,9	711,8	1089,4	
LTT2_p1D_5x15_100%_48_ca	280,1	711,9	1089,5	
LTT2_p1D_5x4_100%_47	280,7	712,5	1089,6	
LTT2_p1D_5x4_100%_46	281,7	713,3	1089,7	
LTT2_p1D_5x4_100%_45	281,7	712,4	1089,7	
LTT2_p1D_5x4_100%_44	281,0	712,2	1089,8	
LTT2_p1D_5x4_100%_43	280,0	711,4	1089,9	
LTT2_p1D_5x4_100%_42			1090,0	
LTT2_p1D_5x4_100%_41MA	325,4		1090,0	Magn
LTT2_p1D_5x4_100%_23	323,3	731,3	1090,5	Magn
LTT2_p1D_5x4_100%_14MA	325,1		1091,1	Magn
LTT2_p1D_5x4_100%_13MA	324,9		1091,5	Magn
LTT2_p1D_5x4_100%_17MA	323,2		1092,1	Magn
LTT2_p1D_5x4_100%_38MA	325,9		1092,5	Magn
LTT2_p1D_5x4_100%_33MA	324,0		1092,5	Magn
LTT2_p1D_5x4_100%_4	324,9		1093,0	Magn
LTT2_p1D_5x4_100%_5	327,1		1093,0	Magn
LTT2_p1D_5x4_100%_8	324,9		1093,0	Magn
LTT2_p1D_5x4_100%_31	323,9		1093,0	Magn
LTT2_p1D_5x4_100%_1MA	323,0		1093,0	Magn
LTT2_p1D_5x4_100%_15MA	325,9		1093,2	Magn
LTT2_p1D_5x4_100%_22MA	325,5		1093,3	Magn
LTT2_p1D_5x4_100%_18MA	324,2		1093,4	Magn
LTT2_p1D_5x4_100%_19MA	324,4		1093,5	Magn
LTT2_p1D_5x4_100%_6	324,9		1093,9	Magn
LTT2_p1D_5x4_100%_7	324,9		1093,9	Magn
LTT2_p1D_5x4_100%_9	326,0		1093,9	Magn
LTT2_p1D_5x4_100%_10	324,9		1093,9	Magn
LTT2_p1D_5x4_100%_11	326,0	737,8	1093,9	Magn
LTT2_p1D_5x4_100%_12	324,9		1093,9	Magn
LTT2_p1D_5x4_100%_25	322,5		1093,9	Magn
LTT2_p1D_5x15_100%_3	325,0		1094,0	Magn
LTT2_p1D_5x15_100%_26	325,1		1094,0	Magn
LTT2_p1D_5x4_100%_24	324,9		1094,0	Magn
LTT2_p1D_5x4_100%_35	326,0	737,9	1094,0	Magn
LTT2_p1D_5x4_100%_40	323,8		1094,0	Magn
LTT2_p1D_5x4_100%_39MA	326,1		1094,2	Magn
LTT2_p1D_5x4_100%_2MA	324,9		1094,6	Magn
LTT2_p1D_5x4_100%_37MA	323,4		1094,9	Magn
LTT2_p1D_5x4_100%_32	326,0		1094,9	Magn
LTT2_p1D_5x4_100%_36	326,0		1094,9	Magn
LTT2_p1D_5x4_100%_34MA	325,0		1094,9	Magn
LTT2_p1D_5x4_100%_50MA	324,8			Magn
LTT2_p1D_5x4_100%_49MA	324,2			Magn
LTT2_p1D_5x4_100%_48MA	324,1			Magn
LTT2_p1D_5x4_100%_47MA	326,2			Magn
LTT2_p1D_5x4_100%_44MA	324,2			Magn

Appendices

LTT2_p1D 5x4_100%_43	324,9			Magn
LTT2_p1D 5x4_100%_42	324,5			Magn
LTT2_p1D 5x4_100%_20	324,2			Magn
LTT2_p1D 5x4_100%_21	324,2			Magn
LTT2_p1D 5x4_100%_27_Rt			RT	Rt
LTT4_A 10x5_100%_15	280,2	712,4	1085,9	
LTT4_A 10x5_100%_9	280,4	712,0	1085,9	
LTT4_A 10x5_100%_7			1086,1	
LTT4_A 10x5_100%_5	279,7	712,3	1086,1	
LTT4_A 10x5_100%_6	281,0	712,5	1086,5	
LTT4_A 10x5_100%_14	280,8	713	1086,5	
LTT4_A 10x5_100%_17	280,2	712,4	1086,6	
LTT4_A 10x5_100%_3	280,7	712,3	1086,7	
LTT4_A 10x5_100%_16	281,2	713,4	1086,8	
LTT4_A 10x5_100%_18	281,0	712,6	1086,8	
LTT4_A 10x5_100%_4	280,2	712,6	1086,9	
LTT4_A 10x5_100%_10	280,5	711,7	1086,9	
LTT4_A 10x5_100%_13	280,2	712,3	1086,9	
LTT4_A 10x5_100%_8	280,9	712,8	1087,0	
LTT4_A 10x5_100%_2	281,1	712,6	1087,1	
LTT4_A 10x5_100%_1	281,5	713,4	1087,2	
LTT4_A 10x5_100%_12	281,7	712,8	1087,2	
LTT4_A 10x5_100%_19	281,6	713,4	1087,3	
LTT4_A 10x5_100%_11	281,5		1087,7	
LTT4_A 10x5_100%_4	326,0		1092,4	Magn
LTT4_A 10x5_100%_13	324,3		1093,5	Magn
LTT4_A 10x5_100%_9	323,9			Magn
LTT4_A 10x5_100%_18	322,2			Magn
LTT4_A 10x5_100%_19	321,8			Magn
LTT4_B 10x5_100%_1	279,6	712,4	1086,3	
LTT4_foram3_shell_3x2_50%		709,4	1083,6	
LTT4_B 10x5_100%_10		703,6	1084,8	
LTT4_B 10x5_100%_8	268,8	711,4	1084,8	
LTT4_B 10x5_100%_9	265,4	711,8	1085,0	
LTT4_foram6_internal			1085,5	
LTT4_foram1_shellinternalwa	283,5	711,9	1085,5	
LTT4_foram6_XX1_4x4_50%	281,0	711,3	1085,5	
LTT4_foram3_shell_2x5_50%	280	711	1086	
LTT4_foram1_shell_2x5_1		711,4	1085,6	
LTT4_foram1_internal			1085,7	
LTT4_foram3_shell_5x3_50%	280,6	711,9	1085,7	
LTT4_foram2_shell_3x5_3	280,9	711,1	1085,7	
LTT4_foram5_internal	335,1		1085,7	
LTT4_foram3_internal	14		1086,0	
LTT4_foram6_shell_4x2_50%	281,2	711,5	1086,0	
LTT4_B 10x5_100%_14	280,8	712,1	1086,0	

Appendices

LTT4 foram5_internal_filling	284,9	711,6	1086,0	
LTT4 B 10x5_100% 20	280,4	712,6	1086,1	
LTT4 foram6_shell_4x2_50%	283,5	713,1	1086,1	
LTT4 foram1_internal_filling			1086,1	
LTT4 foram1_shell_2x5_2	281,0		1086,2	
LTT4 B 10x5_100% 6	278,8	713,1	1086,4	
LTT4 foram6_XX2_4x4_50%	282,3	712,6	1086,4	
LTT4 B 10x5_100% 7 calcit	280,3	712,6	1086,5	
LTT4 foram1_shell_4x2_50%	281,6		1086,7	
LTT4 B 10x5_100% 19	280,6	712,2	1086,7	
LTT4 B 10x5_100% 17	282,6	712,0	1086,7	
LTT4 B 10x5_100% 4	281,2	712,5	1086,7	
LTT4 B 10x5_100% 12	281,2	712,4	1086,8	
LTT4 B 10x5_100% 11 calci	280,8	712,5	1086,8	
LTT4 foram6_XX1_4x4_50%			1086,9	
LTT4 B 10x5_100% 13		713,1	1086,9	
LTT4 foram6_XX2_4x4_50%	284,0	713,1	1087,0	
LTT4 foram2_shell_3x5_2Ne	281,2	712,6	1087,1	
LTT4 B 10x5_100% 5	280,2	713,2	1087,1	
LTT4 B 10x5_100% 15	280,8	713,0	1087,2	
LTT4 B 10x5_100% 18	281,8	713,0	1087,2	
LTT4 foram1_shell_2x2_50%			1087,4	
LTT4 B 10x5_100% 16	281,2	713,7	1087,5	
LTT4 foram1_internal_filling	282,1		1087,6	
LTT4 B 10x5_100% 13	323,4		1091,6	Magn
LTT4 B 10x5_100% 14MAG	322,7		1094,5	Magn
LTT4 B 10x5_100% 16MAG	322,3		1095,5	Magn
LTT4 B 10x5_100% 1MAGN	322,2			Magn
LTT4 B 10x5_100% 15MAG	321,6			Magn
LTT4 B 10x5_100% 17MAG	321,7			Magn
LTT4 B 10x5_100% 18MAG	322,7			Magn
L18 8 5x15_100% 1		327,2		1093,22
L18 8 5x15_100% 2		326,4	737,182	1093,85
L18 8 5x15_100% 3	287,865	327,2	737,668	1094,45
L18 8 5x15_100% 4		324,9	737,77	1094,68
L18 8 5x15_100% 5		324,9	738,74	1092,93
L18 8 5x15_100% 6		324,9	736,8	1093,81
L18 8 5x15_100% 7		325,3	736,8	1093,81
L18 8 5x15_100% 8		324,9		1093,81
L18 8 5x15_100% 9		324,9	736,8	1092,93
L18 8 5x15_100% 10		324,9	736,8	1094,68
L18 9 5x15_100% 2		326,1	738,64	1093,58
L18 9 5x15_100% 3	215	326,6	738,64	1094,45
L18 9 5x15_100% 4		327,1	737,71	1095,4
L18 9 5x15_100% 5		324,3	736,74	1094,52

Appendices

L18 9 5x15 100% 6		326,1	737,71	1093,65
L18 9 5x15 100% 7		327,1	738,68	1094,52
L18 9 5x15 100% 8		327,1		1094,68
L18 9 5x15 100% 9		325	736,74	1093,65
L18 9 5x15 100% 10		327,1	736,74	1093,65
L18 10 5x15 100% 1		326,1	736,74	1094,52
L18 10 5x15 100% 2	288,32	328,2	739,71	1095,55
L18 10 5x15 100% 3	287,29	328,2	738,68	1094,52
L18 10 5x15 100% 4	288,32	328,2	739,71	1095,55
L18 10 5x15 100% 5		327,1	739,71	1094,68
L18 10 5x15 100% 6		324,9	737,77	1094,68
L18 10 5x15 100% 7		328,2	739,71	1094,68
L18 10 5x15 100% 8		327,1	737,77	1094,68
L18 10 5x15 100% 9		327,1	738,74	1094,68
L18 10 5x15 100% 10		326	738,74	1095,55
L18 1 5x15 100% 1		327,2		1093,28
L18 1 5x15 100% 2		326,1	737,58	1094,15
L18 1 5x15 100% 3	288,42	327,2	737,58	1094,15
L18 1 5x15 100% 4		326,1		1093,28
L18 1 5x15 100% 5		326,1	737,58	1094,15
L18 1 5x15 100% 6	321,593	329,1		1093,97
L18 1 5x15 100% 7		325		1094,15
L18 1 5x15 100% 8		326,1	737,58	1094,15
L18 1 5x15 100% 9	288,42	325	736,61	1095,02
L18 1 5x15 100% 10		326,1		1094,15
L18 4 5x15 100% 1		326,1		1094,15
L18 4 5x15 100% 2		326,1		1093,28
L18 4 5x15 100% 3		325		1093,28
L18 4 5x15 100% 4		325	737,58	1093,28
L18 4 5x15 100% 5		325		1093,28
L18 4 5x15 100% 6	288,42	325		1092,49
L18 4 5x8 100% 7		326,1	735,64	1094,15
L18 4 5x8 100% 8		325	737,58	1093,28
L18 4 5x8 100% 9		325,7		1093,8
L18 4 5x8 100% 10		325		1094,15
L18 5 XX 5x15 100% 1		321,8		1036,01
L18 5 XX 5x15 100% 2		321,8		1036,01
L18 5 5x15 100% 3		323,9		1093,28
L18 5 5x15 100% 4		321,8		1062,57
L18 5 5x15 100% 5		325	736,61	1094,15
L18 5 5x15 100% 6		326,4	736,342	1094,19
L18 5 5x15 100% 7		327,2		1093,28
L18 5 5x15 100% 8		324,7		1094,19
L18 5 5x15 100% 9		325	736,61	1093,28
L18 5 5x15 100% 10		325	736,61	1094,15
L18 5b 5x8 100% 1	212,88,6	325,2	736,654	1093,91
L18 5b 5x8 100% 2	288,845	326,2	737,151	1093,25
L18 5b 5x8 100% 3		324,8		1092,5

Appendices

L18_5b_5x8_100%_4		327,6		1093,78
L18_5b_5x8_100%_5	45	319,4	737,001	1093,24
L18_5b_5x8_100%_6		324,4	736,128	1093,24
L18_5b_5x8_100%_7		327,3		1093,2
L18_5b_5x8_100%_8		325,4		1093,6
L18_5b_5x8_100%_9	288,947	324,8	736,521	1093,75
L18_5b_5x8_100%_10		324,2		1093,22
L18_6_5x8_100%_1	286,09	328,3		1093,38
L18_6_5x8_100%_2		324,4		1093,85
L18_6_5x4_100%_3		324,9		1093,45
L18_6_5x8_100%_4		325,7		1094,97
L18_6_5x4_100%_5		324,7		1094,04
L18_6_5x4_100%_6		324,7		1093,97
L18_6_5x4_100%_7		326,1		1094,07
L18_6_5x4_100%_8		326,1	737,758	1093,59
L18_6_5x4_100%_9		324,7	736,433	1093,86
L18_6_5x4_100%_10		327,6		1093,66
L18_7_5x4_100%_1		325,4	736,087	1094,13
L18_7_5x4_100%_2	287,7	326,3	736,553	1093,98
L18_7_5x4_100%_3	287,3	323,7		1092,72
L18_7_5x4_100%_4		327		1093,52
L18_7_5x4_100%_5		323,2		1092,22
L18_7_5x4_100%_6		324,7	734,461	1093,14
L18_7_5x4_100%_7		325,1	737,003	1093,52
L18_7_5x4_100%_8		325,1	737,227	1094,37
L18_7_5x4_100%_9		322,6		1089,53
L18_7_5x4_100%_10		323,6		1093,26